The Influence of High-Frequency Effects due to Inverter Excitation on Permanent Magnet Synchronous Machines

Zur Erlangung des akademischen Grades eines

DOKTORS DER INGENIEURWISSENSCHAFTEN (Dr.-Ing.)

von der KIT-Fakultät für Elektrotechnik und Informationstechnik des
Karlsruher Instituts für Technologie (KIT)

genehmigte

DISSERTATION

von

M.Sc. Narciso Genovese Marmolejo
geb. in San Diego, Kalifornien

Tag der mündlichen Prüfung: 17.05.2024
Hauptreferent: Prof. Dr.-Ing. Martin Doppelbauer
Korreferent: Prof. Dr.-Ing. Dieter Gerling

Erklärung der Selbständigkeit

Hiermit erkläre ich, dass ich die vorliegende Arbeit selbstständig und ohne fremde Hilfe verfasste und keine anderen Hilfsmittel als die angegebenen verwendete.

Insbesondere versichere ich, dass ich alle wörtlichen und sinngemäßigen Übernahmen aus anderen Werken als solche kenntlich machte.

Kurzfassung

Die Reduzierung der Emissionen ist entscheidend, besonders jetzt, während dem globalen Klima seinen ersten Wendepunkten nähert. Daher ist es nicht nur dringlich, jahrzehntelanges Wissen über elektrische Antriebe in Straßen- und Schienenfahrzeuge zu integrieren, sondern auch Maschinen zu entwickeln, die Energie aus erneuerbaren Quellen gewinnen. Ein Teil der erneuerbaren Energiequellen, wie Wind- und Wasserkraft nutzen auch elektrische Antriebe. Die Steigerung ihrer Effizienz würde daher dazu beitragen, dass Elektrofahrzeuge mit der derzeitigen Infrastruktur schneller die Gewinnschwelle bei ihren Produktionsemissionen erreichen und weniger elektrische Maschinen pro produzierter Energieeinheit benötigen, sobald diese Infrastruktur entkarbonisiert ist. Im Großen und Ganzen gibt es zwei Hauptdimensionen, um die Effizienz von E-Antrieben zu steigern: Hardware- und Softwaredesign. Die Software-Entwurfsphase beinhaltet die Maschinensteuerung, die binäre Vektoren für den Wechselrichter berechnet. Diese widerum hängen von Arbeitspunkten ab, deren Eigenschaften die Hardware Entwurf definiert. In dieser Arbeit geht es darum, diese Symbiose zu klären und für elektrische Antriebe im Allgemeinen und für duale Drehstromantriebe im Besonderen zu optimieren. Grundlegende Frequenzeigenschaften des Antriebs, DC-Spannungspegel, Spitzen- und Dauerleistung und andere Designüberlegungen werden typischerweise in der Hardware-Designphase ohne Berücksichtigung der Kommutierungsfrequenzeigenschaften definiert. Diese Arbeit erweitert daher das Wissen über hochfrequenz Maschinenverlustmodelle auf arbiträrphasige und arbiträre Maschinen mit Hilfe des Kopplungskoeffizienten ς und der Erkenntnis, dass die Floquet-Theorie auch für Hochfrequenzmodelle gilt. Letzteres ermöglicht die Modellierung nichtperiodischer Nichtlinearitäten in einem synchronen Rahmen. Steuerungsfunktionen, von denen angenommen wird, dass sie keinen Einfluss auf die Maschinenverluste haben, um die Stromwelligkeit des Zwischenkreiskondensators zu reduzieren, nämlich Verschachtelung für duale Dreiphasenmaschinen, verringern den Wirkungsgrad in der Maschine nachweislich um bis zu 4% je nach Spannungsniveau. Die Kopplung zwischen Teilmaschinen und das Permeabilitätsprofil über das Drehmoment-Drehzahl-Feld erweisen sich als entscheidend für die Bestimmung der Erhöhung der Maschinenverluste durch Verschachtelung. Dabei werden verschiedene PWM-Verfahren, Kommutierungsfrequenzen und Stromabtastraten untersucht und der Stand der Technik auf duale Drehstrommmaschinen erweitert. Optimale Steuervektoren mit den vorherigen Elementen werden für jeden Betriebspunkt gefunden, was ein detailliertes Wechselrichterverlustmodell und ein Gleichgewichtsmaschinenverlustmodell erfordert. Es zeigt sich, dass eine Abtastrate von $f_{sa} = 2f_{sw}$, Stromwelligkeitsprofile nahezu bei $f_{sw} \rightarrow \infty$ aufrechterhält und dies bei sehr niedrigen Verhältnissen der Grundfrequenz zur Schaltfrequenz (f_0/f_{sw}). Alle anderen Abtastraten zwischen synchron ($f_{sa} = f_{sw}$) und $f_{sa} = 2f_{sw}$ erhöhen die Welligkeit vom Fall Synchronabtasten. Obwohl die Stromwelligkeit

wenig Einfluss auf die Verluste im Kupfer hat, dominiert sie in Kombination mit dem hochfrequenten magnetischen Permeabilitätsprofil die hochfrequenten Eisen- und Magnetverluste. Große Schaltfrequenzen sind notwendig, um Eisenverluste nahe der maximalen Leistungsgrenze und möglicherweise nahe dem Modulationsindexwert von $2/\pi$ abhängig von ς und μ zu kontrollieren. Bei niedrigen Grunddrehzahlen dominieren Umrichterverluste und wesentlich niedrigere Schaltfrequenzen sind optimal und erhöhen dort den Antriebswirkungsgrad um 1%. Die Bedeutung der Magnetsegmentierung zur Reduzierung von Hochfrequenzverlusten wird bestätigt und ein Rahmen für die Eisenabschirmung der Magnete für IPMSMs wird unter Verwendung der Poynting-Gleichung entwickelt. Magnetverluste sind wichtig, um eine Entmagnetisierung zu vermeiden und die Anforderungen an die Rotorkühlung besser zu verstehen. Es zeigt sich, dass sich Maschinenkonstruktionsfrequenzen mit Wechselrichter-induzierter Feldwelligkeit überlappen, um Magnetverluste je nach PWM-Methode zu erhöhen oder zu verringern. Insbesondere überlappt die vom Rotor aus gesehene Zahn-pro-Pol-Harmonische mit der verschmolzenen 2nd- und 4th-Subharmonischen der ersten Trägergruppe. Simulationen zeigen, dass für hochgekoppelte zweimal dreiphasige Drehstrommaschinen wie die asymmetrische Maschine das D6ϕ SVM-B2 12-Sektoren-Verfahren den elektrischen Antrieb für alle Betriebspunkte außer dem Feldschwächbereich und niedrigen Drehmomenten optimiert. Für leicht gekoppelte duale Dreiphasenmaschinen teilen sich alle untersuchten DPWM-Verfahren den optimalen Betriebsraum. SVM ist unabhängig vom Kopplungskoeffizienten fast nirgendwo optimal für den elektrischen Antriebsverlust. Simultane Schaltfrequenzen und Optimierung der PWM-Methode zeigen in Simulationen eine Effizienzsteigerung von etwa 1% für eine Isokurve, die sich vom Eckpunkt bis zum Ursprung erstreckt, und bietet dadurch signifikante Verbesserungen.

Abstract

Reducing emissions is critical as global climate approaches its first tipping points. As a result, not only does assimilating decades of electric drives knowledge into road and rail vehicles require urgency, but so does developing machines that harvest energy from renewable sources. Of the plethora renewables, wind and hydraulic energy also use electric drives. Increasing their efficiency would therefore help electric vehicles break even with their production emissions faster using the current infrastructure and require less energy harvesting machines per unit power once that infrastructure de-carbonizes. Broadly, there exist two principal dimensions to increase e-drive efficiency: hardware and software design. The software design stage entails machine control by means of designing sequences of binary vectors for the inverter, which in turn depend on operating points whose characteristics the hardware design stage defines. This work involves clarifying that symbiosis and optimizing it for electric drives in general and for dual three-phase drives specifically. Drive fundamental frequency characteristics, DC voltage level, peak and continuous power, and other design considerations are typically defined at the hardware design stage without consideration for the commutation frequency characteristics. This work therefore expands knowledge regarding high frequency machine loss models to arbitrary-phase and arbitrary-type machines by means of the coupling coefficient ς and the realization that Floquet theory also applies to high frequency models. The latter allows the modeling of non-periodic nonlinearities in a synchronous frame. Control features thought to have no influence on machine losses to reduce DC-link capacitor current ripple, namely interleaving for dual three-phase machines, are shown to decrease efficiency in the machine by up to 4% depending on the voltage level. Coupling between duals and the permeability profile over the torque-speed field prove decisive in determining the increase in machine losses due to interleaving. Different PWM methods, commutation frequencies, and current sampling rates are investigated and the state-of-the art is extended to dual three-phase machines. Optimal control vectors with the previous elements are found for each operating point, something that requires a detailed inverter loss model and an equilibrium machine loss model. It is found that $f_{sa} = 2f_{sw}$ rate sampling maintains $f_{sw} \to \infty$ current ripple profiles over very low fundamental to switching frequency ratios, or f_0/f_{sw}, but anything in between increases ripple from $f_{sa} = f_{sw}$. Although current ripple has little influence regarding losses in copper, it combined with the high frequency magnetic permeability profile dominate high frequency iron and magnet losses. Large switching frequencies are necessary to reduce iron and magnet losses near the modulation index value of $2/\pi$ depending on ς and μ there. At low fundamental speeds, inverter losses dominate and much lower switching frequencies are optimal and increase drive efficiency by 1% there. The importance of magnet segmentation to reduce high frequency losses is confirmed and a framework for iron shielding of the magnets for

6

IPMSMs is developed using the Poynting equation. Magnet losses are important to avoid demagnetization and better understand the needs for rotor cooling. Machine design frequencies are shown to overlap with inverter-induced field ripple to increase or decrease magnet losses depending on PWM method. Specifically, the tooth-per-pole harmonic as seen from the rotor overlaps with the coalesced 2nd and 4th subharmonic of the first carrier group. Simulations show that for highly coupled dual three phase machines like the asymmetric machine, the D6ϕ SVM-B2 12-sector method optimizes the electric drive for all operating points except for the field-weakening region and low torques. For lightly coupled dual three phase machines, all investigated DPWM methods share the optimal operating space. SVM is almost nowhere drive-loss optimal irrespective of the coupling coefficient. Simultaneous switching frequency and PWM method optimization in simulations results in about a 1% efficiency increase for an iso-curve spanning from the corner point to the origin, offering significant and broad improvements.

List of Equations

9

Contents

List of Abbreviations

AC: Alternating current

AFP: Active power filters

AM: Asynchronous machine

ANN: Artificial neural network

BEMF: Back electromotive force

BEV: Battery electric vehicles

CS: Current source

DC: Direct current

DNN: Deep neural network

DPWM: Discontinuous pulse-width modulation

EM: Electric machine

ESR: Equivalent series resistance

EV: Electric vehicles

FEA: Finite element analysis

FEM: Finite element method

FSPM: Flux-switching permanent magnet machine

FT: Fourier transform

GDPWM: Generalized discontinuous pulse-width modulation

GHG: Green-house gas

GPR: Gaussian process regression

IGBT: Insulated-gate bipolar transistor

IM: Induction machine

IPMSM: Interior permanent magnet synchronous machine

LTI: Linear time invariant

LTV: Linear time variant

MMF: Magnetomotive force

MOSFET: Metal-oxide semiconductor field-effect transistor

MTPA: Maximum torque per ampere

MTPF: Maximum torque per flux

MTPL: Maximum torque per loss

MTPV: Maximum torque per volt

NTK: Neural tangent kernel

OP: Operating point

PAM: Pulse amplitude modulation

PI: Proportional-integral control

PMSM: Permanent magnet synchronous machine

PWM: Pulse-width modulation

RMS: Root-mean square

SE: Steinmetz equation

SPMSM: Surface permanent magnet synchronous machine

SRM: Switched reluctance machine

SVM: Space-vector modulation

SVPWM: Space-vector pulse-width modulation

SyRM: Synchronous reluctance machine

TFM: Transverse flux machine

VDPWM: Variable discontinuous pulse-width modulation

VS: Voltage source

WLTP: Worldwide harmonized light vechicles test procedure

WTHD: Weighted total harmonic distortion

List of Variables

B: Magnetic field density vector

E: Electric field vector

F: Force vector

H: Magnetic field vector

I: Identity matrix

J: Current density vector

L: Stator frame inductance matrix

T: Clarke-Park Transformation

f: Force volume-density vector

$\boldsymbol{A}$: Area vector perpendicular to its emanating plane

$\boldsymbol{J}_0$: System Jacobian

$\boldsymbol{J}_*$: Control Jacobian

$\boldsymbol{\Gamma}$: Inductive coupling matrix

$\boldsymbol{f}$: Vector function

$\boldsymbol{h}$: Vector function

$\boldsymbol{u}$: System (plant) input vector

$\boldsymbol{x}$: System state vector

$\mathfrak{I}$: An indexed set

C: Constant

E_a: Activation energy

E_{off}: Switch off energy loss

E_{on}: Switch on energy loss

E_{rr}: Diode reverse recovery energy loss

E_{sw}: Switching energy loss

I: Current, including subscripts

I_C: Capacitor current

I_{dq}: Current vector magnitude

L: Inductance, including subscripts

L_d: $d-$axis dual self-inductance

L_q: $q-$axis dual self-inductance

M: Modulation Index

M_d: $d-$axis mutual inductance between duals

M_q: $q-$axis mutual inductance between duals

P: Power, including subscripts

R: Rotor radius

R_C: Capacitor series-equivalent resistance

R_e: Electrical resistance

R_{th}: Thermal resistance

R_s: Stator phase resistance

T_L: Load torque

T_e: Electromagnetic torque

T_j: Temperature, where $j \in \mathbb{N}_0 \bigcup \{a\}$

V: Volume

V_{DC}: DC link voltage

V_{dq}: Voltage vector magnitude

W: Work-power

Z: Circuit impedance

Δ: Difference, small change

Δi: Current ripple

α: Second dual electrical offset angle

β: Cube body diagonal angle

γ: $\mu_{r,\mathrm{min}}/\mu_{r,\mathrm{max}}$

δ: Electricomagnetic penetration 'skin' depth

η: Efficiency

$\bar{J}$: Complex conjugate

$\hat{X}$: Amplitude of a periodic quantity X

$\hat{z}$: Unit vector of axis z

ι: Rotational moment of inertia

ℓ: Length of a stator slot

λ: Eigenvalue, eigenvalue operator

μ: Magnetic permeability

μ_r: Relative magnetic permeability

∇: Vector derivative

ν: Electrical resistivity

ν_ξ: Control of the $\xi-$axis, $\xi = \{d, q\}$

ω: Angular frequency

ω_e: Angular electrical synchronous frequency

ω_m: Angular mechanical frequency

ϕ: Current vector angle, positive $d-$axis reference

ψ: Magnetic flux linkage

ρ: Electric charge volume density

σ: Electrical conductivity

τ: Second roll angle

θ: Tangential position coordinate

θ_I: Interleaving angle

θ_e: Electrical angular position

φ: Current vector phase offset with voltage vector reference

ς: Inductive coupling coefficient

ϑ: Electromagnetic penetration 'skin' phase

ζ: First roll angle

c: Constant, iso-curve

f: Linear frequency

$f(\cdot)$: Generic function

f_0: Fundamental frequency

f_m: Linear mechanical frequency

f_{sw}: Linear switching frequency

$g(\cdot)$: Generic function

h: Thickness of a lamina

i_d: $d-$axis current

i_q: $q-$axis current

k_b: Boltzmann constant

l: Machine length

p: Pole-pairs

p_e: Power volume-density

q: Electric charge

r: Radial coordinate

t: Time

v_d: $d-$axis voltage

v_q: $q-$axis voltage

w: Width of a lamina, stator tooth width

Chapter 1

Introduction and Motivation

Although this dissertation concerns a niche topic in electric drives, its motivation is anchored to broader concerns. Before the pandemic in 2019, road vehicles contributed to 69% of global green-house gas (GHG) emissions, with Europe and North America leading the world in road vehicle emissions [1]. To limit the increase in mean global temperature to below 1.5°C, global emissions from road vehicles must decrease by 69% according to some models [1], meaning that they must make 21% of global 2019 GHG levels before 2040. Battery electric vehicles, although an improvement to internal combustion vehicles in almost every sense, do not offer a panacea to anthropogenic climate change. Battery electric vehicles (BEV) mostly acquire energy from the grid, which in turn generates electricity mostly by combusting fuel, whether gas, coal, biofuels, oil, or anything else that burns. Fuel-cell electric and hydrogen internal combustion vehicles might offer a solution to problem-offsetting of battery electric vehicles, as well as improved energy storage from renewables. Storing the very volatile energy from renewables [2] would require expensive electro-chemical batteries with a very limited lifespan of about 10 years, polluting manufacturing and disposal processes, and questionable element procurement practices. Gravity batteries offer a better solution, but like wind and solar contraptions, take up much volume. Solar panel production is also comparably polluting to electro-chemical batteries. Hydrogen batteries also potentiate improvement, but might involve more risk than gravity batteries. The problems therefore involve scaling energy volume-density and controllability, both of which nuclear power already addresses. Due to the urgency of addressing climate change [3], more discussion is needed around nuclear power as a non GHG-emitting power source, at least until other technologies scale. Its waste pollutes over centuries, but its quantity is less and its containment mature. The most GHG-emissive countries already have nuclear weapons. However, to eliminate the risk of nuclear weapon proliferation to developing continents fully or partially in the southern hemisphere, more could be invested in fission's more benign cousin, nuclear fusion energy, aside from the aforementioned energy sources.

Aside from power sources for electric vehicles, in general it is best to reduce power consumption per capita as well, preferably without reducing or even increasing quality of life. Combined with the fact that electric vehicles require an electric drive irrespective of the power source, reducing the power consumption of the electric drive in any application contributes to reducing emissions and perhaps even pollution. The goal of this dissertation is to contribute to that goal while maintaining electric drive performance, i.e. increase the efficiency of the electric drive.

Road vehicle electrification has seen a boom in the last decade of companies manufacturing electric vehicles (EV) and traditional automakers increasingly electrifying their fleets. Europe and China lead the world in the number of electric vehicles with about 7.8 million and 13.8 million respectively, as of the end of 2022 [4]. Unfortunately they only make 2.6% and 4.3% of all vehicles on their roads. Public transportation is mostly electrified in both Europe and China, making the source of grid energy the main concern. Despite the meager fraction of total road EVs in the leading territories, EV sales seem to be increasing exponentially, as seen in Figure 1.1. Assuming that the total number of road vehicles does not change over 20 years and the grid has been completely de-emissified in the world, EVs excluding hybrids on the road must increase at least by about 47.3 million per year on average over the next 18 years. The required average yearly increase of BEVs would be 27.7%.
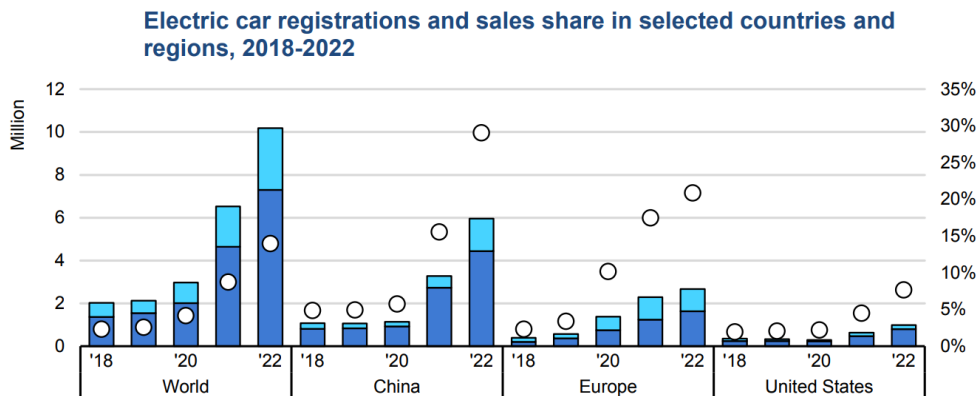
Figure 1.1: EV sales trends taken from [4]

Necessary giant leaps notwithstanding, these recent trends bode well for us, the planet, and electric drives, making their study all the more imperative. Besides their energy storage source, which are typically batteries, electric drives consist of the inverter and the electric machine. The inverter converts direct-current (DC) power from the energy source to an alternating current (AC) power; the electric machine converts that AC electrical power into mechanical power. The basic components of the inverter are the power transistor and the diode. No less important components include the housing and base cooling plate, which dissipate heat produced by the inverter. A large capacitor connected in parallel to the DC voltage source is also necessary to reduce the voltage ripple caused by switching in the inverter. To make a traveling flux from a DC voltage source like a battery, the converter must conduct current to and from the machine over at least two spatially distributed electromagnets, called phases. These AC machines typically have three phases because it increases the DC bus voltage usage by 22%, which is the largest increase for consecutive increments of the number of phases. For that reason among others, most traction electric drives are three-phase drives, and the converter has consequently three legs, or three half-bridges. Inverters may have six insulated bipolar transistors (IGBT) with six freewheeling diodes connected to each of the IGBT's collector and emitter terminals for a three-leg converter. For lower current applications, inverters typically employ six metal-oxide-semiconductor field-effect transistors (MOSFET), but due to their limited current conducting capacity, are often connected in parallel in three-phase topologies. To generate torque, the electric machine usually

has two spatially-offset field sources, which is why the converter may also involve a mechanical commutator.

Such is the case with externally excited synchronous machines (EESM), in which static brushes connected to the battery or stepped-down rails contact a segmented ring where each segment connects to each of the rotor inductors, creating a field in the rotor. Wireless power transfer to the rotor is also possible. In permanent magnet synchronous machines (PMSM), permanent magnets serve as the second field source. An example of a machine class that does not have a second field source is the class switched reluctance machines (SRM) and synchronous reluctance machines (SyRM). In SRMs and SyRMs, magnetic shear is created not by superimposing two magnetic fields, but by spatially varying the distribution of iron and air such that the magnetic shear occurs upon commutating the exciting field. This happens because magnetic fields permeate the iron much more than air, and therefore flux lines prefer to stay in the iron. Interior permanent magnet synchronous machines (IPMSM) use the iron's geometrical salience in addition to the permanent magnet to generate torque. As a result, IPMSMs are typically the most torque and power-dense electric machines per unit currency, since the permanent magnet provides a magnetic field a priori and the iron salience provides additional torque at a lower price than the magnet; lastly, only one exciting field that switches is required. Induction machines (IM) also have only one exciting field. Unlike IPMSMs, IMs have no permanent magnet and little to no salience. Instead, they have a shorted conductor array in the rotor. As the exciting field rotates, it induces a magnetic field in the rotor array, creating magnetic shear at a distance from the rotation axis over an area and therefore torque. Because the rotor array must see a time-varying field to produce torque, the exciting field induced by the stator coils must rotate faster than the rotor speed. Due to the difference between the exciting field and rotor speeds, the machine is also referred to as the asynchronous machine (AM). More copper in the exciting coil and in the rotor, in conjunct with faster exciting frequencies creates more losses during operation than the IPMSM. Up to now we assumed that the torque-producing magnetic shear occurs along the radial component of the magnetic flux density in the circumferential direction, which need not be the case to create rotational motion. Axial flux machines eponymously produce torque by shearing the axial flux in the circumferential direction. Transverse flux machines (TFM) generate torque by shearing the radial flux in the circumferential direction, as usual, except that the exciting coil is not wound in loops, but into one loop on the circumference of the stator inset in a two-pronged iron fork whose flux connects to a rotor with axially-separated permanent magnets of opposite polarity.

This dissertation focuses on the dual three-phase IPMSM, i.e. the permanent magnet synchronous machine with two three-phase windings connected in a star configuration with disconnected neutrals sharing a stator. This machine allows for interleaving, unlike with six-phase machines with connected neutrals and IG-BTs/MOSFETs connected in parallel. Interleaving also reduces the DC capacitor current ripple, allowing a reduction in its size. It is shown how interleaving induces additional losses in the stator iron depending on the coupling between the windings of the duals. A measure of this coupling is proposed. In addition, different commutation strategies, or pulse-width modulation (PWM) methods, and switching frequencies are investigated to arrive at a program that optimizes the dual electric drive efficiency. Other effects, like constructive interference between converter

frequencies and tooth harmonics in the magnet are also investigated.

Chapter 2

Literature Review

This chapter begins with an overview of three-phase and dual three-phase voltage-sourced pulse-width modulation (PWM) methods. PWM is the main strategy to program the sequence of on-off times of the legs of the three-phase inverter to convert DC voltage into AC voltage. PWM generates harmonic content in addition to the desired fundamental frequency and amplitude of the voltage waveform, and a review of the literature on the resulting current ripple in the windings and the capacitor is made. Multi-phase converters have more degrees of freedom due to the increased number of switching half-bridges compared to three-phase converters, and the literature regarding those PWM methods is reviewed. Multi-phase converters need not connect to multi-phase machines, which is why different topologies on the machine side are also reviewed. Also on the machine side, we review the literature concerning copper losses, iron losses, and magnet losses in electric machines. Finally, we review the state-of-the-art regarding steady-state and high-frequency optimizations of the electric drive.

2.1 Voltage-Sourced Drives and Pulse-Width Modulation Methods

The first systematic approach to analyzing losses due to different pulse-width modulation (PWM) methods was [5] and [6], in which several PWM methods and their effects on current ripple were investigated for three-phase converters with large commutation-to-fundamental ratios. Several analytical relations were derived, which highlighted the dependency of current ripple Δi on switching frequency f_{sw}, DC voltage V_{DC}, and modulation index M. For example, the normalized squared current ripple for space-vector modulation (SVM) with a three-phase equivalent inductance L is shown in equation (2.1.1).

$$\left(\frac{8 f_{\mathrm{sw}} L}{V_{\mathrm{DC}}}\right)^2 \Delta i^2 = \frac{1}{6} M^2 \left(1 - \frac{8M}{\pi\sqrt{3}} + \frac{9M^2}{8}\left(1 - \frac{3\sqrt{3}}{4\pi}\right)\right) \qquad (2.1.1)$$
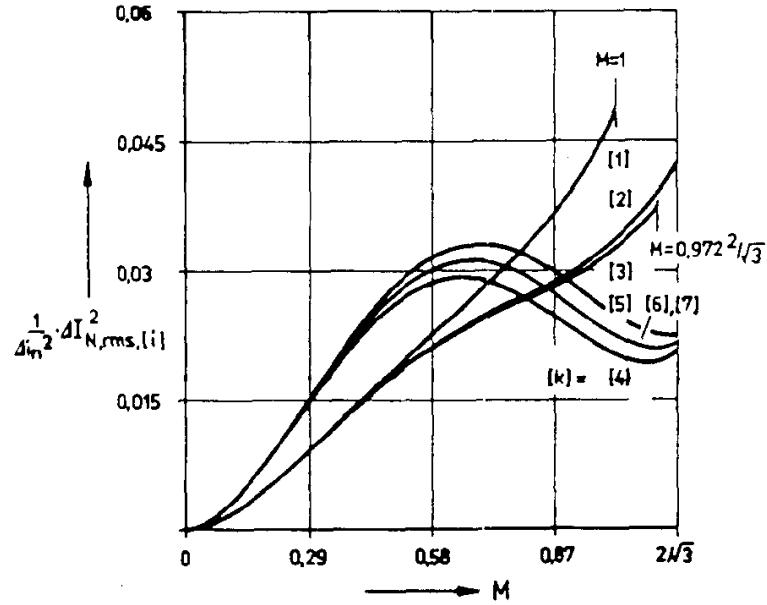
Figure 2.1: Phase current ripple squared with equivalent switching frequencies for (1): sinusoidal PWM, (2): SVM, (3): third harmonic with 1/4 magnitude, (4): DPWM3, (5): DPWM1, and (6): DPWM2 according to [6]
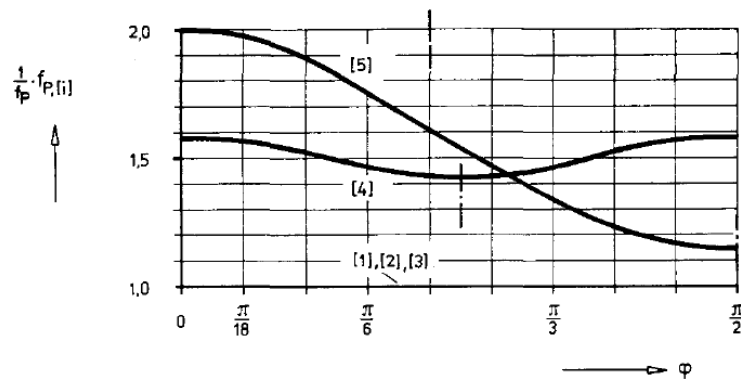
Figure 2.2: Switching frequency factor for equivalent commutations over various current phase delay φ for (1): sinusoidal PWM, (2): SVM, (3): third harmonic with 1/4 magnitude, (4): DPWM3, and (5): DPWM1 according to [5][6]

24

(a) Switching frequency factor for optimal phase current ripple

(b) Optimal current ripple squared
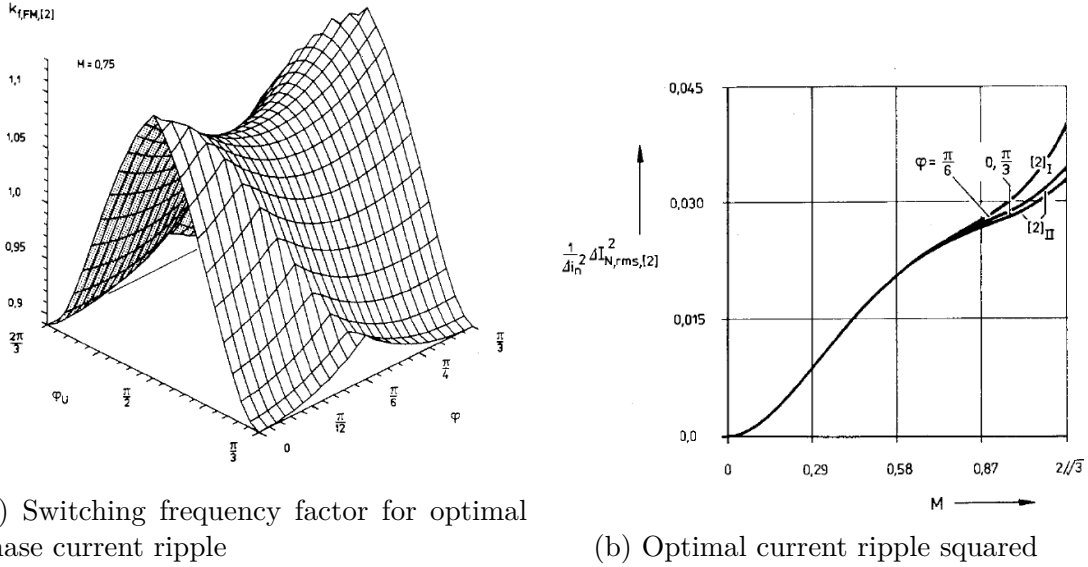
Figure 2.3: Minimal phase current ripple with equivalent mean switching losses over various current phase delay angles φ for (2): SVM according to [6]

Discontinuous PWM methods were found to commute less frequently due to their clamping, and therefore increasing the switching frequency by a current vector phase-dependent gain is necessary. The average of that gain over all phases is about 3/2. Also, since the ripple varies as a function of the voltage vector rotation angle, current phase delay, and modulation index, an optimal switching frequency variation factor was found for space-vector modulation (SVM), which usually varies between 1.1 and 0.9 with the maximum occurring between two switching states. It also keeps the converter losses the same. The ripple amplitude variation within a fundamental period applies to all PWM methods [7], but [5] decided to use SVM as an optimization example. Later studies on the frequency variation within the fundamental period showed that it disperses and flattens spectral peaks [8] which is also beneficial for acoustic reasons [9]. One of the first to recognize the spectral spread of local variable switching frequencies and their acoustic benefits was [10]. Another optimization involved minimizing the converter losses while keeping a constant current ripple root-mean squared (RMS) value [11], reducing switching losses by as much as 19%. With the optimization in [5] for a modulation index of $M = 2/\sqrt{3}$, the maximum modulation index, the squared ripple is reduced by about 18%, as shown in Figure 2.3.

The book [12] expanded the work of [6] by deriving complicated expressions for the Fourier coefficients of the converter voltage, allowing for any switching-to-fundamental frequency ratio. Due to the double-Fourier series nature of the coefficients, it is almost as complicated to compute the expressions as it is to simply simulate the waveforms and extract current ripple information. The work in [12] also qualitatively explained why the spectral peaks appear and that they appear as groupings about multiples of the switching frequency. The distance of the peaks from the carrier groups is determined by even multiples of the fundamental frequency. The approach in [12] also allows for different sampling and carrier signals. For example, spectra of PWM voltages generated by comparison with sawtooth carriers and triangle carriers are compared. Spectra of PWM voltages generated with

25

natural, symmetric, and asymmetric regular sampling are also considered. However, the analysis mostly involves the spectral peaks themselves. The advantage, for example, of asymmetrical sampling for low switching-to-fundamental frequency ratios is plotted as voltage line-to-line harmonic distortion for third harmonic injection methods with various third harmonic amplitudes, as replicated in Figure 2.4, but it is not explored for other, more commonly used PWM methods. The measure of WTHD0 means weighted total harmonic distortion with respect to the fundamental at $M = 1/2$, so that the amplitudes of the Fourier coefficients are normalized to the DC bus voltage.
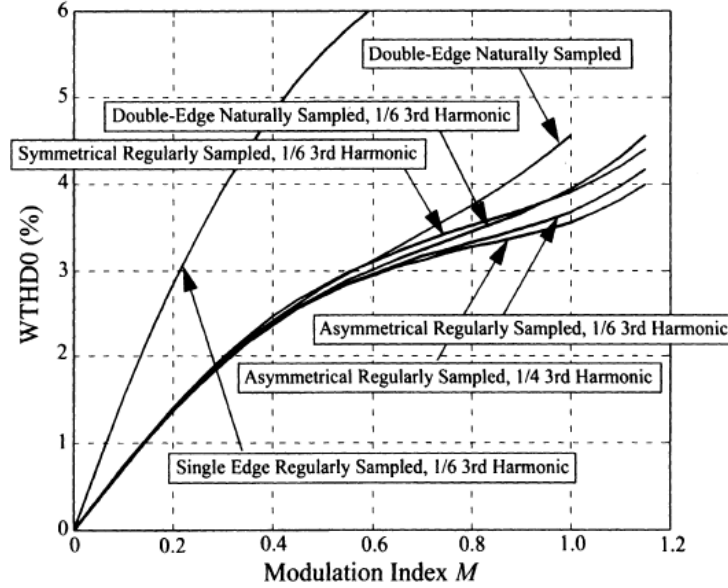
Figure 2.4: WTHD0 of line-to-line output voltage with $f_{sw}/f_0 = 11$ with various third-harmonic amplitudes and sampling techniques [12]

SVM and DPWM methods depend on the voltage angle, which then requires vector projections on each of the switching states to calculate the duration of the pulses over each switching period. That proves complicated and there are three publications which converted the problem of vector projections into reference-carrier signal comparison, which is much simpler and computationally efficient. Calling it hybrid PWM, [13] derived an algorithm to generate the reference waveforms for SVM and any DPWM method by varying a factor k_0 in time, or setting it to $k_0 = 0.5$ for SVM. The variation of k_0 to generate DPWM waveforms was not explicitly derived. The paper [14] first called the method generalized PWM and characterized the current ripple and voltage gains as presented in [13] and already analyzed in [6][5]. In [15] the factor k_0 of [13] was written explicitly in terms of a third-harmonic sinusoid with a phase delay δ, allowing for continuous interpolation between the canonical and max/min DPWM methods. The method in [15] is used in this dissertation.

Three-phase converters usually have a DC link capacitor when connected to a DC voltage source, such as a battery, to reduce or eliminate the AC load on the source. The capacitor has an equivalent series resistance, or R_{ESR}, which dissipates the AC load across it from the switching action as losses. The ripple in the DC link capacitor also heavily depends on modulation index, switching frequency, and current phase delay. Knowing the capacitor RMS current is important for capacitor

dimensioning, as larger current loads mean more heat generation that needs to be dissipated, tying the problem to converter cooling and size requirements. Simple analytical calculations and the dependencies of capacitor ripple are delineated in [16]. The main contribution is the expression in equation (2.1.2), where M is the modulation index, φ is the current phase offset angle, and $I_{\mathrm{RMS}} = I_{dq}/\sqrt{2}$ is the root-mean-squared of the phase current, which also depends on modulation index; its dependence on PWM methods was not investigated.

$$I_{C,\mathrm{RMS}} = I_{dq}\sqrt{M\left(\frac{\sqrt{3}}{4\pi} + \cos^2\varphi\left(\frac{\sqrt{3}}{\pi} - \frac{9}{16}M\right)\right)} \qquad (2.1.2)$$

2.1.1 Multi-phase Machines

The main motivation behind the implementation of multi-phase machines is their added redundancy in the case of a short or open phase and increase in the degrees of freedom allotted to their control. The added redundancy allows the drive to maintain better performance when compared to a similar fault in three-phase machines. Added efficiency is usually not a factor for magnetically-equivalent dual three-phase and three-phase machines [17]. On the inverter side, one may simply double the amount of switches per phase on a three-phase machine and connect them in parallel to achieve similar, if not identical, inverter losses. One of the first papers to analyze the problem of multi-phase induction machine control with reduced phases after a presumed fault was [18]. A thorough overview of multi-phase machines is presented in [19] and later a review of their control methods is presented in [20]. Redundancy algorithms also depend on whether or not the neutral points are connected and what the spatial angular displacement between the neutral-separated machine phases is. In the paper [21], engineers investigated the effect of the spatial distribution of the faulty phases on rated torque and current magnitude, with each spatial distribution having advantages either during open circuit or short circuit faults of one of the two duals. Various winding distributions are also investigated in [22] for a concentrated winding.

Regarding the inverter excitation of multi-phase machines, there are various publications extending the calculations of current ripple from three-phase to multi-phase machines. The literature on PWM-fed multi-phase drives can be divided into three subcategories: current ripple of uncoupled loads, current ripple with coupled loads, and DC link capacitor ripple. Most of the literature for current ripple involves uncoupled loads, with coupled load literature mainly encompassing DC-DC converters.

Multi-phase machines increase the degrees of freedom involved in PWM. The number of states, or space vectors, available are 2^n, where n is the number of phases. A three-phase converter has 8 space vectors, whereas a six-phase converter has 64 space vectors. One of the first papers seeking to explain and optimize PWM in a multi-phase setting −specifically, for dual three-phase machines −was [23] and [24]. At the time, 12-sector space-vector modulation (SVM) was being explored, and [23] showed that choosing just two adjacent vectors in 12-sector SVM sourced odd harmonics not a multiple of 3 like the 5th, 7th, and so forth. Although the exact generating mechanism of those harmonics was not explained, a modulation method proposed in [24] by choosing four adjacent vectors instead of two with very

specific dwell times ameliorated the problem. However, the method still induces 11th and 13th harmonics which worsen with decoupling between machines. Furthermore, a complicated machine model −in this case, an induction machine −needed to be derived for the harmonic basis vector set $\mathcal{S}_k$, which is not necessary if a model is available in the dual $\alpha\beta$ space. Lastly, the vector sequence of the method was not specified; the vector sequence often distinguishes PWM methods in three-phase converters. Choosing four vectors instead of two approaches independent SVM, as it chooses five non-zero space vectors [25]. Independent SVM is the independent control of each dual, which is possible due to their disconnected neutral points. The question of dual coupling is not addressed because the control is done in a fundamental space, which simulates a three-phase machine. Furthermore, harmonic mapping to the subspaces in [24] is not guaranteed, as each harmonic must have a specific phase. In [26], multi-phase machines of arbitrary number in convex connections −for three-phase machines, the connection would be the delta connection, for example −are considered and the current ripple for sinusoidal modulation and n-harmonic injection are derived. Like in [24], [26] does not consider coupled phases.

As opposed to harmonics created by the PWM technique, magneto-motive force (MMF) harmonics, nascent from the winding distribution, could be isolated in a harmonic space, but must be controlled to zero as opposed to using the open-loop approach in [24]. The reason for that is that the transformation used in [24] is always aligned to the voltage vector, whereas harmonics from the winding distribution necessitate realignment for every operating point. Note that compensating for the harmonics using a current regulator will control the harmonics in the current to zero irrespective of its source. Such filters are known as active power filters (APF) [27], which have many applications, including noise cancellation (source 11 in [28]). One popular method of harmonic suppression involves transforming the signal to a harmonic-synchronous frame and controlling the harmonics in this new frame to zero, usually by using the simplest implementation: an integrator. It seems to have first emerged as a patent [29] in 1994, and has appeared several times in the literature for dual three-phase machines, most notably in [30]. There is a plethora of other APF methods summarized in [31], like notch-filters in the stator frame xy, or z_1, z_2 subspace for six phase machines [32] and high-bandwidth PI controllers in the same subspace also for six phase machines [33].

Coupling was introduced as a significant source of changes in current ripple due to different PWM methods for dual three-phase machines in [34], [35], and [36] for induction machines. It was introduced as a factor containing inductance in the harmonic-synchronous space xy as $k_{\sigma xy} = \sigma L_s / L_{lsxy}$ in [35]. Increasing coupling increases the current ripple at large M when using SVM [36] and decreases six-step current harmonics if the differential modes are coupled [34]. This acts like an external filter, which is why it has the opposite effect observed in [36]. The coupling must be in the machine, as mutual inductances between filters which then feed a three-phase machine decrease current ripple, according to [37]. In [38] and [39], different angular displacement between duals and their effects on current ripple are investigated. The same author later clarified and simplified the PWM method specified in [24] and proposed the category of 12 sector-based PWM methods, the 12 sectors shown in Figure 2.5, that differ by the placement of the zero vector. In [36], a category of 24-sector PWM as shown in Figure 2.6 was proposed. Both emphasize the inseparability between coupling and PWM method evaluation based on current

ripple in dual three-phase machines. As with three-phase PWM, each of the 12- and 24-sector PWM methods has a different number of commutations, which will affect the inverter losses.
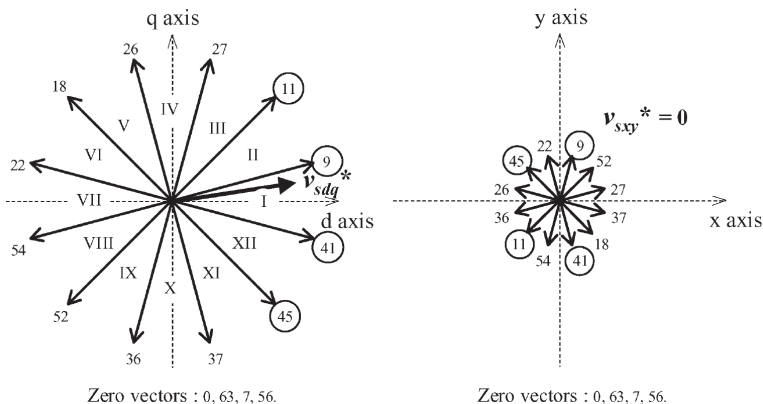
Figure 2.5: 12-Sector SVM with four space-vector selection, [35]

The mutual inductance between coils in a multi-phase machine defines the coupling in the machine and has effects on the torque ripple, with windings 30° electrically offset minimizing the torque ripple at the expense of large 5$^{\text{th}}$ harmonics during six-step operation [40]. Moreover, for dual three-phase machines, the spatial angular displacement and winding pattern determines that coupling, as first suggested by [40] and then by [41][42]. There are two main space-electrical angular displacements for dual three-phase machines: 30° and 60°. Each describes the asymmetrical and symmetrical machine, respectively. Any multiple of 60° yields the symmetrical machine from a control perspective due to the electrical distribution of three-phase machines, but in this dissertation the 180° machine is referred to as the polar machine, since it refers explicitly to the spatial distribution of the windings in the stator, which results in very small coupling between the duals. The spatial distribution was proposed in [43] and the fractional pitch reducing coupling between duals specifically for interleaving at $\theta_I = 180°$ −but not the spatial distribution of the duals−was patented in [44] and described in [45].

Independent control enables interleaving, which is a phase delay in the carrier signal. Its effects on the DC capacitor current ripple are documented in [46] for a three-phase, star-connected load, which considers the angle between the fundamental voltage and current, modulation index, and interleaving angle. No coupling is analyzed in the load. The interleaving angle that minimizes the linking capacitor's ripple depends mostly on modulation index and current-voltage displacement angle, φ. For $M = 0.85$ and $\varphi = 0$, the optimal interleaving angle is $\theta_I = 90°$, whereas if $\varphi = 90°$, the optimal interleaving angle is $\theta_I = 180°$. Computation of the DC link capacitor current ripple without interleaving and coupling was approached by [47] for dual three-phase machines. A 60% reduction in DC current ripple was observed for a dual three-phase induction machine in [48], highlighting an advantage of interleaved converters. In [49], the capacitor current ripple and phase ripple for various operating points for a polar dual three-phase machine was investigated. As with [47], [49] demonstrated a strong dependence on power factor, or the cosine of the current angle from the voltage angle. The effect of interleaving on phase current ripple with strong coupling in dual three-phase electric machines has not been

29
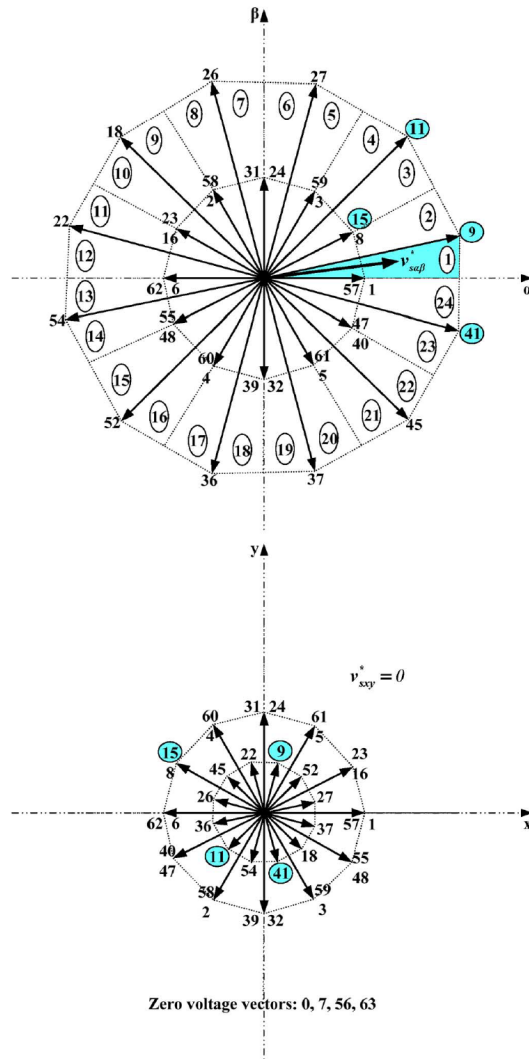
Figure 2.6: 24-Sector SVM with four space-vector selection, [36]

investigated.

An approach of dual three-phase converters, but not machines, with intercell transformers, or filters, considers the coupling of the filters [50]. However, because the coupling does not take place inside of the machine windings, it does not consider machine losses or even the losses in the intercell transformers. Coupling effects between duals in a machine can be considered independent of the load harmonics, or harmonics generated because of the winding distribution MMF.

Usually coupling is built-in with passive filters before connecting the multiple phases in parallel to a three-phase load, usually for filtering purposes [51], but also for three-phase load operation [46] [52] [53]. Combined with interleaving, the idea is to offset switching by $\theta_I = 180°$ whereupon parallel connection of the phases, the phase ripple cancels or is reduced significantly [53] [51]. Having coupling inductors between 180° interleaved converters and their loads to reduce load current harmonic content seems to have emerged in [54]. Having inductors connected in specific topologies and their harmonic cancellation effects with $\theta_I = 90°$ and dual two-phase converters was shown early on in [55] with Jacobi-Anger double Fourier decomposition used in [53] and [12] to analyze other topologies. Common mode coils

30

were added to parallel-connected converter legs to reduce the circulating currents resulting from interleaving by $\theta_I = 180°$ and a reduction in the DC capacitor current ripple was observed compared to a single converter, two parallel and interleaved converters with separated DC link, and two parallel and interleaved converters with the same DC link [51]. In fact, interleaving reduces the size of the filters needed, as shown by [52], and of the DC link due to the reduced harmonic content. The idea was applied to three-phase machines with an external coupling inductor [56] and for both a copuling inductor and common-mode inductors in [57]. In [57], a modified DPWM method was developed to reduce the differential and common-mode circulating currents with fixed interleaving at $\theta_I = 180°$, allegedly reducing the losses in the coupled inductor's core. The method however, increased the overall line current ripple compared to other PWM methods. In [58], the impact of sinusoidal, 8-sector space vector modulation and DPWM methods on the common mode ripple was investigated. It was found that of those, DPWM is the least effective in reducing the common mode ripple. They also found that with sinusoidal and 8-sector space vector PWM, it is best to use an even number of interleaved converters. An earlier paper also observed the effectiveness of interleaving with SVM compared to DPWM1 with the same topology [59]. As opposed to using symmetrically delayed interleaving, [60] proposes asymmetric interleaving between three parallel converters powering a three-phase machine, which reduces the ripple in the machine and the inductance requirement on the common mode filter. What the papers share involving harmonic cancellation is that the phase legs of each converter are connected to their counterpart in parallel. That differs from the case of dual three-phase machines, where each phase leg of each converter is only connected to the other legs of the same converter. That changes the optimum angle for DC link capacitor current reduction, and couples the problem of harmonic cancellation with winding patterns and therefore coupling between the duals in the dual three-phase machine. In [61], coupled inductors were connected in series to the dual three-phase machine, enabling the previous harmonic cancellation after the coupled inductors, reducing the current ripple in the machine. It also reduced acoustic noise by about 15%. The same idea was implemented for dual three-phase machines with connected neutrals in [62]. The main drawback involves the coupled and common mode inductors, which are additional components that take up space and drive up cost. The paper [63] investigated interleaved DPWMMIN with disconnected neutrals on a PM synchronous motor with concentrated windings and without filters and showed a 19% decrease in ripple with $\theta_I = 180°$ and a 0° winding offset. The fractional pitch winding patented in [44] and described in [45] also seeks to remove the need of the additional coupled inductors by incorporating said filters into the machine design. That same machine with the spatial distribution of [43] is investigated in this dissertation to contrast with conventional full-pitch and 30°-offset dual three-phase machines.
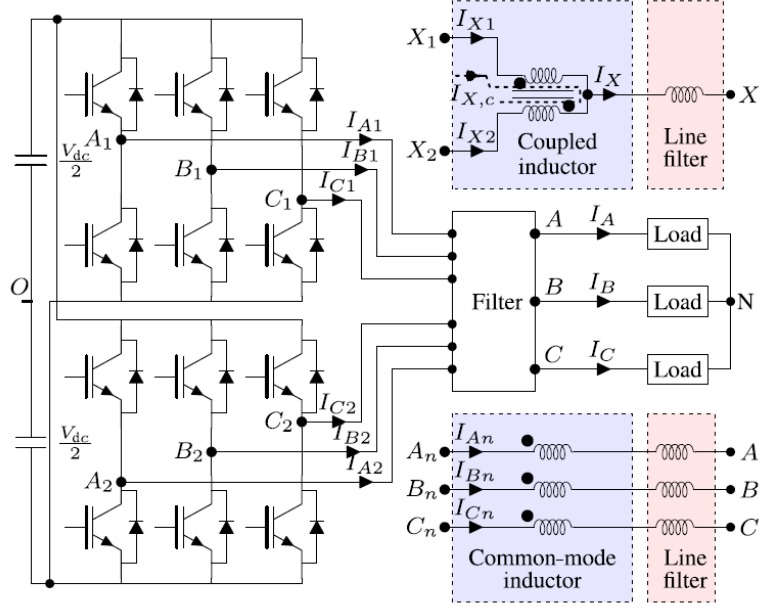
Figure 2.7: Dual three-phase converters powering a three-phase load via a coupled inductor or common-mode filter interface [57]

2.2 Conduction Losses in Copper

Conduction losses, joule losses, and ohmic losses refer to losses caused by the same mechanism: resistance to the flow of charge carriers in a material or medium. This section will focus on conduction losses in the copper windings, which typically create the rotating magnetic field in an electric machine. One may categorize conduction losses into DC and AC losses, of which the latter may be further categorized into proximity and skin effect losses. All conduction losses considered here can be calculated by equation (2.2.1), where the distribution of the bounded current density in space differentiates between conduction loss categories.

$$P_{\text{cond}} = \frac{1}{\sigma} \int |\mathbf{J}|^2 dV \qquad (2.2.1)$$

The variables σ, V, and $\mathbf{J}$ represent the conductivity of the medium, the volume of the medium, and the current density in that volume respectively. If the current density flows in one direction and is uniform within its bounding volume, then the conduction loss in that volume is the elementary $i^2 R_e$, where i is the current and R_e is the conductor resistance. This also applies to time-varying current densities, where the power loss is $i_{\text{RMS}}^2 R_e$. AC losses account for the case when $\mathbf{J}$ is not uniformly distributed. Proximity losses encompass the AC losses caused by external magnetic fields. Skin effect losses refer to AC losses caused by the conductor's own changing magnetic field. Notice that two conductors near one another will have both effects. AC losses may also appear as eddy current losses in the literature, as the eddy currents induced in the conductors due to changing magnetic fields cause the redistribution of the current density in the conductor. In typical electric machines, the stator windings generate leakage and linking flux to the rotor that change in time, generating large proximity losses within them. Because a voltage source generates

voltage operating points using PWM, the current flow also contains high frequency components that mostly cause skin effect losses. Reducing the size of the conductors in a direction perpendicular to the external field and reducing the dimensions of the conductors in general reduces the losses due to proximity and skin effects respectively [64]. With already small conductors, the proximity effect dominates [65], and the reduction in the dimension perpendicular to the magnetic field can be simulated by specific winding configurations that change what magnetic field the same conductor sees in different places about the stator, which may be called flux sharing. These are elementary concepts in machine design delineated in [66]. In [67], hot-spots in the windings were traced to ×8 more equivalent DC resistance at high speeds, increases ultimately caused by proximity and skin effects in a switched reluctance machine (SRM). Peak efficiency was reduced by 3% when considering those effects [67]. It is not clear from [67] whether increases in iron losses also contributed to efficiency reduction, but in peak efficiency regions iron losses typically contribute less than half of the total losses. Reducing the conductor diameter reduces the AC/DC power ratio, roughly a DC resistance factor, hyperbolically, as shown in [68] for a flux-switching permanent magnet machine (FSPM) with a concentrated winding. FSPM have an SRM rotor and circumferentially magnetized permanent magnets in the center of each stator tooth. For a concentrated winding where flux sharing in a series-connected bundle is not possible, [69] investigated different wire shapes and wire distributions about a stator tooth, finding that conductors further away from the airgap, where tangential fields are less prominent, significantly reduced the AC/DC loss factor. Needless to say, proximity losses contribute the most to conduction losses in copper, as the skin effect components are small due to the already small current ripple. Furthermore, because the power loss at high frequencies for relatively large conductors is proportional to $\sqrt{f}$ and J^2 [70] [71], and J is in turn proportional to $1/f$, the losses due to the skin effect actually decrease. In inverter-fed electric machines with f as a switching frequency, skin effect losses are therefore roughly proportional to $1/f^{3/2}$. For smaller conductors, loss is proportional to f^2 at high frequencies [71], which results in roughly no change in skin effect losses in inverter-fed electric machines. That means that if proximity losses are addressed with the winding and conductor distribution, skin effect losses either decrease or stay the same with increasing converter frequency. Because converter losses increase linearly with f, they limit the converter frequency. All of the previous is not to say that losses due to current ripple are negligible: they still create parasitic losses elsewhere in the machine although their loss contribution in copper is indeed effectively negligible.

This led to mislead switching frequency optimization attempts, with [72] using a weighted cost function between converter losses and torque ripple −as in [73]− and a dynamic lower constraint based on rotor speed. However, thinking copper losses are the only consequence of losses due to current ripple overall, and therefore using torque ripple instead, the optimization almost always favored lowering the voltage-source inverter (VSI) frequency in the interior permanent magnet machine (IPMSM) drive. The first step in estimating the losses involves estimating the current ripple, as [74] did by, rather trivially, using inductance tables from 2D FEA for an IPMSM with significant saturation and calculating the ripple in the synchronous frame, like [75] did earlier in a model predictive control setting, [76] to reduce torque ripple, and [77] to reduce losses. The following steps involve quantifying losses in the iron and

the magnets. Since losses ultimately lead to temperature increases, [78] focused on limiting converter temperature to dynamically control current limits, i.e. derate the torque based on converter and winding temperature. Switch and diode temperatures were reduced by reducing the switching frequency in steps of 2 kHz. The paper [78] also constitutes an attempt at global optimization on the converter side, unlike local optimization within a fundamental period seen in [11][5][8][9], which does not mean that the local methods did not increase global system efficiency as shown in [11] and [77] mainly through gains on the converter side. Variable switching may also reduce the cooling requirements for the heat sink and the base plate cooling [79]. The papers [75] and [76] used an objective function to control the machine and to dynamically limit current, and therefore torque ripple like in [72] in an FPGA setting. These papers mainly reduce losses in the converter by either targeting a single peak or RMS current ripple over a fundamental period for every operating point or focusing on converter losses/temperature, ignoring machine losses induced by switching. Other papers did realize the need to characterize the iron losses due to switching in the machine, but that topic is left for the end of this chapter.

Returning to conduction losses in copper, temperature has a considerable effect on the conductivity of a material, with $\nu = 1/\sigma \propto T$, where the proportionality constant is the thermal coefficient of the material. It affects DC resistance adversely, but attenuates AC losses by increasing the skin depth of the material, allowing for larger conductors operating at the same frequency for the same losses or lowering the AC losses for the same conductors at the same frequency. The skin depth δ is shown in equation (2.2.2), where $\omega = 2\pi f$ is the angular frequency and μ is the magnetic permeability of the material. It is the inverse of the eigenvalue of the partial differential equation for the current distribution in a wire with a circular cross-section.

$$\delta = \sqrt{\frac{2\nu}{\omega\mu}} \tag{2.2.2}$$

Since iron and neodymium-iron-boron permanent magnets also conduct and have mostly eddy currents flowing in them due to variations in the flux linkage coming from inverter switching and stator tooth reluctance, increasing the temperature tends to decrease iron and magnet losses up to the materials' respective Curie temperature. This presents a design challenge, since it is best to keep the copper winding cool while warming the iron for optimal spatial temperature control. Furthermore, coercivity reduction and therefore demagnetization are usually the main concerns for magnets at high temperatures, not losses.

2.3 Losses in the Iron Core

There are two main contributions to iron losses: hysteresis losses and eddy current losses. Eddy current losses were discussed in the previous section on conduction losses in copper. Hysteresis losses involve the resistance to realignment of the small magnetic domains in magnetic materials. This means that for a magnetic field vector **H** in a material, that resistance to realignment will self-evidently happen in any circumstance that realignment must occur: when the magnitude of **H** changes, when the direction of **H** changes but its magnitude stays the same, or both. As with eddy current losses but for different reasons, hysteresis losses also decrease

with temperature [80], mainly due to decreased resistance to domain realignment with increasing temperature. Losses do not change much in the range of 25°C to 100°C [80] [81], with maximum differences between models with and without temperature considerations at large frequencies falling to within about 10% [81]. The temperature ranges however, may change for larger machines, as decreases in iron eddy losses between 100°C and 200°C become significant for electrical steel laminations [80].

Instead of using a solid iron core, designers typically use laminations to reduce eddy current losses. Laminating the iron core is physically equivalent to reducing the diameter in a conductor to reduce AC losses. Unlike wire sizing where the diameter is less than the skin depth at the desired switching frequency, designers typically choose lamination thickness based on the skin depth at some fundamental electrical frequency, like the maximum electrical speed of the machine. This makes iron laminations susceptible to high frequency losses due to inverter switching. In [82], tests of different soft magnetic materials with different thicknesses showed an increase in mass-specific losses in all materials of about 15% at and above 10 kHz switching frequency and 1.4 T compared to sinusoidal excitation. The paper [82] also showed that for $B > 0.8$ T, iron losses do not change much with the switching frequency for a toroidal specimen with no airgaps, although an appreciable decrease in iron losses can be seen up to 100 kHz, after which changes in the electric field become significant and iron losses increase again [83]. The author in [84] studied the effects of a variable DC bus voltage and found that AC losses decrease with decreasing voltage. The same was observed in [85] for an induction machine. The analysis was extended once more in [86] via induction machine measurements showing the increasing iron loss increment from sinusoidal excitation with decreasing fundamental line-to-line voltage with a constant DC bus, i.e. with decreasing modulation index. Iron losses may increase up to 120% for low modulation indexes [86]. In [87], the FEA-simulated losses indicate that most of the iron loss changes due to modulation index and switching frequency affect eddy current losses: both total measured iron loss and eddy current loss increase by 20% at $M = 0.9$ and by about 60% at $M = 0.45$ for 0.65 mm sheets. The paper [87] states that a three-phase, three-level inverter was used, but no details on the specimen were given. That is important, because current ripple profiles −and by extension magnetic field ripple profiles −over modulation indexes differ for a single leg half-bridge and a three-phase inverter [12]. Unfortunately, current ripple models for single-leg half bridges have been used to estimate iron losses due to inverter excitation on three phase-excited machines in [88] and [89], therefore overestimating the ripple contribution to iron losses or deriving inverse trends, or both. In [90], a single half-bridge is used and the expected trend with modulation index and switching frequency was successfully predicted; no PWM method was specified. Iron specimen details are also important because cores with airgaps have a larger sensitivity to changes in switching frequency for large switching frequencies [91] than those without airgaps due to leakage flux. That is likely why iron losses did not decrease much after 10 kHz in Epstein frames [82]. Typical electric machines have airgaps and slots which increase the likelihood of the stator flux closing on itself.

There are two main categories of iron loss estimation: first principles-based and experimentally-based curve fitting. One of the first, if not the first, loss formulas for iron loss is the Steinmetz equation (2.3.1) [92], which is a bi-exponential empirical

curve fit to loss measurement data. Most other methods based on the Steinmetz equation perform a similar fit over different time-integrals which provide some advantages when modeling DC-field bias sensitivity, low-order harmonics, and minor loops [92] [93]. Minor loops, including low-order harmonics, were also successfully fit to losses by separating the major and minor loops recursively [94].

$$P_{\text{Fe}} = C_{\text{SE}} f^{\alpha} \hat{B}^{\beta} \tag{2.3.1}$$

Other, first principles-based iron loss calculations, require finite element analysis (FEA) and some parameter fitting based on experiments, especially for the hysteresis loss model. A few more assumptions leads to the Bertotti loss separation model, which uses experimentally-based coefficient fitting [95] and it has the form shown in equation (2.3.2), where f is the cycle frequency of the major loop and C_0, C_1, and C_2 are fitting constants. The separation is a result of a dynamic Preisach model of hysteresis, grounding physical phenomena in mathematical rigor [95].

$$P_{\text{Fe}} = C_0 f + C_1 f^2 + C_2 f^{3/2} \tag{2.3.2}$$

The model in equation (2.3.2) is based on a dynamic and scalar Preisach hysteresis model. The C_0 term is attributed to static hysteresis −as described by [95], as the scale of Barkhausen jumps between domains sketching the DC hysteresis curve −, the C_1 term involves the macro scale where the iron geometry dominates, or the classical eddy current loss, and the C_2 term is associated with the scale of magnetic domains where excess losses due to domain wall movement induce more eddy current losses [90]. However, it does not consider mechanical stress [96] [97], temperature [80] [98], field direction [99], lamination cutting methods [100], minor loops [90] [101] [98], or low-order harmonics and their phases [90] on iron losses. Indeed, [90] showed that narrow waveforms, like a triangle wave, induce less hysteresis losses than flatter waveforms like sinusoids. Because different harmonic amplitudes and their phases affect the final waveform shape for low harmonic orders, both affect hysteresis losses significantly [90]. An example of that for interior permanent magnet machines with different q-winding numbers shows that, because the $q-$number determines low-order harmonics −i.e. waveform shape −, iron losses change according to $q-$number [102]. Figure 2.8 summarizes some of the effects of electrical steel sheet properties on their losses.

Influencing Factor	P_{hyst}	P_{ec}	P_{exc}	J_{s}	H_{c}
Grain size (↑)	↓		↑		↓
Impurities (↑)	↑			↓	↑
Sheet thickness (↑)	↓	↑			↓
Internal stress (↑)	↑				↑
Cutting/punching process (↑)	↑			↓	
Pressing process		↑			
Welding process	↑				
Alloy content (% Si ↑)		↓		↓	
Air gap length (↑)		↑			
Temperature (↑)	↓	↓			↓

Figure 2.8: Influence of different factors on SiFe steel sheet losses and properties (first eight rows from [92])

To take into account these effects, the coefficients are made as functions of the magnetic field and fitted to Epstein frame loss measurements, say, to model i [81]. Then, the losses are calculated, or rather looked-up from model i, everywhere in the FEM-simulated machine and summed. Due to the heavy dependence of the total iron loss on geometry and operating point, those losses are fitted to another Bertotti-like equation (2.3.2) with coefficients changing with operating point, i.e. model k. Due to the geometry dependence, those loss coefficients are separated into rotor and stator coefficients. A summary of this procedure is shown in Figure 2.9. Model i does not have to be a loss model; for example, if loss model j is to be a Preisach [103], Jiles-Atherton, or Prandtl-Ishlinskii type [99], then model i only needs to contain information about the hysteretic properties of the iron specimen, like its anhysteretic curve and its conductivity, to then calculate losses for every element and every time in the FEM using model j.
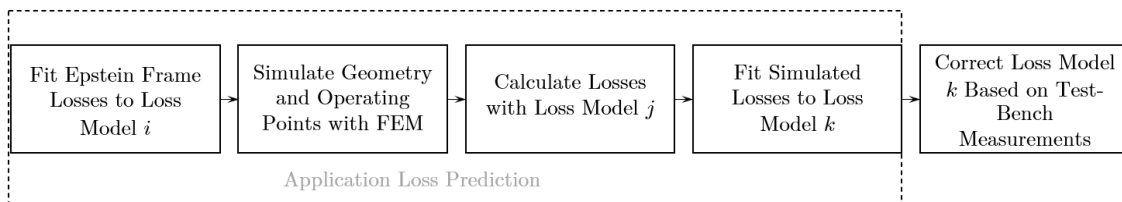
Figure 2.9: Example workflow for iron loss determination

The paper [92] also provides an overview of the different iron loss models, shown in Figure 2.10(a), where the eddy current separation into classical and excess losses should credit Bertotti. Figure 2.10(b) contains an overview of the advantages and disadvantages of each iron loss method overviewed in [92]. Since iron loss modeling is a curve-fitting problem, there is some literature on using neural networks as an iron loss model [104] [96], except that the models might have unpredictable errors if extrapolation is needed. Other methods, like the equivalent iron resistance [105] are very limited in their applicability range for electric machines, but may be useful when approximating machine parameters [106]. All of the methods in Figure 2.10 can be calculated by decomposing the magnetic field density, **B**, into its harmonic components, or replacing it with a time-integral. It was shown that Fourier transform (FT) methods may overestimate the iron losses, especially when

excited by PWM [98]. That is because at the inverter switching frequencies, the skin effect begins to dominate the additional losses, which, as stated before, are proportional to $\sqrt{f}$ instead of f^2. Also, since Epstein frame measurements usually do not have information on losses in the kHz regime, the model kind becomes important. For example, using loss separation but using FT for each direction of $\mathbf{B}$ seems to have given reasonable results for a permanent magnet machine in [107]. In [108], differences were larger between FT and time-domain calculations with a statistical loss model and machine PWM excitation considering excess loss instead of one that neglects it as in [107]. For frequencies below 5 kHz for sufficiently thin laminations and sinusoidal excitation, the difference between FT and time-domain methods do not differ [109], as expected.

(a) Models

Iron loss model	Complex waveforms	Rotating field	Material prior knowledge	Accuracy
Steinmetz Equation (SE)	−	−	small	low
Modified Steinmetz Equation (MSE)	+	−	small	low-medium
Improved Generalized Steinmetz Equation (iGSE)	+	−	small	low-medium
Static/Dynamic Loss Separation model	−	−	medium	medium
Dynamic Preisach model	+	−	high	good
Loss Surface model	+	−	high	good
Magnetodynamic Viscosity Based model	+	−	high	good
Friction Like Hysteresis model	+	+	high	good
Energy Based Hysteresis model	+	+	high	good
Loss separation after magnetizing processes	+	+	model dependent	model dependent

(b) Comparison

Figure 2.10: Iron loss models and comparisons [92]

2.4 Conduction Losses in Permanent Magnets

Conduction losses in the permanent magnets are like the conduction losses in copper except they only have the AC loss component excited by a time-varying magnetic field. Two main components constitute the time-varying field seen by magnets in the rotor: the tooth harmonics and the converter harmonics. Tooth harmonics appear because of the varying reluctance of the main flux path linking to the rotor. The reluctance of the main flux path varies because it must cross iron tooth areas and slot areas filled with the copper winding, each having a magnetic permeability of $\mu_{\mathrm{Fe}} \gg \mu_0$. The spatial reluctance variation is seen by the rotor as a localized time-varying magnetic field. The tooth harmonic is therefore proportional to the number of slots per pole. With converter frequencies, many even sidebands about integers of the carrier frequency coalesce to odd sidebands in the rotor frame. It is also not clear whether in an interior permanent magnet, the iron laminations shield the magnet from the time-varying magnetic fields and to what extent. Most of the literature either merges all rotor losses or the analysis assumes no shielding at all from the rotor iron laminations. A brief and rough analysis may use the RMS of the Poynting equation with a time-varying magnetic field in the airgap as

$$\omega B^2 + \nabla \cdot (\mathbf{E} \times \mathbf{B}) = \sqrt{3}\left(\frac{\mu_{\mathrm{Fe}}}{\sigma_{\mathrm{Fe}}} J_{\mathrm{Fe}}^2 + \frac{\mu_0}{\sigma_{\mathrm{mag}}} J_{\mathrm{mag}}^2\right). \qquad (2.4.1)$$

Let $W := \omega B^2 + \nabla \cdot (\mathbf{E} \times \mathbf{B})$ be the dynamic electromagnetic pressure. Then the dynamic electromagnetic pressure as seen from the magnet is $W_{\mathrm{mag}} = W - \sqrt{3}\mu_{\mathrm{Fe}}J_{\mathrm{Fe}}^2/\sigma_{\mathrm{Fe}}$. In this sense, the more iron losses there are, the less magnet losses

will be induced because the dynamic pressure as seen by the magnet was shielded by the rotor iron.

Unlike AC losses in copper, one may not assume that the magnet is infinitely long because of the relative largess of the other dimensions and the direction of the exciting **B** is not axial. Such two dimensional analysis is known to overestimate magnet losses [110], which requires the introduction of a finite-length factor, a finite axial direction analytical solution, or a 3D FEM simulation. In a rotating electric machine, there are non-negligible tangential fluxes, and even if not, the relative position of a magnet with respect to the radial field introduces a tangential flux-like component to the eddy currents, requiring full 3D FEM simulations. Combined with small time steps required for PWM harmonic modeling, iron lamination shielding effects, finite machine length effects −or end effects −, and the requirement to simulate typical IPMSM rotor geometries in 3D FEM make the problem of eddy currents in magnets a difficult one to study. One of the first to do this and recognize the importance of magnet segmentation for eddy current loss reduction −like reducing the size of the conductor or laminating the iron core −was [111]. This reduction is shown in Figure 2.11.

(a)   (b)
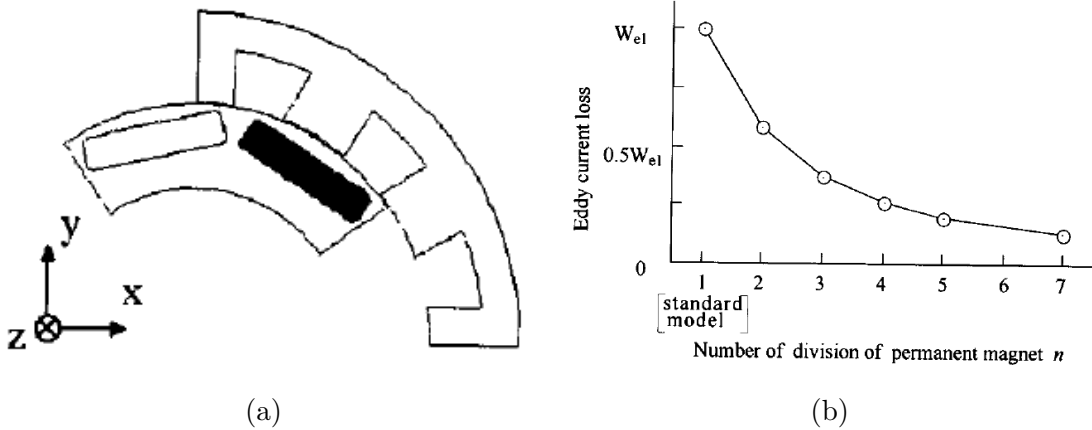
Figure 2.11: Effects of segmentation on magnet losses with concentrated winding [111]

Many analytical solutions have been derived, usually taking into account flux from a single direction. One of the earliest if not the earliest attempt was [89] for 2D surface-mounted permanent magnet machines (SPMSM). Others include several for a rectangular plate in quasi-3D [112] [71], an unclear attempt at 2D SPMSM in [113], a theoretically misguided attempt considering the airgap in quasi-3D [114], and an apparent repetition of [114] in [115]. It is not clear whether summation indexes in [115] refer to the segmentation numbers, as stated, or to the pulsating field in the axial direction, the last of which functions only as a useful model since the field does not pulse in the axial direction. In [114], the same theoretical assumption is made. However, when treating the problem in full with boundary conditions as in [71] and [112], even with the influence of insulation between segments in [116], we see that the definition of the stator current sheet in [114] and the equivalently pulsating magnetic field density in [115] model the geometric harmonics of the rectangular magnet segments. As a result, geometric harmonics are confounded with MMF harmonics in both [115] and [114]. Results concur with FEM analyses because

39

the geometric harmonics are single-dimensioned and odd in the case of modeling the geometry of the rectangular magnet as rectangular current pulses. The reason why a quasi-3D problem can reduce to single-dimensioned geometric harmonics is interesting and may be seen in [71]. One insight from [115] that [114] also applies and [112] does not consider is the airgap and magnet thickness in an integral Ampère loop, which, if $\mu \to \infty$ in iron is assumed, modifies the eigenvalue $1/\delta$ by a factor of $d/(g+d)$ for buried magnets, where g is the airgap distance and d is the magnet thickness. Luckily, since $g \ll d$, the factor is near one, both its neglect in [112] and its approximation in [114] of the factor as d/g for surface-mounted permanent magnets −where d/g is close to unity since $d \approx g$ for SPMSM but is one in actuality because $\mu_{air} \approx \mu_{mag} \approx 1$ −have little influence on the results. Thus the three papers converge to nearly identical trends regarding magnet eddy current losses and segmentation, namely, the trend with a maximum for non-unitary segmentations, as shown in Figure 2.12. Ignoring this trend may lead to incorrect segmentation numbers in applications where magnet losses are of paramount importance, as with axial flux machines [117]. The trend is counter-intuitive based on other geometries that have AC loss and arises due to the consideration of the third dimension, PWM harmonics, and consideration of the reaction field. It can be explained by imagining the eddy currents as flowing inside a torus of minor radius $\delta/2$ inscribed in the rectangular prism-magnet. If the dimensions of the magnet are much larger than δ, then segmentation will only increase the total length of the tori, increasing the resistance, and therefore the losses. Only after one of the dimensions is significantly less than δ will the eddy currents begin to overlap and cancel to reduce overall losses. If δ is already large, as in the case of relatively low slot harmonics, then less segmentation is needed and the intermediary peak is not observed, as in Figure 2.11, which is why it is only observed when considering high PWM carrier harmonics. The paper [118] explains these facts well. It also explains why it is often preferable to segment magnets in the circumferential direction instead of the axial direction when only considering carrier harmonics.

$$(a) \qquad\qquad (b)$$
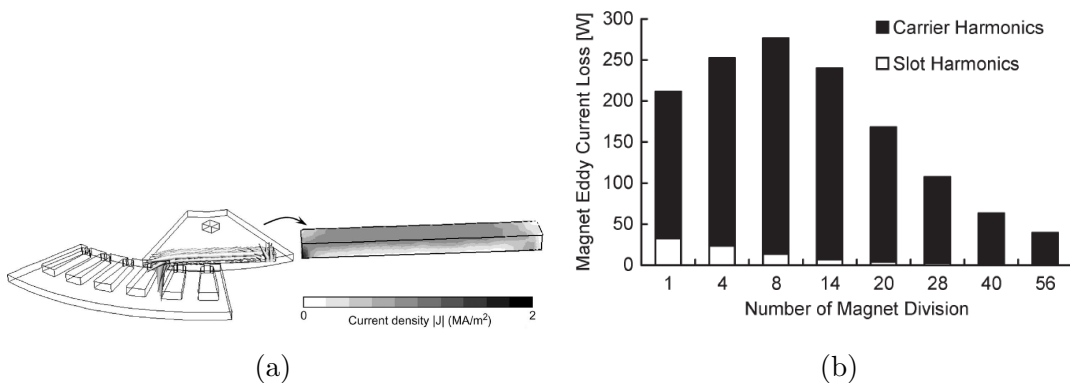
Figure 2.12: Effects of segmentation on magnet losses with distributed winding [112]

Whether the windings are concentrated or distributed and the magnets are buried, inset, or at the surface of the rotor iron also affects magnet eddy current content [119]. According to [119], inset magnets produce the most harmonics over-all, and concentrated windings increase magnet losses due to slot harmonics to an overwhelming degree [119] [120]. As mentioned before, although increasing the con-verter commutation frequency increases losses with constant current ripple, because

the current ripple amplitude decreases faster than the power increases with switching frequency with constant ripple, the eddy current losses decrease overall with increasing switching frequency, including in the rotor with permanent magnets [121]. As also noted by [121] and [122], increasing the temperature of the magnets reduces its magnetic flux, and therefore rotor cooling, as with winding cooling, is the limiting factor for sustained power density.

2.5   Loss Measurement

Power losses translate into temperature increases, and therefore the accurate measurement of losses and their respective origins is important.

Copper loss measurements seem the simplest to compute when not considering AC losses. One may simply calculate the resistance from the winding specifications, verify the calculations with resistance measurements, account for temperature effects with a linear equation for resistance, and multiply it by the squared of the phase currents. Proximity effect losses are almost impossible to isolate from stator iron losses with just measurements, which motivates the necessity of FEM analysis, especially for machines with massive conductors.

Iron losses depend heavily on the Epstein frame measurements and on the model used, and are usually obtained by subtracting the DC copper losses from the total losses. Before that, however, one must also subtract mechanical losses, like viscous drag and bearing friction. The latter measurement proves uncomplicated for induction machines [85], but permanent magnet machines require that the operator replace the magnets with demagnetized versions or fillers, preferably of a similar density to avoid measuring no-load iron losses concurrently. No-load iron losses, or measured losses during an open-circuit test with magnets, are often assumed to encompass iron losses over all other operating points, also heavily loaded points [123]. FEM simulations show that because currents change the magnetic flux paths and the magnetic flux density intensity, the iron has different saturation levels in different places, and therefore loading also affects iron losses as opposed to merely rotor speed, especially at maximum torque and power. Magnet losses and rotor iron losses are typically clumped together in the iron losses, making separation possible only in 3D-FEM [65], unless the operator constructs a special contraption. Even then, losses in the rotor may not be separable from the rotor iron and the magnet.

2.6   Optimization

Many have investigated the optimization of the electric machine, the electric machine and inverter system, and the electric machine-inverter-battery system, i.e. the electric drive. The most well-known optimization for permanent magnet synchronous machines is the maximum torque per ampere, or MTPA. It is usually implemented in steady-state operation since a full dynamic treatment requires solving a partial differential equation in real-time, resulting in the voltage and voltage angle relative to the PM flux for every time step. When the rotor spins to its rated speed, the generated BEMF approaches that of the constant voltage supply before the inverter. In [124], flux-weakening was introduced as a current regulator saturation handler, which resulted in the current trajectory following the voltage ellipse and extending

the operating range of the machine. Inverter current limits were not considered, as well as optimal operation along the maximum power curve, or maximum torque per volt (MTPV). All optimal trajectories with current and voltage constraints with MTPA and MTPV were considered in [125], as shown in Figure 2.13.
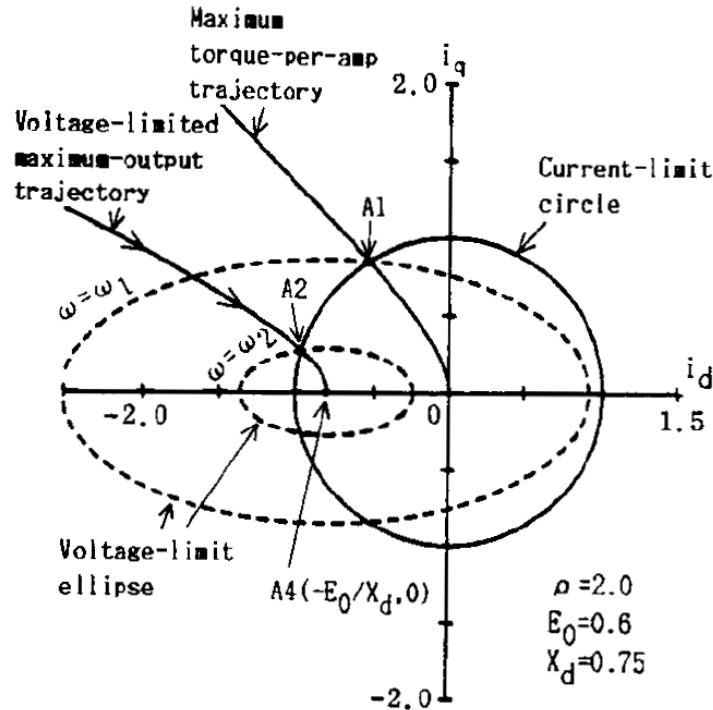
Figure 2.13: Optimal trajectories for an IPMSM [125]

The same author formulated one of the first attempts at maximum torque per loss (MTPL), including the iron loss resistance [126]. As mentioned before, modeling iron loss as a constant resistance is not sufficient. Also, the region where MTPL differs the most from its predecessor, MTPA, is limited to mid-speeds and low torques, since MTPV takes over in the field-weakening torque-speed plane. This means that MTPL suits drives with large DC bus voltages, since its region of significance is extended by delaying field-weakening to faster speeds.

The optimal trajectories heretofore discussed are equilibrium trajectories assuming sinusoidal phase currents. Because electric machines are usually powered by converters, specifically, inverters, they provide another dimension to the optimization. For ultra-high speed machines in the hundreds of thousands of rotations per minute for example, pulse amplitude modulation (PAM) is best to control the machine compared to PWM to minimize losses [127]. PAM varies the DC bus voltage using a buck converter and a three-phase inverter in six-step operation. The two main optimization levers available after hardware design in the machine-inverter system with constant voltage are therefore PWM methods and the switching frequency. In the electric drive, one must also include the DC bus voltage; in traction applications however, the DC bus voltage may vary significantly anyway depending on load due to the battery equivalent resistance and large load currents. Furthermore, the maximum DC bus voltage is usually fixed during design, as incorporating a power DC/DC converter involves another component. Commutation frequency and PWM methods remain as optimization levers, both of which were discussed earlier in this

42

chapter. In [128] like in many other methods, the objective, or cost function, involves penalizing the torque ripple. The paper [128] also penalized total power loss in the objective function for a 2.35 kW surface-mounted synchronous motor, returning an optimal switching frequency of about 9 kHz. Unfortunately, only sinusoidal PWM was considered. Another attempt in [129] on a 70 kW IPMSM comparing SVM and DPWM1 and 8 kHz, 15 kHz, and 24 kHz switching frequencies optimized the WLTP3 cycle. Although the converter kind was not reported, inspecting the power gains as a result of optimization reveals that the switching frequency was reduced and DPWM1 was likely used most of the time, as most of the gains were in the converter with slightly increasing motor losses. Unfortunately, the optimal program was not reported. The motor loss measurements show asymmetry between generating and motoring, with less losses during generating, which probably inflated the energy gain on WLTP3 of about 70 Wh, as expected [129].

Chapter 3

Analysis and Control of Permanent Magnet Machines

This chapter overviews the analysis of permanent magnet machines with saliency —or interior permanent magnet machines (IPMSM) —from first physical principles and the control methods used for three-phase and dual-three phase machines. The torque equation for permanent magnet machines is derived from Maxwell's equations and the Lorentz force assuming a squared sinusoidally-varying permeability. From there, a motor model in the synchronous frame is justified due to the periodic matrix coefficients of the multi-dimensional motor model in the stator frame. The applied current control method used in this dissertation is then explained, followed by a derivation of typical optimal current trajectories incorporating the nonlinearities in the machine due to saturation. The methods are compared to show in later chapters that changing inverter parameters can have a larger effect on losses in the machine than even changing those aforementioned current commissions.

3.1 Theory of Torque Generation from Electromagnetics

In order to relate electromagnetic quantities to mechanical quantities, we will start with Faraday's law of induction and the definition of the force exerted by an electric field on a charge. We will then modify the the equation for force on a charge to a charge density. Then, we will use the definition of torque that relates the proper component of the Lorentz force to the radius at which that force is located. Proceeding with the first step, Faraday's law is

$$\oint_{\partial A} \mathbf{E} \cdot d\boldsymbol{l} = -\frac{d}{dt} \int_A \mathbf{B} \cdot d\boldsymbol{A} \tag{3.1.1}$$

and the force on a charge is $\mathbf{F} = q\mathbf{E}$. According to [130], if we assume that the magnetic field is constant but that the path traced by a closed area from equation (3.1.1) changes in time, then $\mathbf{E} = \boldsymbol{v} \times \mathbf{B}$ is the electric field seen by a point on the path changing with velocity $\boldsymbol{v}$ in a magnetic field $\mathbf{B}$. The force on a charge along said path is then the Lorentz force, or $\mathbf{F} = q\boldsymbol{v} \times \mathbf{B}$. If we then consider the volumetric force density, $\mathbf{f} = \partial \mathbf{F}/\partial V$, and realize that for a continuum of charges

$\partial q/\partial V = \rho$ and that $\rho\boldsymbol{v} = \mathbf{J}$, then

$$\mathbf{f} = \mathbf{J} \times \mathbf{B} \tag{3.1.2}$$

Assuming that the current density, $\mathbf{J}$, is bounded to the rotor magnetic domains, we can modify Ampere's law to read

$$\mathbf{J}_r = \nabla \times \left(\frac{\mathbf{B}_s}{\mu} + \mathbf{H}_m \right) \tag{3.1.3}$$

where the electric field outside of the winding is neglected. Note that this approach is equivalent to one using Maxwell's stress tensor, as it is also derived from equation (3.1.2) for magnetoquasistatic (MQS) problems. What follows nevertheless constitutes a simplified model of torque generation in electric machines. Substituting equation (3.1.3) into (3.1.2) and noticing that $\mathbf{B} = \mathbf{B}_s$, equation (3.1.2) then becomes

$$\mathbf{f} = \left(\nabla \times \mathbf{H}_m + \frac{1}{\mu}\nabla \times \mathbf{B}_s - \frac{1}{\mu^2}\nabla\mu \times \mathbf{B}_s \right) \times \mathbf{B}_s \tag{3.1.4}$$

where the permeability μ represents a bulk permeability along the tangential direction of the rotor. Since we are interested in torque generation, it makes sense to only analyze the tangential component of equation (3.1.4). To generate said component, the cross product must be between the axial, or z-component, of the current density term in the rotor, and the radial, or r-component, of the total magnetic flux density. The volume-specific tangential force then becomes

$$f_\theta = \frac{1}{r}\left(\frac{1}{\mu^2}\frac{\partial\mu}{\partial\theta}B_s - \frac{1}{\mu}\frac{\partial B_s}{\partial\theta} - \frac{\partial H_m}{\partial\theta} \right) B_s \tag{3.1.5}$$

We dropped the subscript specifying the magnetic flux density component because we assume that only radial fields permeate the rotor, both those originating from the stator B_s and those from the permanent magnet $B_m = \mu H_m$. In reality, a tangential flux is necessary because of Gauss's law of magnetism.

We included the variation of the permeability in the tangential direction in order to represent the salience in an electric machine. In fact, machine salience is synonymous with prominent variations in the permeability along the path of a magnetic flux line. The tangential component of the magnetic flux density is neglected. We will show that the tangential variation of the permeability in equation (3.1.5) indeed provides additional torque characteristic of salient synchronous machines.

Proceeding with the derivation, we impose a sinusoidal variation on the field. Since permeability is never less than zero and real in our construction, we impose equation (3.1.8) and also assume that $\gamma = \mu_{r,\min}/\mu_{r,\max}$ approximates the average maximally saturated state $\mu_{r,\min}\mu_0$, where $\mu_0 = 4\pi \times 10^{-7}$ Tm/A and $\hat{\mu} = \mu_{r,\max}\mu_0$. This assumption holds for materials with large permeabilities, like electrical steel. Furthermore, we assumed that μ does not vary in the radial direction. Variables with carats indicate amplitudes and θ represents the tangential coordinate. Lastly, the magnetic field from the winding is placed ϕ radians apart from the permanent magnet field. Explicitly,

$$B_s = \hat{B}_s \cos\left(\theta - \phi\right) \tag{3.1.6}$$

$$H_m = \hat{H}_m \cos\theta \tag{3.1.7}$$

$$\mu = \hat{\mu}\left(\gamma + \cos^2\theta\right) \tag{3.1.8}$$

Substituting equations $(3.1.6)-(3.1.8)$ into $(3.1.5)$ and integrating over the active volume of the rotor yields

$$\int_0^l \int_0^R \int_0^{2\pi} f_\theta \; rd\theta drdl = \pi Rl\left(\hat{B}_s\hat{H}_m\sin\phi - \frac{\hat{B}_s^2}{\hat{\mu}}\sin 2\phi\left(\frac{2\gamma+1}{\sqrt{\gamma(\gamma+1)}} - 2\right)\right) \tag{3.1.9}$$

where l is the length of the rotor. When the tangential force in equation $(3.1.9)$ is multiplied by the lever radius $r_l = R$ to acquire torque per unit length, it results in the torque produced by the machine, which reads

$$T_e = \pi R^2 l\left(\hat{B}_s\hat{H}_m\sin\phi - \frac{\hat{B}_s^2}{\hat{\mu}}\sin 2\phi\left(\frac{2\gamma+1}{\sqrt{\gamma(\gamma+1)}} - 2\right)\right). \tag{3.1.10}$$

Equation $(3.1.10)$ shows several known relations. Namely, that the torque scales with the square of the radius of the machine and with its length. Moreover, if we neglect the $\hat{B}_s^2$ term, the angle between the magnetic flux density induced by the stator winding must have an offset of $\phi = \pi/2$ to the radial permanent magnet magnetic field strength for maximum torque. This corresponds to the angle that gives the maximum cross-product between two vectors. It can be also shown that the $\hat{B}_s^2$ term comes exclusively from the variation of the permeability in the tangential direction, and therefore neglecting it results in the torque equation for a surface permanent magnet machine.

Including the $\hat{B}_s^2$ term therefore models an interior permanent magnet machine. To see this, we first proceed to find the angle that maximizes the torque. The angle that maximizes the torque is

$$\phi = \arccos\left(\frac{\mu_0\hat{H}_m}{8(\sqrt{2}-1)^2\hat{B}_s} \pm \sqrt{\left(\frac{\mu_0\hat{H}_m}{8(\sqrt{2}-1)^2\hat{B}_s}\right)^2 + \frac{1}{2}}\right) \tag{3.1.11}$$

If we then assume that $\hat{B}_s = 2\mu_0\hat{H}_m/5\gamma$, then we take the subtracted solution to yield $-1 < \cos\phi < 0$, indicating that the angle for maximum torque lies in the second quadrant. In this case, $\phi \approx 115°$. Any angle in the second quadrant will give a positive value for $\sin\phi$ and a negative value for $\sin 2\phi$, making the reluctance contribution additive. To prove that saliency offers more torque than when there is no saliency, the ratio of both torque contributions should be greater than one. Simplifying said ratio results in

$$0 > \cos\phi \tag{3.1.12}$$

46

Since $\hat{B}_s$, $\hat{H}_m$, and $\hat{\mu}$ are all positive. The relation in (3.1.12) indicates that the salient machine delivers more torque when the current angle lies in the second and third quadrants.

The previous formulation draws a simplified sketch of the physical principles involved in electromagnetic torque production for synchronous machines, not just permanent magnet synchronous machines (PMSM), as $\mathbf{H}_m$ may readily represent the field strength from a wound rotor. Besides the requirement of orthogonality between the radial magnetic rotor flux and the stator flux, we have established how additional torque production is possible if the permeability varies in the tangential direction. Furthermore, it is important to note that although we did not employ any transformations to rotate the quantities into the rotor reference frame, the equation for torque is independent of the rotor angle, θ. Equation (3.1.11) nevertheless necessitates controlling the different radial magnetic flux density components in two axes synchronous with rotor rotation in order to control the angle ϕ. This implies that, although torque production depends on the magnitude of the radial components of the stator and rotor fields and the angle between them, achieving the angle that maximizes torque may require controlling the magnetic flux densities in the rotor frame. Indeed, that is the approach of the standard field-oriented control, or FOC. In the following section we will review the typical transformations and detailed models used to control interior permanent magnet synchronous machines (IPMSM) using FOC, assuming, for now, that the system is controllable and stable.

3.2 Circuit Representation of Permanent Magnet Synchronous Machines

This section will expand on the previous section by introducing the circuit representation of three-phase and dual three-phase interior permanent magnet machines (IPMSM). We analyze IPMSMs because its equations simplify to surface permanent magnet machines (SPMSM). In accordance to circuit representations, IPMSM's models use inductances, resistances, and back-electromotive force (BEMF) sources. We will first focus on three phase machines, then on dual three-phase machines.

Three phase circuit quantities, like voltage and current, will be defined as

$$\boldsymbol{x}_{UVW} = \begin{bmatrix} X_U \cos\theta_e \\ X_V \cos(\theta_e - 2\pi/3) \\ X_W \cos(\theta_e + 2\pi/3) \end{bmatrix} \tag{3.2.1}$$

If the quantities are balanced, then $X_U = X_V = X_W = X$. Because the system is dynamic, we have that $X = X(t)$. The variable θ_e represents the electrical angle of the circuit quantity. This is done to distinguish it from the mechanically rotating angle for machines with more poles. Generally $\theta_e = p\theta_m$, where the subscript m indicates a mechanical quantity. The machine circuit for an IPMSM may be modeled by a time-varying RL circuit, with an additional voltage source from the rotating magnets. Explicitly, the circuit equation is

$$\boldsymbol{u}_{UVW} = R_s \boldsymbol{i}_{UVW} + \frac{d}{dt}\left(\mathbf{L}\boldsymbol{i}_{UVW} + \boldsymbol{\psi}_{pm}\right) \tag{3.2.2}$$

where R_s is the phase resistance, $\mathbf{L}$ is the time-varying inductance matrix, ω_e is the rotor electrical speed, and $\boldsymbol{\psi}_{pm}$ is the permanent magnet flux linkage linked to the stator windings. As is typical, $\boldsymbol{u}$ and $\boldsymbol{i}$ represent the input phase voltage and the phase current respectively. Arguably, the most complicated component in equation (3.2.2) is the inductance matrix, as shown in equations (3.2.3) and (3.2.4).

$$\mathbf{L} = \frac{1}{3} \begin{bmatrix} L_{11} & L_{12} & L_{13} \\ L_{12} & L_{22} & L_{23} \\ L_{13} & L_{23} & L_{33} \end{bmatrix} \tag{3.2.3}$$

$$
\begin{aligned}
L_{11} &= & L_d + L_q & +(L_d - L_q)\cos\left(2\theta_e\right) \\
L_{12} &= & (L_d + L_q)/2 & +(L_d - L_q)\cos\left(2\theta_e - 2\pi/3\right) \\
L_{13} &= & (L_d + L_q)/2 & +(L_d - L_q)\cos\left(2\theta_e + 2\pi/3\right) \\
L_{22} &= & L_d + L_q & +(L_d - L_q)\cos\left(2\theta_e + 2\pi/3\right) \\
L_{23} &= & -(L_d + L_q)/2 & +(L_d - L_q)\cos\left(2\theta_e\right) \\
L_{33} &= & L_d + L_q & +(L_d - L_q)\cos\left(2\theta_e - 2\pi/3\right)
\end{aligned}
\tag{3.2.4}
$$

The inductance matrix is symmetrical, which corresponds to the fact that mutual inductances between the phases are the same, or $L_{ab} = L_{ba}$. We also see that the inductance matrix varies as a function of twice the electrical rotor angle with various phase offsets. By equation (3.2.1), so does the permanent magnet flux linkage. This introduces the complication that we must take the time derivative of the already complicated inductance matrix. Specifically, the machine is a linear time-varying (LTV) system. If we allow for saturation, which is typical of traction machines, then a strong nonlinearity is introduced in addition to the time-variance complexity. At this point it would help if we could eliminate one of the sources of complexity. The next section explains how that is typically done.

3.3 Floquet Analysis and the Clarke-Park Transformation

3.3.1 Floquet Analysis

As the torque equation (3.1.12) suggested that the electromagnetic torque in the machine is independent of the rotor angle, typical approaches to the analysis of the circuit equation (3.2.2) involve transforming it to the rotor reference frame and to thus eliminate the LTV complexity. If saturation is neglected, the system becomes a linear time-invariant (LTI) system, which is much simpler to analyze and control.

Floquet theory provides the tools to ensure that the analyzed and controlled machine in the rotor frame will have the same desired properties in the stator, or stationary frame. The most important property is stability. Indeed, Floquet theory guarantees the stability of the system in the stationary frame if it is stable in the rotating frame provided that the system matrix, $\mathbf{A}$ is time-periodic. It also guarantees the existence of a transformation, $\mathbf{T}$, that rotates the system to the appropriate reference frame. In this section, we will also see that this transformation

is the Clarke-Park transformation matrix. We will now proceed to modify equation (3.2.2) to conform to the LTV form shown in equation (3.3.1).

$$\dot{\boldsymbol{x}} = \mathbf{A}(t)\boldsymbol{x} + \mathbf{B}(t)\boldsymbol{u} \tag{3.3.1}$$

$$
\begin{aligned}
\boldsymbol{x} &= \boldsymbol{i}_{UVW} \\
\boldsymbol{u} &= \boldsymbol{u}_{UVW} - \frac{d\boldsymbol{\psi}_{pm}}{dt} \\
\mathbf{A}(t) &= -\mathbf{L}^{-1}\left(R_s\mathbf{I} + \frac{d\mathbf{L}}{dt}\right) \\
\mathbf{B}(t) &= \mathbf{L}^{-1}
\end{aligned}
\tag{3.3.2}
$$

where $\mathbf{I}$ is the identity matrix. Equation (3.3.2) shows the circuit equation parameters arranged to conform to the LTV form. Now we need to show that the inverse of the inductance matrix, its time derivative, and the multiplication of both are time-periodic. If we prove that the inverse of the inductance matrix and its derivative are time-periodic independently, then we are ensured that their product is also time-periodic. It is important to note that constants are also time-periodic, so if a matrix is in the form $\mathbf{A}(t) = \mathbf{C} + \mathbf{D}(t)$ and $\mathbf{D}(t)$ is time-periodic, then so is $\mathbf{A}(t)$.

When taking the time derivative of equation (3.2.4), it is clear that, like $\mathbf{L}$, it is also time-periodic with the same period. Proving that the inverse of the inductance matrix is also periodic is a little more involved. We will begin by assuming that the transformation $\mathbf{T}$ exists. Transforming equation (3.2.2) such that $\mathbf{T}\boldsymbol{x}_{UVW} = \boldsymbol{x}_{dq}$ yields

$$
\begin{aligned}
\mathbf{T}\boldsymbol{u}_{UVW} &= R_s\mathbf{T}\boldsymbol{i}_{UVW} + \mathbf{T}\frac{d}{dt}\left(\mathbf{L}\boldsymbol{i}_{UVW} + \boldsymbol{\psi}_{pm}\right) \\
\boldsymbol{u}_{dq} &= R_s\boldsymbol{i}_{dq} + \mathbf{T}\frac{d}{dt}\left(\mathbf{L}\mathbf{T}^{-1}\boldsymbol{i}_{dq} + \boldsymbol{\psi}_{pm}\right) \\
\boldsymbol{u}_{dq} &= R_s\boldsymbol{i}_{dq} + \mathbf{T}\mathbf{L}\mathbf{T}^{-1}\frac{d\boldsymbol{i}_{dq}}{dt} + \mathbf{T}\frac{d}{dt}\left(\mathbf{L}\mathbf{T}^{-1}\right)\boldsymbol{i}_{dq} + \mathbf{T}\frac{d\boldsymbol{\psi}_{pm}}{dt}
\end{aligned}
\tag{3.3.3}
$$

The term $\mathbf{L}_{dq} = \mathbf{T}\mathbf{L}\mathbf{T}^{-1}$ suggests that we may require that $\mathbf{T}$ also diagonalize the inductance matrix. If $\mathbf{L}_{dq}$ is diagonal and time-independent, then its inverse is time-independent and non-singular. Taking the inverse of said matrix in terms of of $\mathbf{T}$ and $\mathbf{L}_{dq}$ yields

$$\mathbf{L}^{-1} = \mathbf{T}^{-1}\mathbf{L}_{dq}^{-1}\mathbf{T} \tag{3.3.4}$$

Because the transformation is periodic, then so is the inverse of the inductance matrix in the stator frame. This shows that the circuit equation can be analyzed according to Floquet theory. Now, because the above results depend on the transformation and diagonalization assumptions on $\mathbf{T}$, we proceed to introduce the Clarke-Park transformation, which fulfills the assumptions made.

3.3.2 Clarke-Park Transformation for Three-Phase Machines

The Clarke-Park transformation consists of two parts: rather obviously, the Clarke and the Park transformation. The Clarke transformation uses the phase offset between the three machine phases to compress the system from three to two phases. The Park transformation is a simple matrix rotation to the rotor frame. Specifically, the Clarke-Park transformation reads

$$\mathbf{T} = \frac{2}{3} \begin{bmatrix} \cos\theta_e & \cos\left(\theta_e - 2\pi/3\right) & \cos\left(\theta_e + 2\pi/3\right) \\ -\sin\theta_e & -\sin\left(\theta_e - 2\pi/3\right) & -\sin\left(\theta_e + 2\pi/3\right) \\ 1 & 1 & 1 \end{bmatrix} \qquad (3.3.5)$$

and the Clarke transformation can be readily recovered by setting $\theta_e = 0$. This transformation diagonalizes and transforms the induction matrix. The overall equation in the rotor reference frame is shown in equation (3.3.6)

$$\boldsymbol{u}_{dq} = \begin{bmatrix} R_s & -\omega_e L_q \\ \omega_e L_d & R_s \end{bmatrix} \boldsymbol{i}_{dq} + \begin{bmatrix} L_d & 0 \\ 0 & L_q \end{bmatrix} \frac{d\boldsymbol{i}_{dq}}{dt} + \begin{bmatrix} 0 \\ 1 \end{bmatrix} \omega_e \psi_{pm} \qquad (3.3.6)$$

where the quantities in the rotor frame are defined in equation (3.3.7).

$$\boldsymbol{x}_{dq} = \begin{bmatrix} x_d \\ x_q \end{bmatrix} \qquad (3.3.7)$$

The circuit equation (3.3.6) is simpler than the circuit equation defined by $(3.2.1)-(3.2.4)$ because of two main reasons. First, the three-phase system was compressed into a two-phase system; second, the LTV system was transformed to a LTI system, assuming constant parameters. We may now proceed with conventional stability analyses for systems of differential equations. The state transition matrix of system (3.3.6) is

$$\mathbf{A} = -\begin{bmatrix} \dfrac{R_s}{L_d} & -\omega_e \dfrac{L_q}{L_d} \\[2ex] \omega_e \dfrac{L_d}{L_q} & \dfrac{R_s}{L_q} \end{bmatrix} \qquad (3.3.8)$$

and its eigenvalues are

$$\lambda = -\frac{R_s}{2}\left(\frac{1}{L_d} + \frac{1}{L_q}\right) \pm \sqrt{\left(\frac{R_s}{2}\left(\frac{1}{L_d} - \frac{1}{L_q}\right)\right)^2 - \omega_e^2} \qquad (3.3.9)$$

which are always stable for $\omega_e^2 > 0$. For $\omega_e = 0$ the eigenvalues are $\lambda_{1,2} = -R_s/L_q, -R_s/L_d$. In addition, if ω_e^2 is larger than the square of the difference of the machine time constants, R_s/L_d and R_s/L_q, then the currents will have oscillating components; this is the case for most traction machines. Ensuring no oscillations in the *dq*-currents is a topic of motor control and will be considered later in the chapter. Lastly, because the electrical system (3.3.6) in the rotating frame is stable, so is system (3.2.2) in the stationary frame.

Having analyzed the electrical portion of the three-phase IPMSM and proven its stability, we now proceed to analyze the dual-three phase electrical system.

3.3.3 Clarke-Park Transformation for Dual-Three Phase Machines

Equation (3.2.1) defined the three-phase state vector. Here we define the six-phase, or dual three-phase state vector, as follows:

$$\boldsymbol{x} = \begin{bmatrix} X_{U1} \cos \theta_e \\ X_{V1} \cos \left(\theta_e - 2\pi/3 \right) \\ X_{W1} \cos \left(\theta_e + 2\pi/3 \right) \\ X_{U2} \cos \left(\theta_e + \alpha \right) \\ X_{V2} \cos \left(\theta_e - 2\pi/3 + \alpha \right) \\ X_{W2} \cos \left(\theta_e + 2\pi/3 + \alpha \right) \end{bmatrix} \tag{3.3.10}$$

Here we have added an additional angle, α, which indicates that the two duals can be controlled with a phase delay between them. This poses two options for modeling the machine. One involves one large transformation matrix which maps all six phases to a single dq-space. The other involves using two separate transformations for each dual. In the latter case, the transformation for the first machine remains unchanged from equation (3.3.5); for the second machine one may simply add α to θ_e. This dual control scheme yields the synchronous frame model shown in (3.3.11) with state vectors shown in (3.3.12).

$$\begin{aligned} \boldsymbol{u}_{dq} &= \begin{bmatrix} R_s & -\omega_e L_{q1} & 0 & -\omega_e M_{q21} \\ \omega_e L_{d1} & R_s & \omega_e M_{d21} & 0 \\ 0 & -\omega_e M_{q12} & R_s & -\omega_e L_{q2} \\ \omega M_{d12} & 0 & \omega_e L_{d2} & R_s \end{bmatrix} \boldsymbol{i}_{dq} \\ &+ \begin{bmatrix} L_{d1} & 0 & M_{d21} & 0 \\ 0 & L_{q1} & 0 & M_{q21} \\ M_{d12} & 0 & L_{d2} & 0 \\ 0 & M_{q12} & 0 & L_{q2} \end{bmatrix} \frac{d\boldsymbol{i}_{dq}}{dt} \\ &+ \begin{bmatrix} 0 \\ 1 \\ 0 \\ 1 \end{bmatrix} \omega_e \psi_{pm} \end{aligned} \tag{3.3.11}$$

$$\boldsymbol{x}_{dq} = \begin{bmatrix} x_{d1} \\ x_{q1} \\ x_{d2} \\ x_{q2} \end{bmatrix} \tag{3.3.12}$$

Where $M_{d,q}$ is the mutual inductance between duals. Equation (3.3.11) can be further simplified because $M_{d12} = M_{d21}$, $M_{q12} = M_{q21}$, $L_{d1} = L_{d2}$, and $L_{q1} = L_{q2}$.

For the other, six-phase option, the Clarke-Park transformation from the first

machine is concatenated with the one from the second and divided by two to yield

$$
\mathbf{T} = \frac{1}{3}
\begin{bmatrix}
\cos\theta_e & \cos(\theta_e - 2\pi/3) & \cos(\theta_e + 2\pi/3) \\
-\sin\theta_e & -\sin(\theta_e - 2\pi/3) & -\sin(\theta_e + 2\pi/3) \\
1 & 1 & 1 \\
1 & 1 & 1 \\
1 & 1 & 1 \\
1 & 1 & 1 \\
\cos(\theta_e + \alpha) & \cos(\theta_e - 2\pi/3 + \alpha) & \cos(\theta_e + 2\pi/3 + \alpha) \\
-\sin(\theta_e + \alpha) & -\sin(\theta_e - 2\pi/3 + \alpha) & -\sin(\theta_e + 2\pi/3 + \alpha) \\
1 & 1 & 1 \\
1 & 1 & 1 \\
1 & 1 & 1 \\
1 & 1 & 1
\end{bmatrix}
\tag{3.3.13}
$$

and the state vector reads like equation (3.3.7). The four bottom rows add all of the phases, the sum which, if each set of three phases is balanced and each dual is connected to its own neutral point isolated from the other, will equal to zero. In the case where the sets of three phases are not balanced, then one may replace the ones with other transformations to isolate the desired frequency components of, for example, the current. Said components would then be concatenated to the state vector and may be independently controlled to equal zero. Because there are only four rows left, only two frequency components can be isolated. In dual three phase machines with $\alpha = 30°$ usually the 5th and 7th harmonics are controlled.

To construct the circuit equations, first notice that the first three entries of the first row, when multiplied by the first dual circuit quantity equal to x_{d1} from equation (3.3.12). The second three entries of the row correspondingly yield the product x_{d2}. In effect, $x_d = (x_{d1} + x_{d2})/2$ and $x_q = (x_{q1} + x_{q2})/2$. Combined with the equivalencies between the inductances, we recover the original three-phase system of equation (3.3.6) except with

$$
\begin{aligned}
L_d &= L_{d1} + M_{d12} &= L_{d2} + M_{d21} \\
L_q &= L_{q1} + M_{q12} &= L_{q2} + M_{q21}
\end{aligned}
\tag{3.3.14}
$$

Because system (3.3.11) can be transformed into the two-phase system (3.3.6) and because we already proved the stability of the latter, then the dual-three phase system is stable in both the rotating and stationary frames. The stability of the two-transformation system however, has not been proven. One may imagine the case in which x_{d1} and x_{d2} have equal but opposite instabilities such that their average is stable. We will assume, for now, that those internal states are indeed stable. Having established the stability of the IPMSM's circuit states, namely the phase currents, we now proceed to describe the torque that the machine generates.

3.3.4 Electromagnetic Torque

One may now write the electromagnetic torque equation in terms of the synchronous variables and parameters as the cross product of the flux linkage and the stator

current vectors in the dq-frame. The cross product of the flux linkage and the stator current as torque follows from the Lorentz tangential force. Specifically,

$$
\begin{aligned}
T_e &= \left(\boldsymbol{r} \times \int_V \mathbf{J} \times \mathbf{B} \; dV \right) \cdot \hat{\boldsymbol{z}} \\
&= \left(\boldsymbol{r} \times \hat{\boldsymbol{\theta}} \int_V J_z B_r \; dV \right) \cdot \hat{\boldsymbol{z}} \\
&= r \int_V J_z B_r \; dV \\
&= r J_z B_r \pi l R^2
\end{aligned}
\tag{3.3.15}
$$

where R is the outer rotor radius and $\hat{\boldsymbol{z}}$ is the unit vector in the axial direction. Equation (3.3.15) is a simplification, but one may nevertheless replace $\mathbf{J} = \nabla \times \mathbf{H}$ to specify that the torque-producing interaction of the magnetic fields takes place in the rotor volume acting on the bounded currents in the iron and magnets. Resuming the simplification, if the lever length $r = R$, $\psi_r = 2\pi R l B_r$, and the current is $i_z = J_z \pi (R + \ell/3) \ell / p$, then

$$
\begin{aligned}
T_e &= \frac{pR^2}{\pi \ell (R + \ell/3)} i_z \psi_r \\
&= \frac{pR^2}{\pi R^2 16/75} i_z \psi_r \\
&= c \left(\boldsymbol{i} \times \boldsymbol{\psi} \right) \cdot \hat{\boldsymbol{z}}
\end{aligned}
\tag{3.3.16}
$$

where ℓ is the length of the stator slot and the effective width where the current is active is taken to be the pole arc at $R + \ell/3$. Also, $\ell = R/5$ is typical. From equation (3.3.16) it is clear that the Faraday torque reduces to the cross-product between the current and the flux linkage up to a unitless constant. Now we can justify equating the cross product between the stator current and the flux linkage in the dq-frame to the electromagnetic torque.

$$
\begin{aligned}
T_e &= c \left(\boldsymbol{i}_{dq} \times \boldsymbol{\psi}_{dq} \right) \cdot \hat{\boldsymbol{z}} \\
&= c \left(\psi_d i_q - \psi_q i_d \right) \\
&= c \left(i_q \psi_{pm} + (L_d - L_q) i_d i_q \right)
\end{aligned}
\tag{3.3.17}
$$

It turns out that the constant $c = 3p/2$, where p is the number of pole pairs in the machine. One must multiply the equation by the number of pole pairs because the torque from equation (3.3.17) is just for one pole pair. Furthermore, an additional factor of $3/2$ is necessary to compensate for the Clarke-Park transformation, which transformed three phases into two using the amplitude model. In that model, amplitudes are the same across coordinate frames, but power and torque require the correction. Finally, the equation for electromagnetic torque reads as follows:

$$
T_e = \frac{3p}{2} i_q \left(\psi_{pm} + (L_d - L_q) i_d \right)
\tag{3.3.18}
$$

which we can readily relate to the torque equation (3.1.12) if we set $i_q = \hat{I}_{dq} \sin \phi$ and $i_d = \hat{I}_{dq} \cos \phi$ to acquire

$$
T_e = \frac{3p}{2} \left(\psi_{pm} \hat{I}_{dq} \sin \phi + \frac{1}{2} (L_d - L_q) \hat{I}_{dq}^2 \sin 2\phi \right)
\tag{3.3.19}
$$

The salience contribution encapsulated in the $L_d - L_q$ term provides additional torque if the current angle, which corresponds to the angle of the magnetic flux said current creates, lies in the second quadrant or third quadrant, as equation (3.1.12) showed. For example, if $\phi \approx 115°$ as in the previous section, then the machine will deliver additional torque because it lies in the second quadrant. The equation (3.1.10) from the previous section corresponds, and, most importantly, is analogous to equation (3.3.19) since $L_d < L_q$. If we instead seek to optimize the current angle as a function of the parameters and the current magnitude, then the optimal angle delivering maximum torque is described in equation (3.3.20). That equation is also analogous to equation (3.1.11).

$$\phi = \arccos\left(\frac{-\psi_{pm}}{4\hat{I}_{dq}\left(L_d - L_q\right)} - \sqrt{\left(\frac{\psi_{pm}}{4\hat{I}_{dq}\left(L_d - L_q\right)}\right)^2 + \frac{1}{2}}\right) \tag{3.3.20}$$

The torque equation is also derivable from the states in the circuit, namely the voltage and the current. The power in the circuit is then

$$\begin{aligned}
P_e &= \frac{3}{2}\boldsymbol{u}_{dq} \cdot \boldsymbol{i}_{dq} \\
&= \frac{3}{2}\left(R_s\left(i_d^2 + i_q^2\right)\right. \\
&\quad + \frac{d}{dt}\left(\frac{1}{2}L_d i_d^2 + \frac{1}{2}L_q i_q^2\right) \\
&\quad \left. + \omega_e i_q\left(\psi_{pm} + \left(L_d - L_q\right)i_d\right)\right)
\end{aligned} \tag{3.3.21}$$

The electrical power can be separated into three main components. The first is the resistive power dissipation due to current conduction in the windings. The second is the time rate-of-change of magnetic energy stored in the phases, which is zero in steady-state and therefore does not represent the iron losses. The third term must therefore represent some sort of scaled mechanical power. Indeed, because $\omega_e = p\omega_m$, and because the mechanical power for a rotating rigid body is the product of its angular speed and torque, we derive equation (3.3.18) exactly. Because circuit variables and their power are derivable from Maxwell's equations, the equivalence between the two approaches to derive the electromagnetic torque justify the derivation of the volume-specific Lorentz force from Faraday's law at the beginning of the chapter.

All of the previous formulations assume constant parameters. The torque formulations nevertheless also conveniently apply for high-power and high-torque machines throughout their operating area, over which parameters change significantly. For large currents the inductances decrease due to iron saturation and resistance increases due to increasing temperature. These parameter changes render the machine a highly nonlinear machine. This means that the state transition matrix (3.3.8) and its eigenvalues (3.3.9) do not even prove the stability of the electrical portion of the machine equations. To control and analyze such a nonlinear machine, local linearization is used by storing the values of the inductances for all possible current combinations. The next section elaborates this idea and justifies its use.

3.4 Local Linearization of the Transformed Nonlinear Machine

Due to the nonlinearity of the inductance terms due to saturation, stability based on eigenvalues of the state transition matrix is not sufficient to ensure the stability of the nonlinear machine for all operating points. We therefore begin this section with a discussion on the stability of the nonlinear machine.

Firstly, it is important to realize that because the inductance saturation is a function of the exciting currents, then our state transition matrix becomes a function of the states to create an autonomous nonlinear system. We can prove or disprove the stability of points in said systems by linearizing the nonlinear vector $\boldsymbol{f}(\boldsymbol{x}) = \mathbf{A}(\boldsymbol{x})\boldsymbol{x}$ in the system $\dot{\boldsymbol{x}} = \boldsymbol{f}(\boldsymbol{x})$ about some equilibrium point $\boldsymbol{x} = \boldsymbol{x}_0$. We must now expand our system to incorporate the mechanical dynamics of the system. For that we need an additional state and corresponding state equation. The new state will be defined as the synchronous electrical speed, ω_e and the state equation concatenated to the system is

$$\frac{d\omega_e}{dt} = \frac{p}{\iota}\left(T_e - T_L\right) \tag{3.4.1}$$

where ι is the rotational inertia, T_L represents the load on the machine, and T_e is the current-dependent electromagnetic torque from equation (3.3.18). We first need to find the Jacobian of $\boldsymbol{f}$ to find that the real part of its eigenvalues are less than zero for a given equilibrium point. The Jacobian is the matrix of partial derivatives of $\boldsymbol{f}$ with respect to the states $\boldsymbol{x}$. We define $\boldsymbol{f}$ as

$$\boldsymbol{f} = \begin{bmatrix} -\frac{R_s}{L_d}i_d + \omega_e\frac{L_q}{L_d}i_q \\[2mm] -\omega_e\frac{L_d}{L_q}i_d - \frac{R_s}{L_q}i_q - \omega_e\frac{\psi_{pm}}{L_q} \\[2mm] \frac{p}{\iota}\left(T_e - T_L\right) \end{bmatrix} \tag{3.4.2}$$

Equation (3.4.2) shows that one equilibrium is the origin, and setting $T_L = 0$. This simplifies the analysis, since the partial derivatives in the Jacobian reduce to

$$\boldsymbol{J}_0 = \begin{bmatrix} -\frac{R_s}{L_d} & 0 & 0 \\[2mm] 0 & -\frac{R_s}{L_q} & -\frac{\psi_{pm}}{L_q} \\[2mm] 0 & \frac{3p^2}{2\iota}\psi_{pm} & -\frac{p}{\iota}\frac{\partial T_L}{\partial \omega_e} \end{bmatrix} \tag{3.4.3}$$

The eigenvalues are

$$\lambda_d = -\frac{R_s}{L_d}$$

$$\lambda_{q,m} = -\frac{1}{2}\left(\frac{R_s}{L_q} + \frac{p}{\iota}b\right) \pm \sqrt{\left(\frac{1}{2}\left(\frac{R_s}{L_q} - \frac{p}{\iota}b\right)\right)^2 - \frac{3p^2}{2\iota}\frac{\psi_{pm}^2}{L_q}} \tag{3.4.4}$$

which are always stable. In the analysis we assumed that $T_L = b\omega_e$ and $b > 0$, which is valid when the load is due to viscous fluids. In this case, the equilibrium

speed remains $\omega_e = 0$. If there is no load, the parameter b can be set to $b = 0$. In addition, it is notable that the $q-$axis and mechanical eigenvalues are coupled. This is because the BEMF voltage, which is due to the mechanical rotation of the rotor, appears only in the $q-$axis.

Another equilibrium point emerges if $T_e = T_L$. For this equilibrium the currents must not necessarily equal zero. It turns out that the equilibrium point corresponds to the short-circuit condition, but only because this entire analysis assumes that the control, or the voltages, are zero. If we do not impose a formula on T_L, then the equilibrium point implies that

$$
\begin{aligned}
i_d &= -\frac{\psi_{pm}}{L_d + \frac{R_s^2}{\omega_e^2 L_q}} \\
i_q &= -\frac{\psi_{pm} R_s}{\omega_e L_q \left(L_d + \frac{R_s^2}{\omega_e^2 L_q}\right)} \\
T_e &= -\frac{3p}{2} \frac{\psi_{pm}^2 R_s}{\omega_e L_q \left(L_d + \frac{R_s^2}{\omega_e^2 L_q}\right)} \left(1 - \frac{L_d - L_q}{L_d + \frac{R_s^2}{\omega_e^2 L_q}}\right)
\end{aligned}
\tag{3.4.5}
$$

Physically this means that because both currents are less than zero, the condition appears to be a generating condition. This is because of the sign of the short-circuit torque equation and the fact that $L_d < L_q$. However, because the terminals have zero voltage, this condition does not pump energy back into a battery, but simply dissipates that energy as heat. Notice that the power losses in the copper due to the current flow is proportional to ψ_{pm}^2, meaning that the stronger the flux from the magnet, the more heat will dissipate in the winding during this equilibrium. It is also important to note that this equilibrium may occur at any speed so long as $T_e = T_L$. If the load should be $T_L = b\omega_e$, then there are four equilibrium speeds, from which only a subset might be physically plausible. Proving whether these equilibria are locally stable or not is much more involved as the Jacobian is fully populated and is a function of the partial derivatives of the parameters with respect to the currents and speed. Finally, because of the arbitrary speed direction and its arbitrary assignment, the signs merely indicate a brake torque as opposed to suggesting asymmetrical motoring and generating characteristics.

We have proven the local stability of the IPMSM at zero currents and zero speed, but we are mostly interested in the stability of the controlled IPMSM where a desired operating point is the new equilibrium. For this task we assume that we already reached the operating point to perform our linearization analysis. After that, we will define controllers that guarantee that the machine reaches the desired operating point, but only when it is near the first operating point.

Assuming that we reached our operating point, we will require that we can perfectly cancel the $\omega_e \psi_{pm}$ term, or the BEMF. We will assume that we can also perfectly cancel the terms in the resistance matrix and add a proportional-integral (PI) controller. That is equivalent to feeding forward the BEMF term, the cross-coupling, and resistance terms to the system. We refer it to as feed-forward because Equation (3.4.6) takes the three-phase system and shows the resulting controlled system with the control $\boldsymbol{u}_{dq}^*$ and PI controller $\boldsymbol{\nu}_{dq}$, meaning that the resulting controller occurs

when $\boldsymbol{u}_{dq} = \boldsymbol{u}_{dq}^*$.

$$\boldsymbol{u}_{dq} = \begin{bmatrix} R_s & -\omega_e L_q \\ \omega_e L_d & R_s \end{bmatrix} \boldsymbol{i}_{dq} + \begin{bmatrix} L_d & 0 \\ 0 & L_q \end{bmatrix} \frac{d\boldsymbol{i}_{dq}}{dt} + \begin{bmatrix} 0 \\ 1 \end{bmatrix} \omega_e \psi_{pm}$$

$$\boldsymbol{u}_{dq}^* = \begin{bmatrix} R_s & -\omega_e L_q \\ \omega_e L_d & R_s \end{bmatrix} \boldsymbol{i}_{dq} + \begin{bmatrix} 0 \\ 1 \end{bmatrix} \omega_e \psi_{pm} + \boldsymbol{\nu}_{dq} \qquad (3.4.6)$$

$$\boldsymbol{\nu}_{dq} = \begin{bmatrix} L_d & 0 \\ 0 & L_q \end{bmatrix} \frac{d\boldsymbol{i}_{dq}}{dt}$$

The feed-forward scheme greatly simplifies the control problem to a decoupled, two-state control problem. The feed-forward portion of the controller ν_{dq} in (3.4.6) utilizes the measured currents to cancel the resistance and reactance terms. To cancel as best as possible, we need the exact parameter values, requiring that we procure previous information about the effect of saturation on the inductances and other variabilities. However, because cancellation is never perfect, other controllers use the commanded current to cancel the reactances. We will first prove stability with the controller in (3.4.6) and then explore the dynamics of the linearized system with several other controllers.

At this point, the problem is diagonalized and we may now begin with the description of the PI controller for stability analysis. Once we have the new system, we will linearize it about the operating point to study its stability. For simplicity, due to the decoupled nature of the problem, we will designate variables associated with the d or q axis with ξ, meaning that $\xi = \{d, q\}$. In other words, what we perform on one equation in one axis also applies to the other. We define the PI controller as

$$\nu_\xi = c_{p\xi} \left(i_\xi^* - i_\xi \right) + c_{i\xi} \int i_\xi^* - i_\xi \ dt \qquad (3.4.7)$$

Where, as expected, $c_{p\xi}$ represents the proportional gain and $c_{i\xi}$ represents the integral gain. Due to integration of the error $i_\xi^* - i_\xi$, we introduce an additional state and the state equation becomes

$$\frac{d^2 i_\xi}{dt^2} + \frac{c_{p\xi}}{L_\xi} \frac{d i_\xi}{dt} + \frac{c_{i\xi}}{L_\xi} i_\xi = \frac{c_{i\xi}}{L_\xi} i_\xi^* \qquad (3.4.8)$$

for constant i_ξ^*. Typical LTI systems are analyzed with dynamic i_ξ^*, but here we are interested in the nonlinear stability first, which implies a constant current command. The integration error term seems to add an unnecessary complexity to the system, but the trade-off between the additional state and the benefits of zero steady-state error is worth the penalty. Due to the second order of the controlled system, we introduce the variables $y_1 = i_\xi$ and $y_2 = \frac{d i_\xi}{dt}$. In total we now have a four-state system, but if we add the mechanical states in (3.4.1), the system is now a five-state system. The Jacobian of said system at the operating point i_d^*, i_q^*, and ω_e is

$$\boldsymbol{J}_* = \begin{bmatrix} 0 & 1 & 0 & 0 & 0 \\ -\frac{c_{id}}{L_d} & -\frac{c_{pd}}{L_d} & 0 & 0 & 0 \\ 0 & 0 & 0 & 1 & 0 \\ 0 & 0 & -\frac{c_{iq}}{L_q} & -\frac{c_{pq}}{L_q} & 0 \\ \frac{\partial f_m}{\partial i_d} & 0 & \frac{\partial f_m}{\partial i_q} & 0 & -\frac{p}{\iota} \frac{\partial T_L}{\partial \omega_e} \end{bmatrix} \qquad (3.4.9)$$

The variable f_m is the mechanical state equation (3.4.1) and its partial derivatives are not calculated because they have no bearing on the eigenvalues of $\boldsymbol{J}_*$ and therefore on the stability of the linearized system about i_ξ^*. The mechanical eigenvalue and the $q-$axis eigenvalues are now unrelated due to the feed-forward cancellation of the BEMF voltage. In this case it is $\lambda_m = -\frac{p}{\iota}\frac{\partial T_L}{\partial \omega_e}$. The other four eigenvalues are

$$\lambda_{d1,d2,q1,q2} = -\frac{c_{p\xi}}{2L_\xi} \pm \sqrt{\left(\frac{c_{p\xi}}{2L_\xi}\right)^2 - \frac{c_{i\xi}}{L_\xi}} \qquad (3.4.10)$$

which are always stable. Besides proving the local stability of the controlled machine at any operating point, equation (3.4.10) lends interpreting the control gains physically. We know that the eigenvalues must have units of rad/s, and therefore $c_{p\xi}$ must have units of rad$\cdot$H/s, where H represents Henries. The integral gain must have units of rad$^2 \cdot$ H/s^2 or, equivalently rad $\cdot \Omega$/s. That each gain is multiplied by a frequency and a circuit parameter unit directs us to set $c_{p\xi} = 2aL_\xi$ and $c_{i\xi} = aR_\xi$ or rather $c_{i\xi} = a^2 L_\xi$, where $a = 2\pi f_c$ and f_c is our desired controlled system critical frequency in Hz. With that dimensional analysis in mind and having proved the stability of the system about a commanded vector current, we can now proceed to design controllers without assuming that i_ξ^* remain constant, provided that any given i_ξ^* stay in the neighborhood of a previous i_ξ^*.

The first controller to consider involves pole placement. Specifically, the controller in equation (3.4.11) cancels the machine pole and replaces it with one at a to create a first order system for both the $d-$ and $q-$axes. The controller in that case would be

$$\boldsymbol{u}_{dq}^* = \left(\frac{a}{s}\begin{bmatrix} R_s & -\omega_e L_q \\ \omega_e L_d & R_s \end{bmatrix} + a\begin{bmatrix} L_d & 0 \\ 0 & L_q \end{bmatrix}\right)\left(\boldsymbol{i}_{dq}^* - \boldsymbol{i}_{dq}\right) + \begin{bmatrix} 0 \\ 1 \end{bmatrix}\omega_e\psi_{pm} \qquad (3.4.11)$$

where s is the complex frequency of the Laplace transform. Although the controller has desirable properties, one can notice that the $q-$axis error is integrated along the $d-$axis command and vice-versa. This may pose problems at high speeds and near voltage actuation limits. As mentioned before, the controller for which we proved the stability of the linearized system is not the one in equation (3.4.11) because we chose to cancel the cross-coupling terms and the resistance terms with measured current-based feed-forward and not with pole cancellation. Furthermore, $\boldsymbol{i}_{dq}^*$ was assumed constant. The proof that controller (3.4.11) has the same first-order properties on each axis is left in the appendix.

A controller that does not involve integrating the error from the other axis and that uses the commanded currents instead of the measured currents for the cancellation of the reactances is

$$\boldsymbol{u}_{dq}^* = \begin{bmatrix} 0 & -\omega_e L_q \\ \omega_e L_d & 0 \end{bmatrix}\boldsymbol{i}_{dq}^* + \begin{bmatrix} 0 \\ 1 \end{bmatrix}\omega_e\psi_{pm} + \boldsymbol{\nu}_{dq} \qquad (3.4.12)$$

For approximate pole cancellation, the integral gains must be

$$\begin{aligned} c_{p\xi} &= aL_\xi \\ c_{i\xi} &= aR_s \ . \end{aligned} \qquad (3.4.13)$$

It can be proven that the resulting system is always Hurwitz, including at different speeds.

It is clear that the machine will exhibit different dynamics depending on the operating point and speed if the gains do not account not only for the changing parameter values, but the synchronous speed of the rotor. We also see that the gains are actually what we deduced from the dimensional analysis. However, even if the controller gains are parameter-scheduled, then first-order behavior with critical frequency $a = 2\pi f_c$ is not guaranteed. The controller also causes damped oscillations at higher speeds, whose current overshoots might trigger over-current errors in a voltage and current-constrained region. This is another reason to rate-limit current commands.

It is important to emphasize that such gains also guarantee approximate first order system behavior with cut-off frequency f_c near the operating point, and therefore commanding another point far away is not guaranteed to be stable, have order one behavior, and therefore have the designed cut-off frequency. This is why during operation of said machines current set-points are often rate-limited to ensure all of the three aforementioned behaviors. Once the system reaches the desired operating point, the system operates as designed provided the appropriate changes to the parameters are made.

We have proven the local stability of the IPMSM machine in both uncontrolled and controlled situations and have designed a control scheme based on the local linearization of the rotating-frame nonlinear system. The analysis, however, required that we schedule both the feed-forward scheme and the control gains based on the inductance values, which change depending on the current magnitude because of saturation. This requires characterizing and storing the machine parameters as functions of the currents before operating the machine. Furthermore, the stability analysis did not have to incorporate the torque equation, which itself is highly nonlinear. The torque has both the saturation nonlinearity and a multiplicative nonlinearity between the states, namely the reluctance torque. The exclusion of the torque from the analysis of uncontrolled and controlled local stability was only possible because we controlled the currents with feedback and not the torque. Unless the system has a torque transducer, the control of IPMSM's requires a parameter-based torque model. For load machines in test benches, the speed is also feedback-controlled. Drivers in cars also function as speed controllers with the tachometer feeding back the speed of the car. In those systems, torque functions as the control input and therefore is the result of the speed feedback controller. If the dynamics of the speed controller are much slower compared to the circuit dynamics, which we have rendered possible based on the arbitrary speed of the current controller and sufficient based on a high enough switching frequency, then we can translate the torque command into current commands and assume that the dynamics of the current controller do not affect the dynamics of the speed controller. This nested design is shown in figure 3.1, where CP represents the Clarke-Park transformation. The torque model with saturation effects as a function of currents therefore needs to be inverted to translate the torque control input from the speed controller and the speed itself into current commands. Due to the nonlinearity of the torque, several i_d and i_q current combinations yield the same torque and therefore we have an additional degree of freedom to choose the current combinations. Furthermore, the
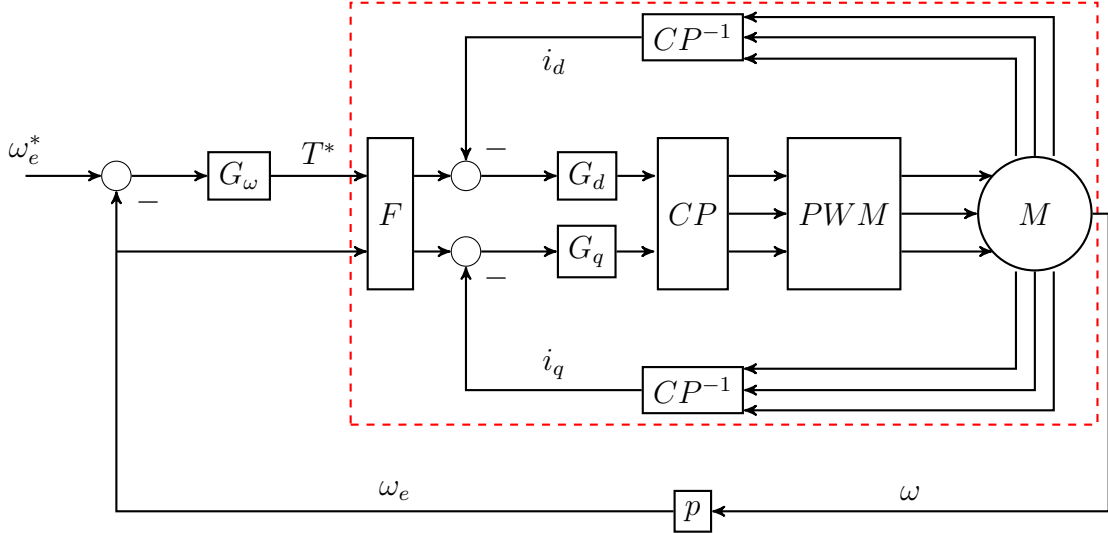
Figure 3.1: Speed control diagram with nested current controller

same currents can control the flux in the machine, especially at high speeds where the permanent magnet flux is large and the voltage actuation limited. Different strategies exist to choose the current combinations depending on the operating point of the machine and the limits on the control input, or voltage. The next section presents the typical methods used to generate said current combinations, represented in Figure 3.1 as F.

3.5 Maximum Torque per Ampere, Volt, and Loss

The problem of inverting the flux and torque commands into direct-current and quadrature-current commands is inherently a multidimensional constrained optimization problem. One constraint was already mentioned in the previous section, namely the actuation, or voltage. Such a strategy is called maximum torque per volt (MTPV). When the operating condition does not reach the actuation limits, we are free to choose another constraint. Usually the constraint is machine loss, and according to the circuit power equation, the only source of loss is the conduction, or resistive loss. Said loss is proportional to the square of the current magnitude, and therefore it is usually chosen as the optimization constraint. Choosing the current magnitude as the constraint yields the maximum torque per ampere (MTPA) strategy. In real machines, iron losses make a significant portion of the losses, especially at low loads and high speeds. If an iron loss model is available, then the maximum torque per loss (MTPL) strategy may be employed. Laplace optimization was used in this thesis to find the optimal current commands in each case. However, in order to incorporate the saturation effects, the typical formulas for the optimal currents in each case were not utilized. Instead, a numerical Laplace optimization procedure was used with the varying parameters as a basis. There are software packages that optimize multidimensional and nonlinear problems with constraints which also have Laplace optimization as a back-end algorithm.

3.5.1 Lagrange Constrained Optimization

The typical Lagrange multiplier method defines a Lagrangian $\mathcal{L} : \mathbb{R}^{n+1} \to \mathbb{R}$ as

$$\mathcal{L}\left(\boldsymbol{x}, \lambda\right) = T\left(\boldsymbol{x}\right) - \lambda g\left(\boldsymbol{x}\right) \tag{3.5.1}$$

where $T : \mathbb{R}^n \to \mathbb{R}$ is the function to be optimized and $g : \mathbb{R}^n \to \mathbb{R}$ is the constraint function. The critical points of the Lagrangian are located where its gradient is zero, and therefore

$$\nabla_{\boldsymbol{x}, \lambda} \mathcal{L} = \nabla T - \lambda \nabla g - g \hat{\lambda} = 0 \tag{3.5.2}$$

Because g is the only non-zero component in the $\hat{\lambda}$ direction, we require that $g\left(\boldsymbol{x}\right) = 0$. To solve the problem, we seek a state $\boldsymbol{x}$ that satisfies

$$\lambda = \frac{\partial T}{\partial x_i} \left(\frac{\partial g}{\partial x_i}\right)^{-1} = \frac{\partial T}{\partial x_j} \left(\frac{\partial g}{\partial x_j}\right)^{-1}_{i \neq j} \tag{3.5.3}$$

As an illustration, we will find the states that maximize the torque for a given current magnitude for constant parameters. In such a case, $n = 2$, $g = i_d^2 + i_q^2 - I_{dq}^2 = 0$ from the definition of the current magnitude, and $T = T_e$. The Lagrange multiplier is then

$$\lambda = \left(\frac{3p}{2}\left(L_d - L_q\right) i_q\right)\left(2i_d\right)^{-1} = \left(\frac{3p}{2}\left(\psi_{pm} + \left(L_d - L_q\right) i_d\right)\right)\left(2i_q\right)^{-1} \tag{3.5.4}$$

and solving for i_d yields

$$i_d = \frac{\psi_{pm}}{4\left(L_d - L_q\right)} - \sqrt{\left(\frac{\psi_{pm}}{4\left(L_d - L_q\right)}\right)^2 + \frac{I_{dq}^2}{2}} \tag{3.5.5}$$

and i_q can be retrieved from the definition of the current magnitude.

The situation for which saturation is considered becomes analytically intractable because the partial derivatives of the inductances also depend on the current. Numerically, one may solve for the MTPA currents using a loop to minimize an error cost function. That however is not necessary if we assume a continuous dependence of the torque on the currents. The continuity assumption permits interpolation between the points, after which a numerical gradient can be taken over a sufficiently small grid. Because the gradient fields are large and we have to take the quotient between each component of the torque and constraint fields, it is advantageous to perform such a task in software that automatically parallelizes the same operation −division −over the array elements. Thereafter, a subtraction operation is necessary. Then, a search for the indexes that give the minimum absolute value difference is the last step to acquire the optimizing currents. The minimum search needs to be along one of the two dimensions. For example, for each index j corresponding to an element of i_q, find the index i corresponding to an element of i_d that has the

minimum and store both indexes. The steps are summarized in equation (3.5.6) for each i_q.

$$i_d = \arg\min \left| \frac{\partial T_e}{\partial i_d} \left(\frac{\partial g}{\partial i_d} \right)^{-1} - \frac{\partial T_e}{\partial i_q} \left(\frac{\partial g}{\partial i_q} \right)^{-1} \right| \tag{3.5.6}$$

Arguably the minimum of the absolute value of the difference will not result in exactly zero as prescribed by the method of Lagrange multipliers to find the critical points. It is assumed that the minimum will give an index near the critical points with an error in the order of the grid discretization.

3.5.2 MTPA

Figure 3.2 shows the MTPA angles and trajectories calculated with constant parameters and calculated numerically. From the figure we may conclude that using constant parameters to calculate the MTPA trajectories is not satisfactory, especially at high currents where conduction losses dominate. We can confirm that the numerical calculation gives the maximum torque per Ampere by inspecting the torque and current magnitude contours. If we imagine a vector field with vectors perpendicular to each contour, then, when the vectors from the torque contours align with those from the current magnitude, we can ensure that that point is the optimal torque given the constraint. For example, again in Figure 3.2, for $T_e = 1.4$ and $I_{dq} = 1.8$, we see that the two perpendicular vectors for the MTPA trajectory with constant parameters do not align. For the same torque, the vectors do align for the numerical MTPA trajectory but at a smaller current. The MTPA angles also show a difference between the calculation methods. They also show that our analysis at the beginning of the chapter regarding the torque angle is near the optimal angle, namely $135°$ or $3\pi/4$ rad. From the figure we may conclude that our optimization must be based on the numerical prescription in equation (3.5.6), and preferably not just for MTPA.

(a) Current angle

(b) Current trajectories
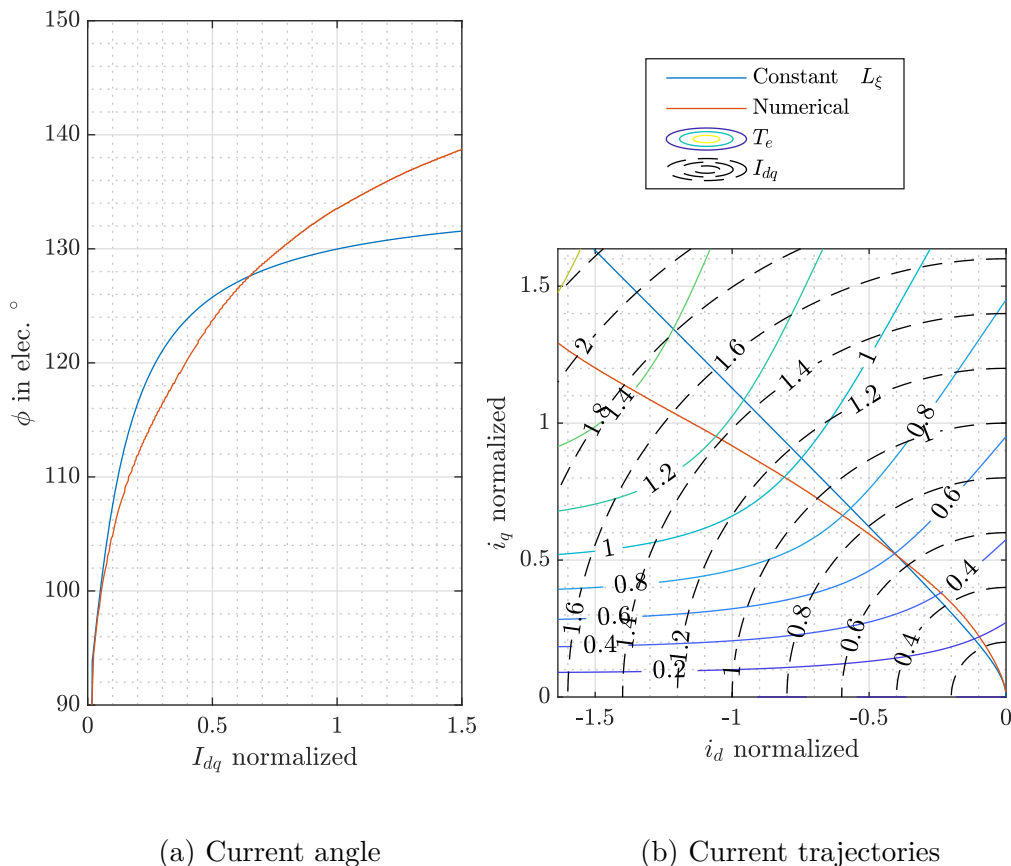
Figure 3.2: Constant vs. Numerical MTPA currents

3.5.3   MTPV

We previously mentioned that due to voltage actuation limits at high speeds, the machine can no longer remain on the MTPA trajectory. Usually, the machine reaches a current limit first. The machine follows the maximum current limit trajectory as the speed increases first because, as will be shown, the MTPV trajectory runs almost parallel to the MTPA trajectory with a i_d offset. The machine follows the MTPV trajectory until reaching the voltage limit. To understand how the voltage limit may be represented in the $dq-$current plane, the equation for the steady-state voltage magnitude as a function of the currents proves necessary. For the analysis, it suffices to analyze the square of the voltage magnitude and to ignore the phase resistance, because the reactances $\omega_e L_\xi$ are much larger that the resistance in the high-speed, voltage-limited region.

$$
\begin{aligned}
V_{dq}^2 &= \omega_e^2 \left((L_q i_q)^2 + (\psi_{pm} + L_d i_d)^2 \right) \\
\frac{V_{dq}^2}{\omega_e^2} &= \psi_q^2 + \psi_d^2
\end{aligned}
\tag{3.5.7}
$$

The equations in (3.5.7) indicate that if we search for the optimal current combination with the flux linkage magnitude as a constraint, then we can find the MTPV trajectory. Up to a constant and sufficiently fast speed, MTPV is then equivalent

to MTPF, or maximum torque per flux. Figure 3.3 shows the MTPF and MTPA trajectories, along with the level curves for the torque and the flux magnitude.

(a) Current angle   (b) Current trajectories
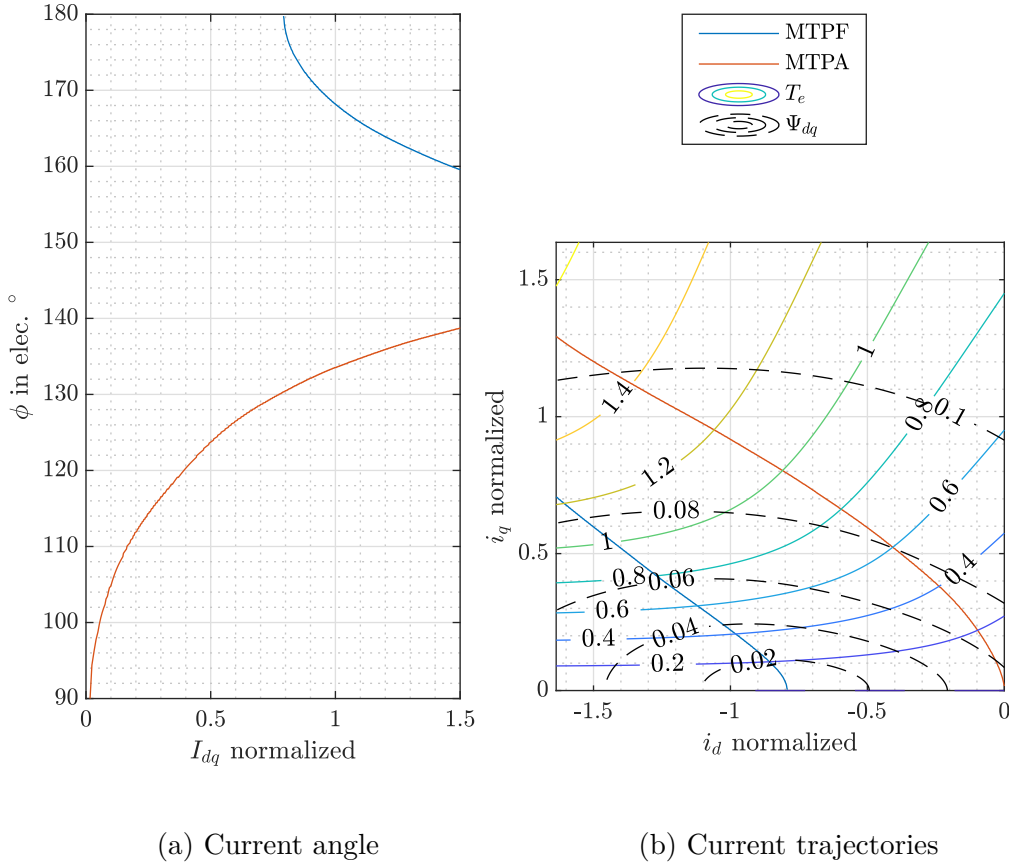
Figure 3.3: Numerical MTPF and MPTA currents

3.5.4 MTPL

The set of maximum torque per loss trajectories can also be found using the same numerical method with the added requirement that we have an iron loss model. Ideally, the iron loss model should take into account the currents and the speed of the machine to make a model $P_{\text{Fe}} : \mathbb{R}^3 \to \mathbb{R}$. This model can be found with an FEM simulation that calculates the magnetic field density throughout the laminations in the machine and then looks-up the losses according to Epstein loss tables specific to the simulated soft magnetic material. The losses can be extracted over different current grids for different speeds and fitted to a model. The model used here is the Bertotti model with coefficients taking a point on the $dq-$current plane to a scalar. The model is

$$
\begin{aligned}
P_{\text{Fe,s}} &= C_{\text{H,s}}\,(i_d, i_q)\,\omega_e + C_{\text{E,s}}\,(i_d, i_q)\,\omega_e^2 + C_{\text{X,s}}\,(i_d, i_q)\,\omega_e^{3/2} \\
P_{\text{Fe,r}} &= C_{\text{H,r}}\,(i_d, i_q)\,\omega_e + C_{\text{E,r}}\,(i_d, i_q, \omega_e)\,\omega_e^2 + C_{\text{X,r}}\,(i_d, i_q)\,\omega_e^{3/2}
\end{aligned}
\tag{3.5.8}
$$

The capitalized subscripts H, E, X indicate that the coefficient models the hysteresis, eddy, and excess losses in the iron. The subscripts s and r indicate stator

and rotor quantities, respectively. The rotor eddy current coefficient is expanded to read

$$C_{\text{E,r}} = C_{\text{E,Fe,r}}\left(i_d, i_q\right) + k_{\text{E,pm}}\left(\omega_e\right) C_{\text{E,pm,r}}\left(i_d, i_q\right) \qquad (3.5.9)$$

where the speed-dependent term scales the eddy current coefficient if the latter was calculated in two spatial dimensions. With this additional iron loss model, we need only add the conduction losses in the windings and repeat those losses over all speeds to form a total loss array $P_{\text{Loss}} \in \mathbb{R}^3$. Although the new constraint array P_{Loss} is three-dimensional, because we seek only the optimal currents for each speed and torque, the optimization itself remains over just the currents at one particular speed and torque. The optimization is repeated over all desired speeds and torques. Therefore the approach in (3.5.6) remains valid, but it must re-calculated over every speed. Again, instead of calculating one speed after another in series, it is faster to create three dimensional arrays for the torque and the loss, but optimize over just two dimensions, if the software automatically parallelizes array element operations.

Figure 3.4 shows the MTPL and MTPA trajectories for two speeds. At zero rotor speed, MTPL and MTPA are indistinguishable because the conduction losses in the windings dominate. At faster speeds the two methods differ. The MTPL trajectory commands more $d-$axis current for a given torque, especially at low torques. This is because iron losses make the largest share of the losses at high speeds and lower loads. At higher torques the MTPL trajectory approaches the MTPA trajectory because the conduction losses once again dominate, even for high speeds. One may also see the change in the overall magnitude of the losses for different speeds from the level curves of the power loss in the machine. Figure 3.5 shows the current angle ϕ for the same conditions. At lower speeds, MTPA and MTPL losses are nearly equivalent. At higher speeds the commanded angle for MTPL is closer to the negative $d-$axis, which corresponds with slightly more $d-$current to weaken the field and therefore induce less iron losses at high speeds by weakening the permanent magnet field flux. It is also important to mention that MTPL is equivalent to maximum torque per efficiency (MTPE) and maximum power per loss (MPPL).

Having described different methods to generate current combinations with different criteria and for different operating regimes of the machine, we now introduce the strategy used to command the currents from a torque-speed pair given voltage and current limits.

(a) Zero speed

(b) Maximum speed
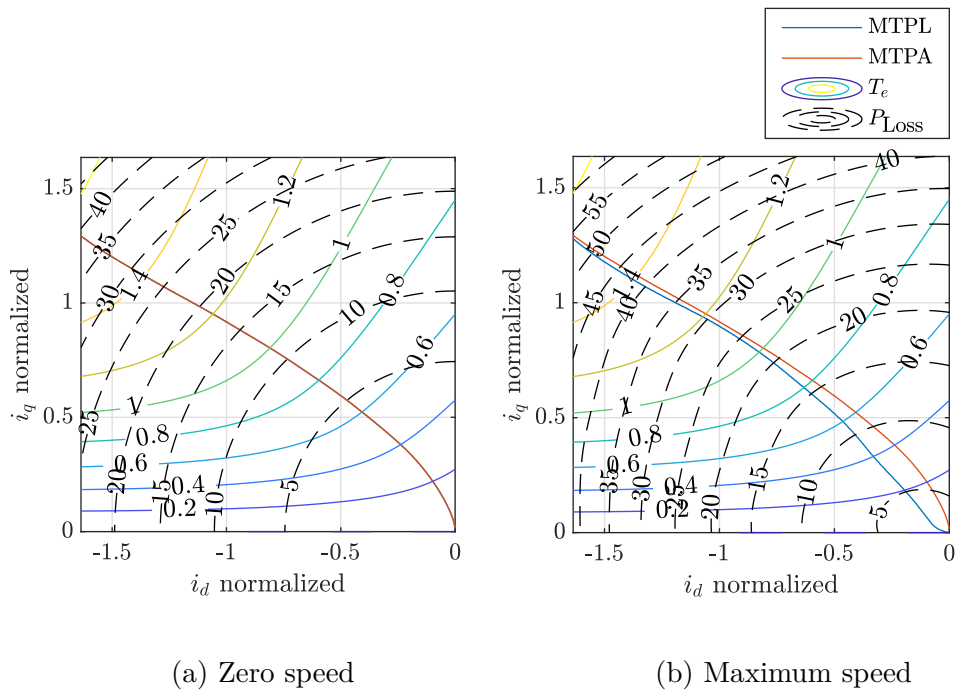
Figure 3.4: Numerical MTPL and MPTA current trajectories

(a) Zero speed

(b) Maximum speed
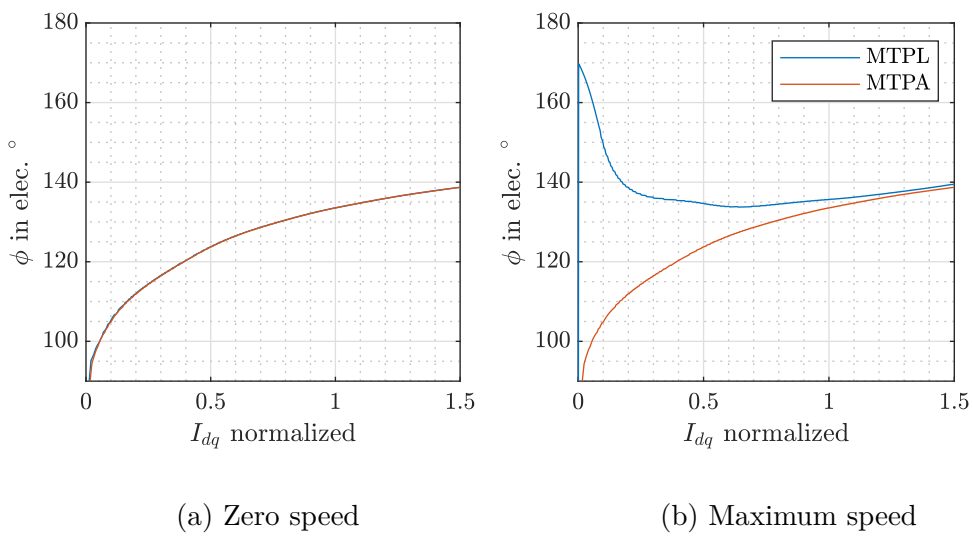
Figure 3.5: Numerical MTPL and MPTA current angles

66

3.5.5 Current Set-Point Determination from Torque and Speed Commands

Up to now, the current set-point generation of MTPA and MTPF were speed-independent; even with MTPF, if we choose a particular flux and wish to have the maximum torque there, the machine need not be limited by voltage or current constraints. MTPL depends on speed, but it also does not prescribe certain dq current combinations in the presence of voltage and current limits. It makes sense that a maximum current amplitude $I_{\max}$ will limit all trajectories since $T_e \to \infty$ as $I_{dq} \to \infty$. This limit exists even at zero speed. If the speed of the rotor is zero or near zero, then this limit will be reached before the voltage limit is reached because the inverter need only feed the machine with voltage if changes in the current set-point are commanded. In this case of no set point changes and slow speed, the voltage would limit the current based on the machine phase resistance $I_{\max} = V_{\max}/R_s$, but this current limit would induce losses in the order of tens of MW, or 10^7 W, because $P_{\text{Cu}} = V_{\max}^2/R_s$ and because $R_s \approx 10^{-3}$ Ω and $V_{\max} \approx 10^2$ Ω for typical traction machines. Before the machine reaches that limit, the system will reach other limits, usually thermal limits in the machine windings or inverter junctions. These limits usually occur at or less than the order of kA, which places the losses in the order of kW for the same phase resistance order. The voltage, then, only becomes the limiting factor at high speeds because the total voltage is proportional to the flux linkage and the speed. We may therefore state that the maximum current limits the maximum torque and that, in combination with that torque limit, the maximum voltage limits the maximum mechanical power of the machine, since $P_m = \omega_m T_e$. This also applies for the speed-dependent MTPL trajectories, since for large loads they approach the MTPA trajectories.

We have established the need to limit current and voltage independently from one another, but we still need to establish a common quantity to account for the two different limits. The common quantity should simplify the set-point generation in a nonlinear context where the optimization formulas are not applicable. We will first consider the case for which we use MTPA and MPTF. If we choose current as the common quantity, the transition from the current limits to the voltage limits would complicate the set-point generation since the current limits are speed-independent and the voltage limits are not. If the machine did not have saturation, the strategy may simply switch from the closed-form current limit equation to the MTPV equation. Since this is not the case, we find that the common quantity over all strategies in all regions is flux. Considering equation (3.5.7), the flux changes as a function of the current, but its level curves depend on the voltage and speed. We can then map the current trajectories from either MTPA or MTPL, the current limit, and MTPF onto the flux and crop them according to the voltage and speed limits. In addition, because MTPF is equivalent to MTPV, the current trajectories will follow the MPTF trajectories at the voltage limit automatically. Simply formulated,

$$\frac{V_{\max}}{\omega_e} \geq \Psi_{dq,\text{opt}} \tag{3.5.10}$$

If the voltage limit is reached before the current limit, the same torque can be achieved but the current combinations that produce that torque will not lie on the MTPA, MTPL, or MTPF trajectories until the speed increases to the extent that

the MTPF trajectory is reached. The trajectory along the current limit is also not an MTPA, MTPL, or MTPF trajectory. These interstitial trajectories connect the MTPA or MTPL trajectories to the MTPF trajectories at high speeds due to the limited voltage. For example, if the voltage limit is reached before the current limit, the same torque is achievable up to the MTPF trajectory, but the current combinations for that torque do not belong to any of the optimized trajectories. Said situation occurs at high speeds and low loads. We therefore have the same torque but for different flux. This requires associating the flux and torque to a current combination not on any of the trajectories we calculated previously, and therefore they are not readily available. It is therefore important to invert the vector map with some procedure $\boldsymbol{h} : \langle \psi, T_e \rangle \rightarrow \langle i_d, i_q \rangle$. Figure 3.6 summarizes the current commissioning procedure.
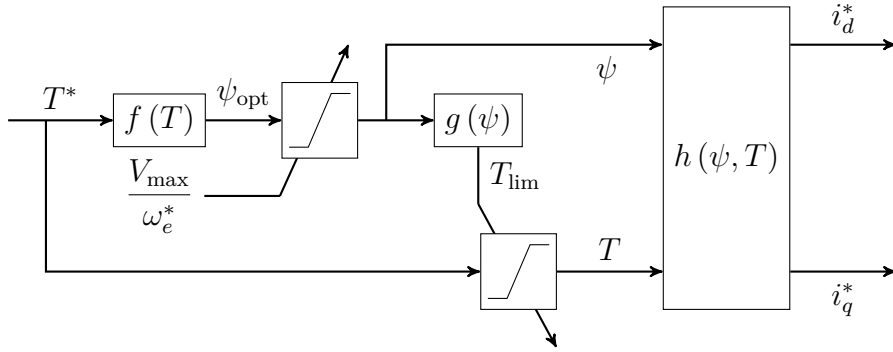
Figure 3.6: Current commissioning diagram [131]

The function $f(T_e^*) = \psi_{\mathrm{opt}}$ contains the MTPA current trajectories mapped onto the flux as a function of torque. If using MTPL, $f = f(T_e^*, \omega_e^*)$. The function f is then limited by the saturation block also described by equation (3.5.10). The function $g(\psi) = T_{\mathrm{lim}}$ maps any given flux to the maximum torque achievable for that flux. The function g therefore contains the MTPF trajectories along the voltage limit. However, if $T_e^* < T_{\mathrm{lim}}$, then the flux-torque pair is not along the MPTF or current limit trajectory but along another interstitial trajectory. The function $\boldsymbol{h} : \mathbb{R}^2 \rightarrow \mathbb{R}^2$ maps the flux-torque pair to a current combination on this interstitial trajectory. It is a general inverse of the nonlinear equations for the torque and the flux as functions of the currents as described from equations (3.3.18) and (3.5.11), respectively.

$$\psi = \sqrt{(L_q i_q)^2 + (\psi_{pm} + L_d i_d)^2} \tag{3.5.11}$$

Our next task involves inverting the vector function $\langle \psi, T_e \rangle$ to find $\boldsymbol{h}$. Since $\psi = \psi(i_d, i_q)$ and $T_e = T_e(i_d, i_q)$, we can visualize the vector function to invert as two sets of level curves on the same i_d, i_q-plane. Since the level curves are by definition the set $\boldsymbol{i}_{dq}^T = \{(i_d, i_q) : T_e = c_T\}$ and $\boldsymbol{i}_{dq}^\psi = \{(i_d, i_q) : \psi = c_\psi\}$ for constant c_T and c_ψ, then, for every $c_T \in T \subset \mathbb{R}$ and $c_\psi \in \Psi \subset \mathbb{R}$, we need to find $\boldsymbol{i}_{dq}^T = \boldsymbol{i}_{dq}^\psi$. In other words, we need to find for what (i_d, i_q) the level curves of $T_e(i_d, i_q)$ intersect with those of $\psi(i_d, i_q)$.

We adopt the method of level curves to invert the vector function instead of a formulaic approach for different reasons from before. Before, the nonlinear characteristics of the induction served as the reason for numerical optimization since the

formulaic optimization assumed constant parameters. In that case calculating the target quantity analytically gave the wrong result. We can pursue the analytical approach here because no partial derivatives are involved. The reason we do not is rather banal: fourth-order roots as a function of parameters are notoriously long. First we would have to solve for i_d in equation (3.5.12). Then, we would have to insert each of the four i_d currents into equation (3.5.13), yielding eight i_q currents per flux-torque pair. From there we can employ several filters to ensure that the current combinations are real numbers and lie in the operating area.

$$\left(\psi_{pm} + (L_d - L_q)\, i_d\right)^2 \left(\psi^2 - (L_d i_d)^2\right) = \frac{4}{9p^2} L_q^2 T_e^2 \tag{3.5.12}$$

$$i_q = \pm \frac{1}{L_q} \sqrt{\psi^2 - (\psi_{pm} + L_d i_d)^2} \tag{3.5.13}$$

(a) i_d normalized

(b) i_q normalized
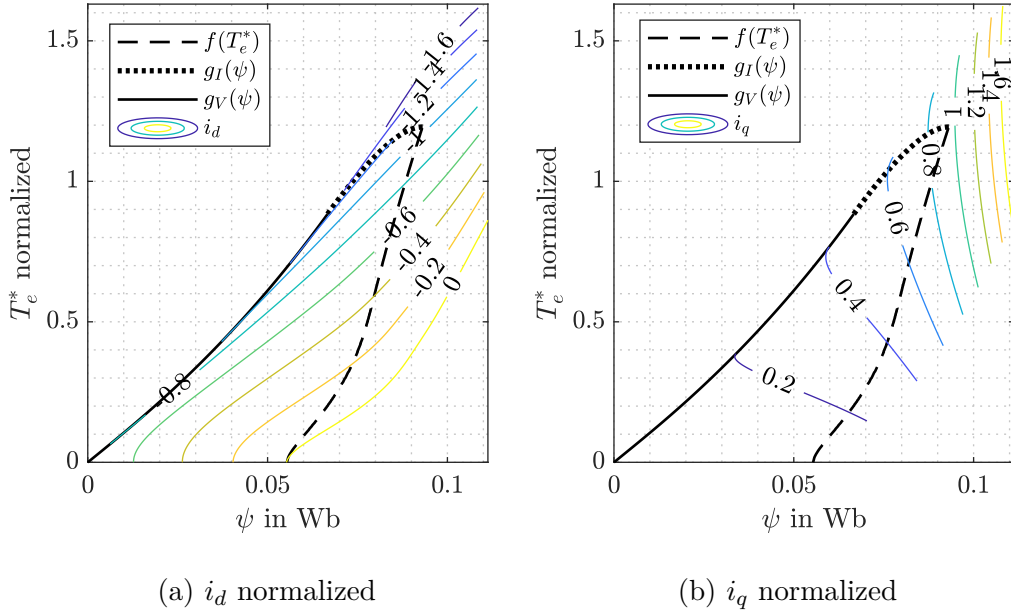
Figure 3.7: Current commissioning functions on current contours with MTPA

Figures 3.7 and 3.8 show the current commissioning functions f and g on the current contours for MTPA and MTPL, respectively. The subscripts I and V designate where the function $g(\psi) = T_{e,\text{lim}}$ limits the torque based on the current limit or on the MTPF trajectory, or voltage limit. The allowable current combinations lie within the boundaries traced by the current commissioning functions. Figure 3.8 shows that the MTPL strategy changes those boundaries for different speeds. Figure 3.9a shows the overlaid contours of ψ and T_e and figure 3.9b shows their inverse $\boldsymbol{h}$. Because the flux traces ellipses, the inverse is not single-valued everywhere. Comparing the g function and the upper torque boundary on 3.9b, we see that the MTPF branch of the function g traces where the currents are single-valued. The allowable currents are the portion of the inverse that result in the minimal currents that achieve a given torque and flux.

(a) i_d normalized

(b) i_q normalized
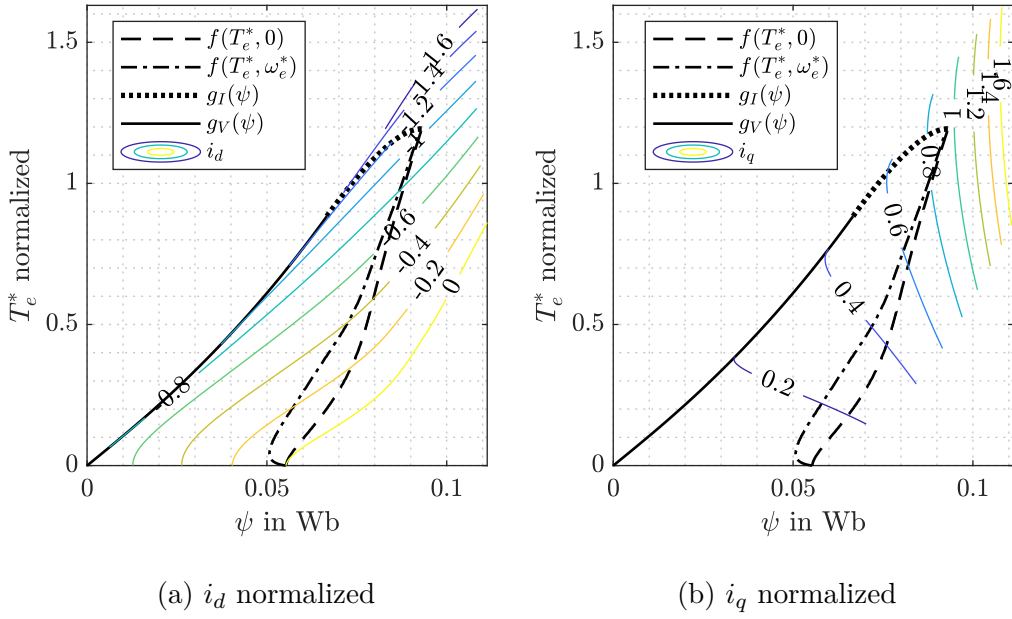
Figure 3.8: Current commissioning functions on current contours with MTPL

Figures 3.10 and 3.11 show the MTPA and MTPL current commissions for $V_{DC} = 325$ V. In the base-speed region one may notice that MTPA currents remain constant over different speeds. Due to the addition of the iron loss model and its dependence on speed, the MTPL currents do not remain constant over different speeds, especially at low loads and for the $d-$current. Paradoxically, more current needs to be commanded to achieve maximum torque per loss: in order to reduce the permanent magnet flux more $d-$current is required and to achieve the same torque with the weakened flux more $q-$current is required. However, the additional current reduces the iron losses by weakening the permanent magnet flux in the base-speed region, reducing overall losses. Figures 3.12 and 3.13 show the MTPA and MTPL current commissions for $V_{DC} = 400$ V. Here we see that the larger DC-bus voltage broadens the base-speed region, making a loss-minimizing current commissioning strategy all the more important there.

(a) $\langle \psi, T_e \rangle$ (b) $\langle i_d, i_q \rangle$
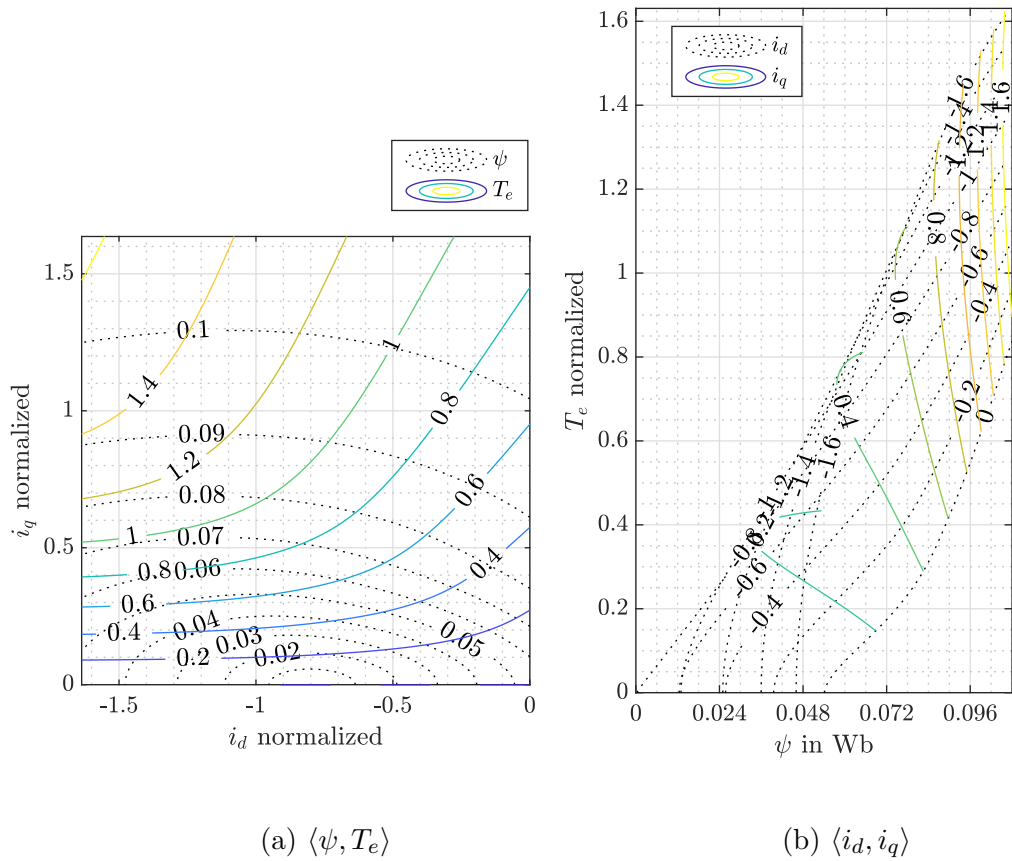
Figure 3.9: Vector inversion of torque-flux pairs

(a) i_d in A   (b) i_q in A
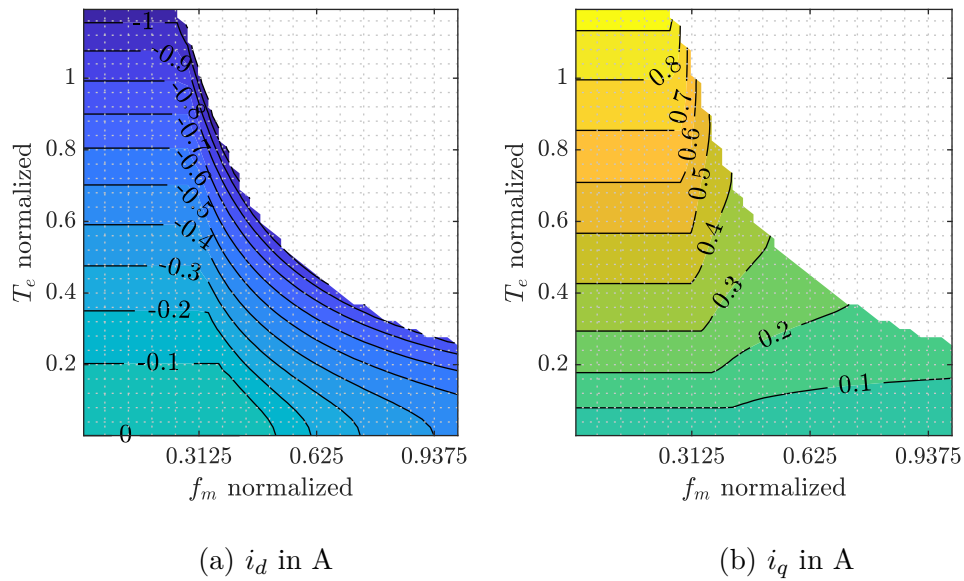
Figure 3.10: MTPA current commissions as functions of torque-speed pairs with $V_{\mathrm{DC}} = 325$ V

71

(a) i_d in A

(b) i_q in A
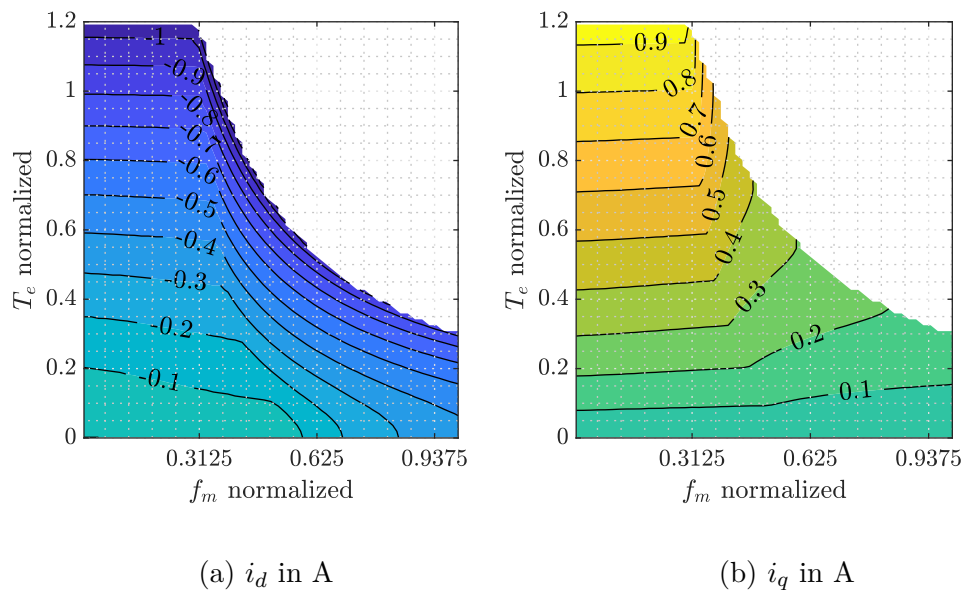
Figure 3.11: MTPL current commissions as functions of torque-speed pairs with $V_{\text{DC}} = 325$ V

(a) i_d in A

(b) i_q in A
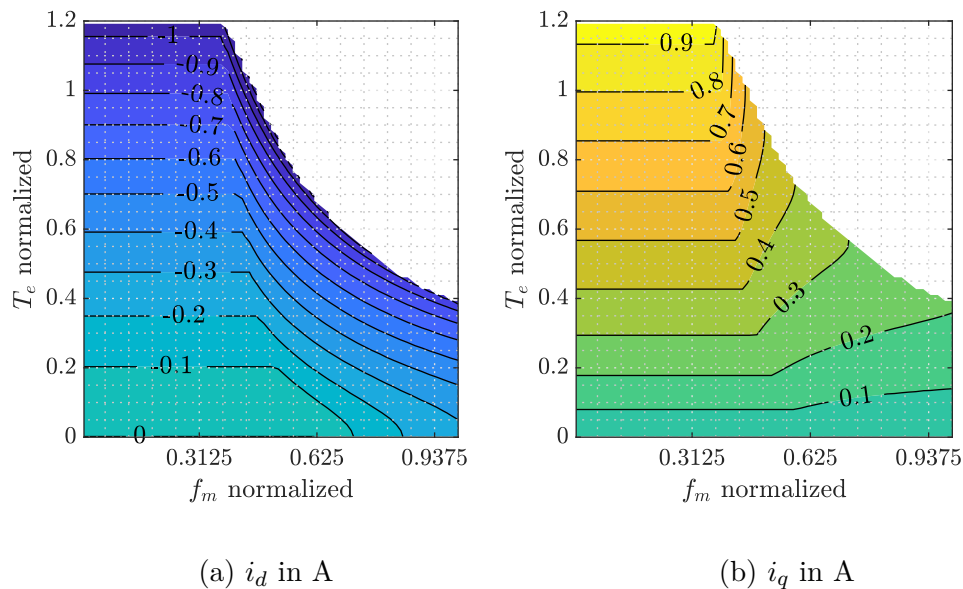
Figure 3.12: MTPA current commissions as functions of torque-speed pairs with $V_{\text{DC}} = 400$ V

(a) i_d in A

(b) i_q in A
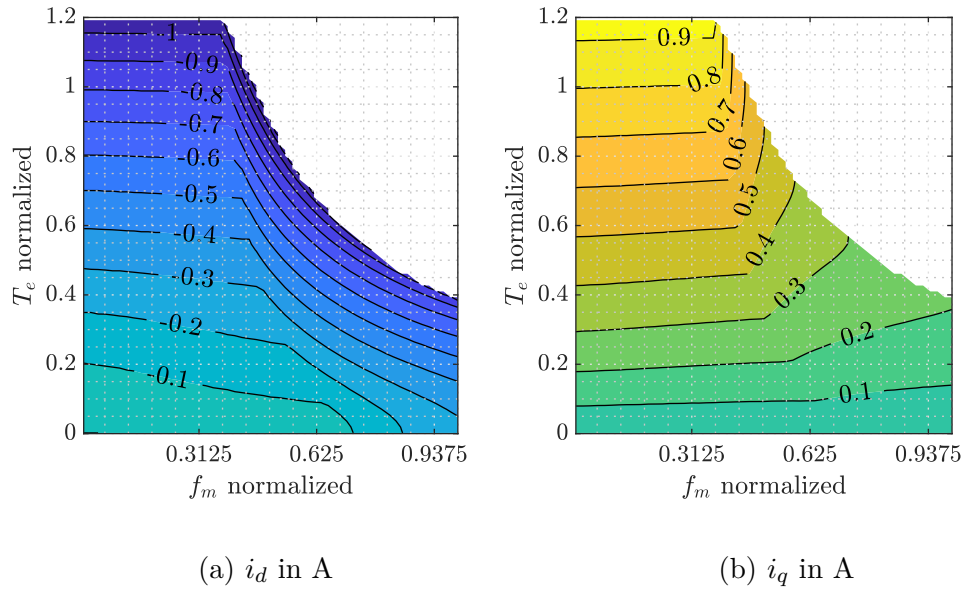
Figure 3.13: MTPL current commissions as functions of torque-speed pairs with $V_{\mathrm{DC}} = 400$ V
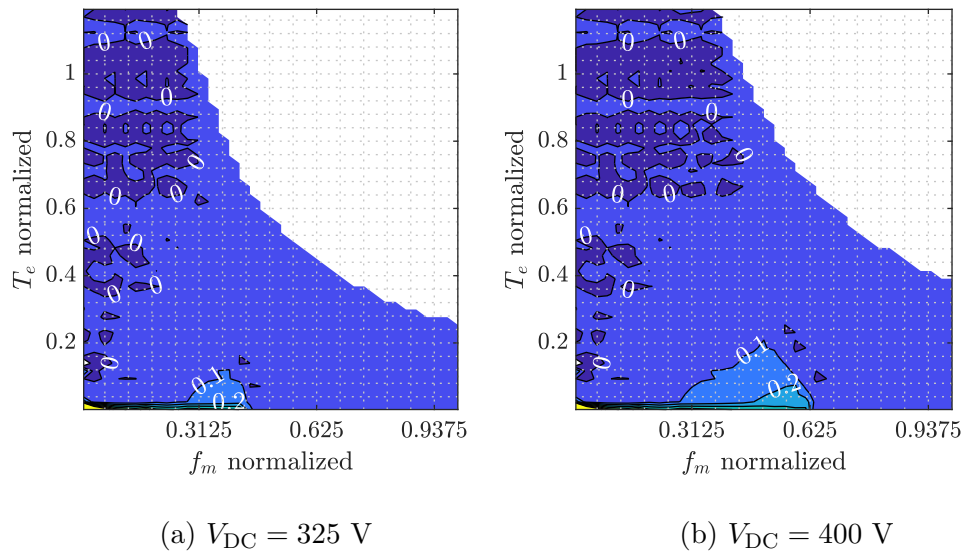
(a) $V_{\mathrm{DC}} = 325$ V

(b) $V_{\mathrm{DC}} = 400$ V

Figure 3.14: Efficiency difference $\Delta\eta = \eta_{\mathrm{MTPL}} - \eta_{\mathrm{MTPA}}$ for $V_{\mathrm{DC}} = 325$ V and $V_{\mathrm{DC}} = 400$ V

73
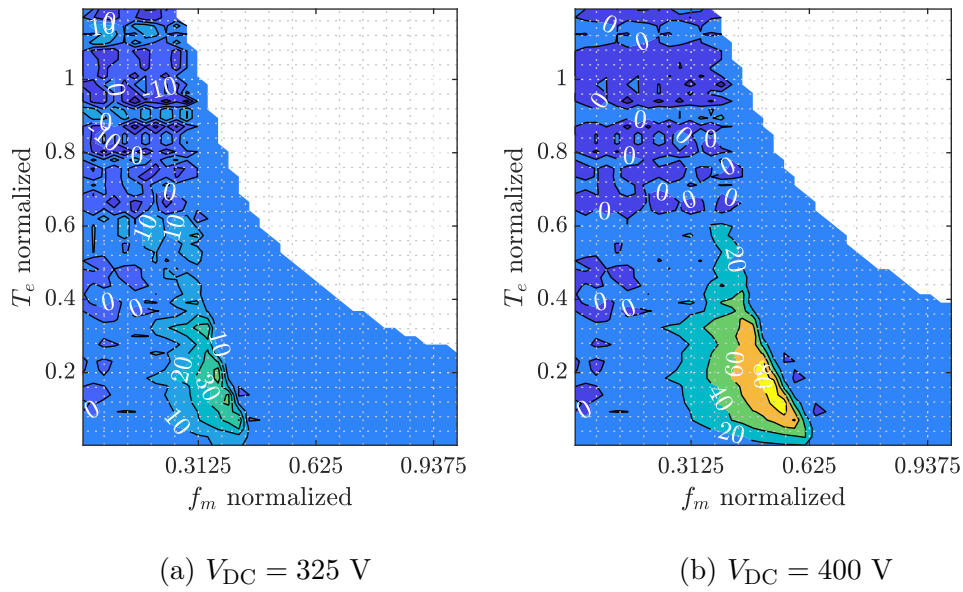
(a) $V_{\mathrm{DC}} = 325$ V

(b) $V_{\mathrm{DC}} = 400$ V

Figure 3.15: Power loss difference $P_{\mathrm{Loss}} = P_{\mathrm{Loss,MTPA}} - P_{\mathrm{Loss,MTPL}}$ for $V_{\mathrm{DC}} = 325$ V and $V_{\mathrm{DC}} = 400$ V

For completeness, figures 3.14 and 3.15 show the difference in machine efficiency and in power losses between MTPA and MTPL strategies for the two voltages. As is evident, a maximum difference of about 0.2% in efficiency and a maximum difference of about 100 W power loss is not much, but significant. In the next chapter we will explain the inverter's operating principles to later show that its influence on losses in the machine is much more pronounced compared to changing even the current commissions.

74

Chapter 4

Inverter Excitation of Permanent Magnet Machines

The inverter is a hardware component that changes direct-current (DC) voltage into alternating-current (AC) voltage. In an electric drive the inverter converts the DC battery voltage into an amplitude and frequency-controlled AC voltage source. The ability to control the amplitude and frequency of the fundamental AC voltage enables the control of the full range of degrees of freedom in the electric machine, which involves controlling torque at any speed. The DC to AC conversion is performed by means of strategically switching between the full DC voltage source (high) and zero (low) at a frequency much larger than the desired AC fundamental frequency. The relative amount of time that a load is connected to high −the duty cycle −over a given period of time −the switching period −is proportional to the desired amplitude of the AC voltage signal. The time spent connected to low is bound by the time connected to high and the switching period, meaning that $t_{sw} = t_H + t_L$. The computation converting the desired AC voltage amplitude for every switching period to the time 'width' spent connected to high is pulse width modulation (PWM), because the pulses of high and low DC voltages are commutated for a given 'width' of time at a higher frequency than the fundamental, thus modulating the fundamental signal. This chapter explains the principles of inverter-sourced three-phase and dual three-phase machines, PWM methods, and their effects on drive performance.

4.1 Three-Phase Voltage-Sourced Drives

An electrical drive consits of a DC voltage source −typically a battery for mobile drives −, a large DC link capacitor, a three-phase inverter, and a three-phase machine. Figure 4.1 shows all components and their connections. Electric motors are usually depicted as inductive loads, but the resistance of the coils, as well as a secondary voltage source, namely the back-electromotive force (BEMF), is implied. From this inverter topology one may notice that each phase, depicted in Figure 4.1 as one inductor, is either connected to DC high (+), or DC low (−). For simplicity and to highlight the binary switching action, DC high and low are represented as 1 and 0 respectively. Since there are three phases, there are 2^3 possible switching states, shown in Table I. Since S_0 and S_7 involve all phases being connected to 1 or 0, the potential difference across the load is zero.
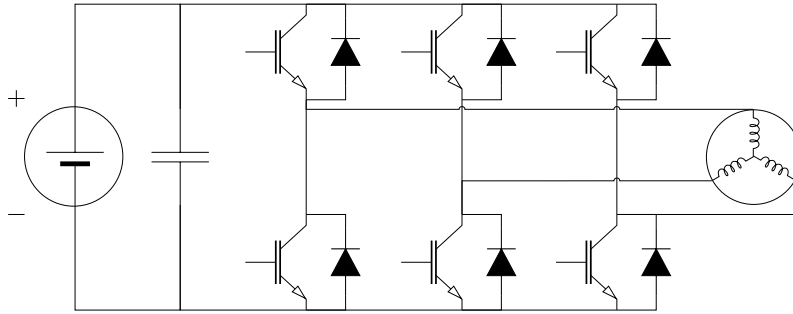
Figure 4.1: A three-phase drive

TABLE I: Inverter Switching States

	Phase U	Phase V	Phase W
S_0	0	0	0
S_1	1	0	0
S_2	1	1	0
S_3	0	1	0
S_4	0	1	1
S_5	0	0	1
S_6	1	0	1
S_7	1	1	1

(a) S_0

(b) $S_{1,3,5}$

(c) $S_{2,4,6}$

(d) S_7
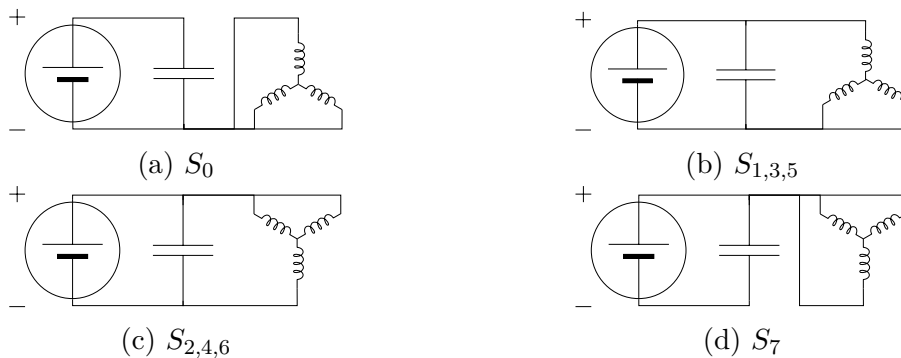
Figure 4.2: Switching states and their connections

The states in Table I corresponding to the connections in Figure 4.2 map to a vector space in $\mathbb{R}^3$. Indeed, one may visualize the different states as the vertices of the cube, with each phase connection to either 1 or 0 acting as their coordinates in $\mathbb{R}^3$. Because there are two zero states, one can rotate the state cube so that both zero states align along the $z-$axis. Because both zero states now lie on the origin of the $xy-$plane, the transformation results in the mapping of all states onto the $xy-$plane, which now also represent the potential difference states across the load. This means that the switching states in $\mathbb{R}^3$ can be mapped to voltage states whose vertices trace a hexagon in $\mathbb{R}^2$. The rotation to align the zero voltage states involves one rotation about the $z-$axis first, with a roll angle of $\zeta = -\pi/4$, then a rotation about the $y-$axis (yaw) of $\beta = -\mathrm{atan}\sqrt{2}$. The angle $|\beta|$ is the body diagonal angle of the cube as measured from the $z-$axis. A last rotation about the $z-$axis over an

76

angle $\tau = \pi/3$ is necessary to align the phases. Specifically,

$$\begin{bmatrix} U' \\ V' \\ W' \end{bmatrix} = \begin{bmatrix} \cos\tau & -\sin\tau & 0 \\ \sin\tau & \cos\tau & 0 \\ 0 & 0 & 1 \end{bmatrix} \begin{bmatrix} \cos\beta & 0 & \sin\beta \\ 0 & 1 & 0 \\ -\sin\beta & 0 & \cos\beta \end{bmatrix} \begin{bmatrix} \cos\zeta & -\sin\zeta & 0 \\ \sin\zeta & \cos\zeta & 0 \\ 0 & 0 & 1 \end{bmatrix} \begin{bmatrix} U \\ V \\ W \end{bmatrix}, \quad (4.1.1)$$

where $U, V, W \in \{0, 1\}$ as in Table I. Notice that if equation 4.1.1 is multiplied by $\sqrt{2/3}$, which is separable to $2/3\sqrt{3/2}$, one acquires the transformation

$$\begin{bmatrix} U_\alpha \\ U_\beta \\ U_z \end{bmatrix} = \frac{2}{3} \begin{bmatrix} 1 & -\frac{1}{2} & -\frac{1}{2} \\ 0 & \frac{\sqrt{3}}{2} & -\frac{\sqrt{3}}{2} \\ \frac{1}{\sqrt{2}} & \frac{1}{\sqrt{2}} & \frac{1}{\sqrt{2}} \end{bmatrix} \begin{bmatrix} U \\ V \\ W \end{bmatrix}, \quad (4.1.2)$$

which is the Clarke transformation. Figure 4.3 is a visualization of the transformation in equation 4.1.1.

(a) State cube rotation

(b) Projection onto the xy-plane
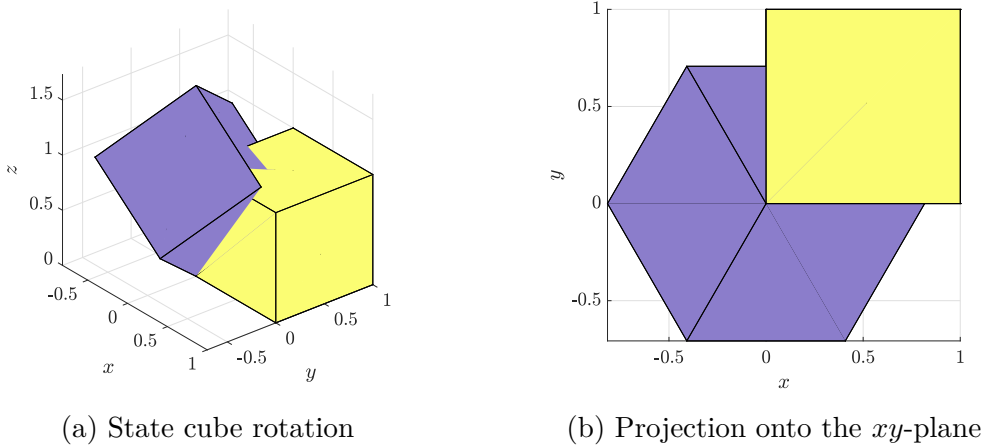
Figure 4.3: From the state cube (yellow) to the voltage hexagon (purple)

Up to now the only correspondence assigned between the states and the potential difference across the load were the zero states. To assign the non-zero states a voltage, we need only notice that the equivalent circuit equation is

$$V_{\text{DC}} = \frac{3}{2} ZI, \quad (4.1.3)$$

Z is the per-phase impedance and I is the equivalent current flowing through the load. With the goal of acquiring an equivalent per-phase voltage, 4.1.4 becomes $2V_{\text{DC}}/3 = ZI$. Because the hexagon spans negative numbers, we wish to be able to represent them on the voltage hexagon. Notice that $v_{S_1} = -v_{S_4}$ relative to the phases, as an example. We therefore construct a virtual neutral point and require that the hexagon-transformed battery provide voltage between $V_{\text{DC}}/2$ and $-V_{\text{DC}}/2$, which is equivalent to the usual range. Equation 4.1.4 then becomes

$$v := \frac{4}{3} \left(\frac{V_{\text{DC}}}{2} \right) = ZI. \quad (4.1.4)$$

From here, the definition of the modulation index, M, follows, as v is the per-phase voltage, and

$$M := \frac{|v|}{V_{\mathrm{DC}}/2}. \tag{4.1.5}$$

The modulation index hexagon is shown in Figure 4.4. The inscribed circle has a radius of $M = 2/\sqrt{3}$ and each state has an amplitude of $M = 4/3$ corresponding to $v = V_{\mathrm{DC}}/\sqrt{3}$ and $v = 2V_{\mathrm{DC}}/3$, respectively.
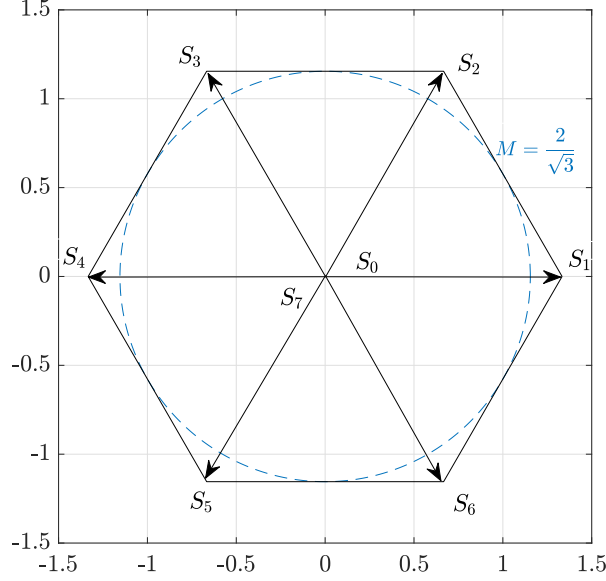
Figure 4.4: Voltage hexagon in terms of M

The fact that the phase-to-neutral voltage magnitude, v is $2V_{\mathrm{DC}}/3$ and that U is aligned along S_1, V along S_3, and W along S_5 indicates that the projection of any other states onto those three fundamental state vectors on the voltage hexagon describes the phase-to-neutral voltage of their respective phases. This means that each phase has five possible voltage levels: 2/3, 1/3, 0, -1/3, and -2/3 times V_{DC}. That is a direct consequence of the circuit topology and arises despite the fact that each phase is commuted only between V_{DC} and zero. Mathematically, the phase-to-neutral voltage is calculated for each phase by dotting the first row of the Clarke transformation with the voltage vector in equation 4.1.2. The phase switching state in Figure 4.5(a) then is equivalent to the normalized phase-to-neutral voltage shown in Figure 4.5(b).

Lastly, any switching period-averaged voltage vector with $|v| \leq V_{\mathrm{DC}}/\sqrt{3}$ and $f_e \leq f_{\mathrm{sw}}/6$ is achievable as a superposition of states. For example, one may command an average voltage vector with the desired magnitude and phase between S_1 and S_2 by commuting between S_1, S_2, and S_0 or S_7. The next section delineates how PWM translates the desired waveform into switching states.
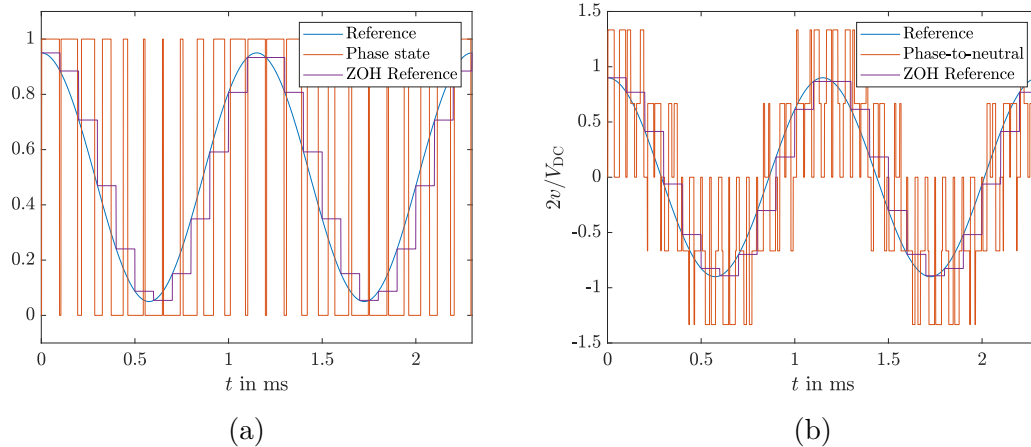
Figure 4.5: Phase switching state and phase-to-neutral normalized voltage

4.2 Pulse-Width Modulation Methods

A goal of PWM is to convert desired voltage AC signals into a series of switching-period equivalent pulses of the states mentioned in Chapter 4.1. Another goal is to maximize the available per-phase AC voltage amplitude for a given DC bus. The latter implies maximizing the modulation index and the former implies an additional degree of freedom for zero state sequences. A specific zero sequence determines the PWM method.

The modulated signal is typically produced by comparing the reference signal against a carrier signal. The reference signal is the desired waveform and the carrier signal 'carries' the modulation frequency, which is much higher than the fundamental reference signal. If the reference is larger than the carrier, the driver circuit instructs the switches to connect the phase to V_{DC} and to zero otherwise.

The carrier signal is usually a triangle wave. Depending on what kind of sampling strategy is used, the reference waveform changes. For example in a closed-loop with current control, the current is sampled at the beginning of the switching period, the control voltage is calculated, and the duty cycles are executed by the converter at the beginning of the next switching period. That introduces a delay into the control, albeit one as small as the switching period. In the previous example, the switching and sampling periods are also synchronized. Because the calculated voltage is held throughout the switching period, the sampling in the example is called sample and hold, or zero-order hold (ZOH). That is the method used throughout this dissertation for experiments, though sampling and switching are not always synchronized. Double and non-integer sampling is explored in simulations. Because it results in different duty cycles for each half-sampling period, double sampling is often called asymmetric sampling.

79
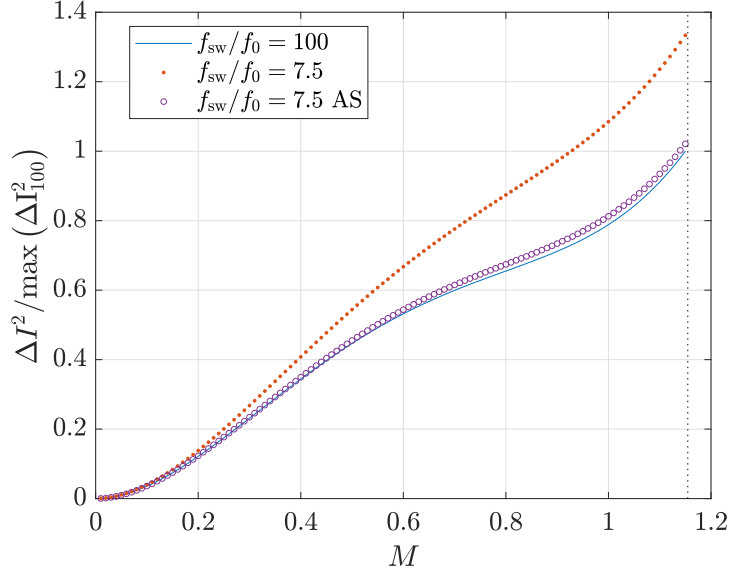
Figure 4.6: SVM phase current ripple squared with different f_{sw}/f_0 and asymmetric sampling (AS)

As a result of the connections discussed in Chapter 4.1, one may also inject the reference signal for all phases, with an arbitrary, yet identical zero sequence signal, u_0. Notice that as a result of the phase-to-neutral transformation, each phase voltage will not see the injected zero sequence signal. Injecting specific zero sequence signals changes the switching patterns that each phase sees, but maintains the desired fundamental waveform. A zero sequence of zero is the rudimentary sinus PWM, or SPWM. A zero sequence of a specific triangle wave is space-vector PWM (SVPWM or SVM); its reference-carrier implementation is also referred to as super sinus PWM.

Discontinuous PWM, or DPWM, acquires its name from the discontinuous reference signals its zero sequences have. The main advantage of DPWM methods involves their phase clamping for a certain duration of the fundamental voltage period, which reduces the number of switching instants by a nominal 2/3. Although it reduces the number of switching instants and the fundamental voltage is replicated on average, the switching patterns create large current ripple for inductive loads. Increasing the switching frequency so that the effective switching frequency remains the same as other PWM methods reduces the current ripple for some modulation indexes but increases it for others.

The zero sequences of both SVM and DPWM contain a third harmonic component that reduces the peak value of the reference signal. This is important since that third harmonic component will ideally vanish in the phase-to-neutral voltages, but allows for a larger fundamental voltage to be commanded due to the reduced peak value during carrier-reference comparison, ultimately increasing the maximum modulation index. The maximum modulation index achievable for the linear modulation range is $M = 2/\sqrt{3}$, as shown in Figure 4.4. Both SVM and DPWM achieve that modulation index. SPWM only achieves a maximum of $M = 1$ and is therefore rarely used in practice. Figure 4.7 shows the reference waveforms for some PWM methods with $M = 0.9$. Figure 4.8 shows the different phase current ripple magnitudes due to different PWM methods for nominally equivalent switching periods.

80

(a) SVPWM

(b) DPWM1

(c) DPWM2$^+$

(d) DPWM3
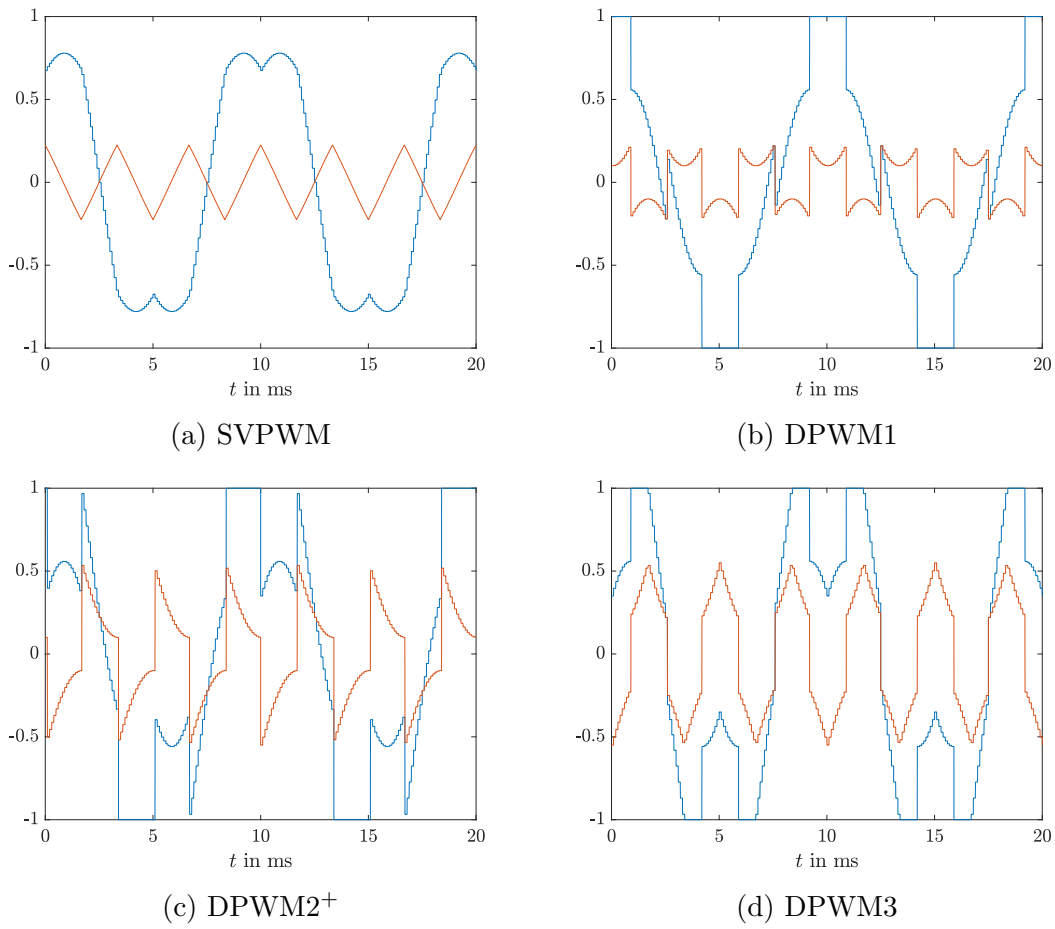
Figure 4.7: PWM ZOH reference (blue) and zero sequence (red) signals, $M = 0.9$
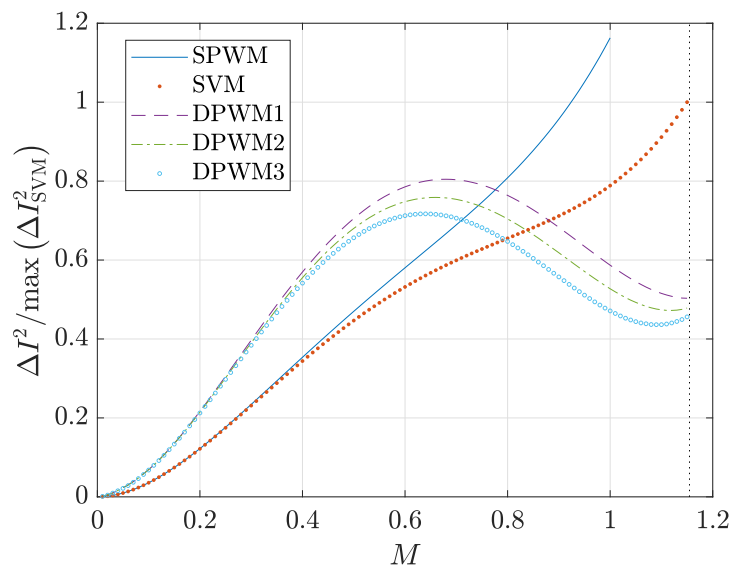
Figure 4.8: PWM method phase current ripple squared with equivalent switching frequency

81

From Figure 4.8 it is clear that for a $f_\text{sw}/f_0 = 100$, or switching frequency to fundamental reference ratio, one can halve the squared ripple in the machine at $M = 2/\sqrt{3}$ for the same losses in the inverter $-$pending the current-voltage angle as specified in [6] $-$by using DPWM3 instead of SVM.

4.2.1 Switching Frequency and Converter Losses

The switching frequency is the average number of commutations of all of the switches per second. As equation (2.1.1) in Chapter 2.1 shows, the current ripple amplitude for large f_sw/f_0 is inversely proportional to the switching frequency and proportional to a function of the modulation index $g(M)$ depending on the PWM method for three-phase machines, as shown in equation (4.2.1). That means that, in general, increasing the switching frequency reduces the current ripple, and therefore the machine losses due to switching.

$$\Delta i^2 = \frac{V_\text{DC}^2}{64 f_\text{sw}^2 L^2} g(M) \qquad (4.2.1)$$

A more detailed picture of the dependence of current ripple on switching frequency requires taking into account the switching to fundamental frequency ratio, sampling strategy, current-voltage angle, and magnetic coupling. The sampling strategy was addressed in the previous section, current-voltage angle and magnetic coupling will be addressed in the following section, and the fundamental frequency ratio effects are as follows: as said ratio decreases, the current ripple increases everywhere, almost as if the switching frequency were being reduced. As Figure 4.6 shows, a low ratio can be compensated by asymmetric sampling. The ratio of equivalent commutations between DPWM and continuous methods, however, decreases from 3/2 to about 6/5 with decreasing f_sw/f_0, necessitating compensation. This changing ratio of equivalent commutations was not found in the literature.
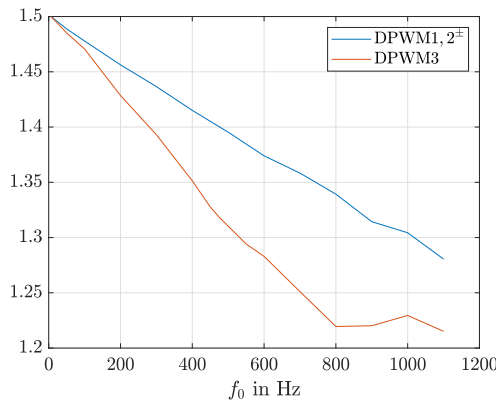
Figure 4.9: Commutation ratio between discontinuous and continuous PWM for different fundamental frequencies

The effect of switching frequency on converter losses is more straight-forward for continuous PWM methods, as it involves voltage rising slopes overlapping with drain current drop slopes in time. Since the slopes differ between rising edges and falling edges, their overlap time, and therefore the energy loss due to switching, also differs.

Every on-off cycle has a loss of $E_{\mathrm{sw}} = E_{\mathrm{on}} + E_{\mathrm{off}}$, and therefore the power loss due to switching $P_{\mathrm{sw}} \propto E_{\mathrm{sw}} f_{\mathrm{sw}}$. The energy losses depend linearly on DC bus voltage and the current flowing through the transistor, and therefore $E_{\mathrm{sw}} \propto |i(t)| V_{\mathrm{DC}}$. They also depend slightly on temperature and more so on gate resistance. Also, every time the diode ceases to conduct current, the current undershoots zero and therefore the current flow across the diode reverses for a small amount of time. During that same time, the blocking voltage increases, inducing losses every time the diode ceases to conduct, or once every switching period. This reverse recovery loss usually depends on voltage and current as $E_{\mathrm{rr}} \propto V_{\mathrm{DC}}\sqrt{|i(t)|}$. Depending on the module, it may be bulked into the transistor switching losses.

For DPWM methods, switching losses depend heavily on the current phase offset relative to the voltage reference signal. That dependence emerges from DPWM's state clamping relative to the current peak [6]. Consider for example DPWM1 in Figure 4.7(b). If the current waveform is in-phase with the DPWM1 reference, then at peak current the module does not switch states on one leg; the leg starts to switch for times away from the current peak, reducing overall switching losses. This fact allows for a further increase in the switching frequency from the nominal factor of 3/2 at specific phase offsets to achieve equivalent switching losses. Figure 4.10 shows the current phase relative to the voltage angle, and equivalent switching loss maps for various DPWM methods; the maps include the f_{sw}/f_0 ratio compensation shown in Figure 4.9.

(a) $\varphi = \theta_{i_{dq}} - \theta_{v_{dq}}$

(b) f_{sw} in kHz for DPWM1

(c) f_{sw} in kHz for DPWM2$^-$

(d) f_{sw} in kHz for DPWM3
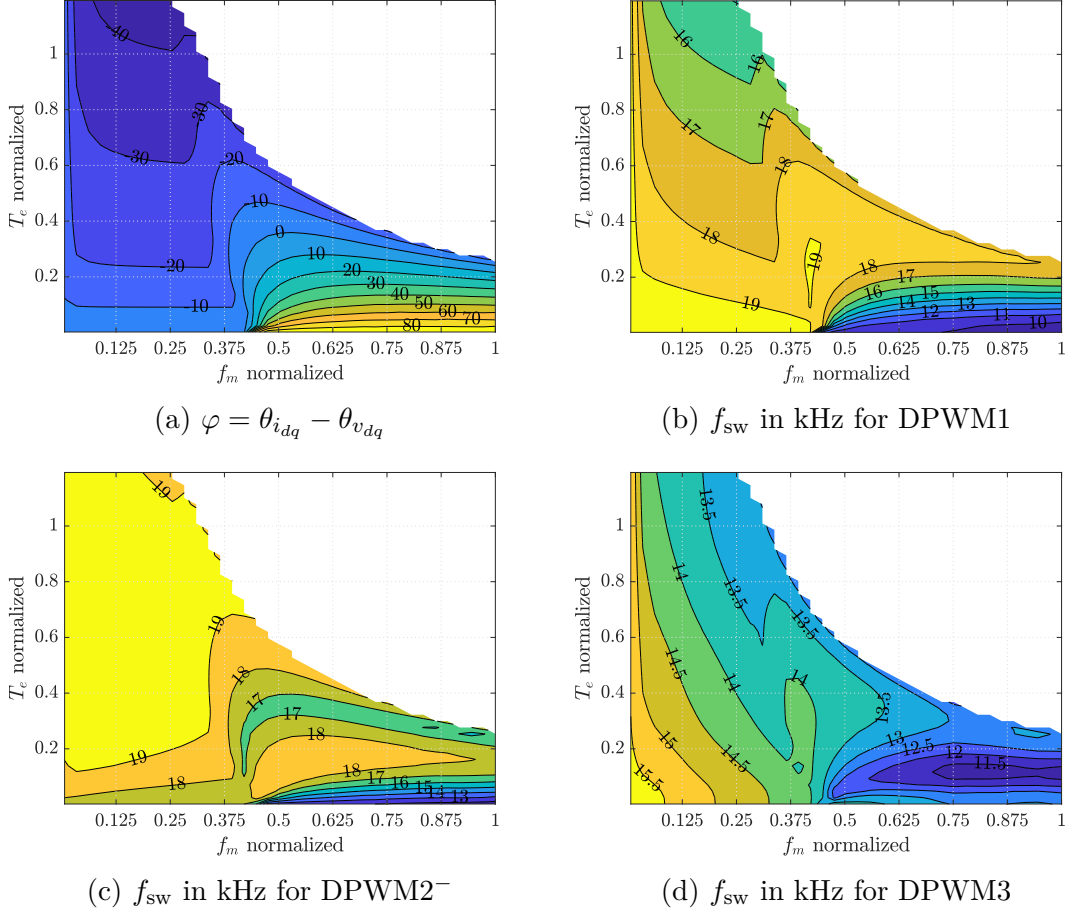
Figure 4.10: Simulated equivalent switching frequency in kHz for converter switching losses equal to continuous PWM methods at 10 kHz

The transistor-diode pair also has conduction losses that depend on current and current direction relative to the transistor or the diode. The transistor and diode can only conduct in opposite directions, which translates into a loss dependency on current direction which in turn implies a dependency on the phase offset of the current relative to the voltage reference signal: at the peak of the reference signal with zero current phase offset, the current is positive −meaning that charge flows, say, into the machine −and mostly the high-state transistor conducts compared to the low-state diode. As the phase offset increases, the conduction load is shared more by the low-state diode, changing the loss profile if the conducting resistances and the forward voltages of the transistor and diode differ. Conduction losses depend on the previous quantities as shown in equation (4.2.2), where $v_{f,j}$ is the forward voltage and R_j is the conducting resistance. The index j chooses between transistor and diode subscripts.

$$P_{\text{cond},j} = v_{f,j} i_j(t) + i_j(t)^2 R_j \tag{4.2.2}$$

The conduction losses therefore qualify the benefits DPWM methods have in reducing switching losses if transistor and diode forward characteristics differ. For in-phase current and voltage and transistor forward characteristics larger than diode forward characteristics for example, the benefits of DPWM1's switching loss reduc-

tion decrease. That is typical. However, in the converse case for forward characteristics with in-phase current and voltage waveforms, the benefits of DPWM1's switching losses are amplified. Since current phase changes with machine operating point, this complicates the situation of finding an optimal switching frequency and PWM method depending on module parameters, even for minimizing converter losses only.

4.3 Dual Three-Phase Machines

Dual three-phase machines are usually connected as shown in Figure 4.11 with a spacial electrical angle offset α between the duals in a common stator.
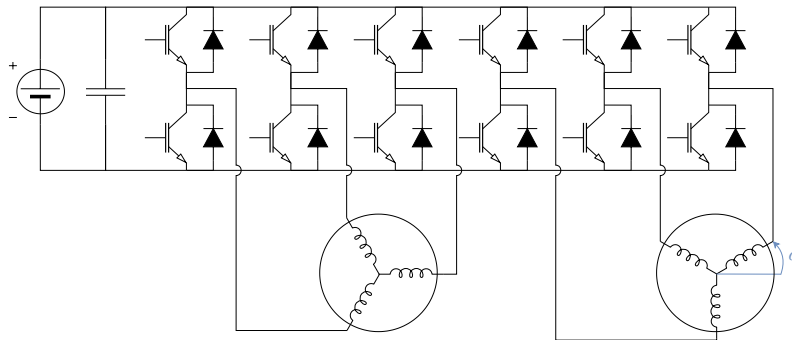
Figure 4.11: A dual three-phase drive

There are two fundamental approaches for commissioning duty cycles with dual-three phase machines: independent control and 12-sector space-vector decomposition. In independent control, one replicates the PWM methods shown in Chapter 4.2 and commands duty cycles to one dual machine independently. 12-Sector space-vector decomposition expands the idea of the Clarke transformation to all available states in a dual-three phase machine to command duty cycles as if it were a three-phase machine. In that case, the states would be transformed onto the orthographic projection of the hexeract, or 6-cube, with the four zero states at the origin. The circuit topology of separate neutrals actually limits the amount of states, which means that 12-sector SVM will always have one dual machine with a zero state for an extended period of time. This creates a rectangle-like pulse with the fundamental frequency, thus inducing odd harmonics in the system. As usual with three-phase machines, including dual three phase machines, the harmonics with multiples of three cancel and the system contains large $5^{th}, 7^{th}, 11^{th}, 13^{th}, ...$ harmonics. Figure 4.12(a) shows the clamping of one dual during a half-cycle, inducing odd harmonics.

If the neutrals of the two dual machines are disconnected, each of the states from one machine is independent of the one in the other machine from a phase-to-neutral voltage perspective. This means that there are $2^4 - 4 = 12$ unique non-zero voltage states. Distributed over two dual machines, one acquires six non-zero voltage states per dual and the zero voltage, making the machine controllable as two three-phase machines. That is the idea behind a dual three-phase machine. A six-phase machine has connected neutrals, which recovers the full richness of voltage states from the hexeract, with only two zero states.

Because the machine under investigation in this dissertation is a dual three-phase machine −two disconnected neutral points −and because independent control
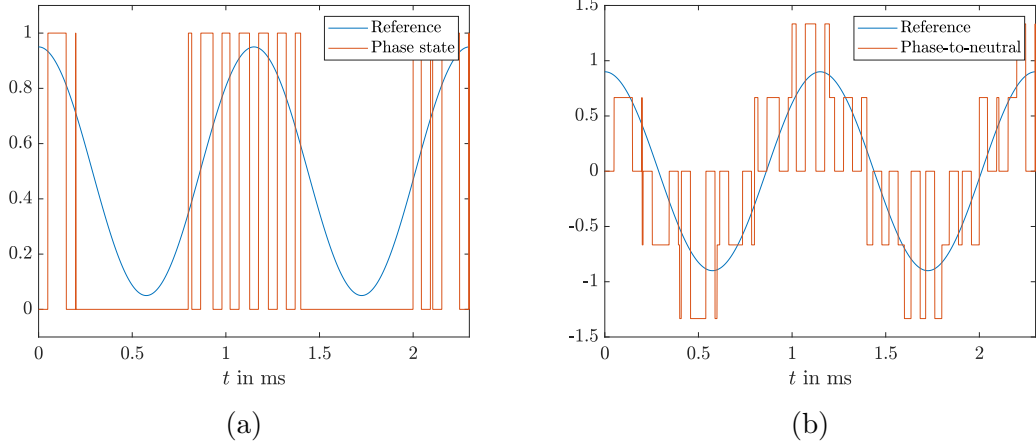
Figure 4.12: 12-sector SVM phase switching state and phase-to-neutral normalized voltage

does not induce additional harmonics −unlike 12-sector SVM −, the duals in this dissertation are controlled using independent, or dual, control. 12-sector methods with compensation are investigated with simulations.

4.3.1   PWM Methods with Coupling

Firstly we define the coupling coefficient ς as in equation 4.3.1:

$$\varsigma^2 = \sum_k \Gamma_k \, , \tag{4.3.1}$$

where $\Gamma \coloneqq \{(\lambda_i - \lambda_j)^2/(\lambda_i\lambda_j)\}$ is the set of all unique combinations with the specified elements, Γ_k is an element of Γ, $\lambda_i = \lambda(\mathbf{L}^{-1})$, $\lambda(\cdot)$ signifies the eigenvalue operator, and $\mathbf{L}^{-1}$ is the inverse inductance matrix in the synchronous frame. Notice how a value of $\varsigma = 0$ means no coupling and corresponds to the case when $L_d = L_q$ and $M_d = M_q = 0$. Large coupling coefficients imply a large difference between the self inductances L_{dq} and large mutual inductances M_{dq}. Taking the inductance matrix as

$$\mathbf{L} = \begin{bmatrix} L_d & 0 & M_d & 0 \\ 0 & L_q & 0 & M_q \\ M_d & 0 & L_d & 0 \\ 0 & M_q & 0 & L_q \end{bmatrix} \tag{4.3.2}$$

results in the following eigenvalues for its inverse:

$$\begin{aligned} \lambda_{1,2} &= (L_d \pm M_d)^{-1} \\ \lambda_{3,4} &= (L_q \pm M_q)^{-1} \, . \end{aligned} \tag{4.3.3}$$

The resulting coupling coefficient is therefore

$$\varsigma^2 = 4\left(\frac{1}{L_d^2/M_d^2 - 1} + \frac{1}{L_q^2/M_q^2 - 1}\right) + \sum_{s_d=[-1,1]} \sum_{s_q=[-1,1]} \frac{(L_q - L_d + s_q M_q - s_d M_d)^2}{(L_d + s_d M_d)(L_q + s_q M_q)} \, . \tag{4.3.4}$$

The coupling measure ς can therefore measure high frequency magnetic coupling for arbitrary inductance matrices $\mathbf{L}$. This coefficient differs from that in [34], [35], and [36] as it is more general. It should be taken as a measure of how much one may expect a system's current ripple to deviate from the canonical function in equation (2.1.1). To compute a system's current ripple with anisotropy or coupling exactly, the one must compute it directly, as other factors such as the relative current angle $\varphi = \Delta\theta_{i,v}$ also play an important role.

(a) Asymmetric dual three-phase machine   (b) Polar dual three-phase machine
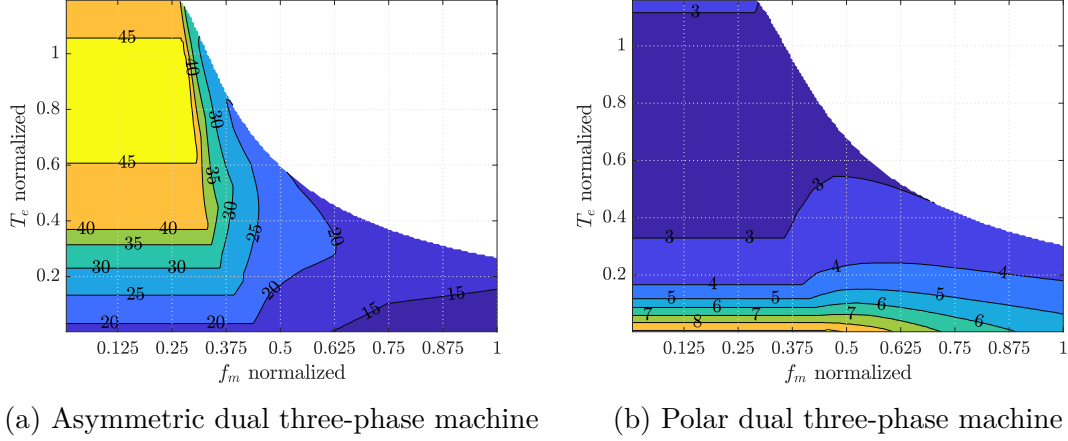
Figure 4.13: ς^2

The coupling coefficient ς is also a measure of inductance anisotropy, as Figure 4.13(a) shows for a machine with large M_{dq} (asymmetric machine) and 4.13(b) shows for a machine with $M_{dq} \sim 0$ (polar machine, effectively a three-phase machine with $L_d \neq L_q$).

(a) $\varsigma = 6.96$, $f_{\text{sw}}/f_0 = 54$ (b) $\varsigma = 4.51$, $f_{\text{sw}}/f_0 = 54$
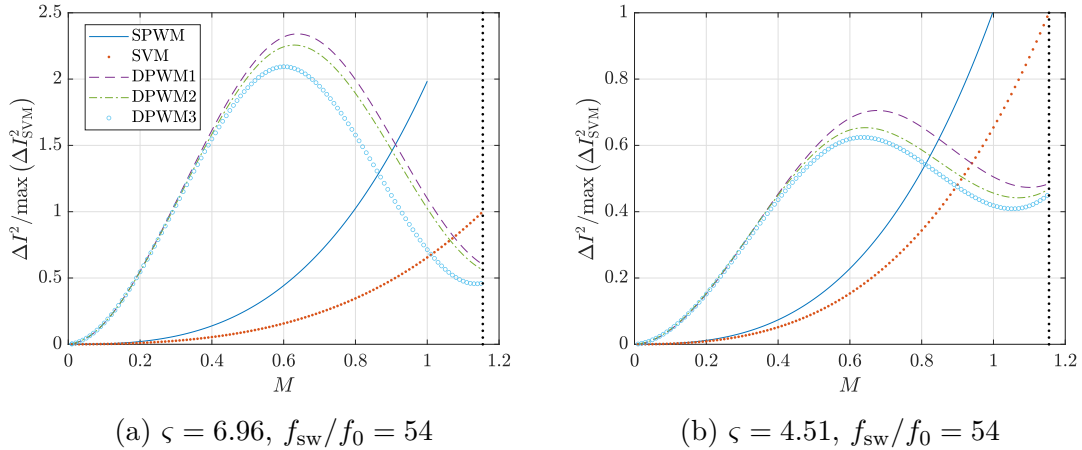
Figure 4.14: PWM method phase current ripple squared with equivalent switching frequency for two different coupling coefficients ς

Larger ς signify larger differences in current ripple between different PWM methods for $M \leq 0.9$, which in turn implies larger high frequency losses. Due to iron saturation, a single machine may span the range of ς shown in Figure 4.14. Notice also that for large M, it is always more convenient to use any of the DPWM methods, particularly DPWM3, as in the decoupled case. The largest difference between

SVM and DPWM3 is about 60% at $M \approx 1.05$, making it imperative to commute with DPWM3 for $M \geq 1$, which covers a broad range in the torqe-speed plane. In fact, it might cover the entire field-weakening region.

(a) $\varsigma = 6.96$, $f_{\mathrm{sw}}/f_0 = 54$ (b) $\varsigma = 4.51$, $f_{\mathrm{sw}}/f_0 = 54$
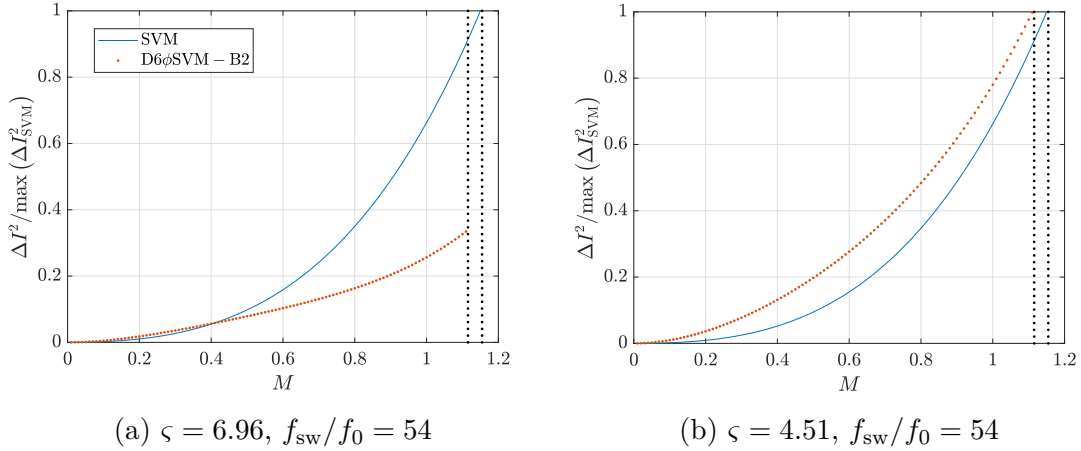
Figure 4.15: PWM method phase current ripple squared with equivalent switching frequency for two different coupling coefficients ς

Other PWM methods exploiting the additional degrees of freedom include D6ϕ SVM-B2, which as Figure 4.15 shows, has about 66% less squared current ripple as dual SVM for a broader range than dual DPWM3 for large coupling coefficients. For smaller coupling coefficients, dual SVM has a modest 8% less squared current ripple as D6ϕ SVM-B2, for which DPWM3 boasts the smallest squared current ripple. D6ϕ SVM-B2 uses the degrees of freedom offered by dual three-phase converters to eliminate the large 5th and 7th harmonics inherent in 12-sector PWM, which limits its maximum modulation index to $M = \sqrt{2/3 + 1/\sqrt{3}} \approx 1.115$. Because current ripple varies widely according to modulation index, coupling coefficient, and current-voltage angle, there are multiple optima over those parameters. An optimization of the current ripple by means of PWM method selection for a machine will have different optimal PWM methods at different operating points.

Bulges for all PWM methods except for dual SVM methods having troughs in the phase current ripple occur near the modulation index $M = 0.6$. In fact, they occur near $M = 2/\pi$ or $M = \pi/3\sqrt{3}$, since the largest relative ripple should occur when the so-to-speak local duty cycle in the phase-to-neutral voltage approaches half of the maximum local duty cycle. The maximum local duty cycle happens during six-step operation, which has a modulation index of $4/\pi$, creating bulges or troughs near half that index.

4.3.2 Interleaving

Dual control allows for offsetting the pulses in each dual by a certain phase offset called the interleaving angle. The main advantage of interleaving involves reducing the DC capacitor current and is mostly thought to have little effect on the dual machine losses, mainly because of the assumption that most losses would be copper losses. Figure 4.16 shows the typical DC-linking capacitor current ripple for different interleaving angles using SVM, DPWM1, DPWM2$^{\pm}$, and DPWM3.
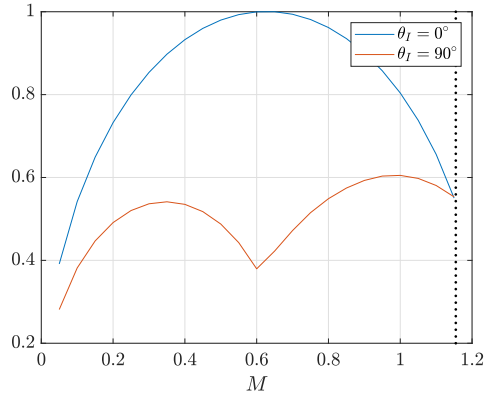
(a) SVM
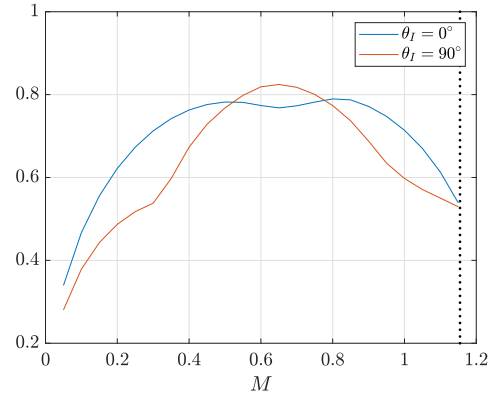
(b) DPWM1
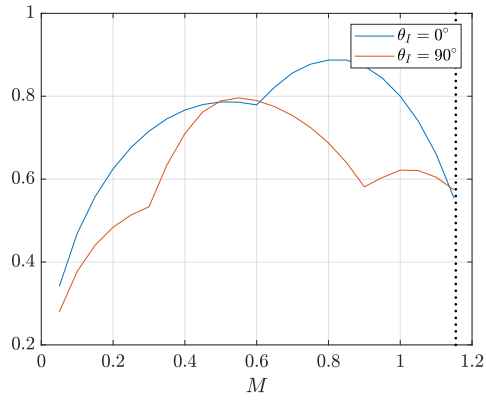
(c) DPWM2$^+$
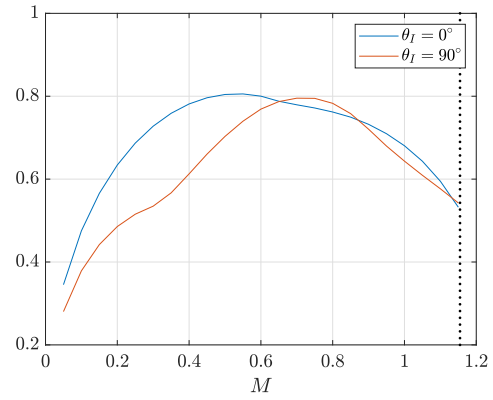
(d) DPWM2$^-$
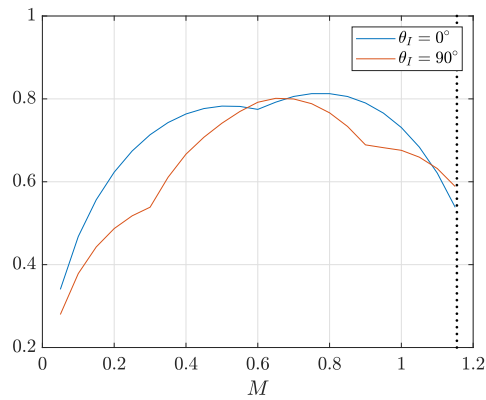
(e) DPWM3

Figure 4.16: Normalized DC-link capacitor RMS current ripple, $\varphi = -36.9°$

Notice that SVM creates the largest capacitor RMS current ripple difference between the interleaving angles $\theta_I = 0°$ and $\theta_I = 90°$. Knowing that the capacitor current ripple depends heavily on the relative current phase angle φ, few reasons remain to justify the invariance of the trends in Figure 4.16 over different relative current phase angles. Indeed, as Figures 4.17−4.20 show, the minimum capacitor ripple changes with relative current phase angle.

The trough in Figure 4.16(a) can be explained in terms of local duty cycles, like the bulges for phase current ripple. Also notice that for all of the PWM methods, the maximum phase current ripple occurs near or at $\theta_I = 90°$ for all M and $\Delta\theta_{i,v} = \varphi$. The θ_I corresponding to the minimum capacitor current ripple, in contrast, changes depending on PWM method, M, and φ. That makes the problem of optimizing the interleaving angle interesting and nontrivial for the coupled machines considered.

(a) Phase ripple for $\varphi = -36.3°$

(b) Phase ripple for $\varphi = -5.7°$

(c) Capacitor ripple for $\varphi = -36.3°$

(d) Capacitor ripple for $\varphi = -5.7°$
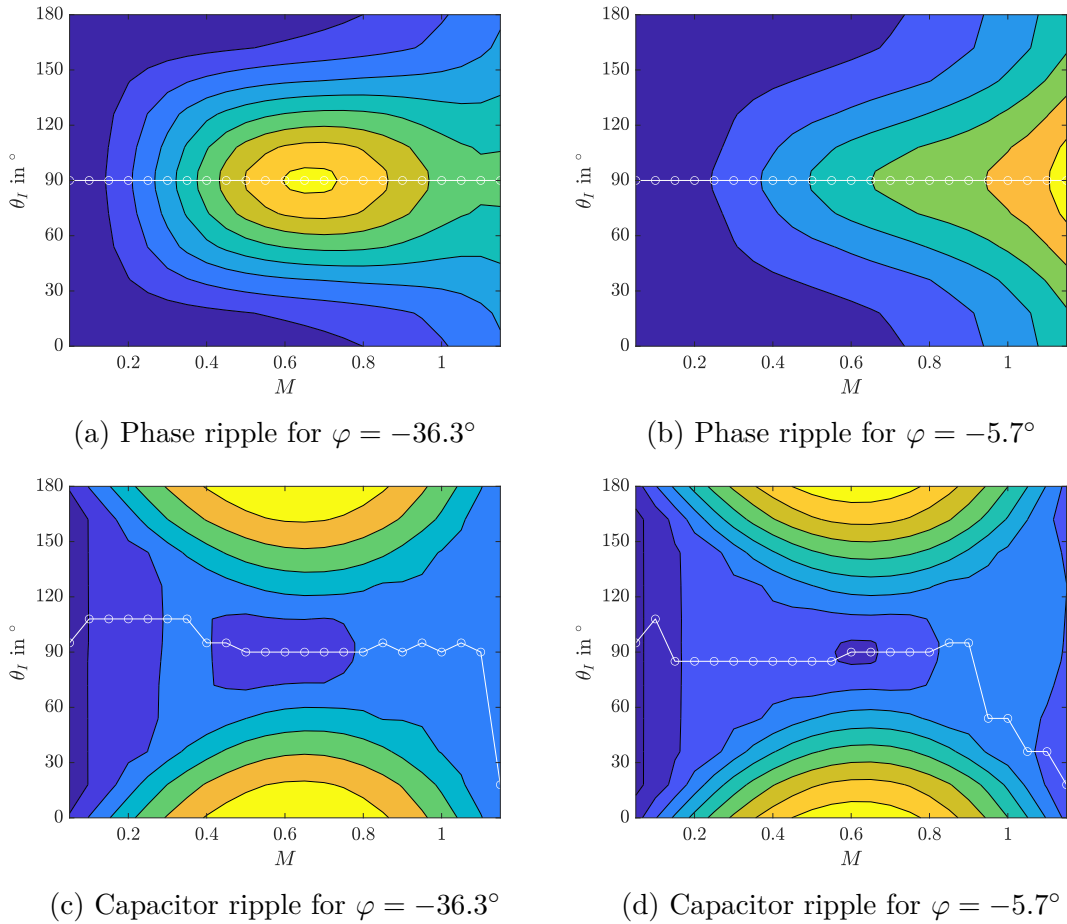
Figure 4.17: SVM phase and capacitor current ripple squared for two different relative current angles φ and $f_{\text{sw}}/f_0 = 54$. (a) and (b) also show the maximum phase ripple and (c) and (d) the minimum capacitor ripple per M with connected circles
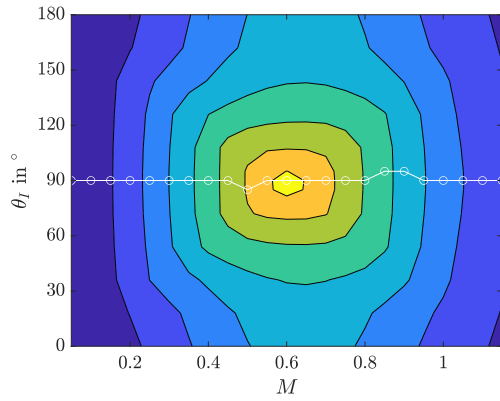
(a) Phase ripple for $\varphi = -36.3°$
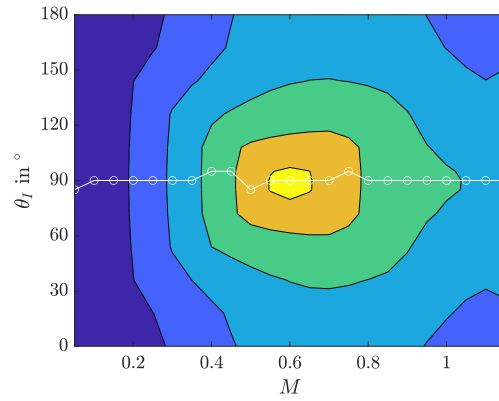
(b) Phase ripple for $\varphi = -5.7°$
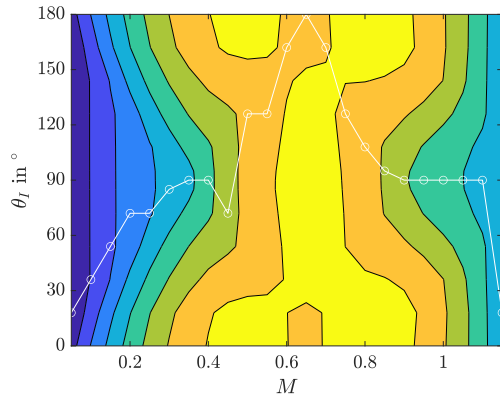
(c) Capacitor ripple for $\varphi = -36.3°$
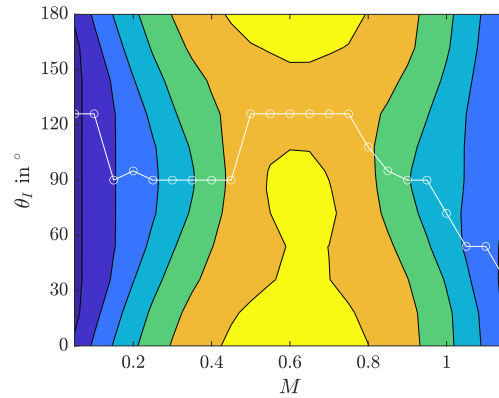
(d) Capacitor ripple for $\varphi = -5.7°$

Figure 4.18: DPWM1 phase and capacitor current ripple squared for two different relative current angles φ and $f_{\mathrm{sw}}/f_0 = 54$. (a) and (b) also show the maximum phase ripple and (c) and (d) the minimum capacitor ripple per M with connected circles

(a) Phase ripple for $\varphi = -36.3°$

(b) Phase ripple for $\varphi = -5.7°$

(c) Capacitor ripple for $\varphi = -36.3°$

(d) Capacitor ripple for $\varphi = -5.7°$
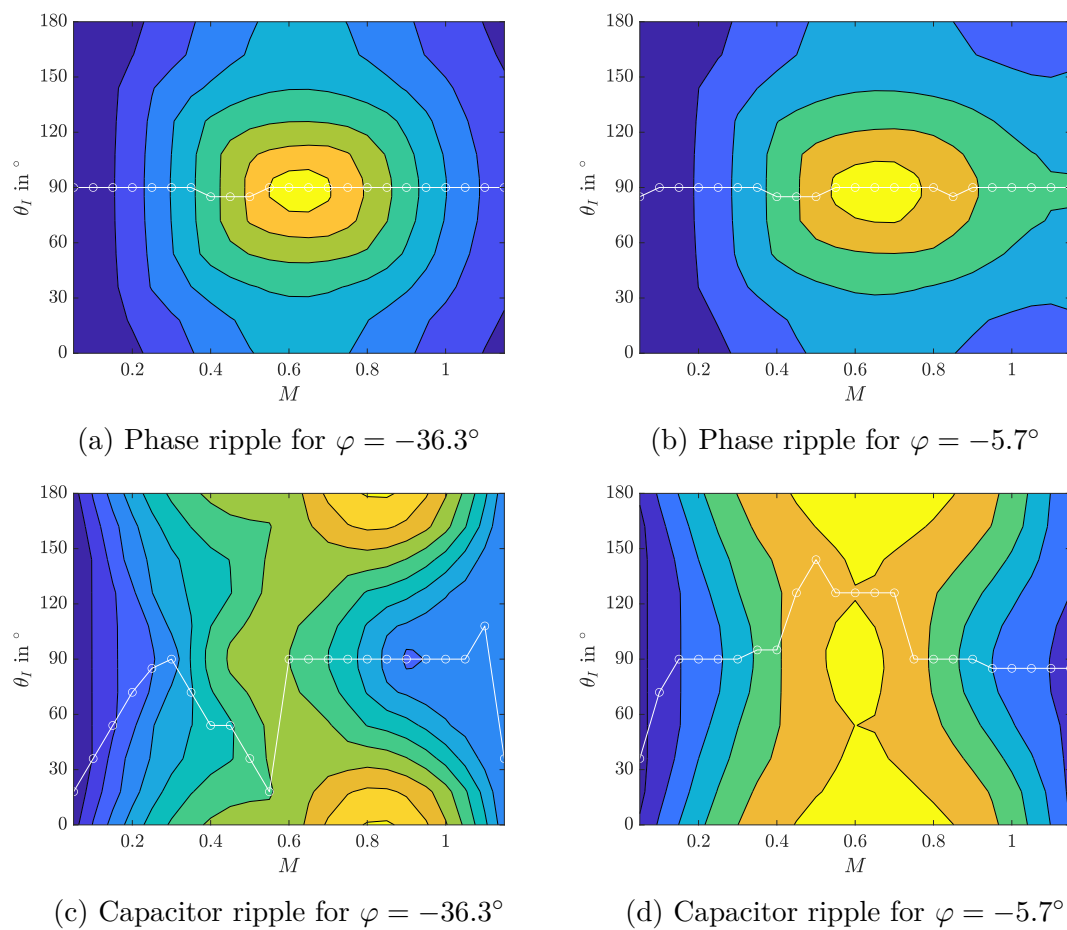
Figure 4.19: DPWM2 phase and capacitor current ripple squared for two different relative current angles φ and $f_{sw}/f_0 = 54$. (a) and (b) also show the maximum phase ripple and (c) and (d) the minimum capacitor ripple per M with connected circles
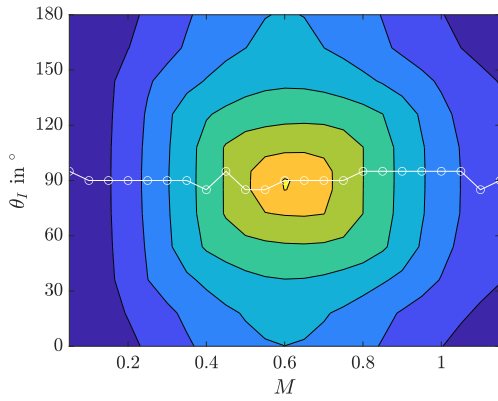
(a) Phase ripple for $\varphi = -36.3°$
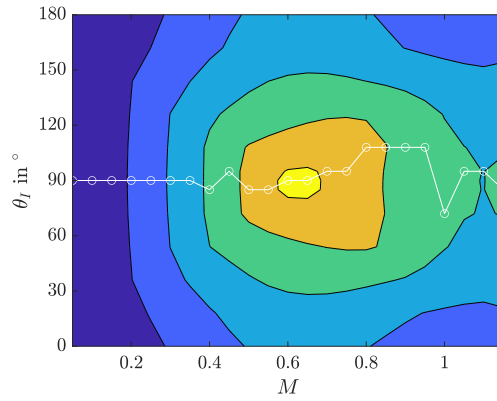
(b) Phase ripple for $\varphi = -5.7°$
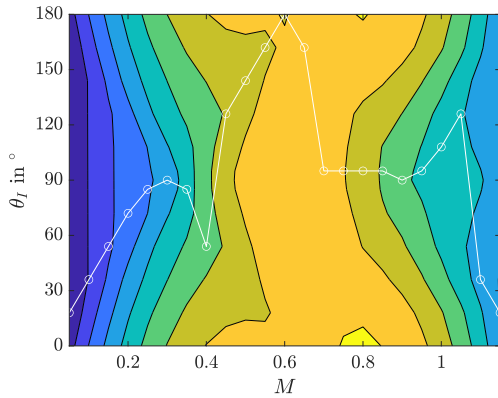
(c) Capacitor ripple for $\varphi = -36.3°$
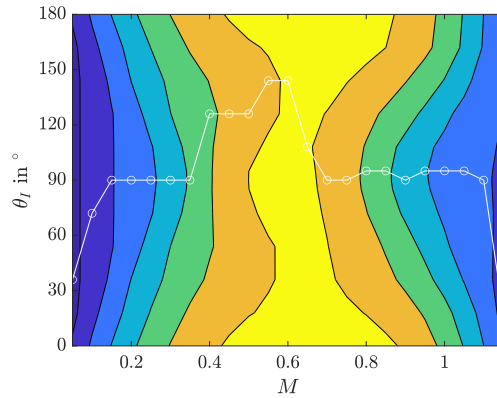
(d) Capacitor ripple for $\varphi = -5.7°$

Figure 4.20: DPWM3 phase and capacitor current ripple squared for two different relative current angles φ and $f_{\mathrm{sw}}/f_0 = 54$. (a) and (b) also show the maximum phase ripple and (c) and (d) the minimum capacitor ripple per M with connected circles

Chapter 5

Simulation Results

This chapter shows the results of the finite element analysis (FEA/FEM) simulations to study the effects of inverter excitation on machine losses, especially interleaving. Two machines with different windings are simulated: the asymmetric and polar machines. It is shown by means of iron loss distributions that include FEM-calculated eddy currents with reaction fields that most of the losses due to interleaving occur in the asymmetric machine in the stator teeth; most of those losses are eddy-current losses. Losses do not increase as markedly in the polar machine due to spatially separated duals, i.e. less coupling between the duals. Interleaving reduces the simulated efficiency of the machine by about 3% in the asymmetric machine and by about 1% in the polar machine. The effect of switching frequency changes and pulse-width modulation (PWM) methods on magnet losses are also investigated. It is found that for certain PWM methods, switching frequencies, and speeds, magnet losses increase due to tooth-reluctance harmonics and inverter-induced harmonic overlap. Lastly, current differences in the DC-link capacitor are reviewed. It is found that the loss savings in the DC-link capacitor due to interleaving are much less than the loss savings in the asymmetric machine when not interleaving. Due to computational constraints of simulating FEM-calculated eddy currents with reaction fields with smaller-than converter commutation time scales, only 16 of the points most visited from a WLTC cycle during motoring were simulated.

5.1 Asymmetrical and Polar Dual Three Phase Machines

The machines being investigated are the asymmetrical and polar dual three phase machines. The asymmetrical machine has an electrical 30° offset between the two dual machines and the polar machine has the two duals wound on two different halves of the cylinder, i.e. it has a mechanical 180° offset with a control electrical angle offset of 0°. Figures 5.1 and 5.2 show the phases as they are wound on the stator with a marker indicating the separation between the duals.
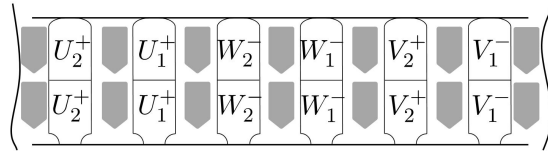
Figure 5.1: Winding of the asymmetrical machine.
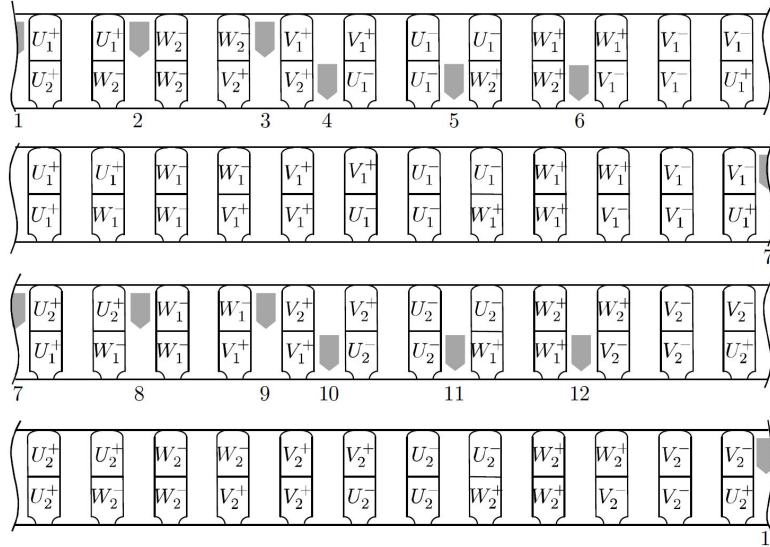
Figure 5.2: Winding of the polar machine.
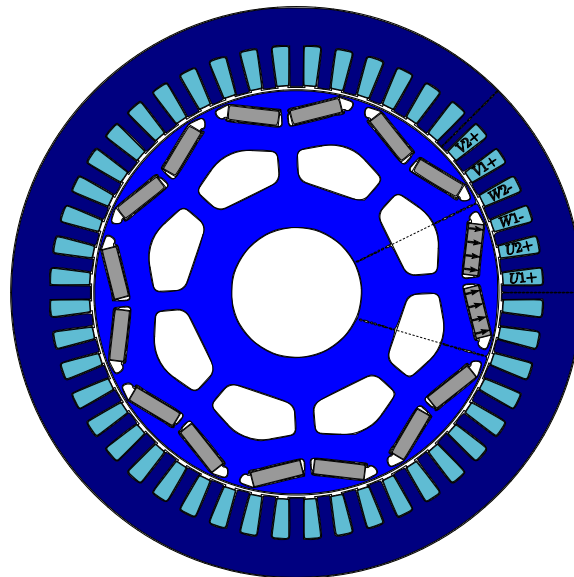
Figure 5.3: Cross-section of the asymmetric machine.

95

5.1.1 Conduction Losses in the Windings

Since the machine is wound with small diameter cables, the skin effect in the cables due to high frequency switching in the inverter is negligible, as is the related proximity effect from the rotating field. As such, the current density distribution is not taken into account in the FEM conduction loss in the copper windings. This section summarizes the differences in conduction losses in the windings due to interleaving.

Figure 5.4 shows an overview of the losses by displaying the mean copper loss over each simulated operating point. Two features come to the fore: the difference in losses in the copper due to interleaving are negligible in both machines, and the asymmetrical machine has slightly more losses in the copper than the polar machine.
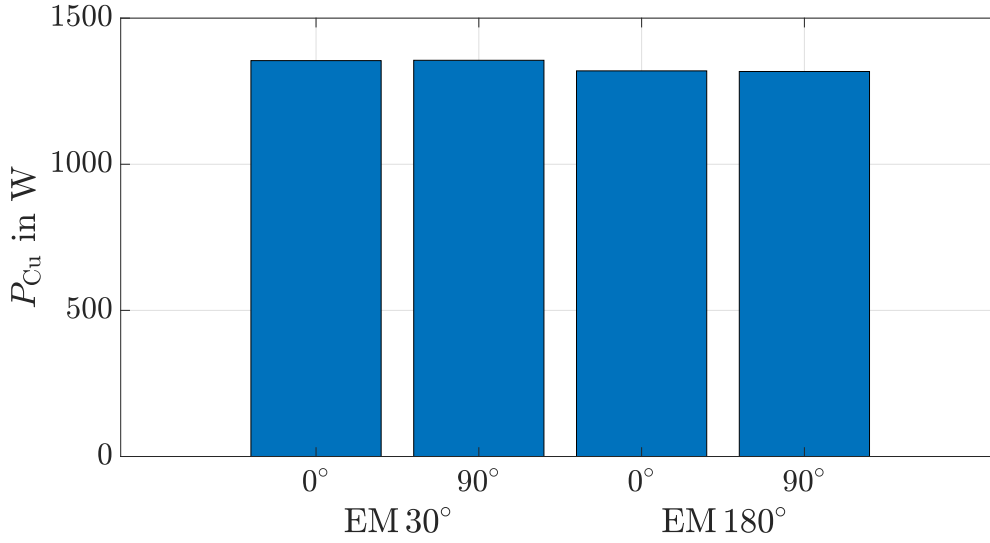
Figure 5.4: Copper loss averaged over all simulated operating points.

(a) Interleaving on, $\theta_I = 90°$

(b) Interleaving off, $\theta_I = 0°$
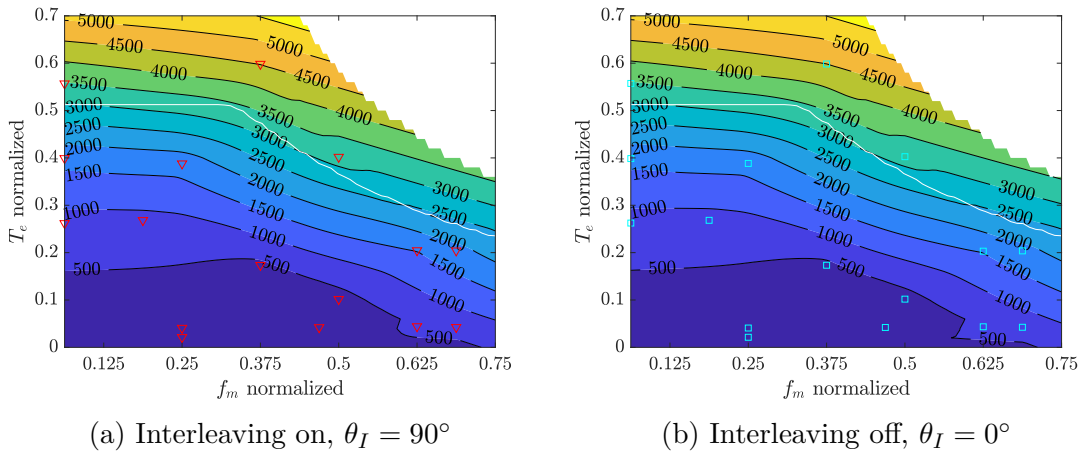
Figure 5.5: Copper losses for the asymmetric machine in W

(a) Interleaving on, $\theta_I = 90°$

(b) Interleaving off, $\theta_I = 0°$
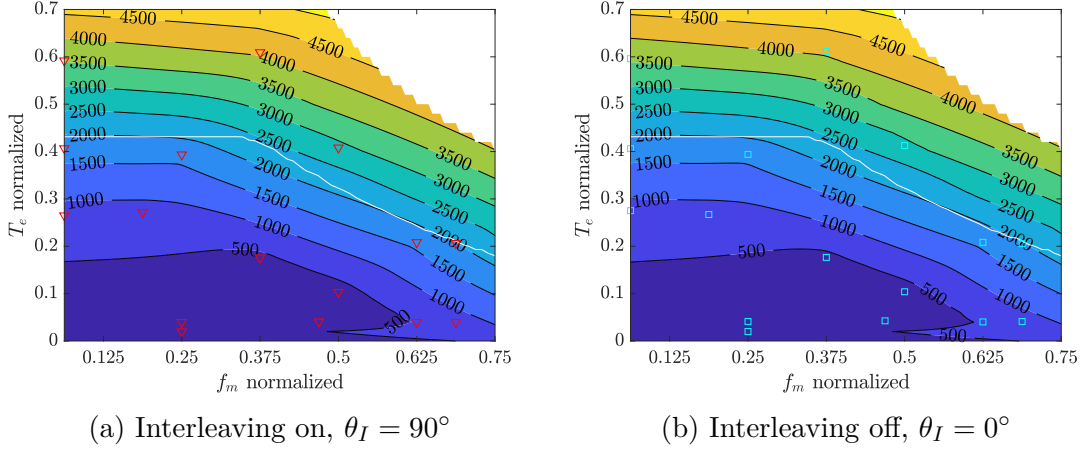
Figure 5.6: Copper losses for the polar machine in W

(a) Asymmetric machine

(b) Symmetric machine
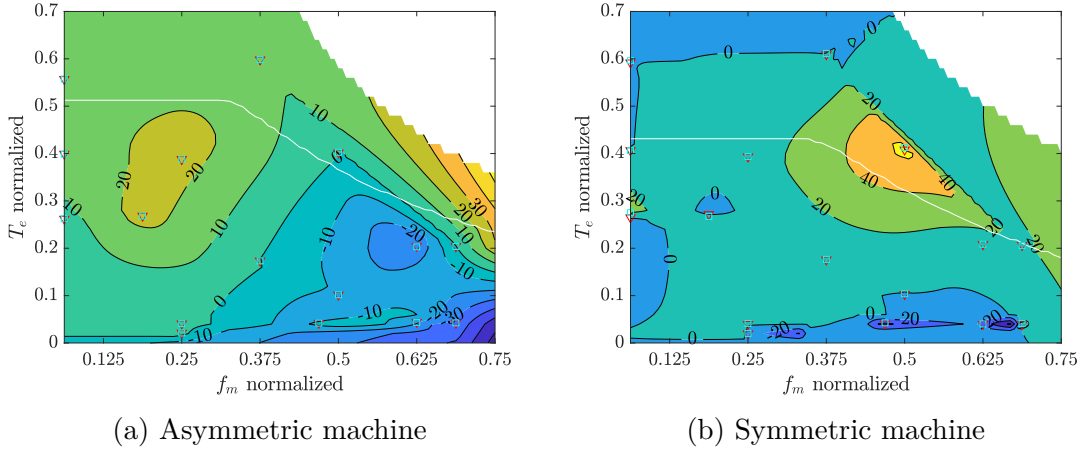
Figure 5.7: Copper loss difference, $P_{\mathrm{Cu}}(90°) - P_{\mathrm{Cu}}(0°)$ in W

Figures 5.5 and 5.6 show the copper loss over the torque-speed plane and their scattered interpolation. Iso-loss curves droop at lower speeds rather than at the corner point due to the lack of simulated points there. The number of simulations had to be kept at a minimum, since to simulate high-frequency effects with interleaving, the time step must be at least one order of magnitude smaller as the interleaving delay, about 1 μs. As Figure 5.7 shows, the differences in copper losses due to interleaving remain small, i.e. below 1% for the asymmetric machine and below 1.7% for the polar machine. One may conclude that the copper losses do not change much due to interleaving, even accounting that, in some regions, interleaving increases losses and decreases them in others. Larger regional deviations in opposite directions might have explained the unchanging copper losses seen in Figure 5.4, but Figure 5.7 dispels that possibility.

Sampling ratios $f_{\mathrm{sa}}/f_{\mathrm{sw}}$ contribute significantly to the current ripple amplitude as already shown in Figure 4.6, where asymmetric sampling corresponds to $f_{\mathrm{sa}}/f_{\mathrm{fw}} = 2$. Figure 5.8 shows the simulated current ripple magnitude for $f_{\mathrm{sa}} = 10$ kHz at one operating point for the asymmetric (strongly coupled duals) and an uncoupled machine. Figure 5.8 shows that the current ripple is at a minimum for $f_{\mathrm{sa}}/f_{\mathrm{fw}} = 1$ and that coupling increases the current ripple.

(a) Coupled duals

(b) Not coupled duals
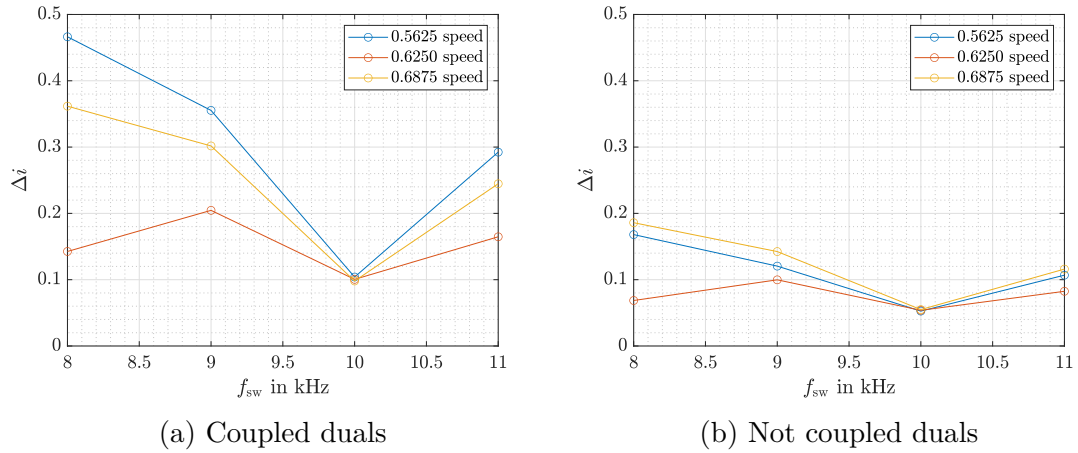
Figure 5.8: Simulated normalized current ripple magnitude with 10 kHz sampling frequency for 0.1 norm. moment

To emphasize the point, Figure 5.9 displays the current ripple for various speeds at 0.1 normalized moment for the coupled machine and the fictitious uncoupled machine at various sampling and switching frequencies. The diagonal is marked with a cyan line to indicate the minimum current ripple and the gold circles rimmed in blue are the simulated points.
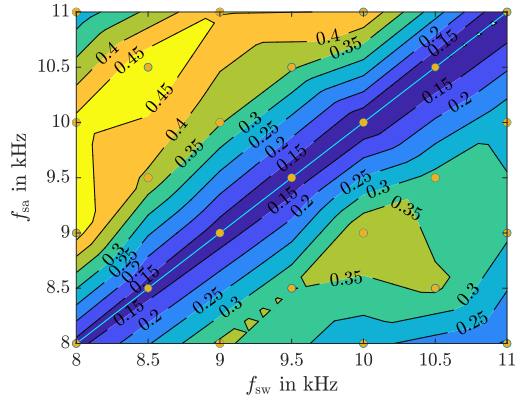
(a) 0.5625 norm. speed, coupled
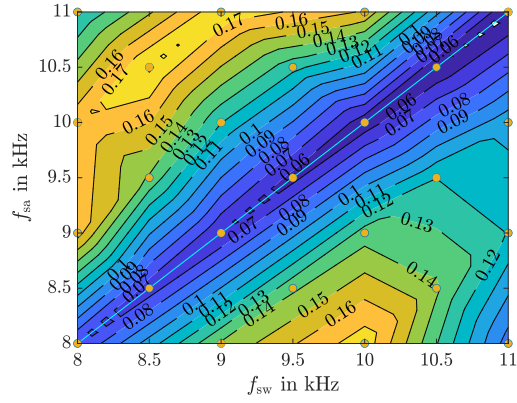
(b) 0.5625 norm. speed, not coupled
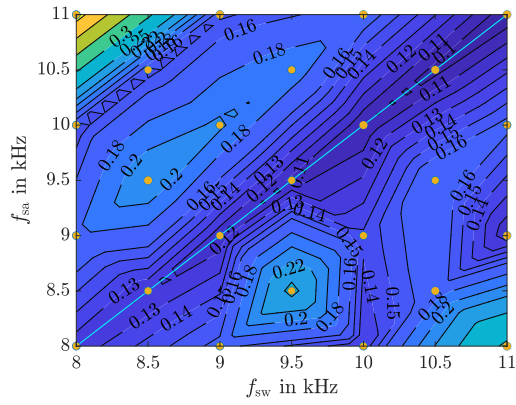
(c) 0.625 norm. speed, coupled
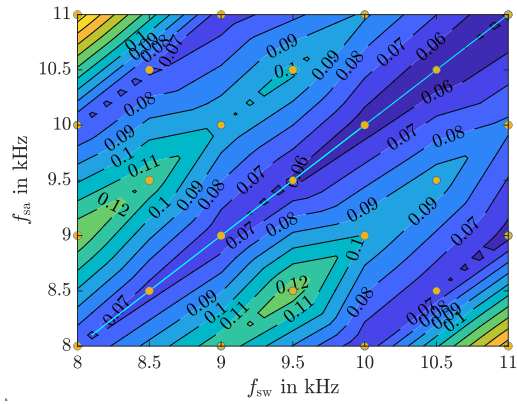
(d) 0.625 norm. speed, not coupled
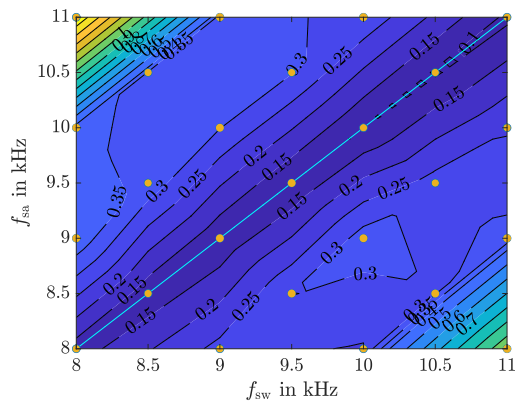
(e) 0.6875 norm. speed, coupled
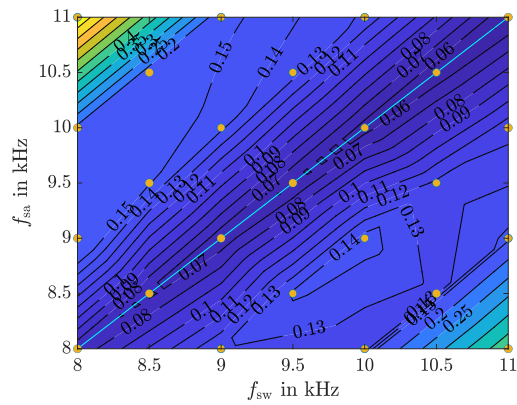
(f) 0.6875 norm. speed, not coupled

Figure 5.9: Simulated normalized current ripple for various switching and sampling frequencies at 0.1 norm. moment; $\theta_I = 0°$

.

Although the current ripple causes negligible losses in the copper, the same ripple causes ripples in the flux, causing iron losses. The next section further renders changes in copper losses due to interleaving, sampling ratios, and switching frequency as negligible, as the regional changes in iron loss reach 40% as opposed to the changes below 2% simulated in copper.

5.1.2 Iron Losses

The losses in the iron can be separated into eddy current losses and hysteresis losses. A third category of iron losses, anomalous losses, typically describe the additional losses not accounted for when modeling the previous two categories upon comparing theoretical or simulated iron losses to experimental results. Consequently, this section on simulated iron loss considers only the iron loss separation into eddy current losses and hysteresis losses. Furthermore, the terms eddy current losses, joule losses, and conduction losses are all used interchangeably. Because a loss model based on Fourier transforms of the magnetic field density is known to overestimate joule losses in iron and effectively approximates the eddy currents with a formula containing the magnetic field, the FEM simulation instead calculates the eddy currents in the iron directly, from which the joule losses can be calculated in a straight-forward fashion. The eddy currents are calculated considering the lamination thickness, which amounts to 0.35mm.

The step time for the FEM simulations is $1\mu s$ to investigate the effects of interleaving on iron losses. Due to the need to calculate the current density distribution in the iron and the small step size, only half a fundamental period was simulated in [132]. The results shown for the asymmetric machine are for one fundamental period and those for the polar machine are for one-half period, since the entire machine −as opposed to just one-eighth of the machine in the case of the asymmetric machine −must be simulated as a result of the winding distribution. As a result of the longer simulation time for the asymmetric machine, results differ slightly from those in [132], but nevertheless reinforce the conclusions therein.
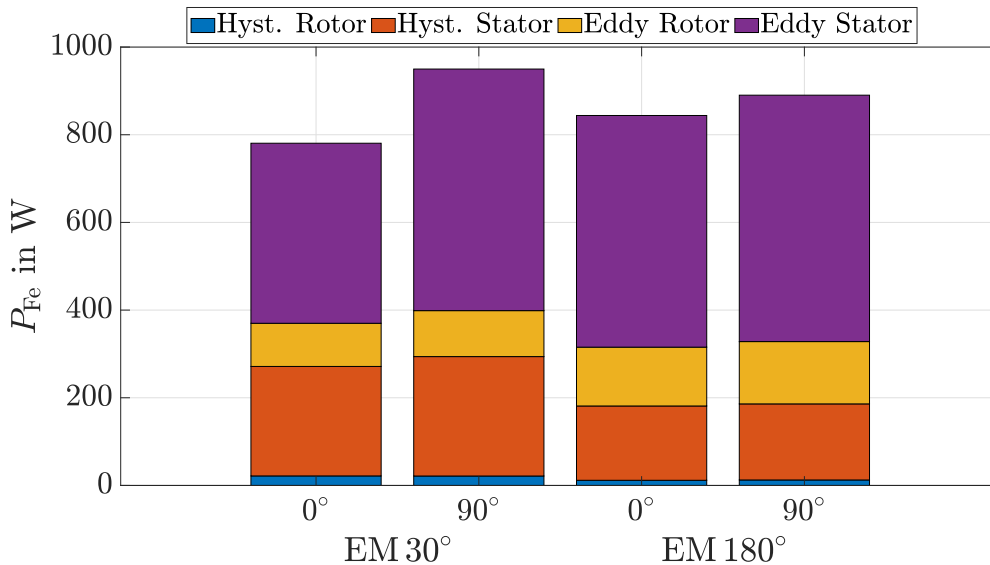
Figure 5.10: Iron loss separation averaged over all simulated operating points.

Figure 5.10 shows the averaged iron losses over the 16 FEM-simulated points separated into their respective iron loss type and generation place. In both the asymmetric and polar machines, the iron losses are concentrated in the stator, as expected from the larger volume of iron in the stator. Most of the increases in losses due to interleaving are also in the stator. Lastly, most loss increases due to interleaving comprise of eddy current loss increases. The reason for the additional eddy loss increase in iron is left for later in this section.

The specific loss distributions over the torque-speed range with interleaving on and off and their difference are shown for hysteresis and eddy losses for the asymmetric machine in Figures 5.11 and 5.12 and for the polar machine in Figures 5.13 and 5.14. Figure 5.11(a) and (c) show that hysteretic loss in the rotor mostly depends on the speed of the rotor. One can expect this speed dependence to furthermore depend on the number of teeth per pole-pair and coalesced MMF harmonics from the dual three-phase machine, namely the 12th and 6th harmonics respectively. The linear dependence on speed in the base speed region also validates the linear dependence on frequency of the Bertotti hysteresis model. Hysteretic losses in the rotor nevertheless remain small, and the changes due to interleaving in the rotor are even smaller, as Figure 5.11(e) shows. The order of single Watts is negligible for this class of machines. Hysteresis loss changes in the stator on the other hand, are in the order tens of Watts, as Figure 5.11(f) makes clear. However, as Figures 5.11(b) and (d) show, the hysteretic losses in the stator are about 300 W, which makes the change in maximum hysteresis loss due to interleaving about 20% of that number. Although not insignificant, the reader must consider that the total losses add up to about 700 W, making the change in hysteresis losses less than 10% of the total iron losses. The hysteretic losses in the stator also have a strong dependence on speed like those in the rotor, except with a slight dependence on torque as well. Higher torque implies larger magnetic fields, which for sufficiently large frequency, encloses an non-negligible area of the hysteresis curve. This justifies the use of operating point-dependent Bertotti hysteresis coefficients.

The hysteretic losses were calculated as a part of a software package that takes the magnetic field waveform at every finite element and identifies periodic loops in the waveform to map them to hysteresis curves based on the material's anhysteretic curve. That way the software captures the losses in the minor loops of the hysteresis curve per finite element with the so-called DC offset. In this case the DC offset entails the magnitude of the fundamental waveform, since the higher frequency components ride atop that fundamental and are of much higher frequency. This waveform-based hysteresis model is therefore independent of the Bertotti hysteresis model. This independence validates the comparisons and modifications to the Bertotti model as shown in equation (3.5.9).

Figure 5.12 reinforces the dominance of eddy losses in the iron over all operating points. The rotor eddy current losses are in the order of the stator hysteresis losses, as is the stator eddy loss difference due to interleaving. This means that interleaving mostly induces additional eddy current losses in the stator iron. In the rotor where the interleaving eddy loss difference makes about 20% of the losses (see Figure 5.12(e)), one can roughly neglect converter effects in Figure 5.12(c) to infer a stronger dependency on torque than hysteresis loss. This is due to eddy loss' square proportionality not only to frequency, but to magnetic field amplitude.

(a) Rotor, $\theta_I = 90°$

(b) Stator, $\theta_I = 90°$

(c) Rotor, $\theta_I = 0°$

(d) Stator, $\theta_I = 0°$

(e) Rotor, $P_\mathrm{H}(90°) - P_\mathrm{H}(0°)$

(f) Stator, $P_\mathrm{H}(90°) - P_\mathrm{H}(0°)$
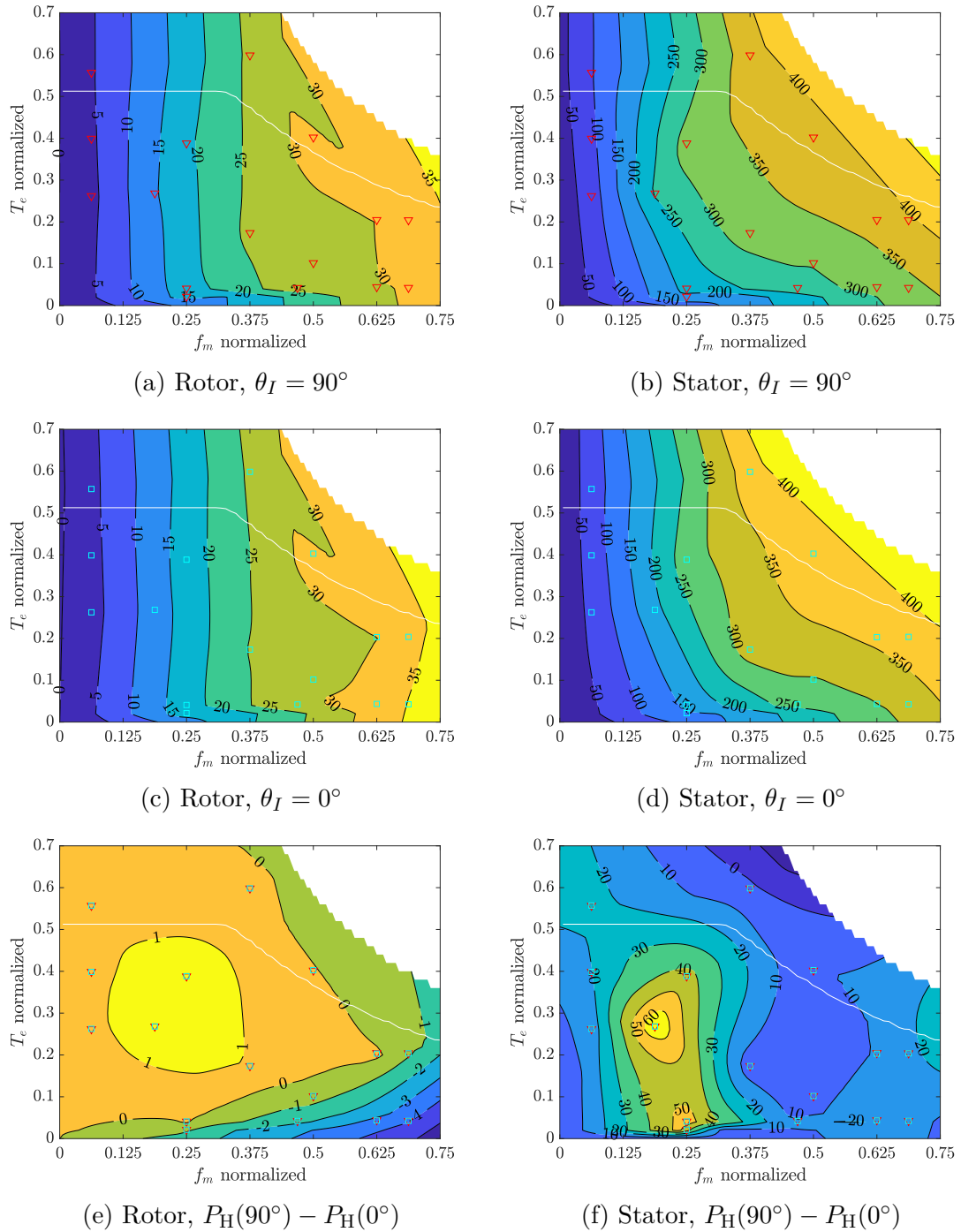
Figure 5.11: Hysteretic losses in W in the asymmetric machine for various operating points

Like hysteretic losses, the torque dependence implies a dependence on the magnetic field, which in turn implies a dependence on the current vector; that again justifies the use of the model in equation (3.5.9). Since the eddy losses in the stator nearly double upon interleaving, such a trend is not derivable from Figure 5.12(b) but is replicated slightly in Figure 5.12(d). More importantly, the near doubling of the eddy current losses in the stator for middle operating points upon interleaving renders the model in equation (3.5.9) moot when modeling high frequency eddy losses.

As already stated, the eddy current losses in iron are calculated based on a finite element treatment of the eddy currents considering the thickness of the lamina without the reaction field. The inclusion of the reaction field simply means that instead of just using Faraday's law of induction, the calculation includes Ampère's law, which couples the magnetic field back to the electric field via Ohm's law. This coupling models the proximity and skin effects and automatically includes the changing eddy loss dependency on frequency from a squared proportionality to one to the power of $3/2$. The calculation also takes into account the spatially and time-varying magnetic permeability in the iron, which is necessary because of its inclusion in Ampère's law. This level of detail is unfortunately absent from the FEM post-processing package. Temperature dependencies of the iron conductivity are also not accounted. The software computes the eddy losses after computing the exciting field over all elements at all simulated times, precluding an exact power balance calculation. However, because the FEM simulation already calculates the quasi-magnetostatic magnetic potential, Faraday's law's inclusion at the end only couples to the high frequency components of the field, which do not interact with its torque-producing fundamental frequencies. That means that the energy injected by the converter at those frequencies are all converted to losses or spatially canceled. Since the power balance with electromagnetic fields involves volume-specific power, it is also important to account where the converter injects its high frequency energy. With interleaving, the converter injects the same energy into the machine as when not interleaving, except that by virtue of the time delay involved and the coupled winding distribution in the asymmetrical machine ($\alpha = 30°$ spatial dual separation, or one tooth separation), that energy produces a high-frequency magnetic field, which in turn induces additional losses in the machine. This discussion depends on the spatial distribution of the high frequency components, which necessitates the analysis of the power distribution in the machine. Figures 5.15 to 5.21 show the power loss density difference between interleaving on and off.

It suffices to say that the hysteretic and eddy losses in the polar machine shown in Figures 5.13 and 5.14 follow the same trends as with the asymmetric machine, except that the polar machine has more iron losses with $\theta_I = 0°$, but less losses with $\theta_I = 90°$ compared to the asymmetric machine. The polar machine has more hysteresis losses, but less eddy current losses than the asymmetric machine with both interleaving angles. Like for the asymmetric machine, iron losses in the stator dominate. Lastly, the hysteresis loss difference between engaged and disengaged interleaving stays under 10 W in the stator, a hardly remarkable amount; the eddy current loss difference in the stator for the polar machine is as much as the hysteresis loss difference in the stator for the asymmetric machine. Combined, one arrives again at the dominance of the eddy loss in the asymmetric machine's stator, suggesting again that the dual coupling in the asymmetric machine plays the key role.

(a) Rotor, $\theta_I = 90°$

(b) Stator, $\theta_I = 90°$

(c) Rotor, $\theta_I = 0°$

(d) Stator, $\theta_I = 0°$

(e) Rotor, $P_{\mathrm{E}}(90°) - P_{\mathrm{E}}(0°)$

(f) Stator, $P_{\mathrm{E}}(90°) - P_{\mathrm{E}}(0°)$
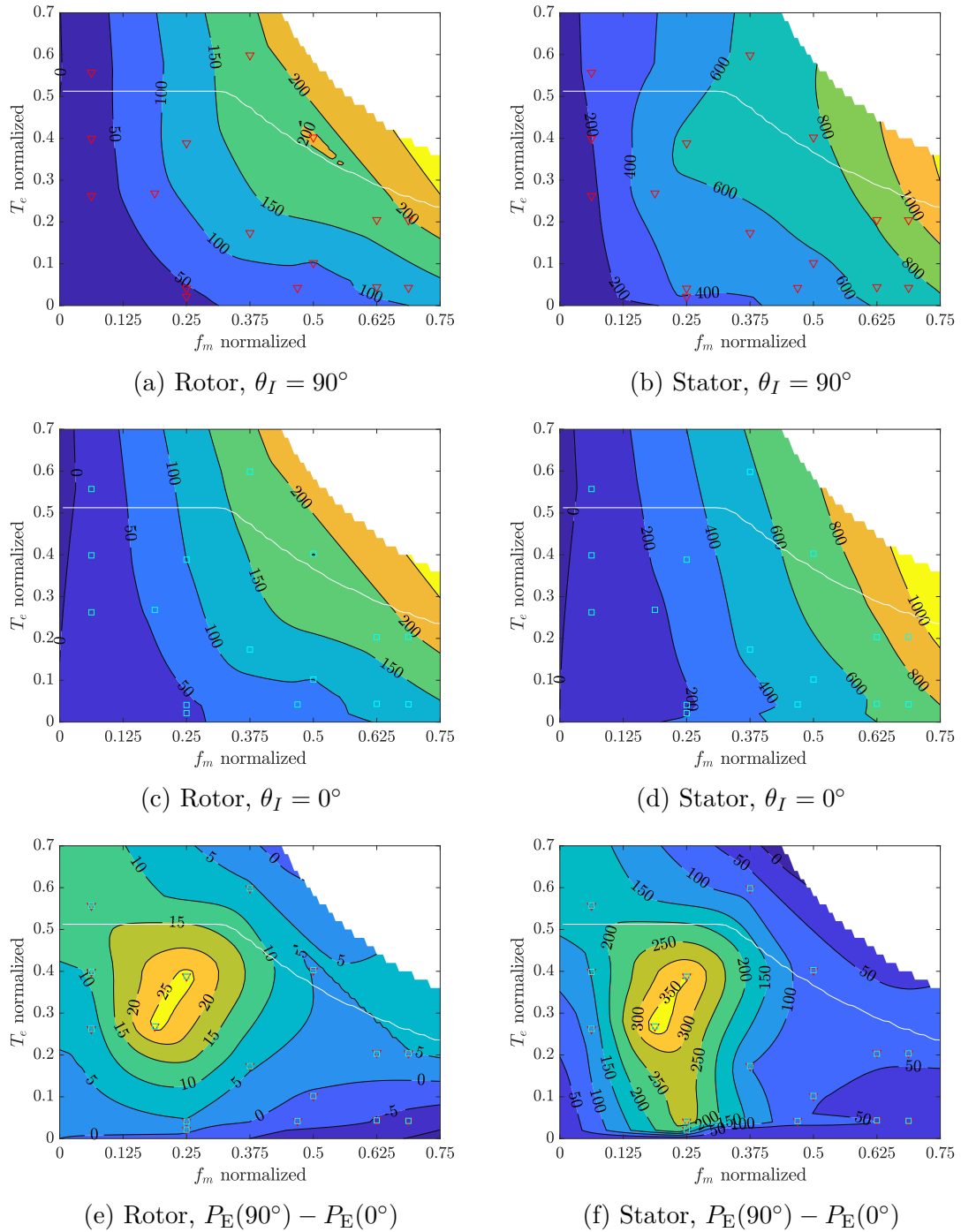
Figure 5.12: Eddy losses in W in the asymmetric machine for various operating points
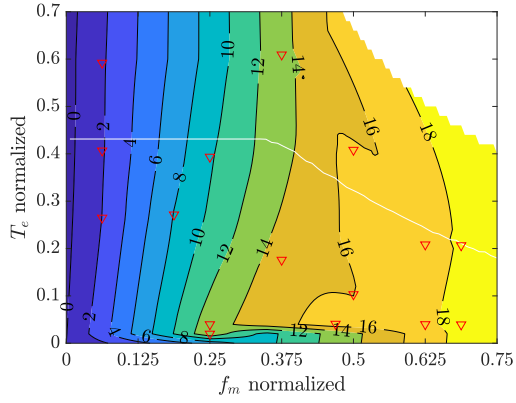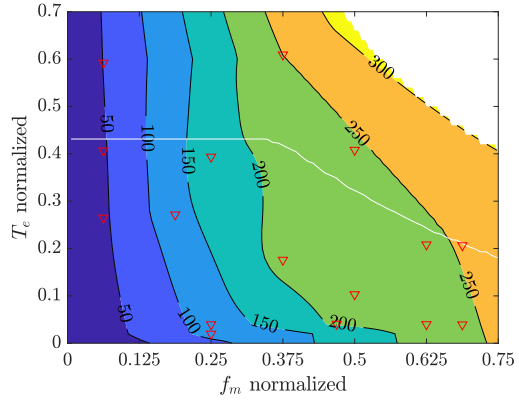
(a) Rotor, $\theta_I = 90°$

(b) Stator, $\theta_I = 90°$
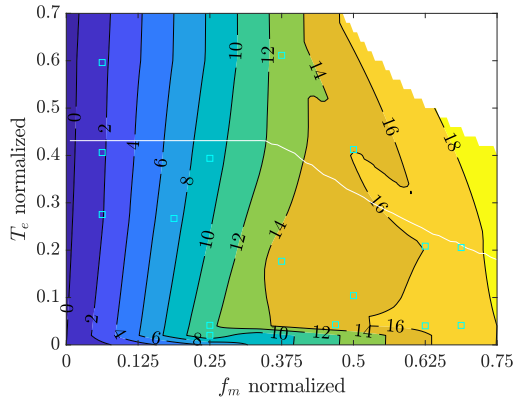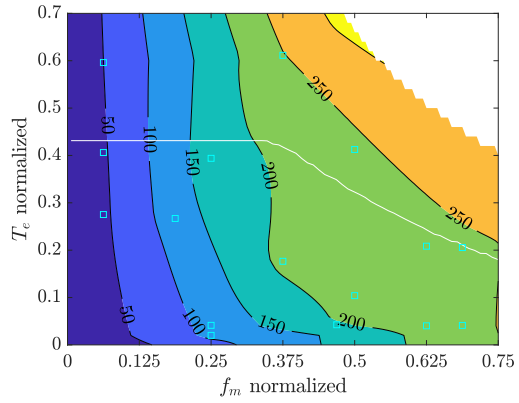
(c) Rotor, $\theta_I = 0°$

(d) Stator, $\theta_I = 0°$
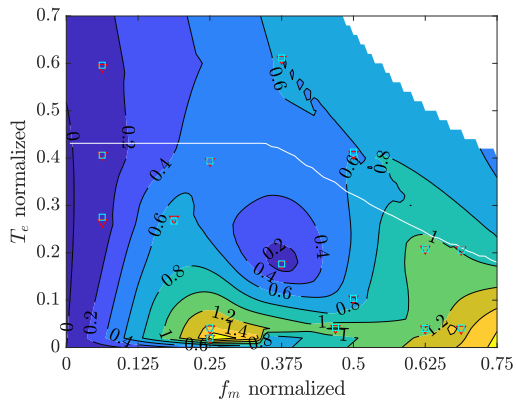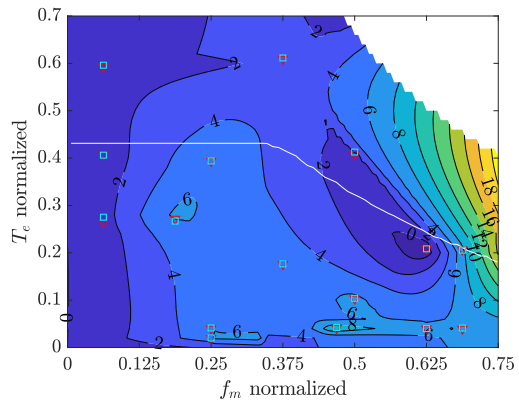
(e) Rotor, $P_{\mathrm{H}}(90°) - P_{\mathrm{H}}(0°)$

(f) Stator, $P_{\mathrm{H}}(90°) - P_{\mathrm{H}}(0°)$

Figure 5.13: Hysteretic losses in W in the polar machine for various operating points

(a) Rotor, $\theta_I = 90°$

(b) Stator, $\theta_I = 90°$

(c) Rotor, $\theta_I = 0°$

(d) Stator, $\theta_I = 0°$

(e) Rotor, $P_E(90°) - P_E(0°)$

(f) Stator, $P_E(90°) - P_E(0°)$
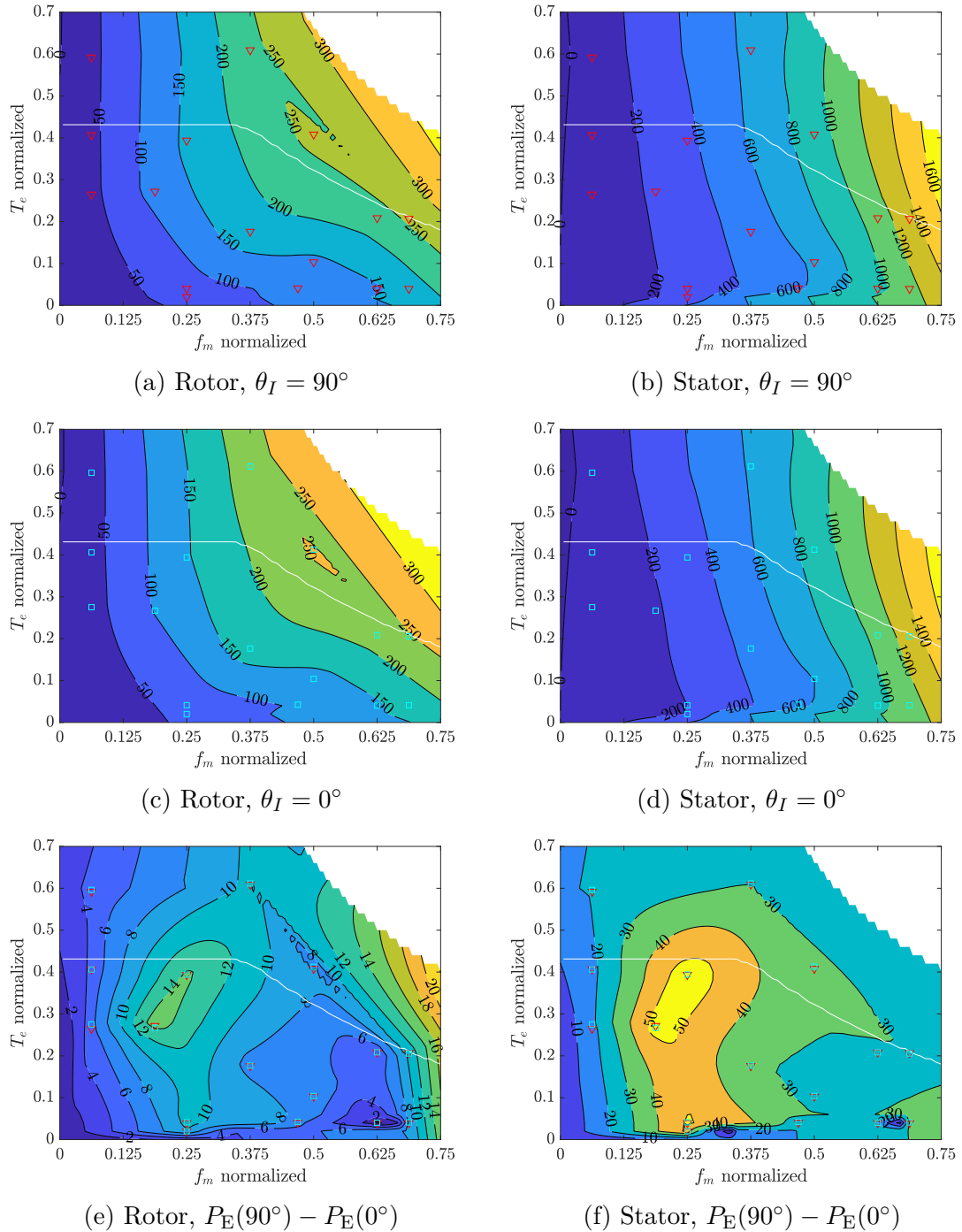
Figure 5.14: Eddy losses in W in the polar machine for various operating points

(a) 0.26 norm. moment, 0.0625 norm. mechanical speed

(b) 0.4 norm. moment, 0.0625 norm. mechanical speed

(c) 0.56 norm. moment, 0.0625 norm. mechanical speed

(d) 0.26 norm. moment, 0.1875 norm. mechanical speed

(e) 0.02 norm. moment, 0.25 norm. mechanical speed

(f) 0.04 norm. moment, 0.25 norm. mechanical speed
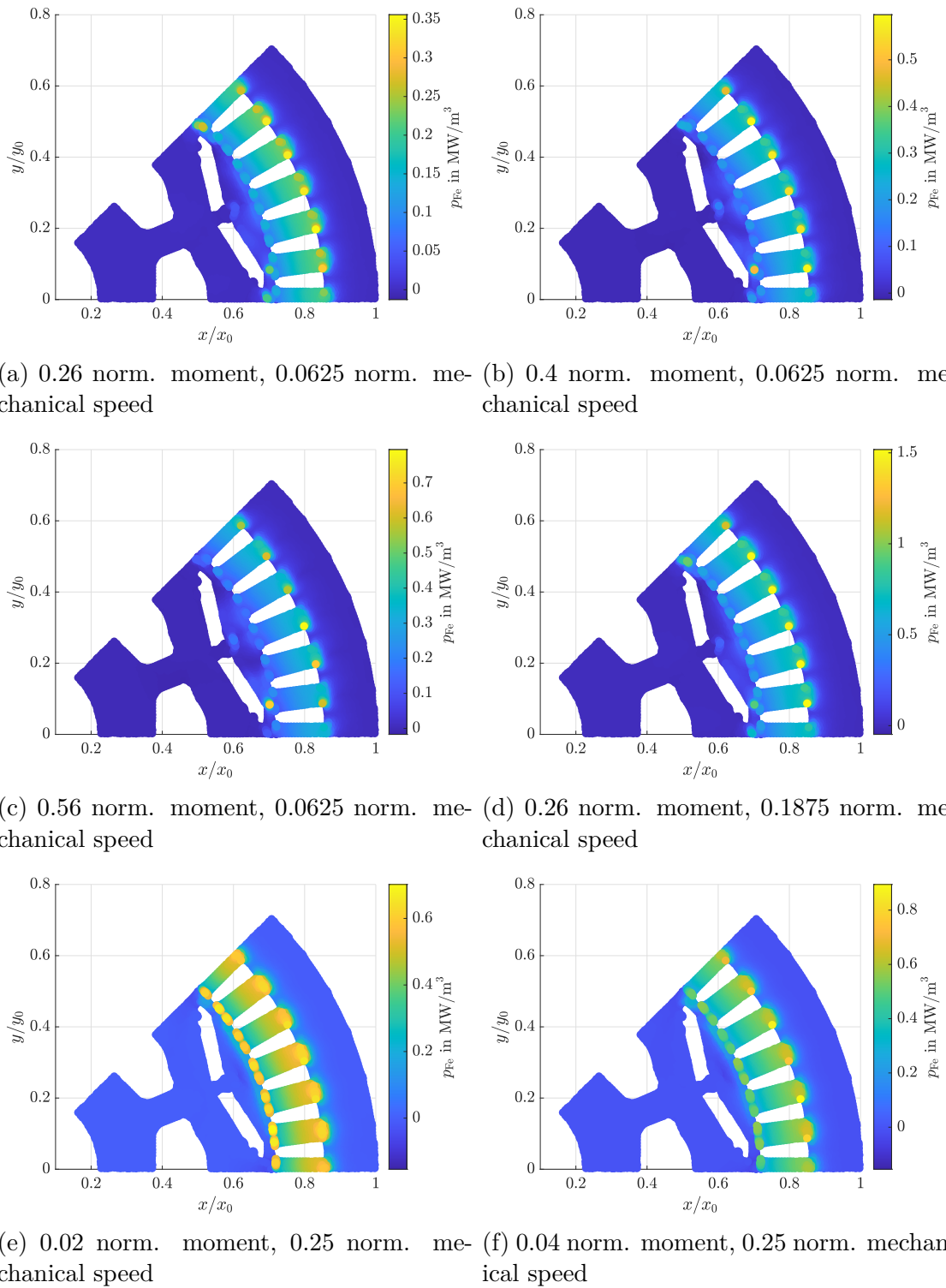
Figure 5.15: Asymmetric machine iron loss density difference, $p_{\mathrm{Fe}}(90°) - p_{\mathrm{Fe}}(0°)$, for various operating points
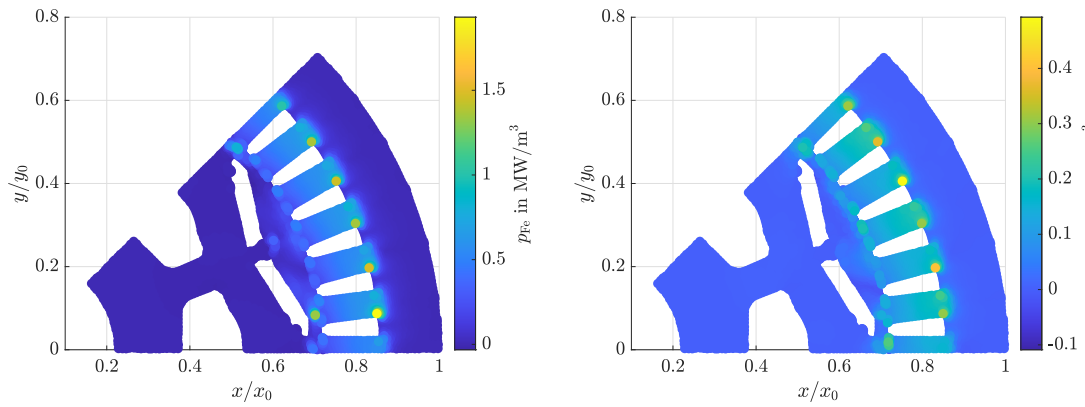
(a) 0.38 norm. moment, 0.25 norm. mechanical speed

(b) 0.18 norm. moment, 0.375 norm. mechanical speed
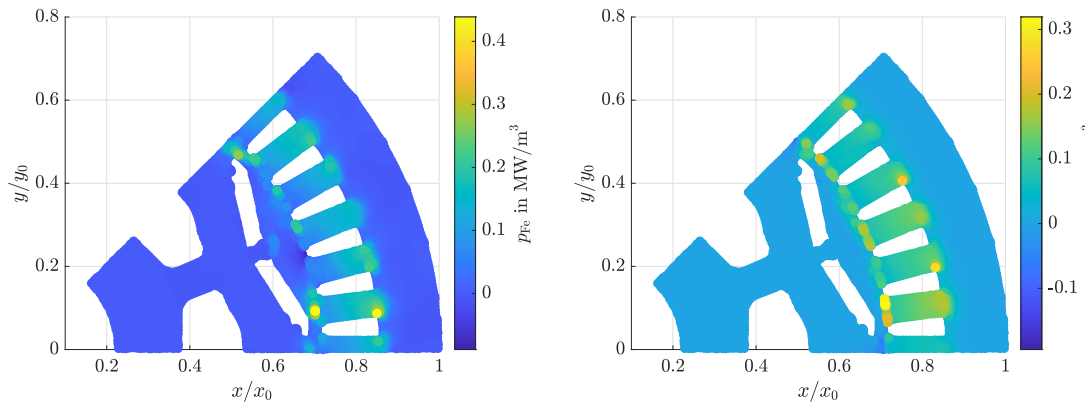
(c) 0.6 norm. moment, 0.375 norm. mechanical speed

(d) 0.04 norm. moment, 0.46875 norm. mechanical speed
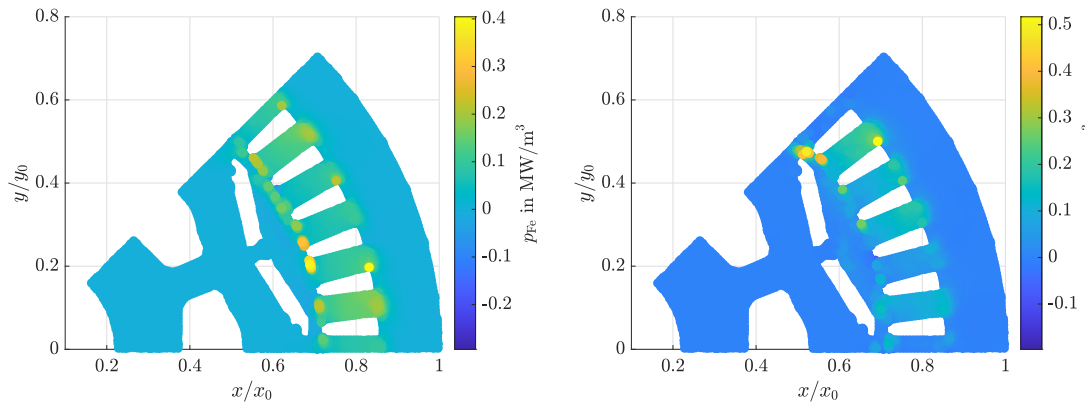
(e) 0.1 norm. moment, 0.5 norm. mechanical speed

(f) 0.4 norm. moment, 0.5 norm. mechanical speed

Figure 5.16: Asymmetric machine iron loss density difference, $p_{\text{Fe}}(90°) - p_{\text{Fe}}(0°)$, for various operating points
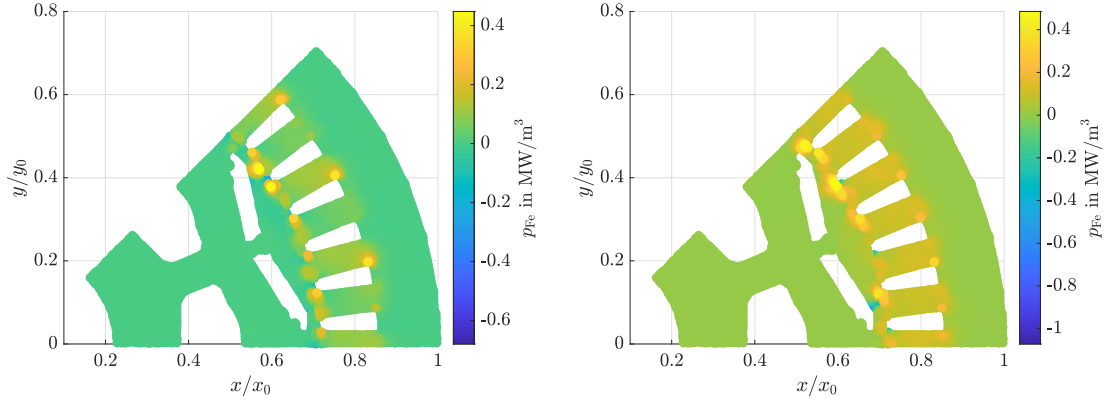
(a) 0.04 norm. moment, 0.625 norm. mechanical speed

(b) 0.2 norm. moment, 0.625 norm. mechanical speed
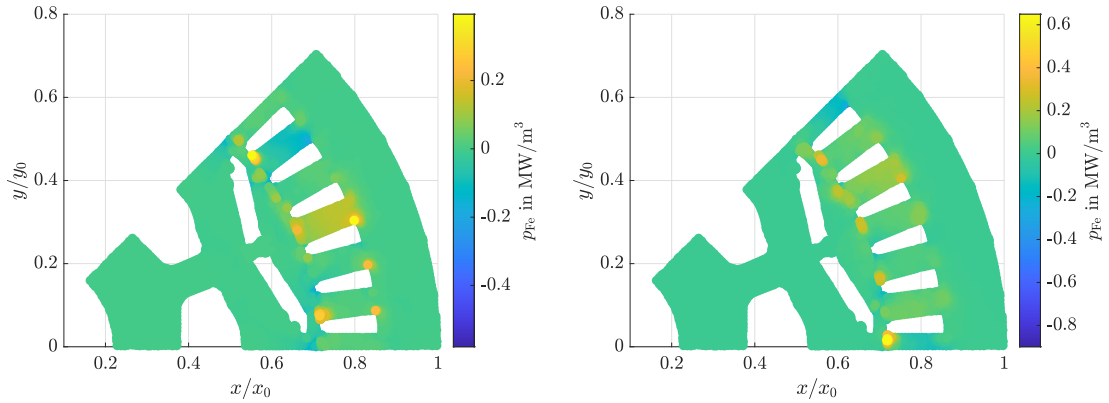
(c) 0.04 norm. moment, 0.6875 norm. mechanical speed

(d) 0.2 norm. moment, 0.6875 norm. mechanical speed

Figure 5.17: Asymmetric machine iron loss density difference, $p_{\mathrm{Fe}}(90°) - p_{\mathrm{Fe}}(0°)$, for various operating points

Figures 5.15 to 5.17 show the asymmetric machine's volume-specific iron loss distribution in both the stator and rotor. From them and Figure 5.21(a), the reader may infer that most of the loss difference concentrates in the stator teeth between engaged and disengaged interleaving. In order to understand why, it is important to juxtapose the asymmetric machine's iron loss distributions for different operating points with those of the polar machine in Figures 5.18 to 5.20 and Figure 5.21(b). The polar machine continues to have the most loss difference in the stator teeth, but over fewer teeth than the asymmetric machine. The teeth with the most loss difference seem to be concentrated in the first and third quadrants over all operating points. It turns out that those quadrants have teeth separating the two duals. Going back to the asymmetric machine, all teeth separate the duals. We can therefore infer that the inductive coupling between the duals concentrates in the iron tooth between them, thus inducing more losses there.

(a) 0.26 norm. moment, 0.0625 norm. mechanical speed

(b) 0.4 norm. moment, 0.0625 norm. mechanical speed

(c) 0.56 norm. moment, 0.0625 norm. mechanical speed

(d) 0.26 norm. moment, 0.1875 norm. mechanical speed

(e) 0.02 norm. moment, 0.25 norm. mechanical speed

(f) 0.04 norm. moment, 0.25 norm. mechanical speed
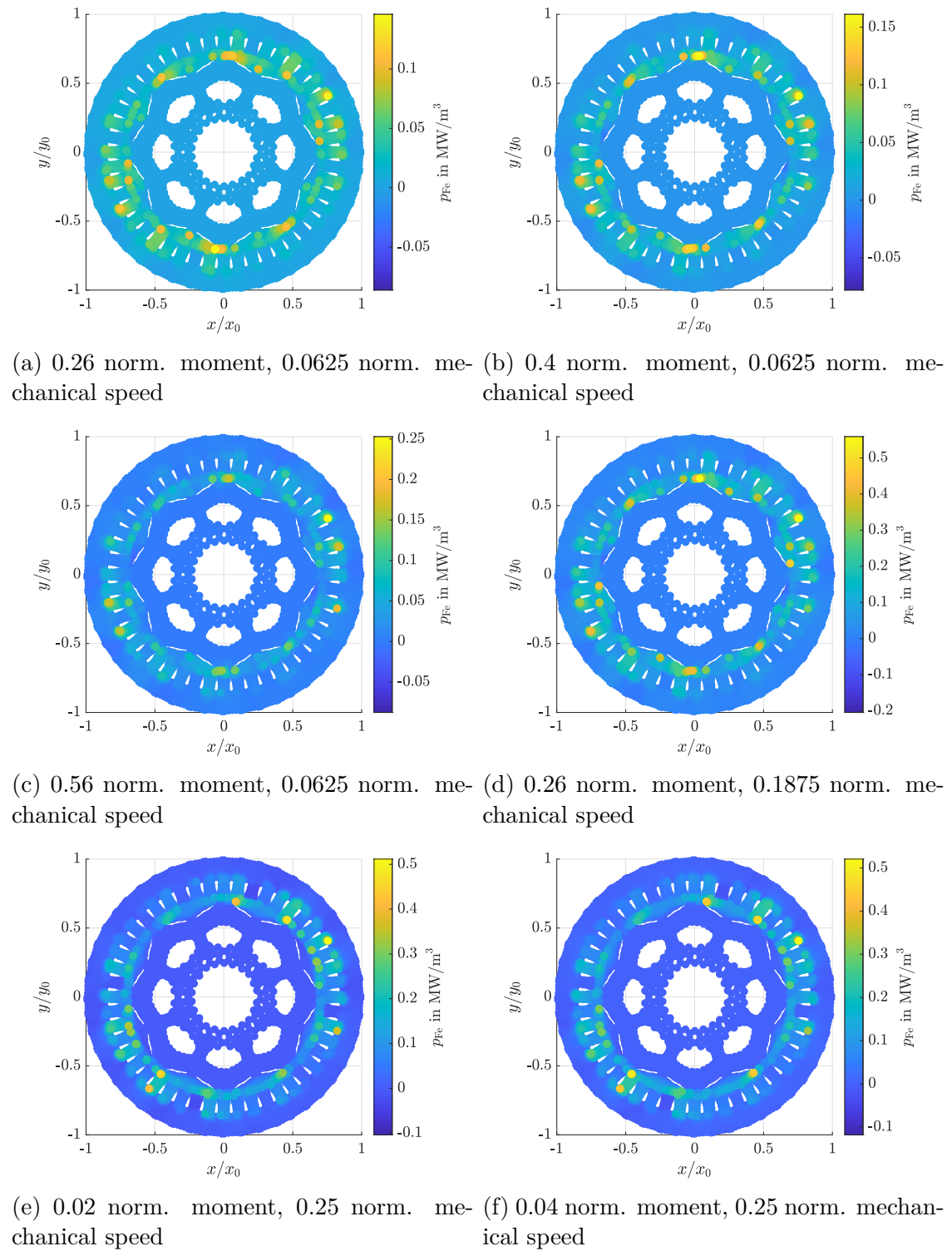
Figure 5.18: Polar machine iron loss density difference, $p_{\mathrm{Fe}}(90°) - p_{\mathrm{Fe}}(0°)$, for various operating points
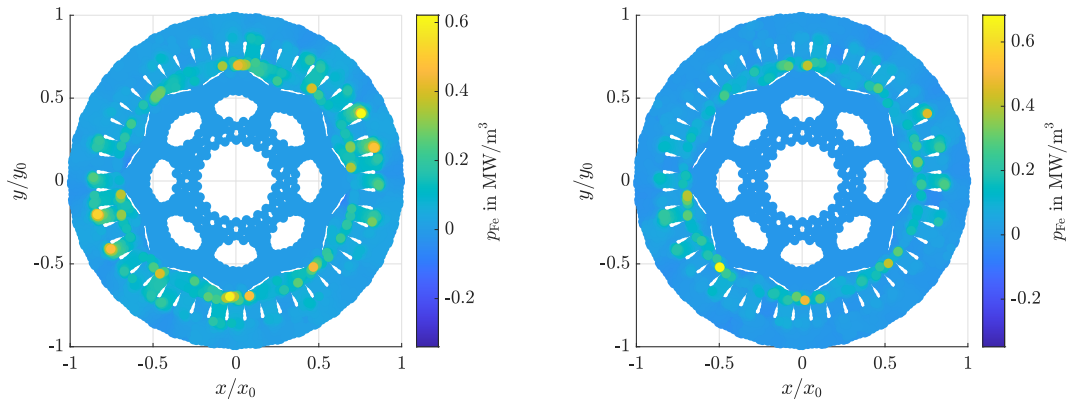
(a) 0.38 norm. moment, 0.25 norm. mechanical speed

(b) 0.18 norm. moment, 0.375 norm. mechanical speed
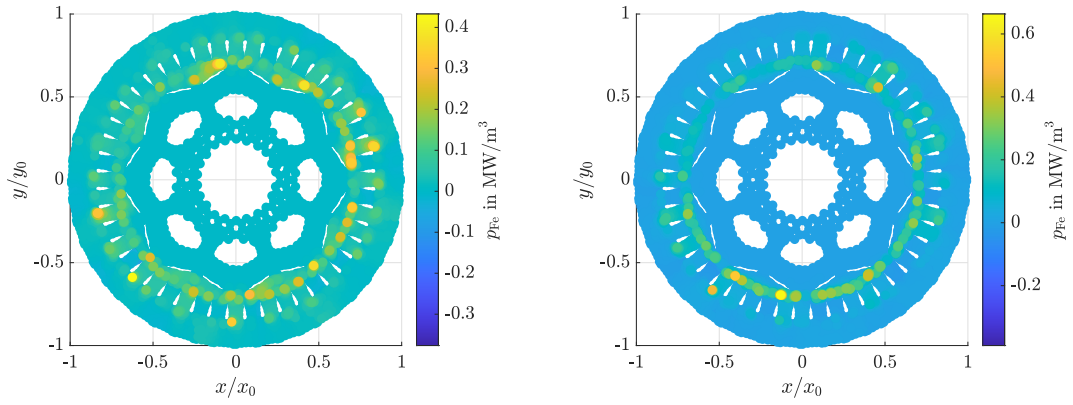
(c) 0.6 norm. moment, 0.375 norm. mechanical speed

(d) 0.04 norm. moment, 0.46875 norm. mechanical speed
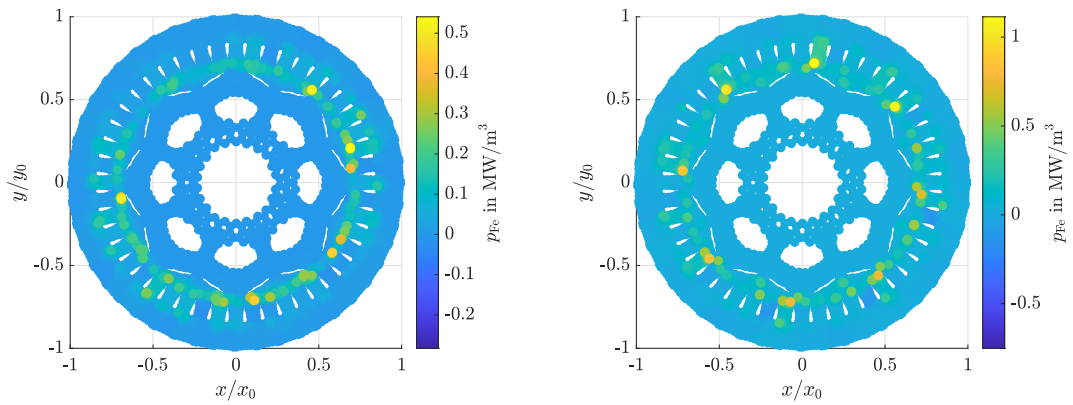
(e) 0.1 norm. moment, 0.5 norm. mechanical speed

(f) 0.4 norm. moment, 0.5 norm. mechanical speed

Figure 5.19: Polar machine iron loss density difference, $p_{\mathrm{Fe}}(90°) - p_{\mathrm{Fe}}(0°)$, for various operating points
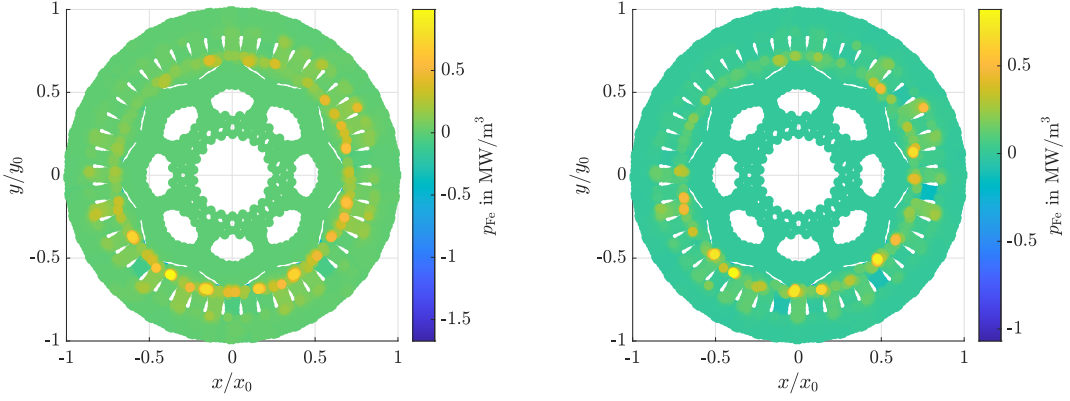
(a) 0.04 norm. moment, 0.625 norm. mechanical speed

(b) 0.2 norm. moment, 0.625 norm. mechanical speed
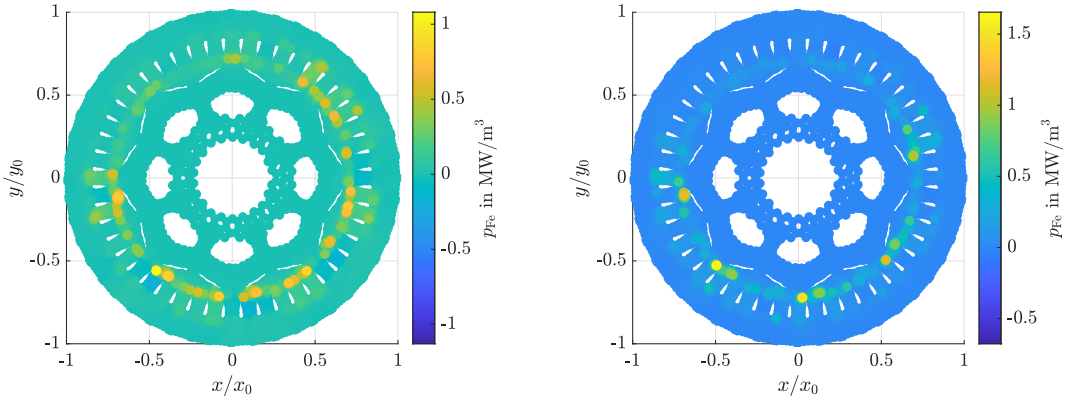
(c) 0.04 norm. moment, 0.6875 norm. mechanical speed

(d) 0.2 norm. moment, 0.6875 norm. mechanical speed

Figure 5.20: Polar machine iron loss density difference, $p_{\text{Fe}}(90°) - p_{\text{Fe}}(0°)$, for various operating points

The total iron losses are shown for both the asymmetric and polar machines in Figures 5.22 and 5.23 respectively. The contrast between Figure 5.22(a) and (b) is remarkable: the typical iron loss trend that follows slightly curved contours increasing with speed breaks upon interleaving. In contrast, Figure 5.23 does not noticeably change. Figure 5.24(b) shows the iron loss difference between interleaving on and off, which is about an order of magnitude less than the difference for the asymmetric machine shown in Figure 5.24(a). As stated before, eddy losses increase the most upon interleaving in both machines. However, due to the higher degree of localized inductive coupling in the asymmetric machine, eddy losses increase much more there than in the polar machine. From a torque-speed map perspective, the losses seem to localize near $f_m = 0.25$ and $T_e = 0.3$ for both machines. Indeed, the distribution of losses across the torque-speed map cannot be explained by the localized loss model alone.

(a) Asymmetric machine
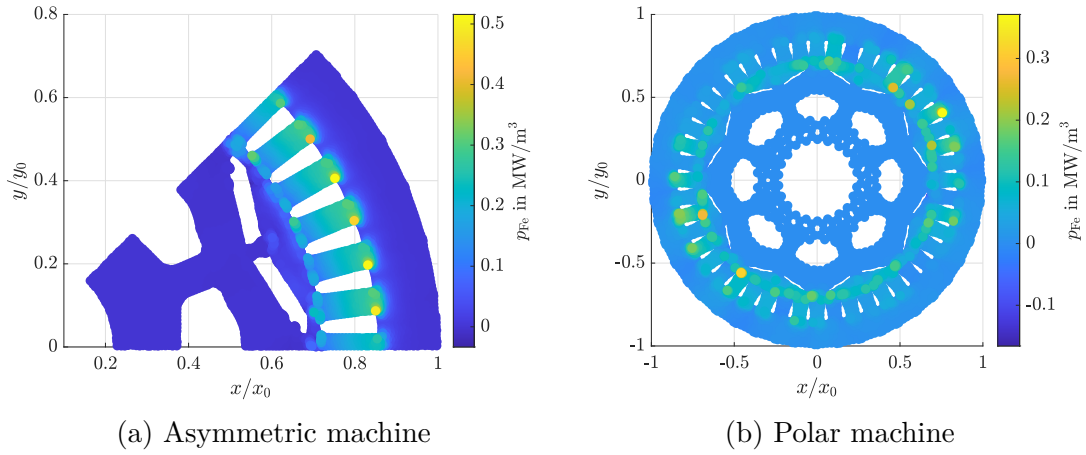
(b) Polar machine

Figure 5.21: Mean iron loss distribution difference, $p_{\text{Fe}}(90°) - p_{\text{Fe}}(0°)$, over all operating points

(a) Interleaving on, $\theta_I = 90°$

(b) Interleaving off, $\theta_I = 0°$
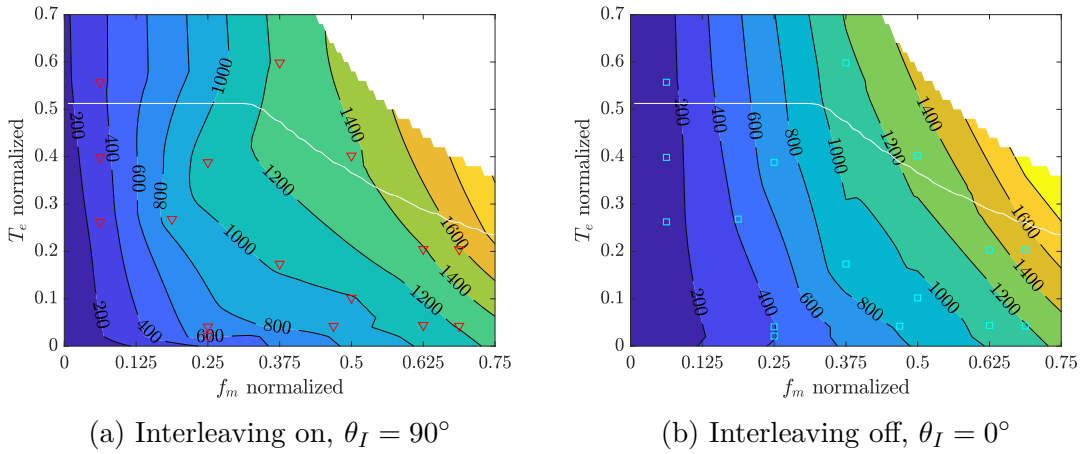
Figure 5.22: Iron losses for the asymmetric machine in W

(a) Interleaving on, $\theta_I = 90°$

(b) Interleaving off, $\theta_I = 0°$
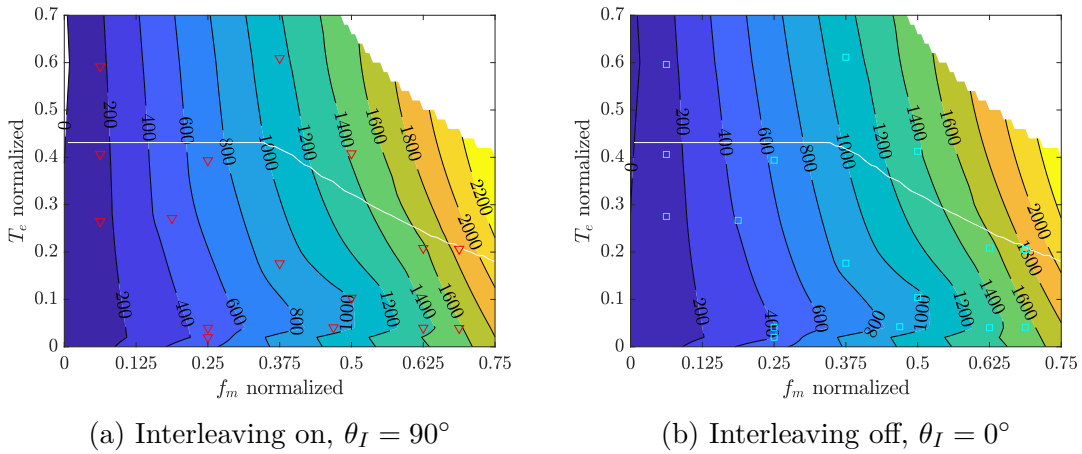
Figure 5.23: Iron losses for the polar machine in W

(a) Asymmetric machine
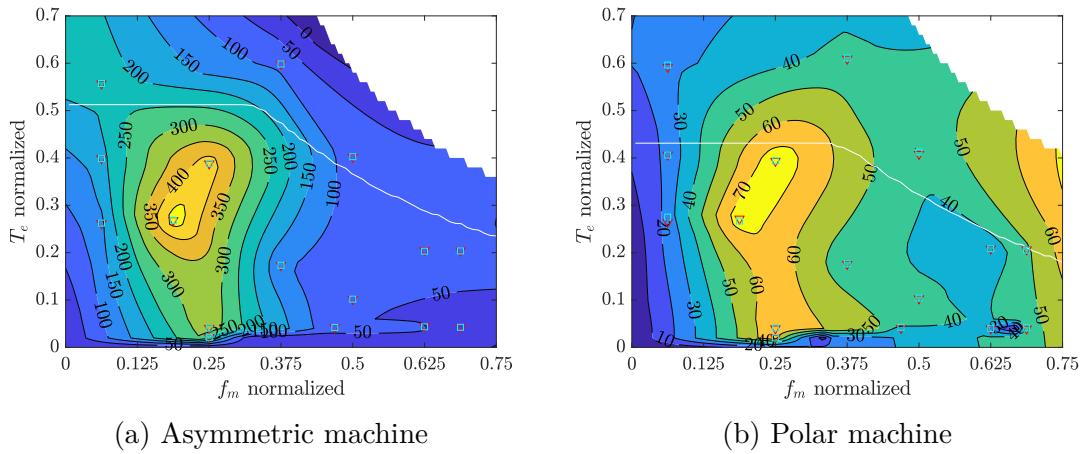
(b) Polar machine

Figure 5.24: Iron loss difference, $P_{\mathrm{Fe}}(90°) - P_{\mathrm{Fe}}(0°)$ in W

(a) Interleaving on, $\theta_I = 90°$

(b) Interleaving off, $\theta_I = 0°$
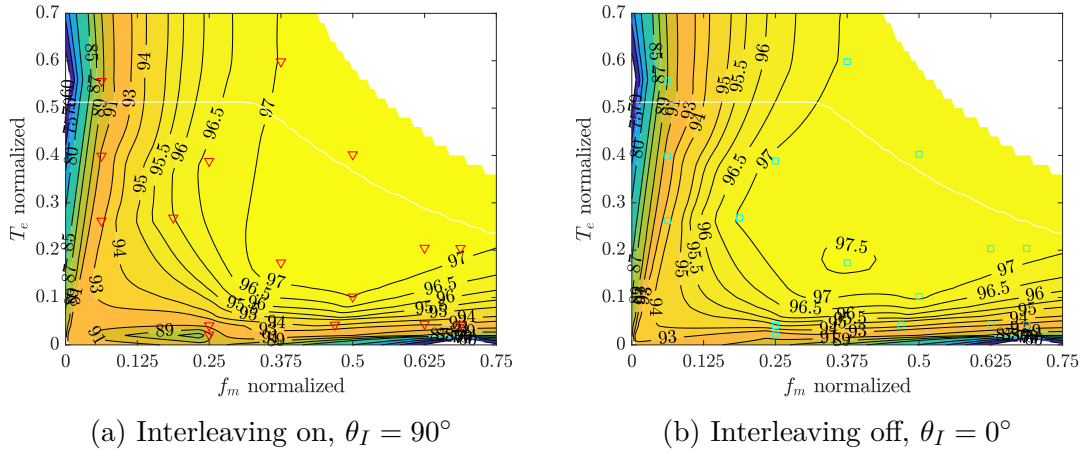
Figure 5.25: Efficiency for the asymmetric machine in %

(a) Interleaving on, $\theta_I = 90°$

(b) Interleaving off, $\theta_I = 0°$
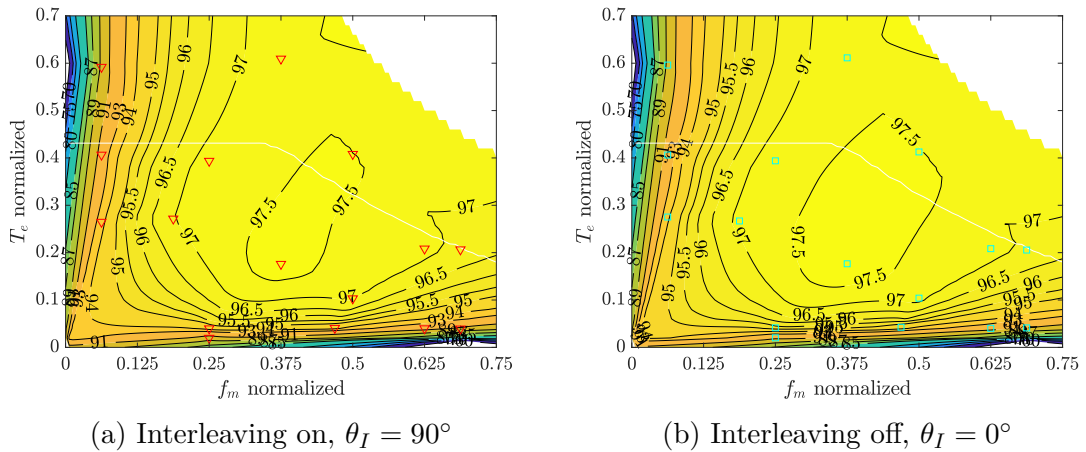
Figure 5.26: Efficiency for the polar machine in %

The loss distribution in Figures 5.22 and 5.23 are incorporated into the typical efficiency contours for an IPMSM in Figures 5.25 and 5.26. The efficiency difference is more noticeable on both machines over both contours, but how the differences are distributed across the torque-speed map become much clearer in Figure 5.27. The efficiency decrease in the polar machine remains below about 1% in lower load areas; in larger load areas, it does not exceed 0.1%. That number increases for the asymmetric machine for larger loads to 1%, and to 3% for smaller loads.

(a) Asymmetric machine

(b) Polar machine
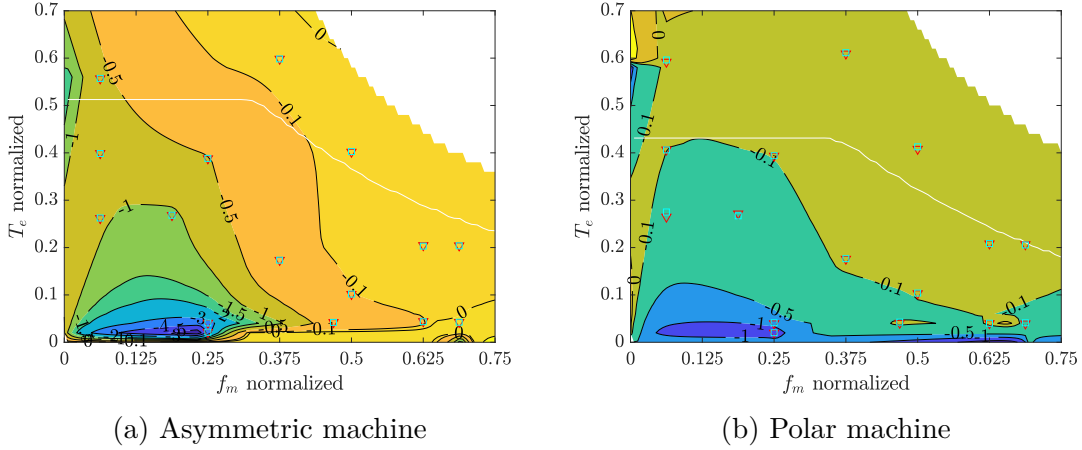
Figure 5.27: Efficiency difference, $\eta(90°) - \eta(0°)$ in %

Since interleaving causes significant additional iron losses in the asymmetric machine, and because simulating the μs time steps requires lots of computation time and capability, a simplified model incorporating the source of interleaving, i.e. the inverter, would accelerate the analysis over the entire torque-speed map. As delineated in [132], the high-frequency components of the current function as the boundary conditions to the magnetic field in the iron lamina, which in turn induce the lossy eddy currents in the stator teeth. An approximation of the losses in laminated rectangular cores appears in [116], which is modified here to consider the phases from the duals functioning as boundary conditions. Equation (5.1.1) describes the eddy current power for the Fourier-transformed high-frequency current density difference between phases surrounding a stator tooth lamina, where ℓ is the thickness of the lamina, w is the lamina width, h is the length of the tooth, n_l is the number of laminae, ω_j is the jth angular frequency, μ is the permeability of the iron, σ is the iron conductivity, and $J_{0,i,j}$ is the jth Fourier coefficient of the ith phase pair current density enclosing a stator tooth.

$$P_{\text{E}} \approx \frac{n_l w \ell^2 h}{2} \sum_{j}^{\infty} \sum_{i \in I} J_{0,i,j} \bar{J}_{0,i,j} \sqrt{\frac{\mu \omega_j}{2\sigma}} \tag{5.1.1}$$

The set of boundary phase pairs $\mathfrak{I}$ is determined by Figure 5.1 for the asymmetric machine and Figure 5.2 for the polar machine. The unique boundary conditions on the stator teeth are shown in Table I and II, where the operator Δ indicates taking the high frequency components greater than the switching frequency, f_{sw}, of the quantity. For example, Δi signifies the current ripple, whereas $\Delta \Delta i_{\mathfrak{I}}$ signifies the difference between two current ripples in the set of boundary phase pair indexes. The current density $J_{0,i,j} = (\Delta \Delta i)_{i,j}/A$, where A is the active area of the phase.

TABLE I: Asymmetric Machine Unique Boundary Conditions on Stator Teeth

$\mathfrak{I}$, Diff. Duals	$\Delta\Delta i_{\mathfrak{I}}$
U_2^+, U_1^+	$\Delta i_{U_2} - \Delta i_{U_1}$
U_1^+, W_2^-	$\Delta i_{U_1} + \Delta i_{W_2}$
W_2^-, W_1^-	$-\Delta i_{W_2} + \Delta i_{W_1}$
W_1^-, V_2^+	$-\Delta i_{W_1} - \Delta i_{V_2}$
V_2^+, V_1^-	$\Delta i_{V_2} + \Delta i_{V_1}$
V_1^-, U_2^-	$-\Delta i_{V_1} + \Delta i_{U_2}$

TABLE II: Polar Machine Unique Boundary Conditions on Stator Teeth

$\mathfrak{I}$, Diff. Duals	$\Delta\Delta i_{\mathfrak{I}}$	I, Diff. Phases Only	$\Delta\Delta i_{\mathfrak{I}}$
V_2^-, U_1^+	$-\Delta i_{V_2} - \Delta i_{U_1}$	U_2^+, W_2^-	$\Delta i_{U_2} + \Delta i_{W_2}$
U_1^+, W_2^-	$\Delta i_{U_1} + \Delta i_{W_2}$	W_2^-, V_2^+	$-\Delta i_{W_2} - \Delta i_{V_2}$
W_2^-, V_1^+	$-\Delta i_{W_2} - \Delta i_{V_1}$	V_1^+, U_1^-	$\Delta i_{V_1} + \Delta i_{U_1}$
V_1^-, U_2^+	$-\Delta i_{V_1} - \Delta i_{U_2}$	U_1^-, W_1^+	$-\Delta i_{U_1} - \Delta i_{W_1}$
U_2^+, W_1^-	$\Delta i_{U_2} + \Delta i_{W_1}$	W_1^+, V_1^-	$\Delta i_{W_1} + \Delta i_{V_1}$
W_1^-, V_2^-	$-\Delta i_{W_1} + \Delta i_{V_2}$	V_2^+, U_2^-	$\Delta i_{V_2} + \Delta i_{U_2}$
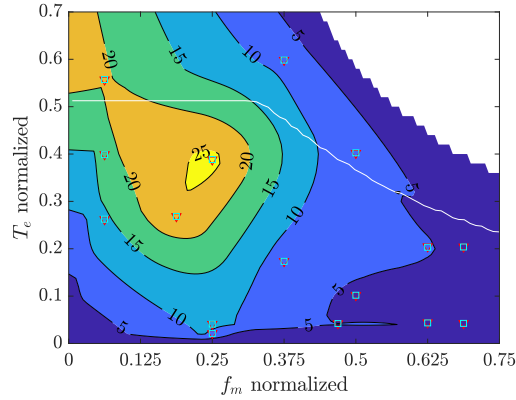
Figure 5.28: Asymmetric machine current ripple difference, $\Delta\Delta i_{\mathfrak{I}}(90°) - \Delta\Delta i_{\mathfrak{I}}(0°)$, for $f > f_{\text{sw}}$ in Ampères
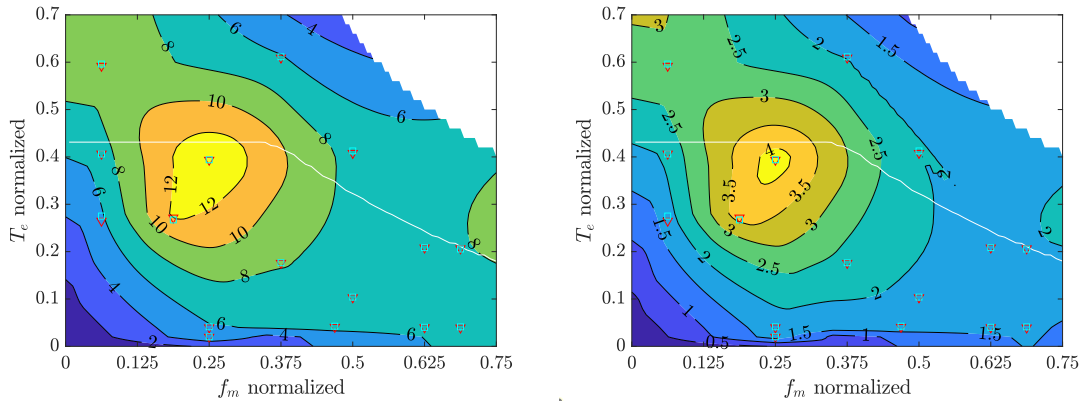
(a) Different duals one tooth apart

(b) Different phases one tooth apart

Figure 5.29: Polar machine current ripple difference, $\Delta\Delta i_{\mathfrak{I}}(90°) - \Delta\Delta i_{\mathfrak{I}}(0°)$, for $f > f_{\text{sw}}$ in Ampères

Figures 5.28 and 5.29 show correspondence with the eddy current loss differences in Figures 5.12 and 5.14. Furthermore, the current difference magnitude between different duals separated by one tooth (Figure 5.29(a)) is greater than the current difference magnitude between different phases belonging to the same dual separated by one tooth (Figure 5.29(b)). This confirms that the additional coupling between duals contributes the most to the iron loss increase upon interleaving, as the currents of the asymmetric machine in Figure 5.28 initially suggest. Only the polar machine's current coupling shown in Figure 5.29, however, could confirm that, since the machine contains different teeth separating duals and different phases, whereas the asymmetric machine only contains teeth separating both duals and different phases simultaneously. Dividing the current differences by the active area and performing a Fourier transform yields the $J_{0,i,j}$ boundaries in equation (5.1.1), resulting in Figure 5.30. After inspecting Figure 5.30, which just considers the eddy current loss in the stator teeth, it is evident that most of the losses are generated there in the form of eddy currents. Faraday's law with Ohm's law inspired this construction, as $\nabla \times \mathbf{J} = -\sigma \partial \mathbf{B}/\partial t$ in cylindrical coordinates for the radial magnetic field component results in

$$\frac{1}{r}\frac{\partial J_z}{\partial \theta} = -\sigma \frac{\partial B_r}{\partial t} \; . \tag{5.1.2}$$

(a) Asymmetric machine

(b) Polar machine
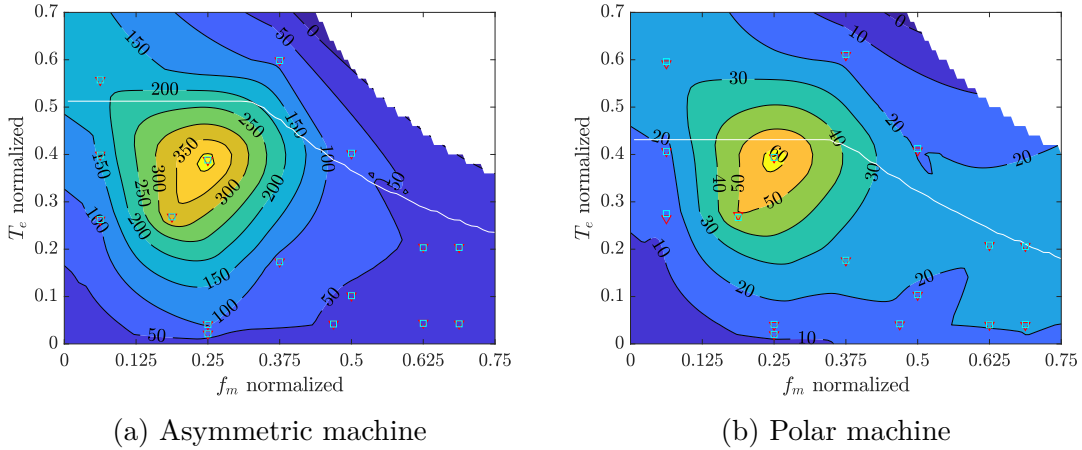
Figure 5.30: Eddy current iron loss approximate difference in the stator teeth, $P_{\mathrm{E}}(90°) - P_{\mathrm{E}}(0°)$, for $f > f_{\mathrm{sw}}$ in Watts

Equation (5.1.3) describes another high frequency iron loss model that does not need FEM simulations to approximate the eddy current losses based on equation (25) in [71].

$$P_{\mathrm{E}} = \frac{V}{\sigma \ell^2} \sum_{j=1}^{\infty} H_{0,j} \bar{H}_{0,j} \vartheta_j \frac{\sinh \vartheta_j - \sin \vartheta_j}{\cosh \vartheta_j + \cos \vartheta_j} \tag{5.1.3}$$

where

$$\vartheta_j = \ell \sqrt{\frac{\omega_j \mu \sigma}{2}} \; , \tag{5.1.4}$$

$H_0 = \hat{i}/(2\pi R/p + 2l)$, and V represents the volume of a section of the electrical steel core. R is the inner stator radius and l is the length of the machine. Since the

permeability of the iron changes with the operating point but the conductivity does not change much with temperature, knowing the permeability at each operating point is important. The model takes a bulk permeability for the stator based on material data and the flux magnitude ψ at every operating point. That method is used to generate the eddy current iron loss difference in Figure 5.31. For Figure 5.32, the flux is interpolated with the current magnitude as query points only along the $q-$axis at every operating point because the stator iron saturates largely irrespective of the current angle. There, the magnet losses are also extracted by using the same current magnitude-based permeability to build a magnetic circuit. Equation (17) in [71] is used to estimate the magnet losses using the postulated high-frequency flux path due only to interleaving starting at one stator tooth, bending to the yoke to the next tooth, crossing the airgap, going through some iron before crossing the magnet, flowing through iron again to lastly cross the airgap and end at the tooth at which the flux path started.

(a) $\Delta i(90°) - \Delta i(0°)$ (b) $P_{\mathrm{E}}(90°) - P_{\mathrm{E}}(0°)$
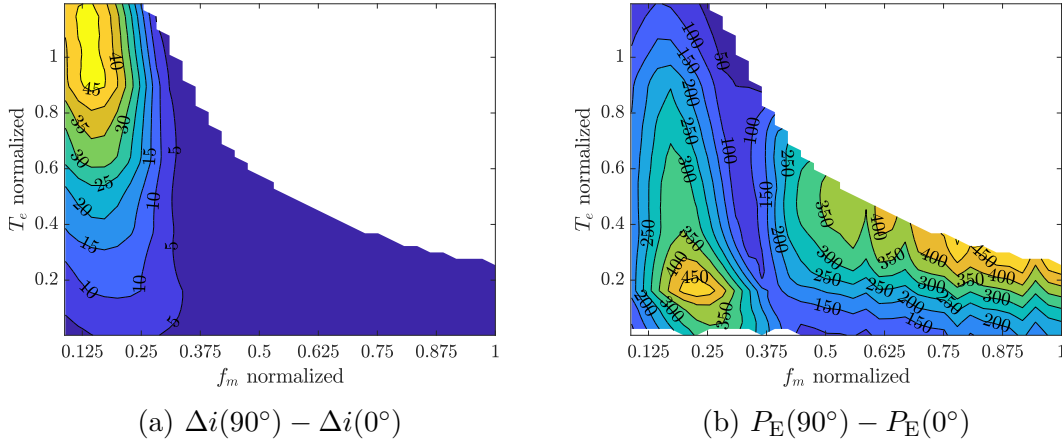
Figure 5.31: Current ripple difference and current ripple, coupling, and permeability-based eddy current loss model difference

(a) $P_{\mathrm{E,stator}}(90°) - P_{\mathrm{E,stator}}(0°)$

(b) $P_{\mathrm{mag}}(90°) - P_{\mathrm{mag}}(0°)$

(c) $P_{\mathrm{mag}}(90°) + P_{\mathrm{E,stator}}(90°) - P_{\mathrm{mag}}(0°) - P_{\mathrm{E,stator}}(0°)$
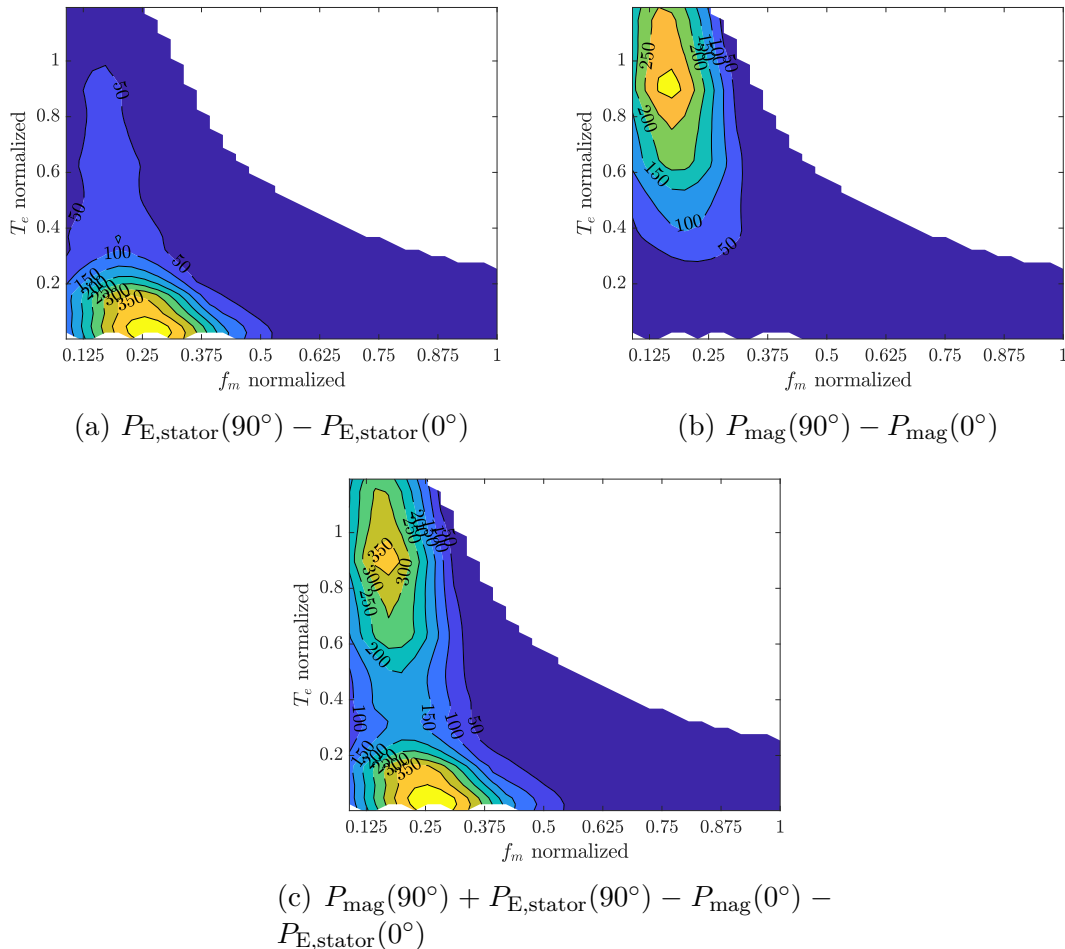
Figure 5.32: Current ripple, coupling, and current magnitude-interpolated permeability-based eddy current loss model difference and magnet losses based on magnetic circuit

5.1.3 Conduction Losses in the Permanent Magnets

The magnets in both the asymmetrical and polar machines were segmented insofar to allow skewing, but no additional segmentation was present. To clarify, the simulation did not simulate rotor skewing, as the computation time with the given resources would have been impractical. Instead, the model exploits the tangential and axial symmetries of the machine by simulating one pole and half of an axial segment [133]. Segmenting just for skewing might not sufficiently decrease the eddy current losses in the magnets due to switching in the inverter, as it sources the largest losses there for distributed windings and additional segmenting indeed reduces losses after a critical number of segments [112] [134]. This section shows the magnet losses for the asymmetrical machine at 325 V.

Due to the absence of the 5$^{\mathrm{th}}$ and 7$^{\mathrm{th}}$ harmonics in the polar machine, it is expected that the magnet losses due to the winding configuration are less than those in the asymmetrical machine. Slotting losses should stay relatively the same. Also, magnet losses are expected to increase with increasing DC-bus for the same machine, as the current ripple, and by extension the linkage flux ripple, increase with increasing DC-bus voltage. Lastly, hysteresis losses in the magnet, even with minor

loops, are negligible compared to its conduction losses. The tested points are shown in Figure 5.33. For each point, a 3D FEM simulation was done in JMAG for different
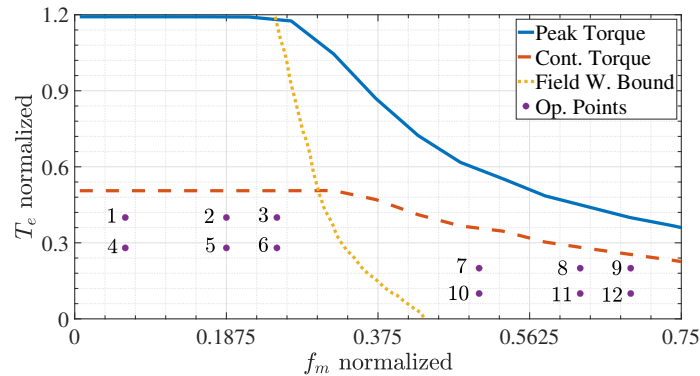
Figure 5.33: Simulated operating points

power sources. The power sources include a current source (CS), an analogue voltage source (VS), and inverter voltage-sourced with different PWM methods, as shown in Figure 5.34. The simulation using current sources does not model the magnet losses well; the analog voltage source captures some of the losses at higher speeds, but at all speeds, an inverter model is needed to ascertain the losses in the magnet, especially at low speeds when the losses in the magnet are almost exclusively due to inverter excitation.
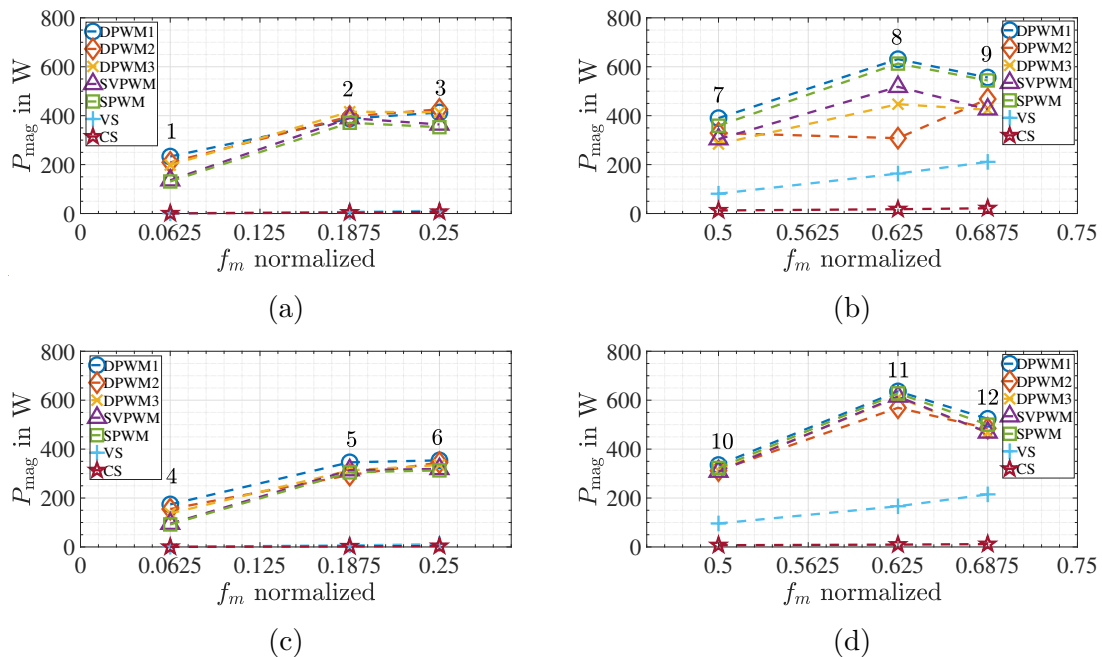
Figure 5.34: Magnet losses at different operating points for different power sources. Inverter voltage is switched at 10kHz.
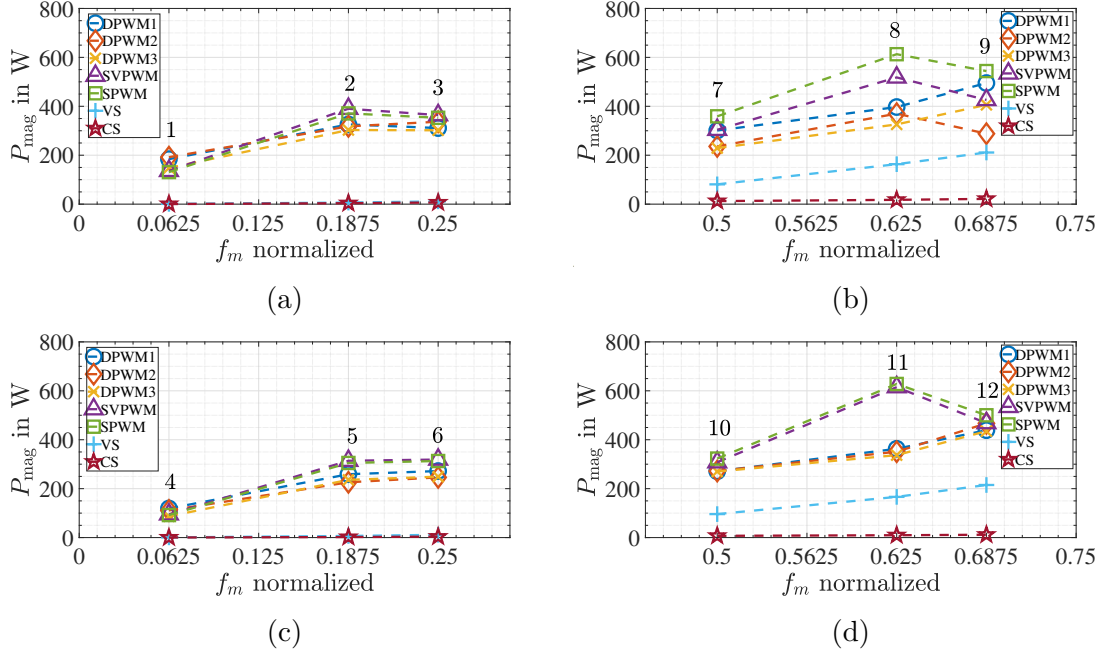
Figure 5.35: Magnet losses at different operating points for different power sources. Inverter voltage is switched at 15kHz when operated with DPWM.

The flux ripple as seen in the rotor frame due to inverter switching increases the losses significantly because of the magnet's large conducting mass and large voltage excitation and switching frequency. However, because the current ripple $\Delta i \propto 1/\omega$, where ω stands for the switching frequency, and the current density ripple in the magnet is roughly $J \propto \Delta i$, according to the thick plate, volume-specific power loss [71],

$$
\begin{aligned}
p_e &\approx \frac{J\bar{J}}{\ell}\sqrt{\frac{\omega\mu}{2\sigma}} \\
&\propto \frac{V_{\mathrm{DC}}^2}{\ell}\sqrt{\frac{\mu}{2\sigma\omega^3}}
\end{aligned}
\tag{5.1.5}
$$

where ℓ is the thickness of the plate, μ is the permeability of the magnet, σ is the conductivity of the magnet, and $\bar{J}$ indicates the complex conjugate of J. Ironically then, what generates the eddy currents in the magnets in the first place is the time-varying magnetic field linked across the air-gap, or Faraday's law applied on Ohm's law as $\nabla \times \mathbf{J} = -\sigma \partial \mathbf{B}/\partial t$, also dampens the power losses as the time-variation, or angular frequency ω, increases.

(a) Operating point 10

(b) Operating point 7

(c) Operating point 11

(d) Operating point 8

(e) Operating point 12
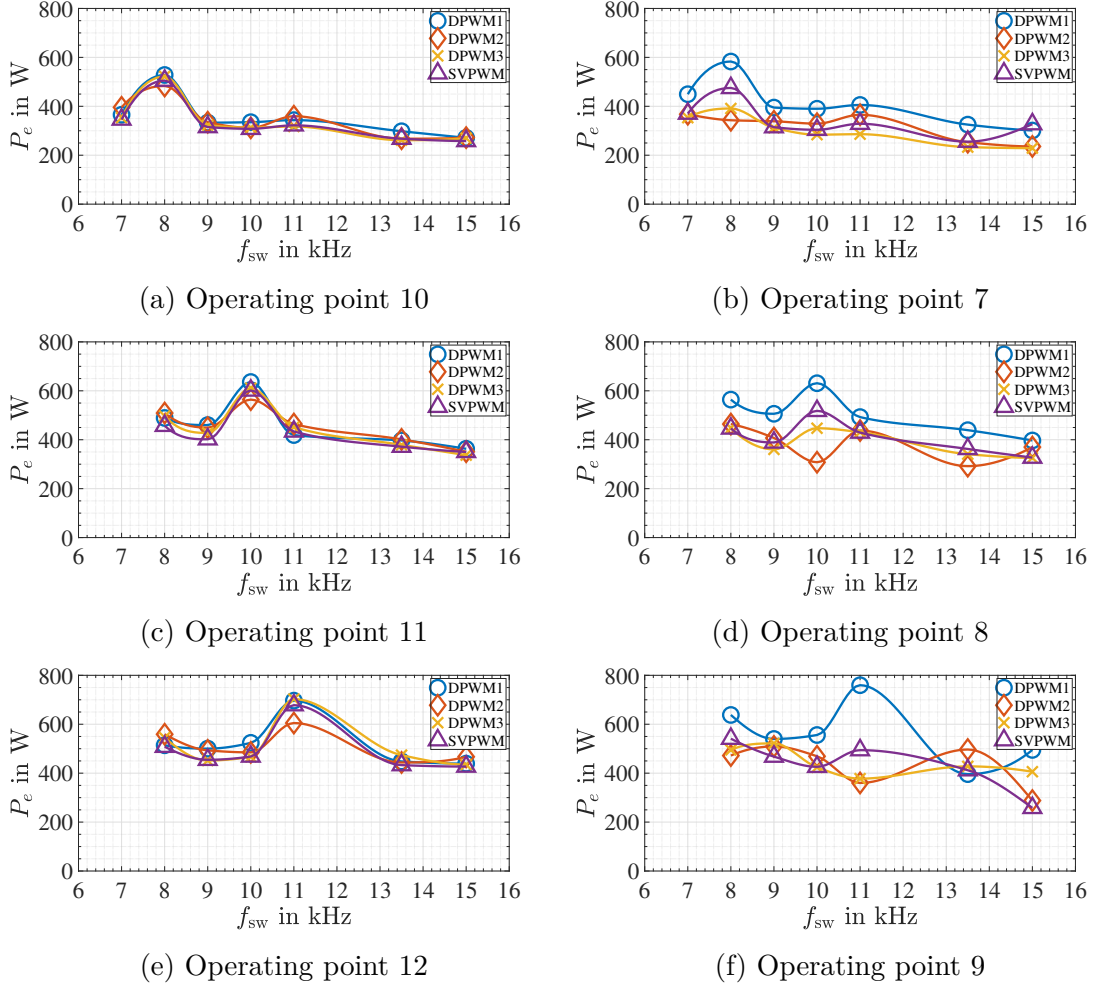
(f) Operating point 9

Figure 5.36: Magnet losses for various switching frequencies and PWM methods.

These trends can be seen in Figure 5.36 where the different operating points are ordered by increasing torque from left to right and increasing speed from top to bottom. Overall, losses increase with increasing speed and decrease with increasing switching frequency, with a peak or a trough where the machine harmonics and inverter subharmonics interact. One may verify the speed and switching frequency trends by inspecting the increasing mean loss with speed and $\partial P_e / \partial f_{sw} < 0$, or negative linear best fit slope, shown in Table III. It might appear as if the approx-

TABLE III: PM Loss Trends

OP	Torque, norm.	Speed, norm.	Mean Loss in W	$\partial P_e / \partial f_{sw}$ in W/kHz
10	0.1	0.5	342	-19.4
11	0.1	0.625	451	-22.3
12	0.1	0.6875	509	-12.5
7	0.2	0.5	341	-25.5
8	0.2	0.625	422	-24.9
9	0.2	0.6875	468	-23.8

imation from equation (5.1.5) supports $\partial P_e / \partial f_{sw} < 0$ but the increasing loss with speed contradicts both. It is however, a simple manner that the losses trend dif-

ferently for the lower frequencies associated with speed than the higher frequencies associated with switching and that the losses come from two different sources: lower frequency losses trend quadratically and come from the reluctance variation due to slotting as seen by the rotor magnets; higher frequency losses trend with the square root of the frequency and come from the inverter whose excitation is proportional to $1/f_{\mathrm{sw}}$. The power density loss trends for a constant exciting current density J at the edges of the magnet are shown in Figure 5.37
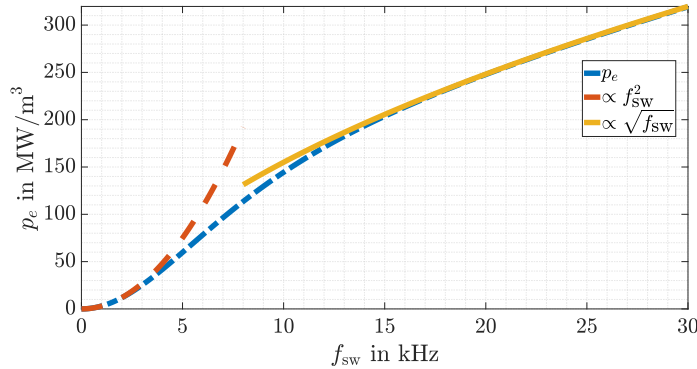
Figure 5.37: Analytical power density and its approximation at different frequencies [71].

The relationships between the machine and inverter harmonics can be traced by inspecting the spectra of the phase voltage, phase currents, currents in the rotor frame, magnetic field as seen from the rotor, the current density in the magnet, and finally the loss density in the magnet. The process is summarized in Figure 5.38
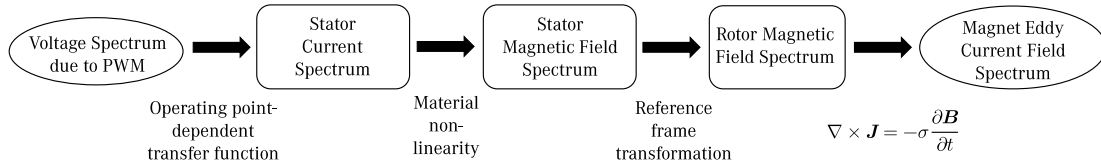
Figure 5.38: Simplified process chain of magnet eddy current creation due to inverter feeding.
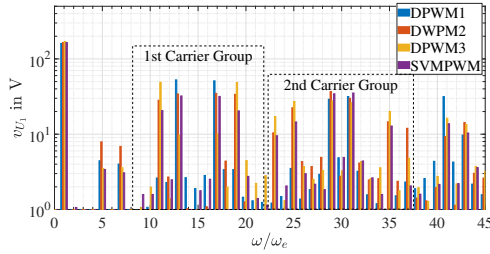
(a) $f_{\mathrm{sw}} = 11\,\mathrm{kHz}$
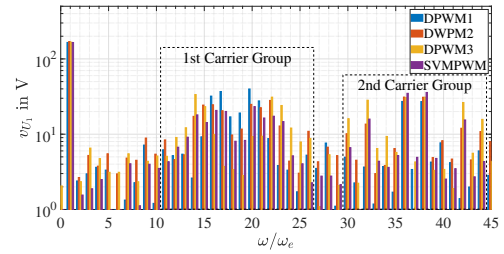
(b) $f_{\mathrm{sw}} = 13.5\,\mathrm{kHz}$
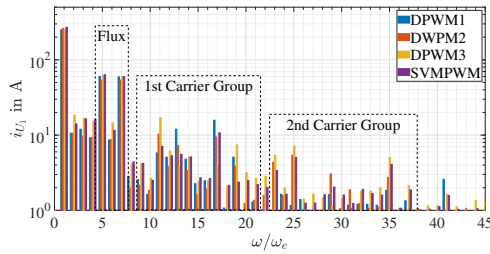
(c) $f_{\mathrm{sw}} = 11\,\mathrm{kHz}$
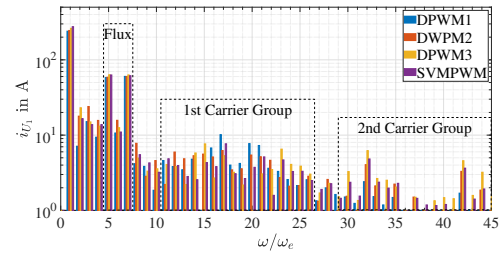
(d) $f_{\mathrm{sw}} = 13.5\,\mathrm{kHz}$
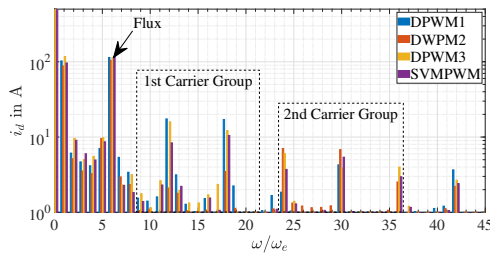
(e) $f_{\mathrm{sw}} = 11\,\mathrm{kHz}$
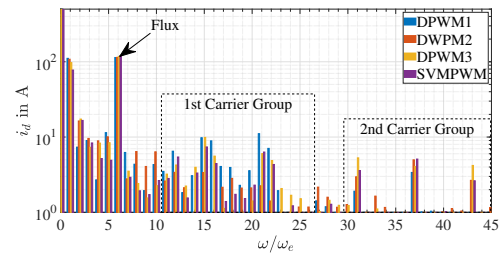
(f) $f_{\mathrm{sw}} = 13.5\,\mathrm{kHz}$
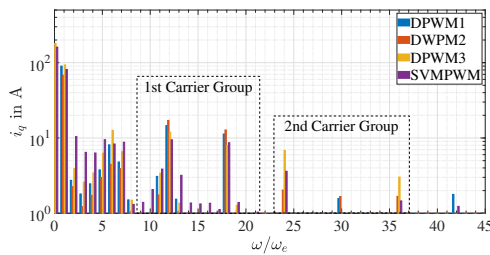
(g) $f_{\mathrm{sw}} = 11\,\mathrm{kHz}$
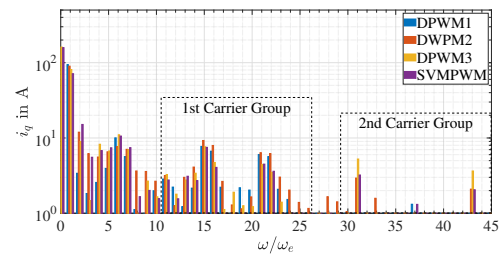
(h) $f_{\mathrm{sw}} = 13.5\,\mathrm{kHz}$

Figure 5.39: Spectra of v_{U1}, i_{U1}, i_{d1}, and i_{q1} for various PWM methods at operating point 9.

As expected from Figure 5.39, the voltage excitation harmonics translate to the phase current harmonics. In addition, several other harmonics appear in the phase current labelled as 'Flux'. Due to the opposite wavenumber sign of the sideband harmonics, many harmonic pairs coalesce to their harmonic center. The most relevant harmonic in the rotor frame is the 12th harmonic, as it represents the harmonic due to slotting and is large enough to interact with subharmonics from the first carrier group, notwithstanding interactions with the 24th harmonic and second carrier group subharmonics, which have smaller amplitudes. As their namesake suggests, slotting harmonics engender from the number of stator teeth per pole-pair, as the gaps between the stator teeth constitute a tangential reluctance variation, and therefore a magnetic field time-change, in the rotor frame. Both the asymmetric machine and the polar machine have 12 teeth per pole-pair.
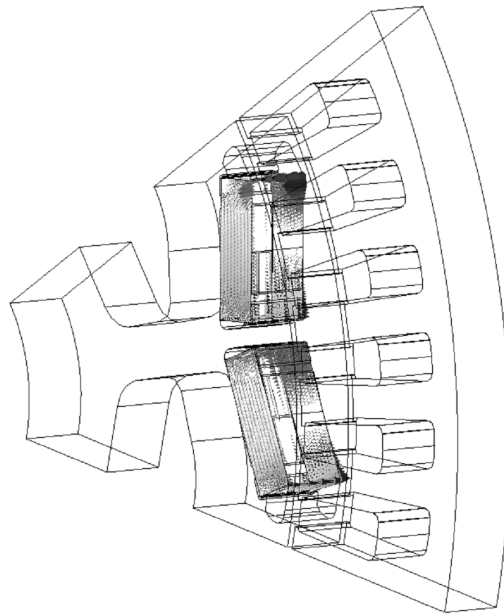
Figure 5.40: FEM magnet eddy currents for SVPWM, 11 kHz excitation at OP 9 for the 1st stator tooth harmonic. A half segment of one machine pole is shown.
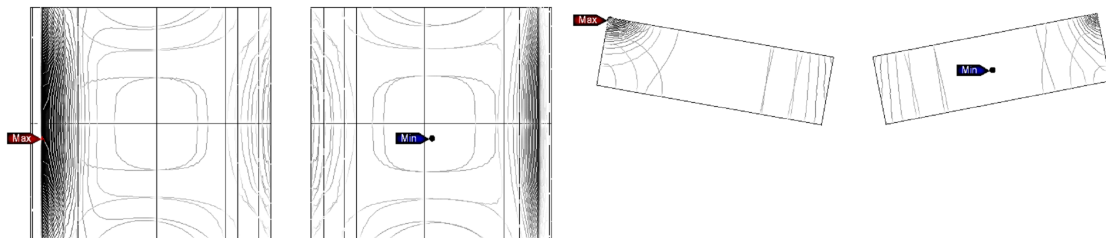
(a) Top

(b) Front

Figure 5.41: Joule loss density contours for SVPWM, 11 kHz excitation at OP 9 for the 1st stator tooth harmonic.
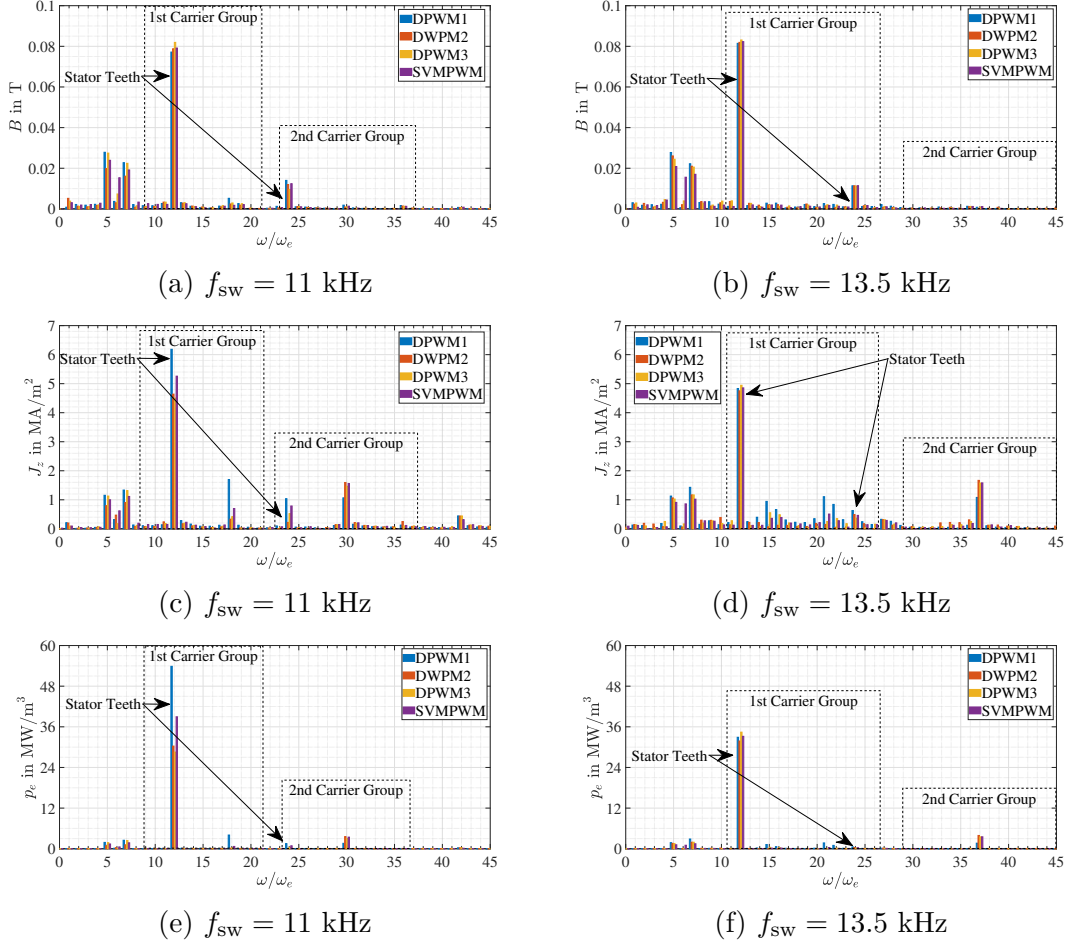
Figure 5.42: Spectra of B, J_z, and p_e at the maximum point from Figure 5.41.

Contrary to the implication that the gradient of the scalar potential reaches the magnet in [133], the correlation between the $d-$axis current 12th harmonic trends over different PWM methods does not correlate with the magnetic field amplitude in Figures (5.42)(a) and (b) although it does for Figures (5.42)(c) and (d) —and consequently also for Figures (5.42)(e) and (f) —because the magnetic field is a superposition of the loss-exciting field in the magnets and the flux reaction as a result of those eddy currents. Overall, the slotting harmonics interact with the first subharmonic in the first carrier group of each PWM method to increase magnet losses for low torques, and interact in different ways for larger torques, or load power factors, as shown in Figure 5.36. Although the hierarchy of loss magnitudes in Figures (5.34) and (5.35) can be explained by the current ripple [6] for a modulation index of 0.9 corresponding to the 12% voltage reserve, the harmonic interaction, or resonance, cannot. Similarly, due to the absence of loss hierarchies in the base-speed region, magnet losses may not simply be correlated to current ripple variations due to different PWM methods. Rather, current ripple seems to excite a baseline amount of eddy currents in the magnets, after which harmonic interactions dominate at high speeds.

The spectra in Figures (5.39) and (5.42) suffer from broad frequency resolution due to the short simulation time. To address this and to definitively show that harmonic interaction causes the additional magnet losses, we trace the spectra from

126

the maximal point current density to the sum of the d−axis currents in Figures
(5.43)-(5.46) over ten fundamental periods for OP11. The latter influence the magnet losses the most, as they are directly aligned with the magnet rotor flux and can
be used to observe the harmonic interaction experimentally, after which one may
infer additional magnet losses.

(a)
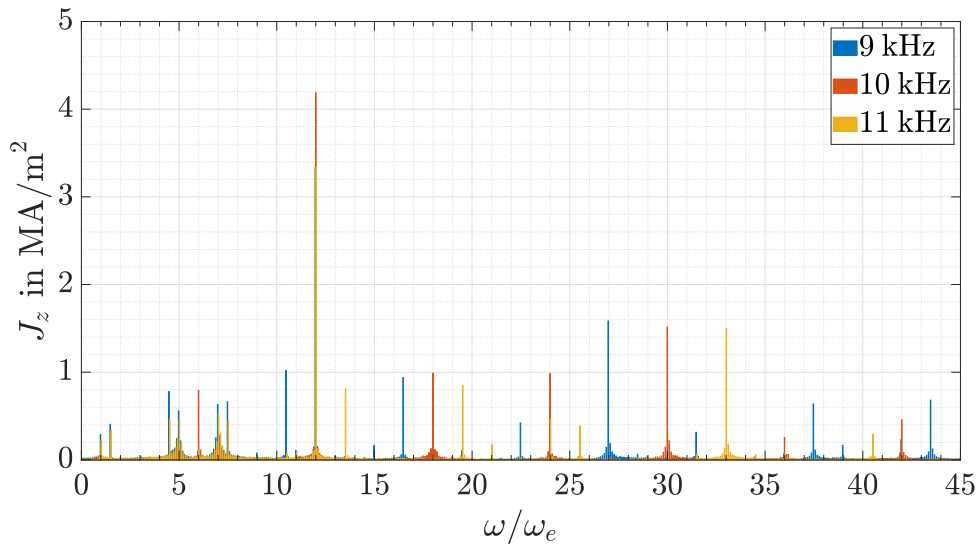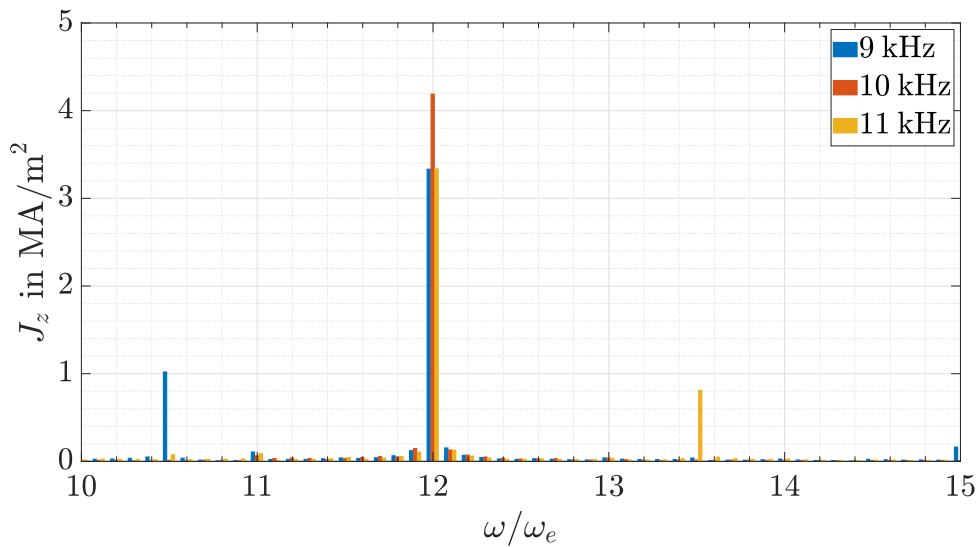
(b) Zoomed (a)

Figure 5.43: Maximal axial current density at OP11 with DPWM2 for various
switching frequencies and simulated for 10 electrical periods.

(a)
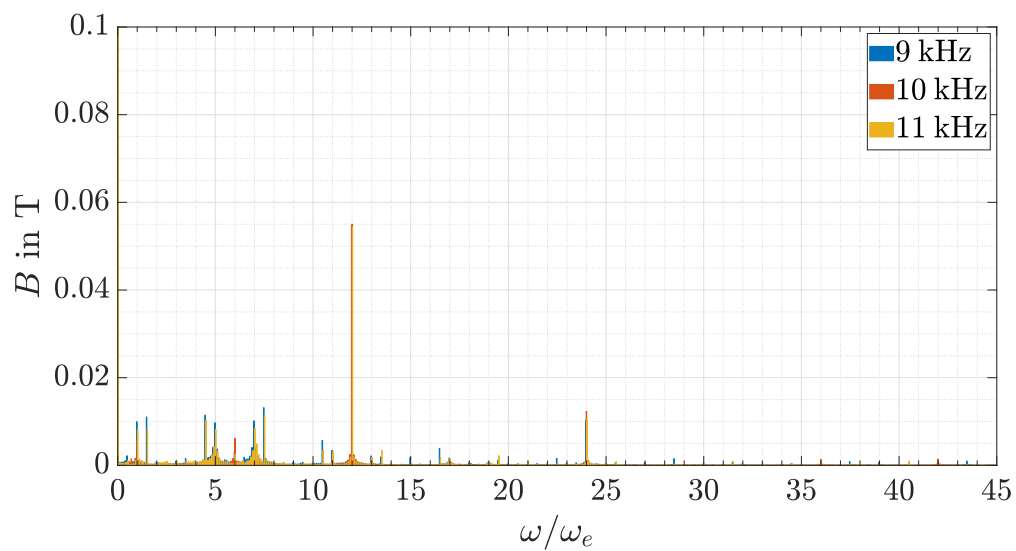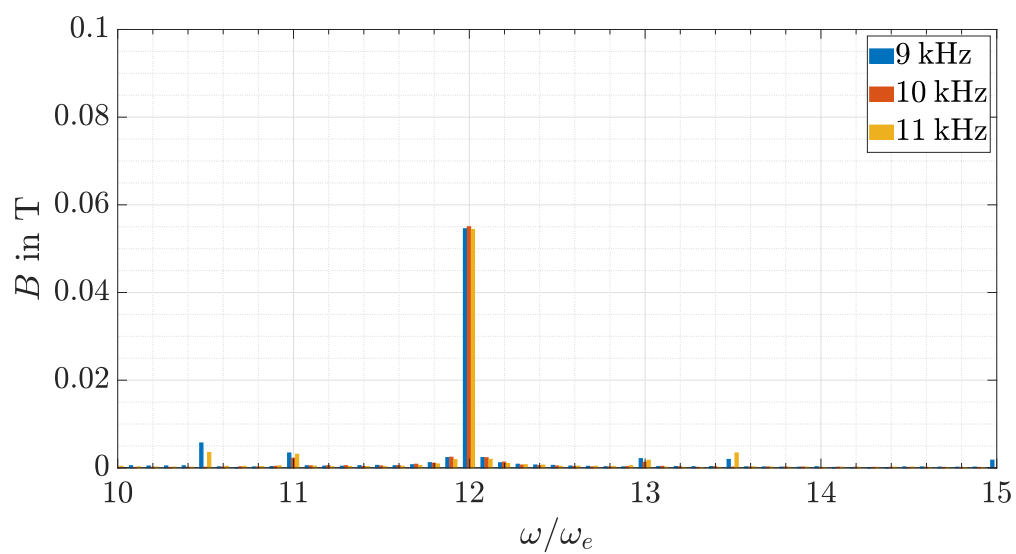
(b) Zoomed (a)

Figure 5.44: Maximal magnetic field amplitude at OP11 with DPWM2 for various switching frequencies and simulated for 10 electrical periods.

(a)
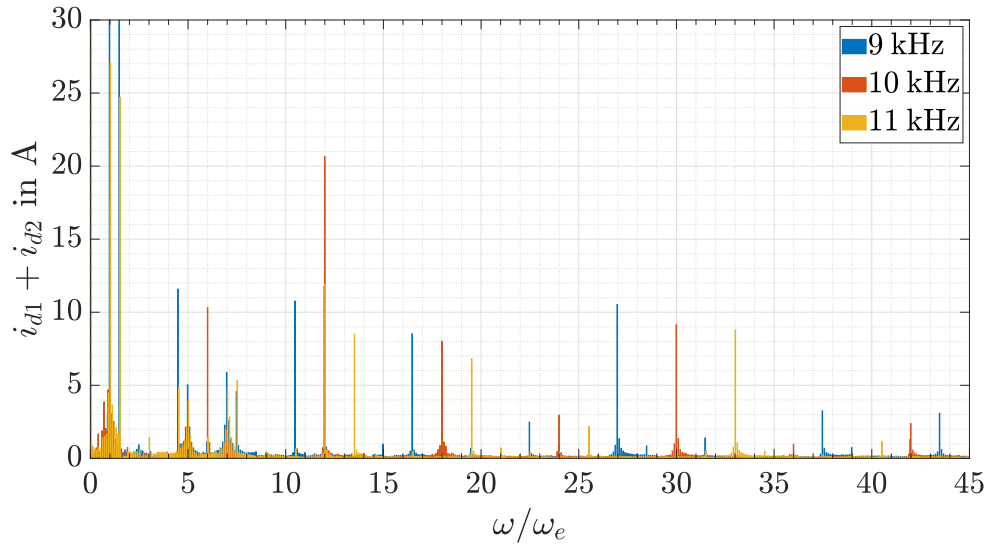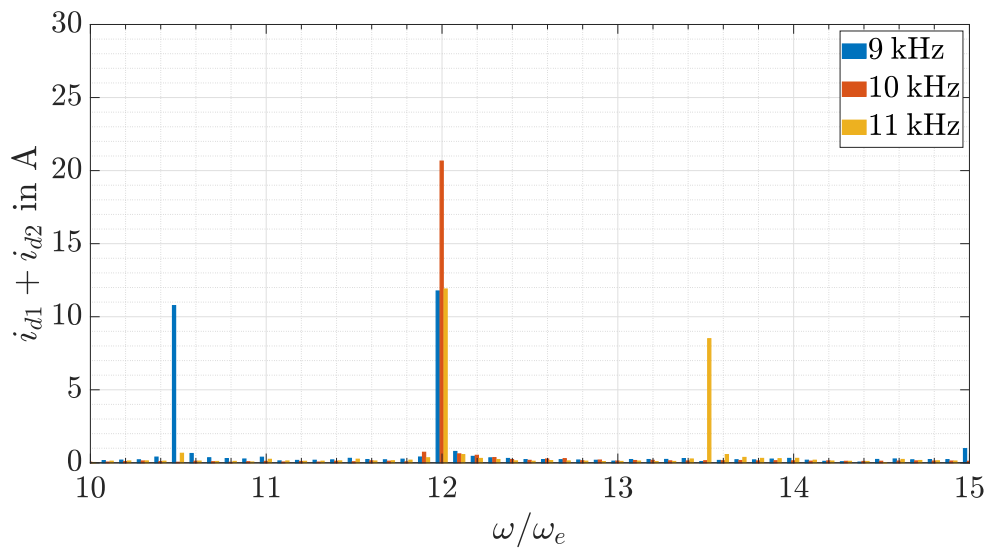
(b) Zoomed (a)

Figure 5.45: Sum of $d-$axis currents at OP11 with DPWM2 for various switching frequencies and simulated for 10 electrical periods.

(a)
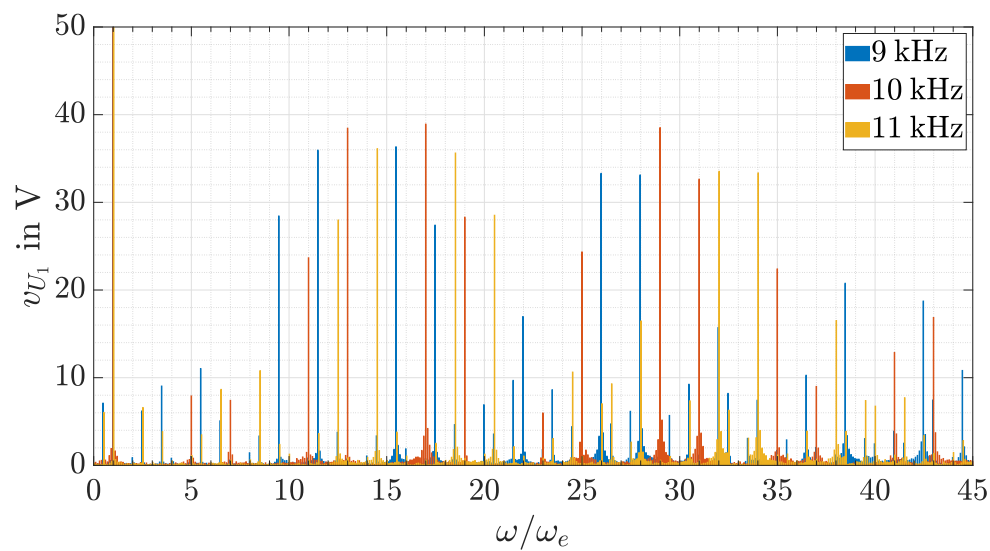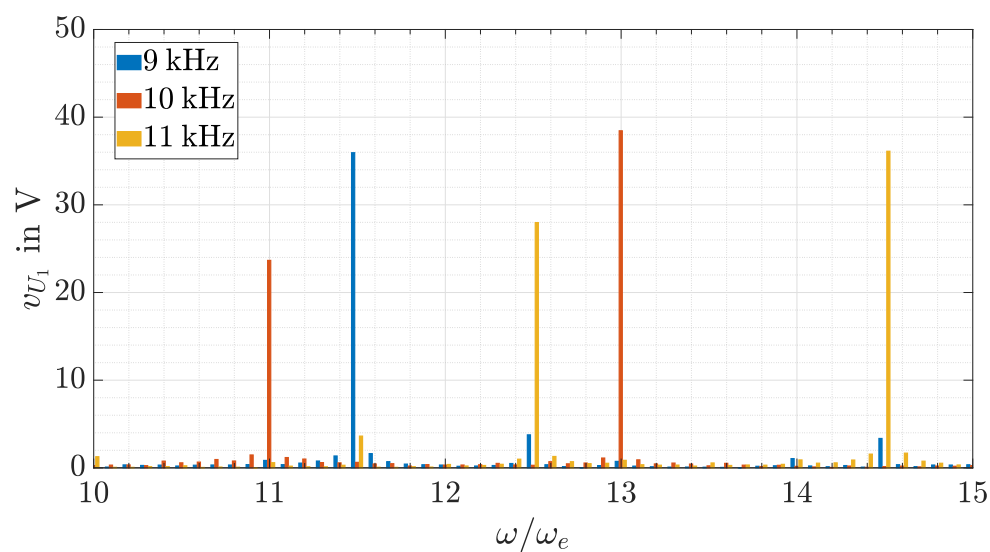
(b) Zoomed (a)

Figure 5.46: $U1$ phase-to-neutral voltage at OP11 with DPWM2 for various switching frequencies and simulated for 10 electrical periods.

5.2 Losses in the Direct-Current Linking Capacitor

Losses in the DC link capacitor are usually small, especially in automotive applications where polypropylene film and metallized polypropylene film capacitors offer lower equivalent series resistance (ESR) values compared to aluminium electrolytic capacitors. Their values are typically in the tenths of $m\Omega$. As a result, one might think that the quantity to evaluate the capacitor's influence on the system should rely on life expectancy. Using the Arrhenius law model due to temperature changes [135] [136],

$$t_\ell = t_0 e^{\frac{E_a}{k_b}\left(\frac{1}{T} - \frac{1}{T_0}\right)} \ ,$$ (5.2.1)

where k_b is the Boltzmann constant, E_a is the activation energy of the system fittable from datasheet curves, and t_ℓ is the expected lifetime of the capacitor. Using a simple conduction model with thermal resistance R_{th} and some ambient temperature T_a, then the capacitor temperature during operation is $T = I_{C,\mathrm{rms}}^2 R_C / R_{th} + T_a$. Taking another operating temperature-current pair and subtracting them results in $T_1 - T_2 = (I_{C,\mathrm{rms},1}^2 - I_{C,\mathrm{rms},2}^2) R_C / R_{th}$. Dividing by $T_1 - T_a$ and realising that the current corresponding to the ambient temperature is zero, one obtains

$$T_2 = T_1 - (T_1 - T_a)\left(1 - \frac{I_{C,\mathrm{rms},2}^2}{I_{C,\mathrm{rms},1}^2}\right) \ .$$ (5.2.2)

Since the correspondence between the subscripts in equation (5.2.1) are arbitrary, we can pick any two temperature-lifetime pairs so that $t_0 \to t_1$ as $T_0 \to T_1$ for $T_1 > T_a$. Also, the subscript 2 was arbitrary, so that we can pick any $T_2 \to T$ and corresponding current with respect to the temperature-current pair with subscript 1. This results in the lifetime equation as a function of capacitor rms current as

$$t_\ell = t_1 \exp\left(\frac{E_a}{k_b}\left(\frac{1}{T_1 - (1 - \gamma^2)(T_1 - T_a)} - \frac{1}{T_1}\right)\right) ,$$ (5.2.3)

where $\gamma := I_{C,\mathrm{rms}}/I_{C,\mathrm{rms},1}$. Since t_ℓ is a decreasing function of γ, a candidate cost function must increase with γ, indicating that the DC-link capacitor rms current must be minimized, as expected. However, as will be shown in the beginning of Chapter 8.1, capacitor cost per ampere is orders of magnitude lower than the cost per unit power over the capacitor lifetime for the asymmetric machine. As a result, the interleaving angle for highly coupled machines should be set to zero. However, because the losses due to interleaving in the polar machine are much lower, an optimization for overall minimal losses is possible. Figure 5.47 and Figure 5.48 show the RMS capacitor current ripple for the asymmetric and polar machines from the FEM respectively, each showing the results with two interleaving angles. Figure 5.49 shows the RMS capacitor current ripple difference between the interleaving angle for the asymmetric and polar machines. As expected, interleaving reduces the capacitor current ripple overall.

(a) Interleaving on, $\theta_I = 90°$ (b) Interleaving off, $\theta_I = 0°$
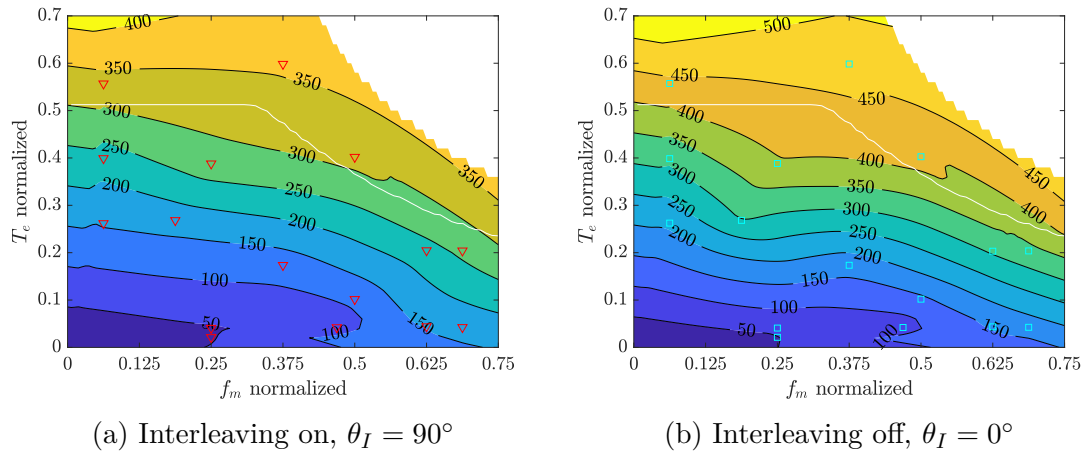
Figure 5.47: RMS capacitor current ripple for the asymmetric machine in A

(a) Interleaving on, $\theta_I = 90°$ (b) Interleaving off, $\theta_I = 0°$
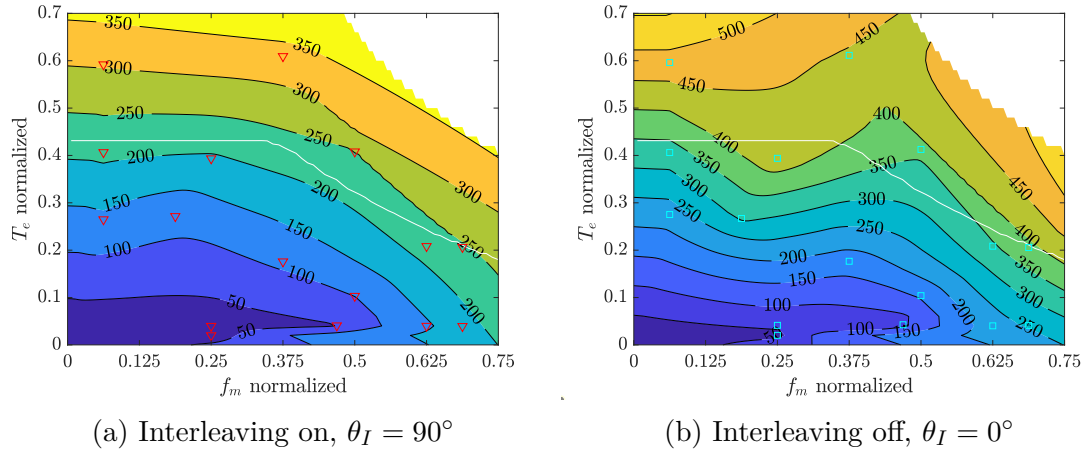
Figure 5.48: RMS capacitor current for the polar machine in A

(a) Asymmetric machine   (b) Polar machine
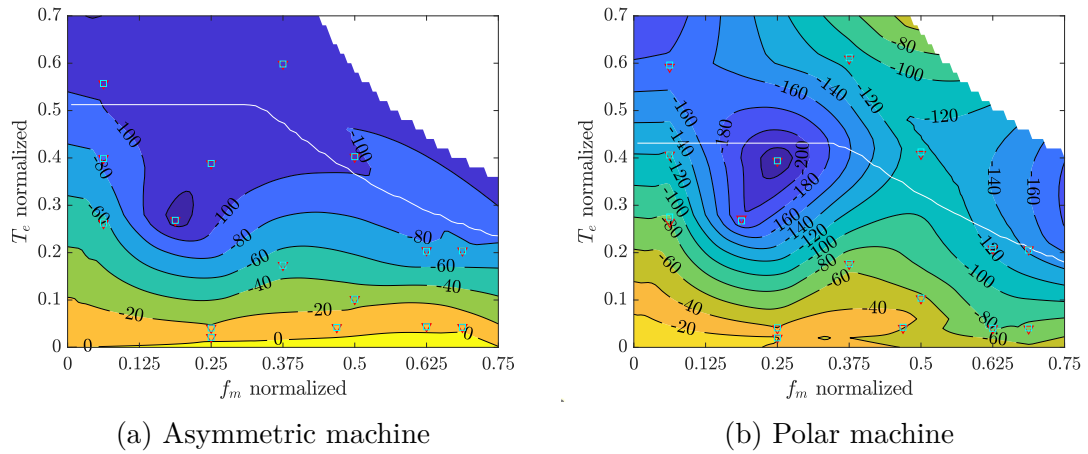
Figure 5.49: RMS capacitor current ripple difference, $I_{\mathrm{DC}}(90°) - I_{\mathrm{DC}}(0°)$ in A

Chapter 6

Optimization of the Simulation Results

Broadly speaking, high frequency conduction losses in copper are less than high frequency conduction losses in iron due to the often small skin depth of the eddy currents in the iron compared to the lamination thicknesses. The high frequency iron loss model in equation (5.1.3) along with the bulk permeability profile over the operating space is decisive in finding optimal switching frequency and PWM method programs over the operating space in simulations. Whereas the switching frequency program varies more for the asymmetric machine than the one for the polar machine, the situation is reversed for the PWM program. The switching frequency range simulated spans 4 kHz to 20 kHz; SVM, DPWM1, DPWM2, DPWM3, VDPWM, and D6ϕ SVM-B2 are the investigated PWM methods. Six-step switching is not investigated due to the large currents and losses it incurs, along with a relative loss of control robustness. A median efficiency improvement for both machines of 1% from the corner point to the origin, a significant figure, results from the optimization.

6.1 Numerical Optimization of the Interleaving Angle

As stated in the previous chapter, iron losses due to interleaving are too large for the small series equivalent resistance R_C of the capacitor for the asymmetric machine. Due to reduced coupling in the polar machine, however, a nontrivial interleaving map comes to the fore, as shown in Figure 6.1. In regions where iron loss dominates, namely below the continuous operation boundary, it is best to set the interleaving angle to $\theta_I = 0°$; for larger torque and power, $\theta_I = 90°$ is best for the polar machine. The objective function minimized is the sum of the DC link capacitor loss with $R_C = 0.5 \text{ m}\Omega$ and iron losses as calculated by the FEM software package.

(a) Asymmetric machine

(b) Polar machine
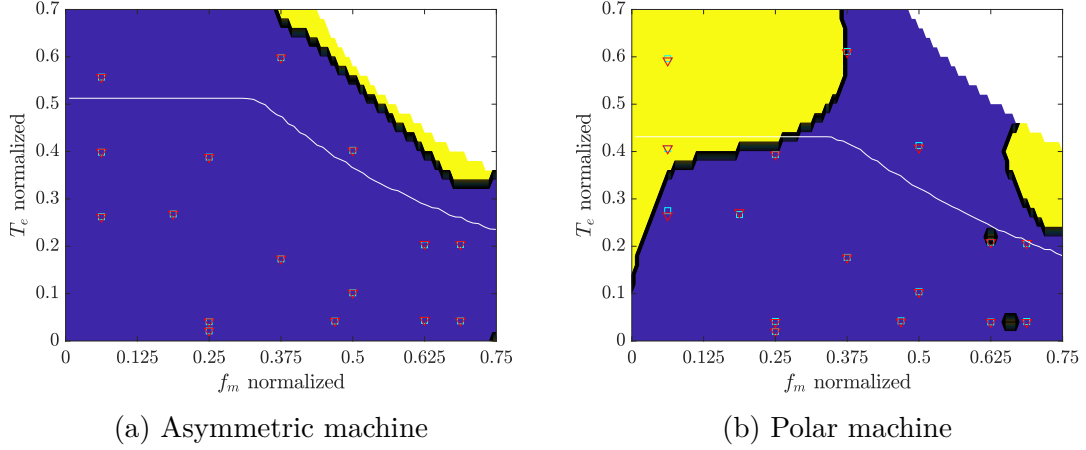
Figure 6.1: Optimal interleaving map from FEM with blue $\theta_I = 0°$ and yellow $\theta_I = 90°$ setting $R_C = 0.5$ mΩ

Expanding the simulation area by using a high frequency coupling model and the iron loss model specified in equation (5.1.3) results in Figure 6.2 for two different capacitor series-equivalent resistances R_C. Similarly, Figure 6.3 shows the optimal interleaving map when choosing between two interleaving angles for the polar machine. Only $R_C = 0.5$ mΩ is realistic for metallized polypropylene film capacitors. As before, because the asymmetric machine induces more iron losses due to interleaving than the polar machine, only at large torque where copper losses dominate does interleaving lend itself for overall power loss reduction; due to the weaker coupling in the polar machine, interleaving lends itself in more areas. However, Figure 6.1(b) and Figure 6.3(a) do not match, especially at low torques and low speeds. That is simply due to the different iron loss models used in the FEM and the high frequency coupling model. However, there is better agreement between Figure 6.1(a) and Figure 6.2(a) for the asymmetric machine. Moreover, one may expect better agreement between the high frequency coupling model and experiments, as a comparison between Figure 5.31 and Figure 7.4 shows.

(a) $R_C = 0.5$ mΩ

(b) $R_C = 10$ mΩ
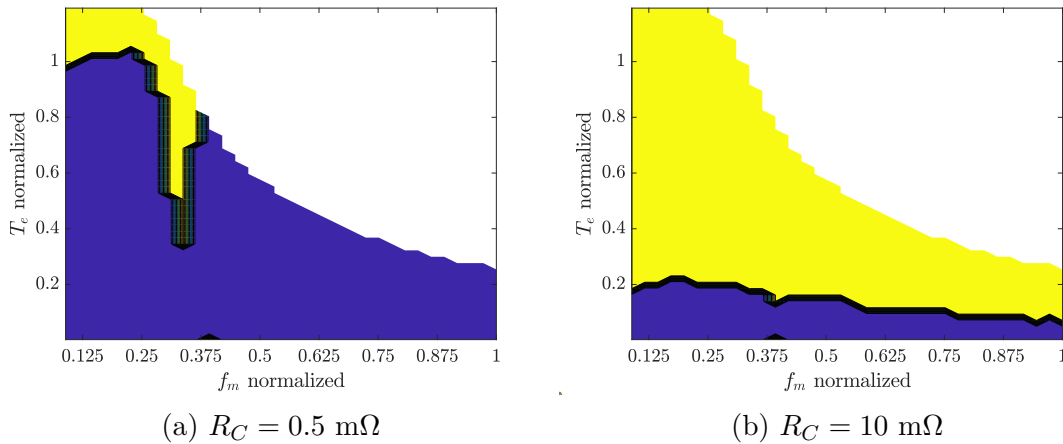
Figure 6.2: Optimal interleaving map from the high frequency coupling model with blue $\theta_I = 0°$ and yellow $\theta_I = 90°$ for the asymmetric machine

(a) $R_C = 0.5$ mΩ

(b) $R_C = 10$ mΩ
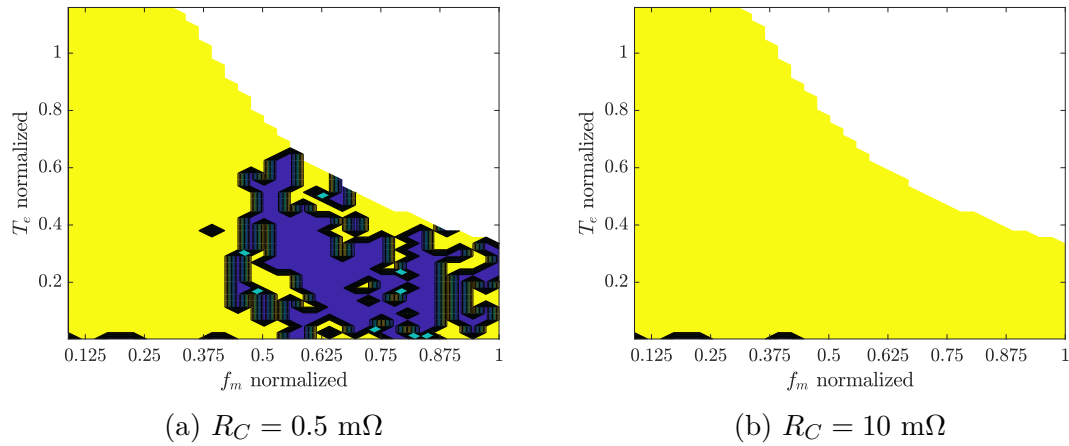
Figure 6.3: Optimal interleaving map from the high frequency coupling model with blue $\theta_I = 0°$ and yellow $\theta_I = 90°$ for the polar machine

Figures 6.4 and 6.5 show the efficiency gains and power savings for the asymmetric and polar machines respectively. Notice how setting $\theta_I = 0°$ is more important in the asymmetric machine compared to the polar machine due to the unexpectedly large iron losses due to interleaving and that said increase in losses occurs in the continuous operation regime of the torque-speed plane.

(a) $\Delta\eta$ in %
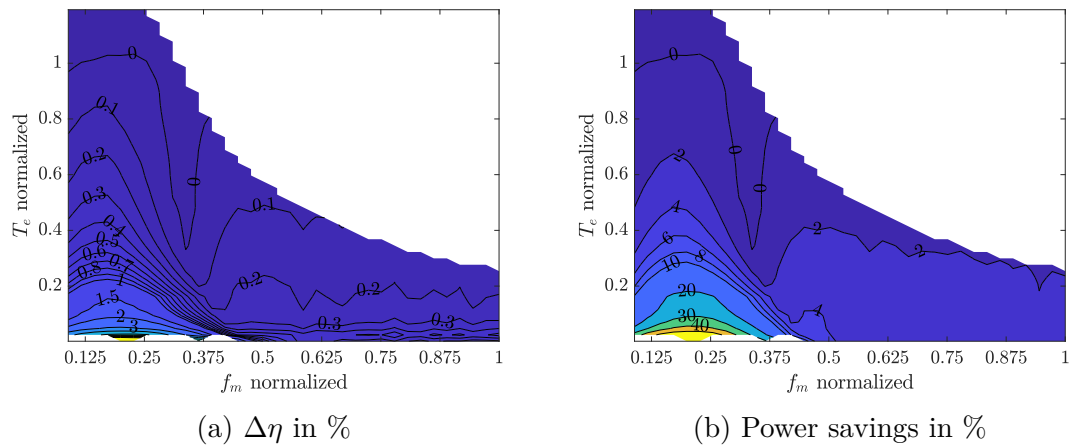
(b) Power savings in %

Figure 6.4: Efficiency gains and power savings when $\theta_I = 0°$ compared to $\theta_I = 90°$ for the asymmetric machine and $R_C = 0.5$ mΩ

135

(a) $\Delta\eta$ in %
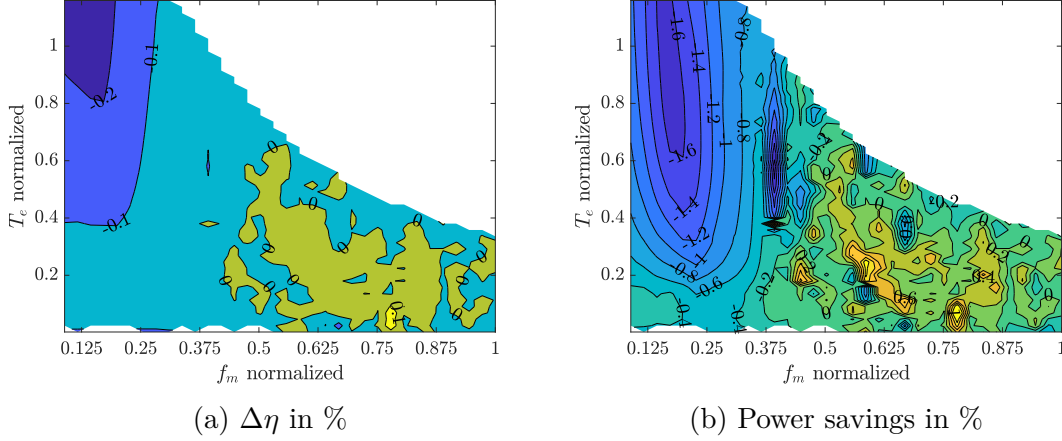
(b) Power savings in %

Figure 6.5: Efficiency gains and power savings when $\theta_I = 0°$ compared to $\theta_I = 90°$ for the polar machine and $R_C = 0.5$ mΩ

6.2 Switching Frequency Optimization

The entire torque-speed plane was simulated using the same high-frequency model for different switching frequencies between 4 kHz and 20 kHz and $\theta_I = [0°, 90°]$. The sampling frequencies were synchronous with the switching frequencies for all simulations unless otherwise noted. Figure 6.8 shows the optimal switching frequency for minimal drive losses over various PWM methods for the asymmetric machine and Figure 6.15 shows them for the polar machine. The variable discontinuous PWM method (VDPWM) is a method using the clamping angle in generalized PWM and having it track the current vector phase offset from the voltage vector. The rationale behind that strategy involves minimizing inverter switching losses since the number of commutations are minimized at peak current. More details are explained in the following section. Notice how the optimal switching frequency increases with increasing speed and decreasing torque for all PWM methods and both machines. The reason for that requires the observation that high frequency losses in iron increase with decreasing switching frequency, but since at low torques switching losses are low, those losses in iron may be decreased by increasing the switching frequency. The low-torque, mid-speed region is critical for continuous machine operation and it happens to have the most variability as to the optimal switching frequency, according to simulations. Comparing Figures 6.8 and 6.15 show that the asymmetric machine requires more changes in the switching frequency irrespective of the PWM method. The large torque and low speed region, meaning the short-time operating regions, require 4 kHz switching frequencies or lower for both machines, since inverter losses dominate. The inverter model was fitted to the asymmetrical dual three-phase IGBT inverter's power loss measurements; due to the additional 5th and 7th harmonics in the measurements but absent in the model, the inverter model embeds the additionally measured harmonics into forward voltage and conduction resistance parameters, possibly biasing the inverter losses especially for large currents. This partly explains the lack of variability in the optimal switching frequency for the polar machine, as shown by Figure 6.15. Therefore it is likely that measured results will have larger switching frequencies at mid-speeds and large torque for both machines. It is also likely that the optimal switching frequency will increase in the

large torque, low speed region with inverters having more efficient SiC components and more effective cooling. Furthermore, if $\theta_I = 90°$, losses increase for all torques near $f_m = 0.25$ normalized speed: a larger switching frequency can compensate for those additional interleaving losses in the asymmetric machine as shown in Figure 6.6. One may expect little change in the optimal switching frequency profile for the polar machine upon setting $\theta_I = 90°$, as Figure 6.7 shows, due to the weak coupling between duals.

(a) $\theta_I = 0°$ (b) $\theta_I = 90°$
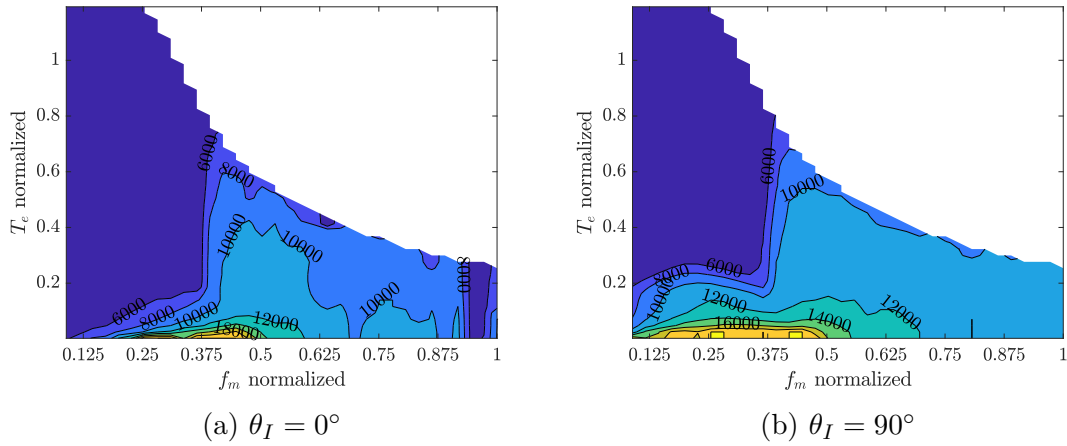
Figure 6.6: Optimal switching frequency for various interleaving angles for the asymmetric machine

(a) $\theta_I = 0°$ (b) $\theta_I = 90°$
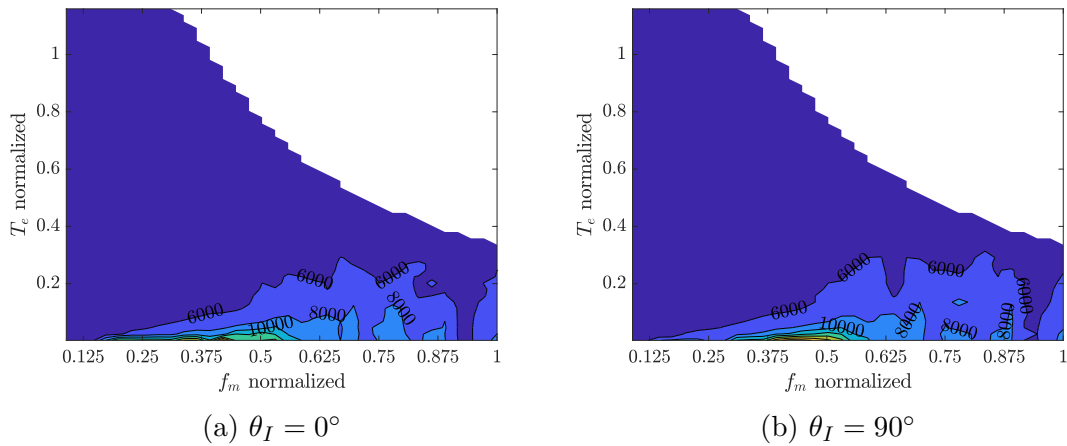
Figure 6.7: Optimal switching frequency for various interleaving angles for the polar machine

(a) SVM

(b) DPWM1

(c) DPWM2

(d) DPWM3

(e) VDPWM

(f) D6ϕ SVM-B2
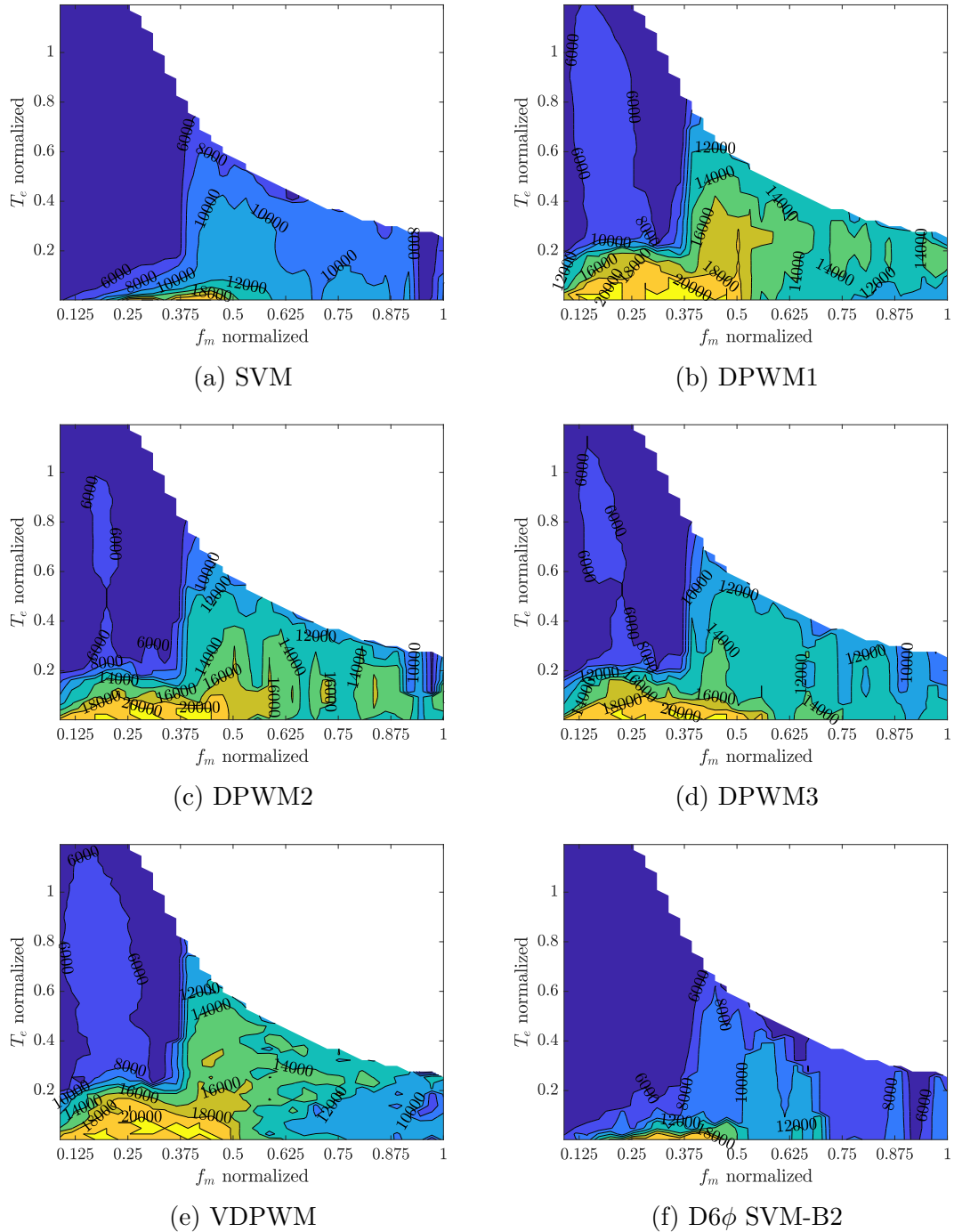
Figure 6.8: Optimal switching frequency for various PWM methods for the asymmetric machine with $\theta_I = 0°$

Alluding to Figures 6.9-6.14, notice how for highly coupled machines and DPWM methods, the efficiency and power gains shift to the low torque and mid speed regions compared to SVM methods and lightly coupled machines. That is likely because clamping excites larger harmonics in regions with large coupling at large torques, reducing the benefits of variable switching frequency operation for a given DPWM method. Whereas SVM shows efficiency improvements of 1% for an approximately constant-speed over many torques, DPWM methods only show an improvement of 0.5% in similar regions and for a more limited operating space.

(a) $\Delta\eta$ in %
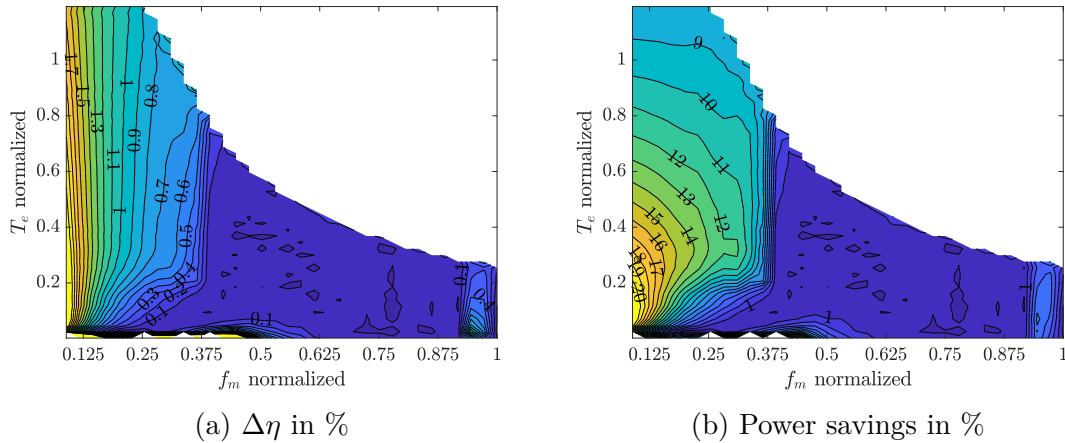
(b) Power savings in %

Figure 6.9: Efficiency gains and power savings between $f_{\text{sw,opt}}$ and 10 kHz when $\theta_I = 0°$, SVM, and $R_C = 0.5$ mΩ for the asymmetric machine

(a) $\Delta\eta$ in %
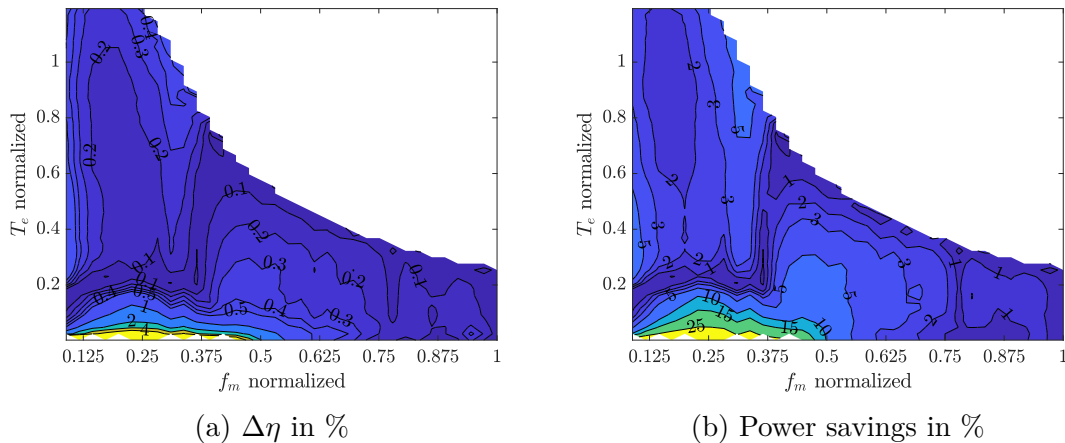
(b) Power savings in %

Figure 6.10: Efficiency gains and power savings between $f_{\text{sw,opt}}$ and 10 kHz when $\theta_I = 0°$, DPWM1, and $R_C = 0.5$ mΩ for the asymmetric machine

139

(a) $\Delta\eta$ in %   (b) Power savings in %
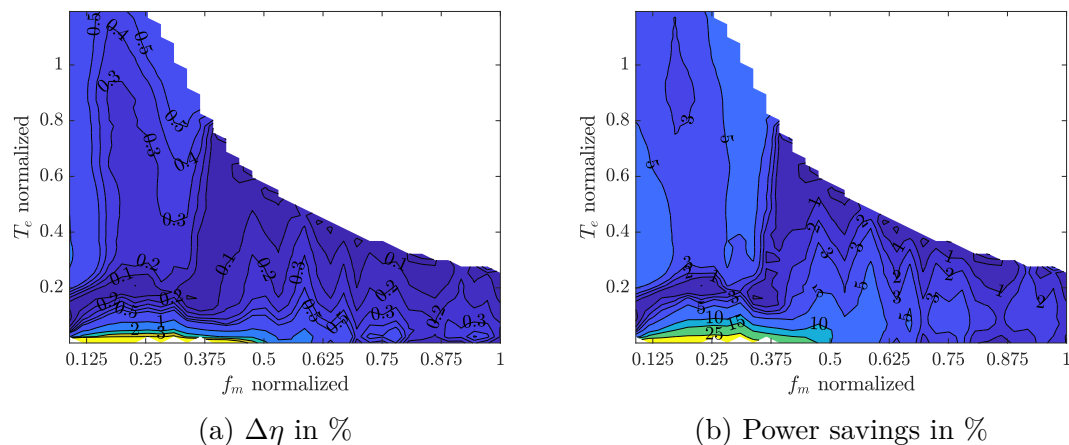
Figure 6.11: Efficiency gains and power savings between $f_{\text{sw,opt}}$ and 10 kHz when $\theta_I = 0°$, DPWM2, and $R_C = 0.5$ mΩ for the asymmetric machine

(a) $\Delta\eta$ in %   (b) Power savings in %
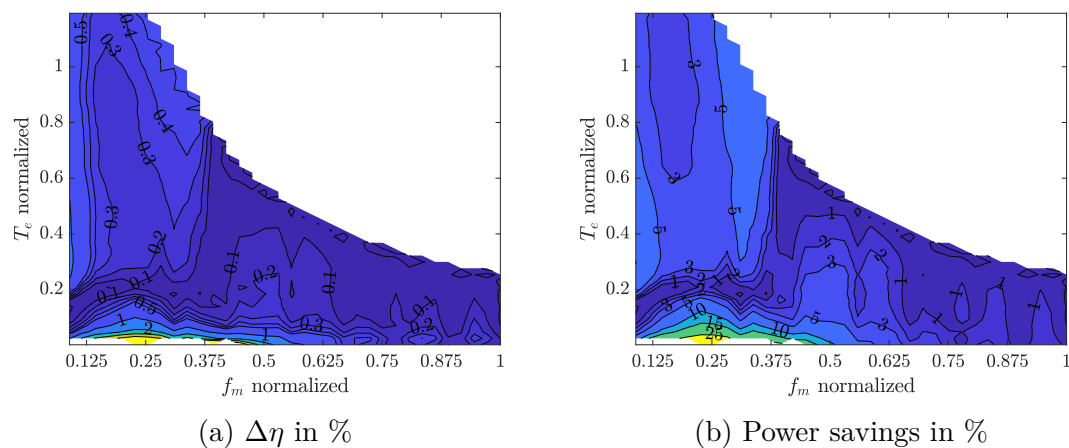
Figure 6.12: Efficiency gains and power savings between $f_{\text{sw,opt}}$ and 10 kHz when $\theta_I = 0°$, DPWM3, and $R_C = 0.5$ mΩ for the asymmetric machine

(a) $\Delta\eta$ in %
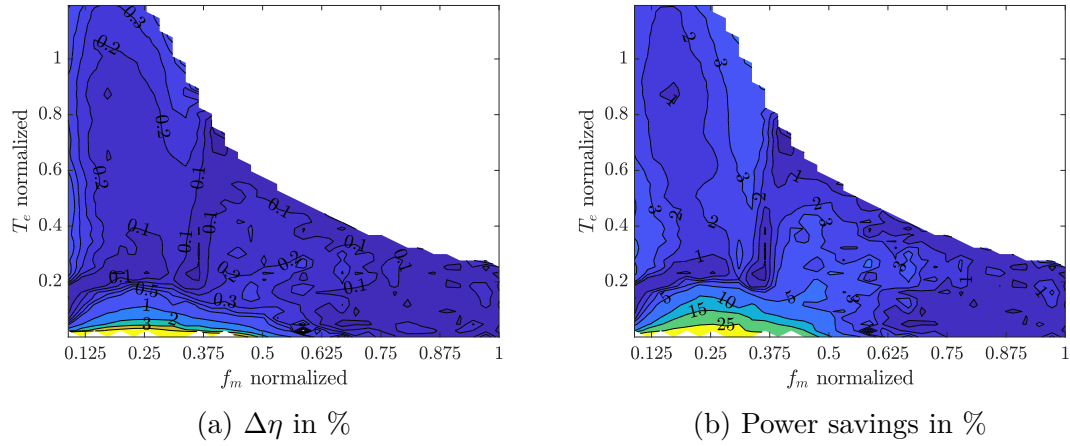
(b) Power savings in %

Figure 6.13: Efficiency gains and power savings between $f_{\text{sw,opt}}$ and 10 kHz when $\theta_I = 0°$, VDPWM, and $R_C = 0.5$ mΩ for the asymmetric machine

(a) $\Delta\eta$ in %
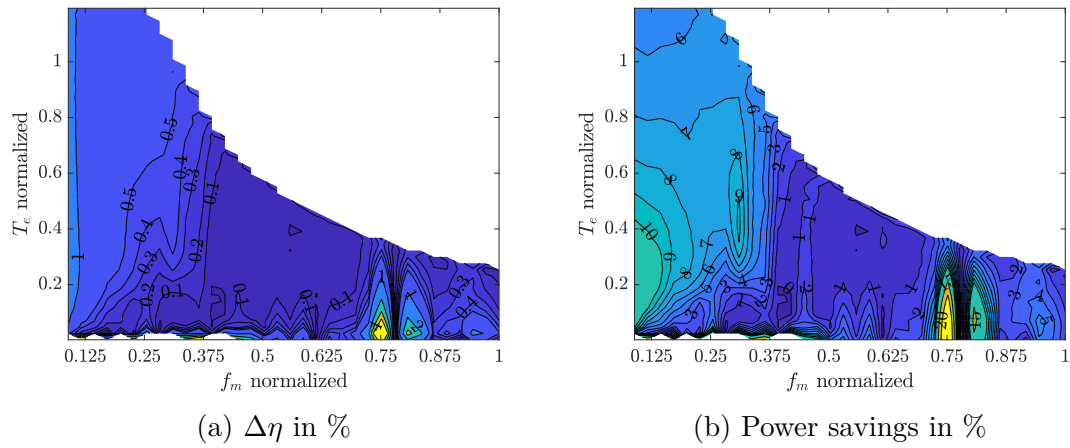
(b) Power savings in %

Figure 6.14: Efficiency gains and power savings between $f_{\text{sw,opt}}$ and 10 kHz when $\theta_I = 0°$, D6ϕ SVM-B2, and $R_C = 0.5$ mΩ for the asymmetric machine

(a) SVM

(b) DPWM1

(c) DPWM2

(d) DPWM3

(e) VDPWM

(f) D6ϕ SVM-B2
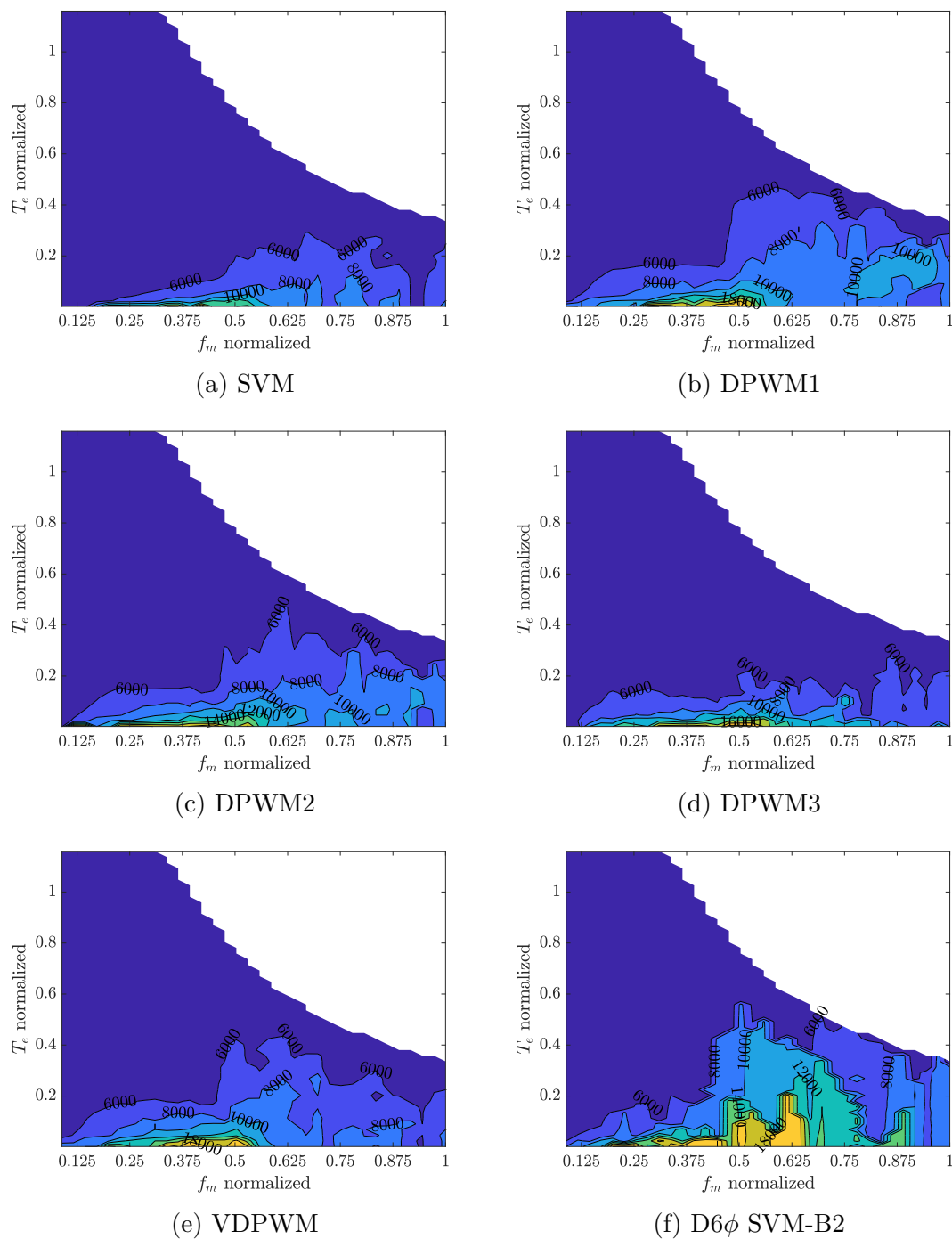
Figure 6.15: Optimal switching frequency for various PWM methods for the polar machine with $\theta_I = 0°$

As mentioned before, the inverter loss model has asymmetric machine winding harmonics embedded into its parameters, skewing the optimal switching frequency per PWM method to the lower end, explaining the dominance of 4 kHz as the optimal switching frequency, as shown in Figure 6.15. Despite that, a similar improvement in efficiency and power gains as shown in Figures 6.16-6.21 is expected, especially because coupling is near a minimum in the large torque and mid speed regions for the polar machine whereas coupling was near its maximum in the same region for the asymmetric machine. Notice that, unlike with the asymmetric machine, the small coupling in the polar machine in the aforementioned region changes the efficiency and power improvement contours to resemble those of SVM with the asymmetric machine, similarly increasing the efficiency to at least values greater than 0.5%.

(a) $\Delta\eta$ in %   (b) Power savings in %
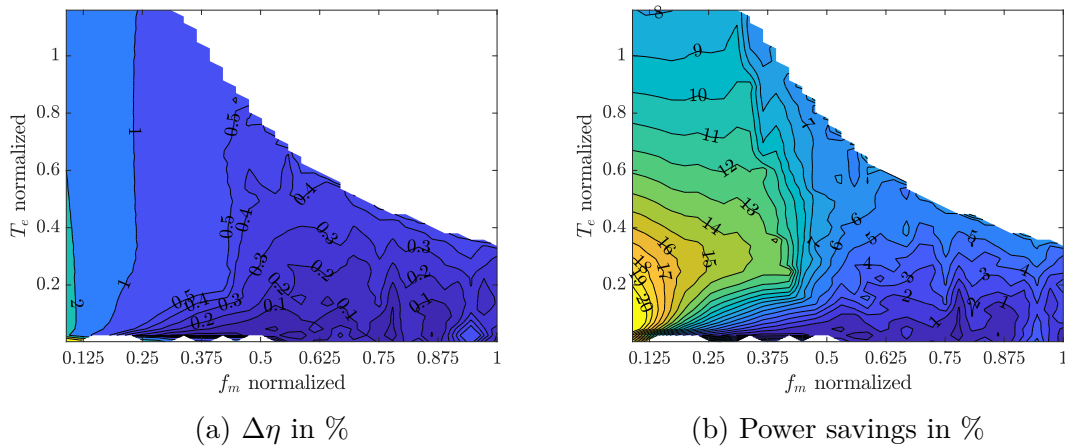
Figure 6.16: Efficiency gains and power savings between $f_{\text{sw,opt}}$ and 10 kHz when $\theta_I = 0°$, SVM, and $R_C = 0.5$ mΩ for the polar machine

(a) $\Delta\eta$ in %   (b) Power savings in %
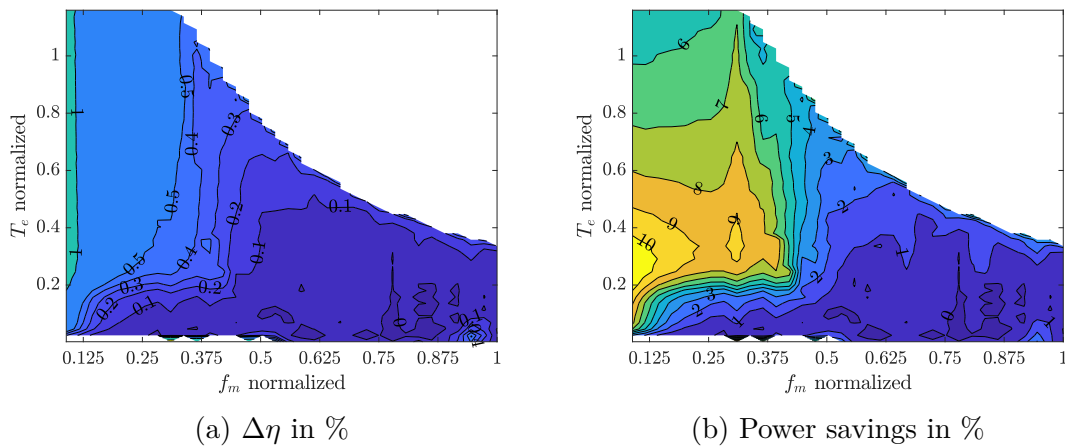
Figure 6.17: Efficiency gains and power savings between $f_{\text{sw,opt}}$ and 10 kHz when $\theta_I = 0°$, DPWM1, and $R_C = 0.5$ mΩ for the polar machine

(a) $\Delta\eta$ in %
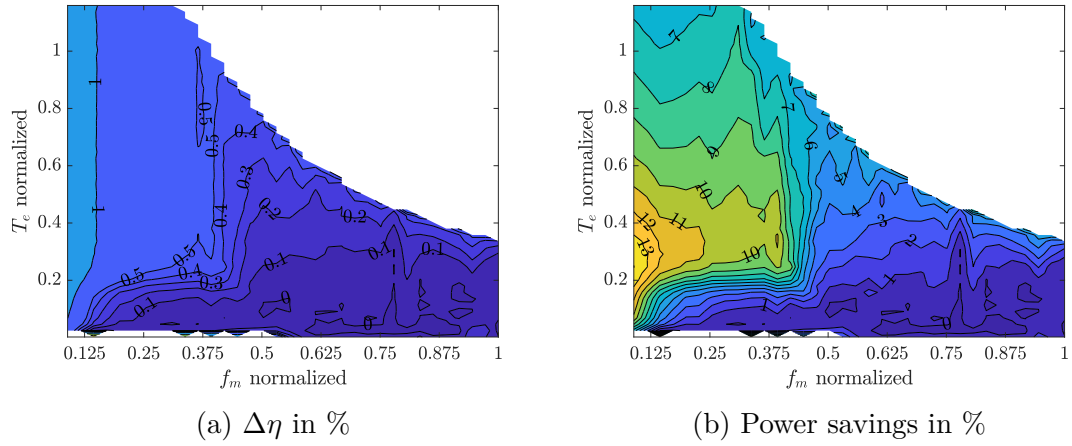
(b) Power savings in %

Figure 6.18: Efficiency gains and power savings between $f_{\mathrm{sw,opt}}$ and 10 kHz when $\theta_I = 0°$, DPWM2, and $R_C = 0.5$ mΩ for the polar machine

(a) $\Delta\eta$ in %
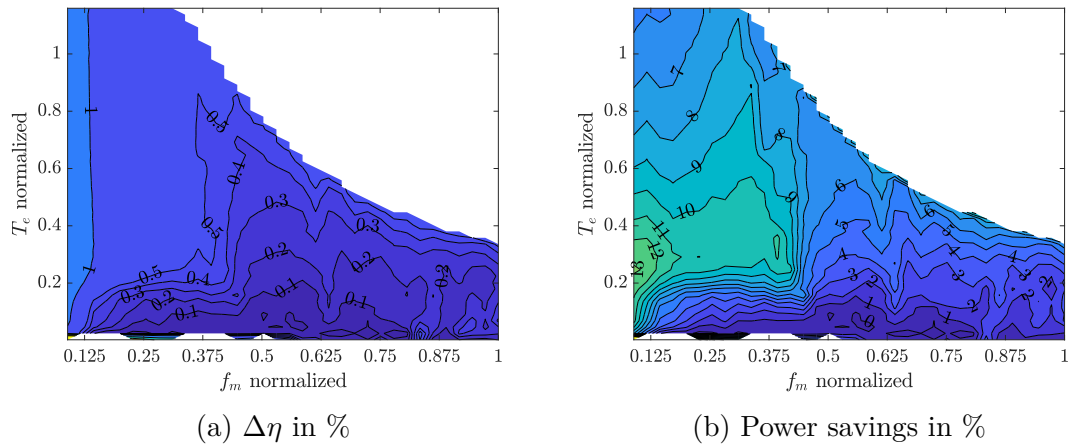
(b) Power savings in %

Figure 6.19: Efficiency gains and power savings between $f_{\mathrm{sw,opt}}$ and 10 kHz when $\theta_I = 0°$, DPWM3, and $R_C = 0.5$ mΩ for the polar machine

(a) $\Delta\eta$ in %
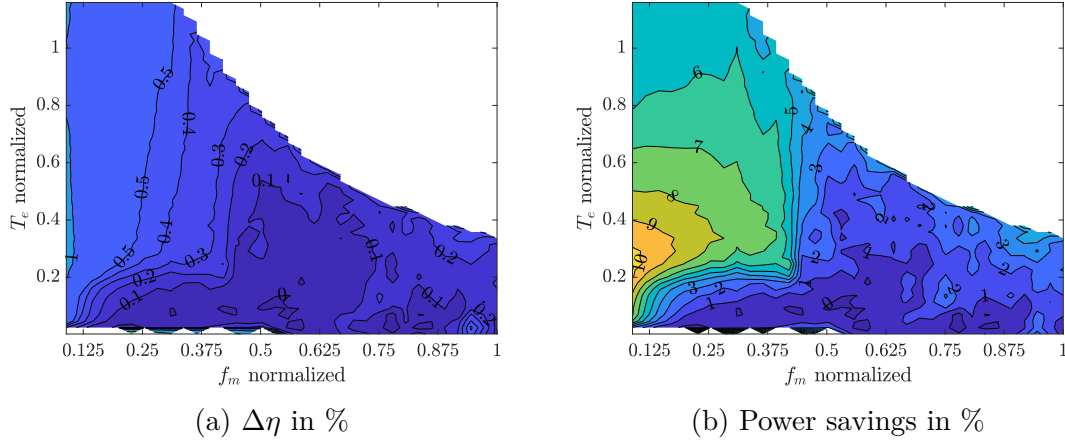
(b) Power savings in %

Figure 6.20: Efficiency gains and power savings between $f_{\mathrm{sw,opt}}$ and 10 kHz when $\theta_I = 0°$, VDPWM, and $R_C = 0.5$ mΩ for the polar machine

(a) $\Delta\eta$ in %
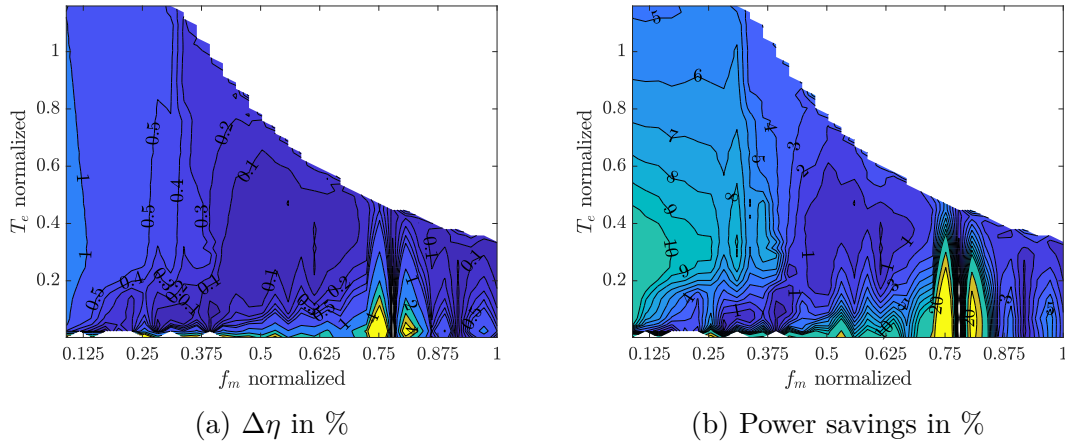
(b) Power savings in %

Figure 6.21: Efficiency gains and power savings between $f_{\mathrm{sw,opt}}$ and 10 kHz when $\theta_I = 0°$, D6ϕ SVM-B2, and $R_C = 0.5$ mΩ for the polar machine

6.3 PWM Method Optimization

Out of the investigated PWM methods in the asymmetric machine, D6ϕ SVM-B2, a 12-sector PWM method, and VDPWM are optimal for most of the operating space except the lower torque region where DPWM2 dominates, as Figures 6.22(a)-6.25(a) show. For the polar machine shown in Figures 6.22(b)-6.25(b), no single method dominates the operating space: it is shared between D6ϕ SVM-B2 in the high power region, VDPWM in the base speed region, and DPWM1 in the low torque field weakening region.

A clear trend between methods is that DPWM methods are optimal for leading current angles and VDPWM is optimal for lagging current angles. For highly coupled machines like the asymmetric machine, the D6ϕ SVM-B2 dominates near the zero current angle and low torques, if not everywhere for low switching frequencies. For lightly coupled machines like the polar machine, D6ϕ SVM-B2 is optimal at operating points with large power. D6ϕ SVM-B2 introduces additional 11th and

13$^{\text{th}}$ harmonics, which may worsen existing winding harmonics to increase machine losses during experiments. Its main advantage, however, remains that it commutes an by a factor of 5/12 with little increase in ripple, thus significantly reducing inverter losses with little machine loss penalties. Regarding the optimality of DPWM2 over VDPWM for low torques in the field-weakening region in the asymmetrical machine, one may posit the possibility that DPWM2 balances conducting and switching losses better than VDPWM. This unexpected result, however, actually motivates seeking an optimal clamping angle for minimal e-drive losses for a given switching frequency. Lastly, notice that SVM is nowhere optimal except for low switching frequencies in a small region near very low torques and mid speeds in the polar machine. DPWM3's optimality is similarly limited to low switching frequencies but spreads over a broader field-weakening region as shown in Figure 6.22(b).

(a) Asymmetric machine   (b) Polar machine
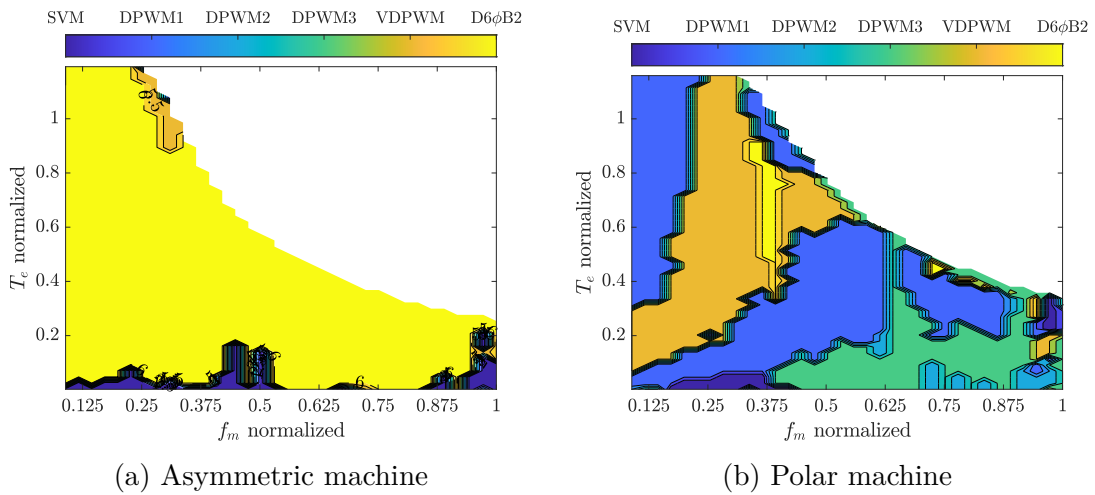
Figure 6.22: Optimal PWM method for $f_{\text{sw}} = 6$ kHz methods with $\theta_I = 0°$

(a) Asymmetric machine   (b) Polar machine
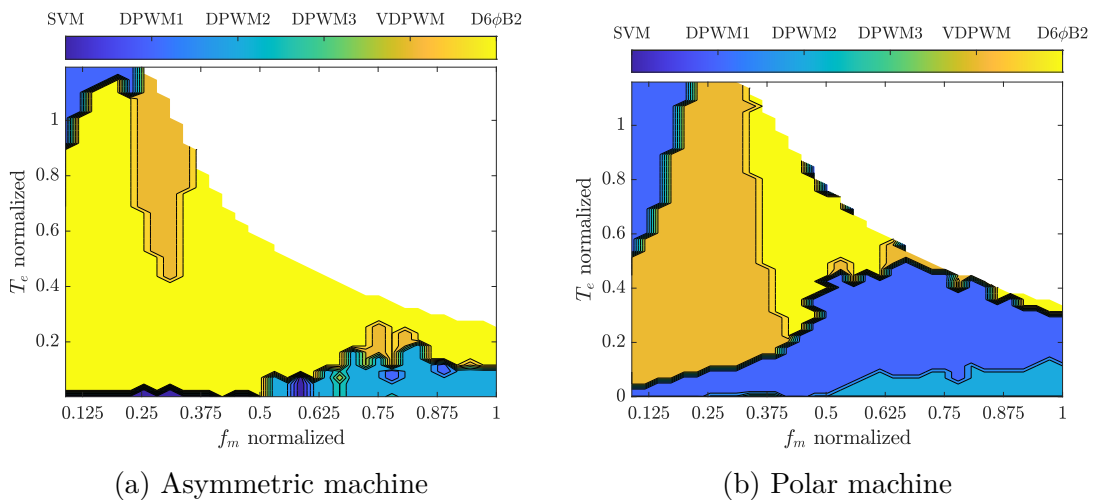
Figure 6.23: Optimal PWM method for $f_{\text{sw}} = 10$ kHz methods with $\theta_I = 0°$

(a) Asymmetric machine

(b) Polar machine
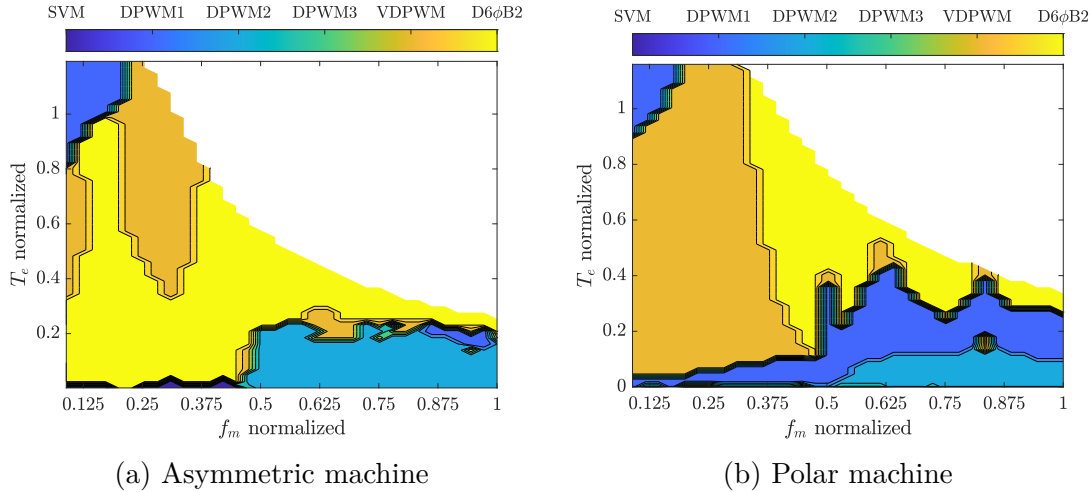
Figure 6.24: Optimal PWM method for $f_{\text{sw}} = 16$ kHz methods with $\theta_I = 0°$

(a) Asymmetric machine

(b) Polar machine
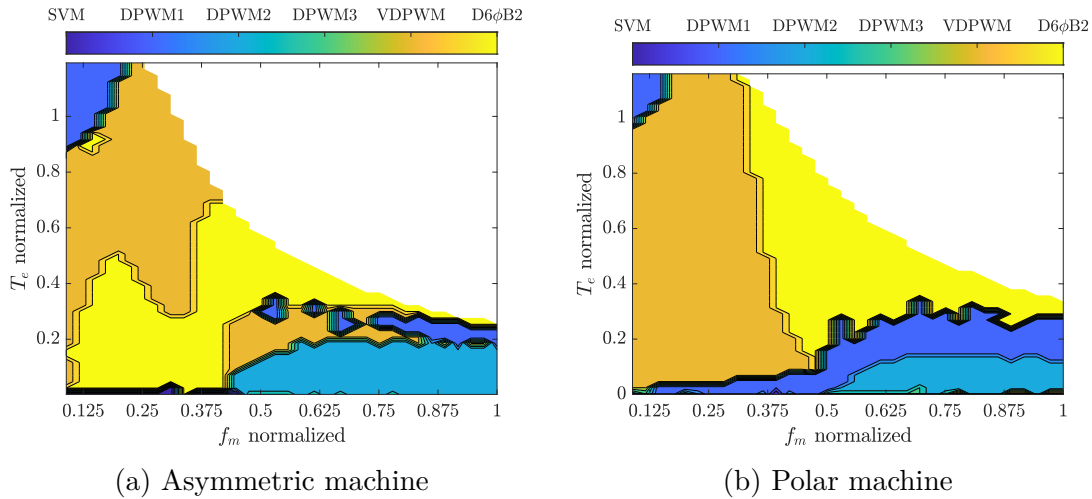
Figure 6.25: Optimal PWM method for $f_{\text{sw}} = 20$ kHz methods with $\theta_I = 0°$

As Figures 6.26-6.29 convey for the asymmetric machine, optimizing the PWM method delivers at least a maximum efficiency improvement of 1 % in large torque regions, with the benefits of PWM optimization increasing to about 2% and increasing to 1% in large power regions with increasing switching frequency. Like with switching frequency optimization, the power savings are most significant in the continuous operating region near mid speeds and low-mid torques. As we will see, that trend continues for the polar machine, which is more representative of typical three phase machines.

(a) $\Delta\eta$ in %
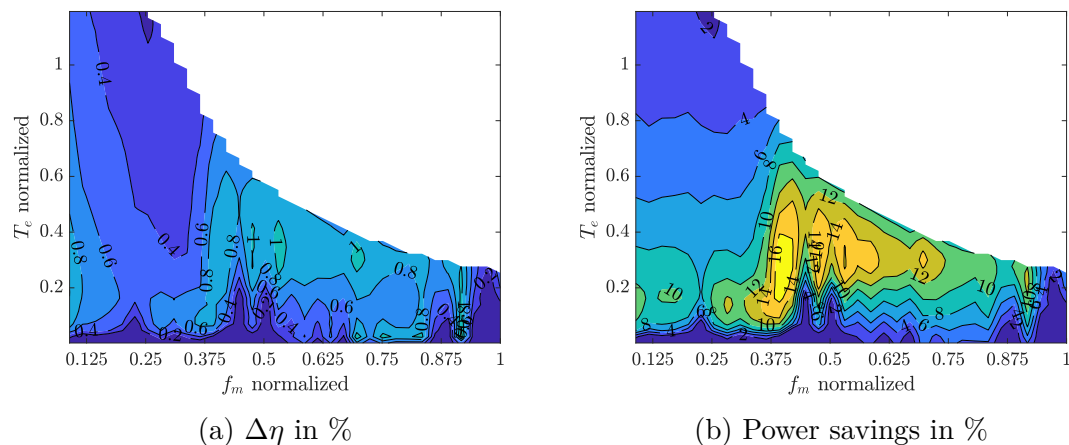
(b) Power savings in %

Figure 6.26: Efficiency gains and power savings between the optimal PWM program and SVM for $f_{\mathrm{sw}} = 6$ kHz with $\theta_I = 0°$ and $R_C = 0.5$ mΩ for the asymmetric machine

(a) $\Delta\eta$ in %
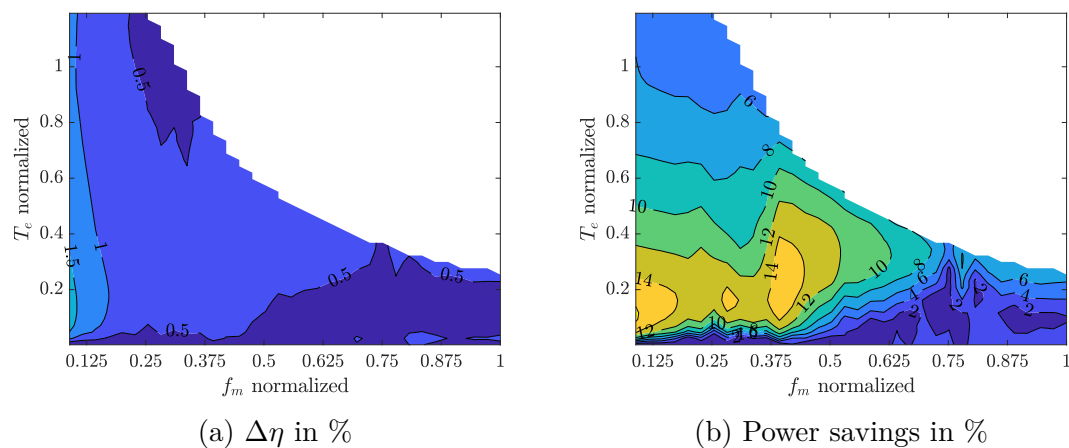
(b) Power savings in %

Figure 6.27: Efficiency gains and power savings between the optimal PWM program and SVM for $f_{\mathrm{sw}} = 10$ kHz with $\theta_I = 0°$ and $R_C = 0.5$ mΩ for the asymmetric machine

(a) $\Delta\eta$ in %
(b) Power savings in %
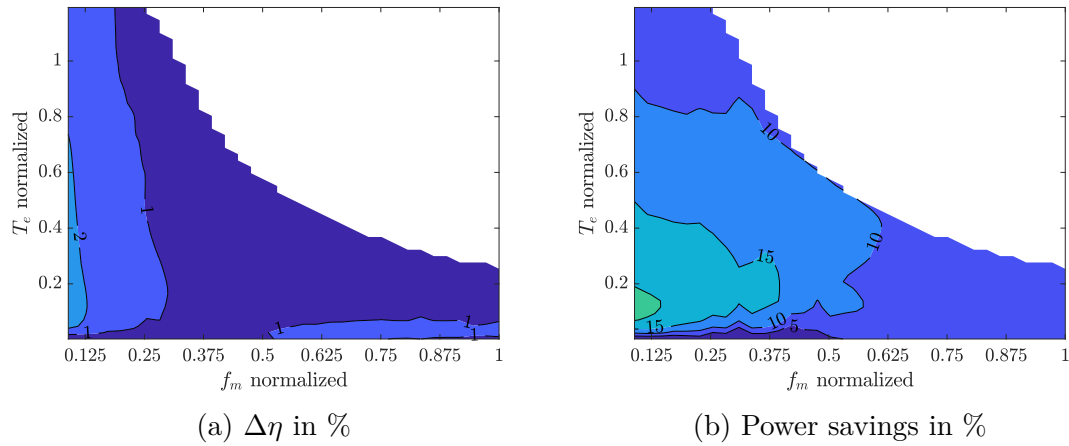
Figure 6.28: Efficiency gains and power savings between the optimal PWM program and SVM for $f_{\mathrm{sw}} = 16$ kHz with $\theta_I = 0°$ and $R_C = 0.5$ mΩ for the asymmetric machine

(a) $\Delta\eta$ in %
(b) Power savings in %
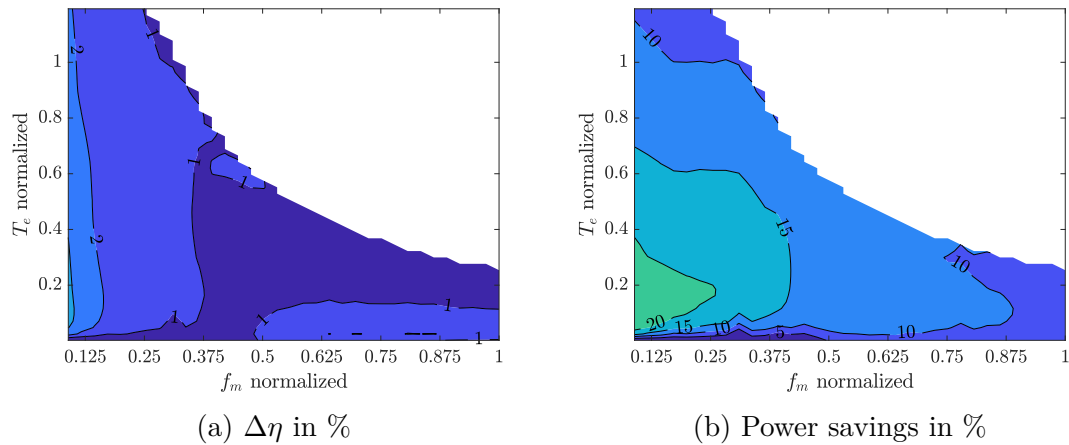
Figure 6.29: Efficiency gains and power savings between the optimal PWM program and SVM for $f_{\mathrm{sw}} = 20$ kHz with $\theta_I = 0°$ and $R_C = 0.5$ mΩ for the asymmetric machine

Inspecting Figures 6.30-6.33 reveals that in the polar machine, there is at least about 0.5% efficiency improvement, with improvements due to PWM optimization increasing as the switching frequency increases. The 1% iso-curve drifts to faster speeds as the switching frequency increases. In light of the fact that the polar machine resembles a typical three phase machine and the broader availability of more efficient inverters, optimizing for the PWM method is paramount from a power-savings perspective.

(a) $\Delta\eta$ in %
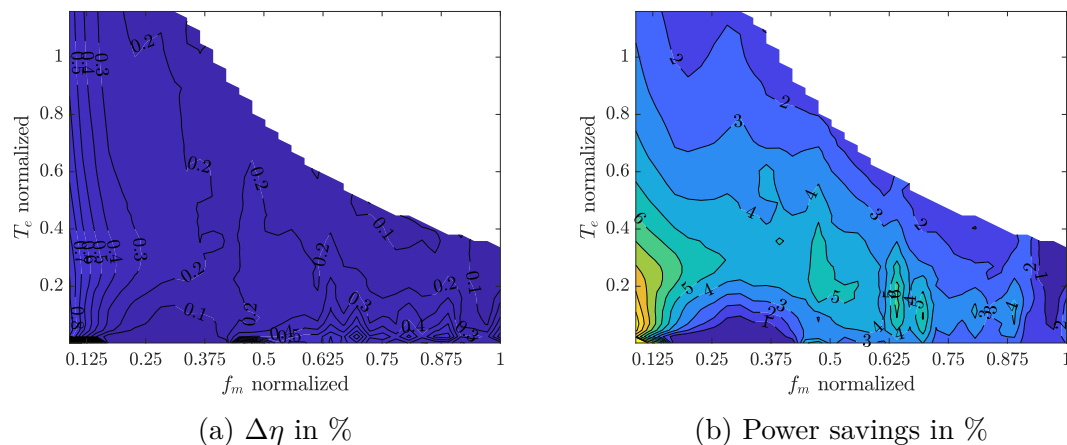
(b) Power savings in %

Figure 6.30: Efficiency gains and power savings between the optimal PWM program and SVM for $f_{\mathrm{sw}} = 6$ kHz with $\theta_I = 0°$ and $R_C = 0.5$ mΩ for the polar machine

(a) $\Delta\eta$ in %
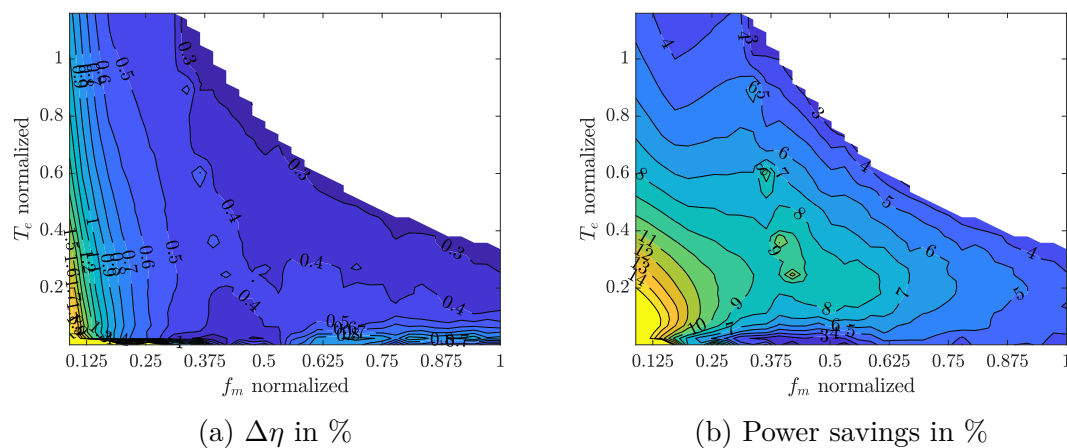
(b) Power savings in %

Figure 6.31: Efficiency gains and power savings between the optimal PWM program and SVM for $f_{\mathrm{sw}} = 10$ kHz with $\theta_I = 0°$ and $R_C = 0.5$ mΩ for the polar machine

150

(a) $\Delta\eta$ in %
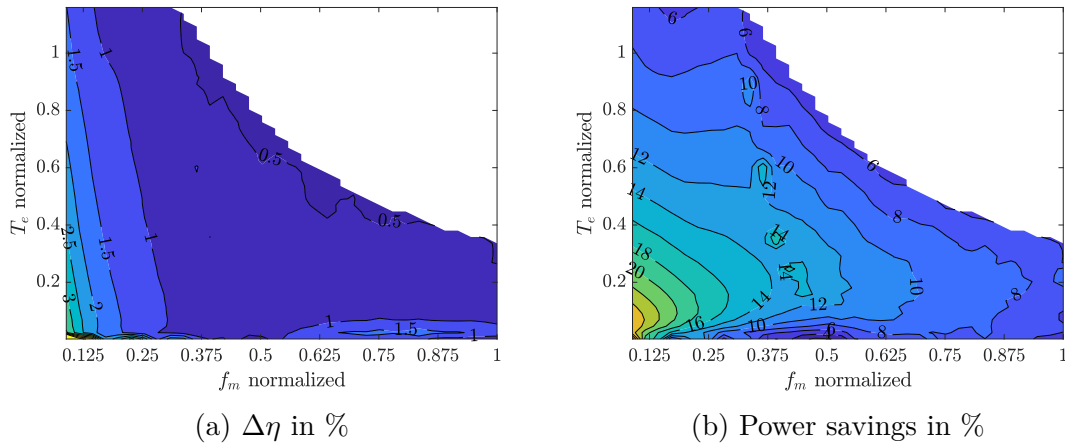
(b) Power savings in %

Figure 6.32: Efficiency gains and power savings between the optimal PWM program and SVM for $f_{\text{sw}} = 16$ kHz with $\theta_I = 0°$ and $R_C = 0.5$ mΩ for the polar machine

(a) $\Delta\eta$ in %
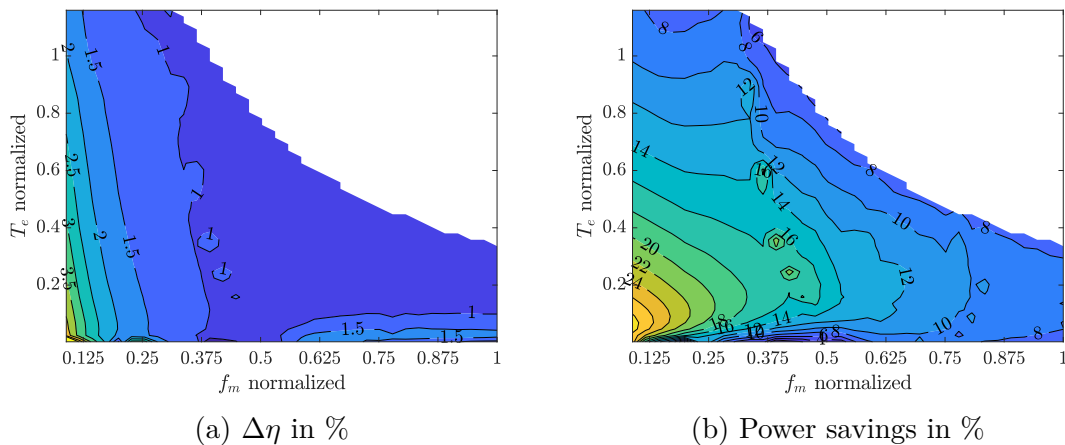
(b) Power savings in %

Figure 6.33: Efficiency gains and power savings between the optimal PWM program and SVM for $f_{\text{sw}} = 20$ kHz with $\theta_I = 0°$ and $R_C = 0.5$ mΩ for the polar machine

6.4 Switching Frequency and PWM Optimization

For a machine with overall large coupling coefficient ς like the asymmetric machine, D6ϕ SVM-B2 dominates the operating space with moderate switching frequencies in the field-weakening region. DPWM1 is optimal only for low torques in the field-weakening region, as Figure 6.34(b) shows. As mentioned before, the very low switching frequencies for large torques and low speeds may be due to the fitted inverter model, and SiC inverters will increase the optimal switching frequency in that region as well. The efficiency increase is significant, as the 1% iso-curve stretches for nearly all torques from the corner speed to zero torque, as Figure 6.35(a) conveys. The contribution to the efficiency increase from the switching and PWM optimizations are nearly equal but vary with operating point, as expected. SVM is almost nowhere optimal.

(a) Optimal f_{sw} program

(b) Optimal PWM method program
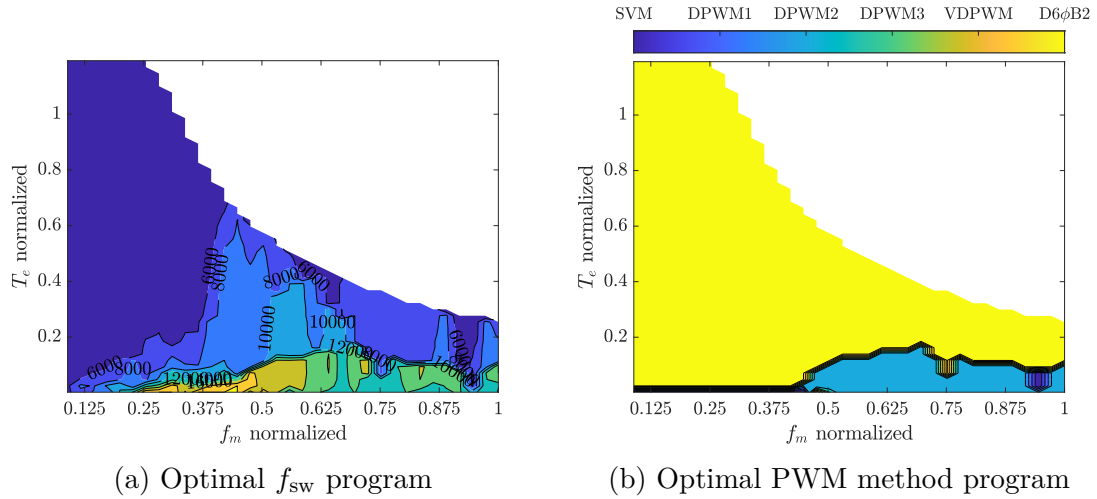
Figure 6.34: Optimal programs for the asymmetric machine

(a) $\Delta\eta$ in %
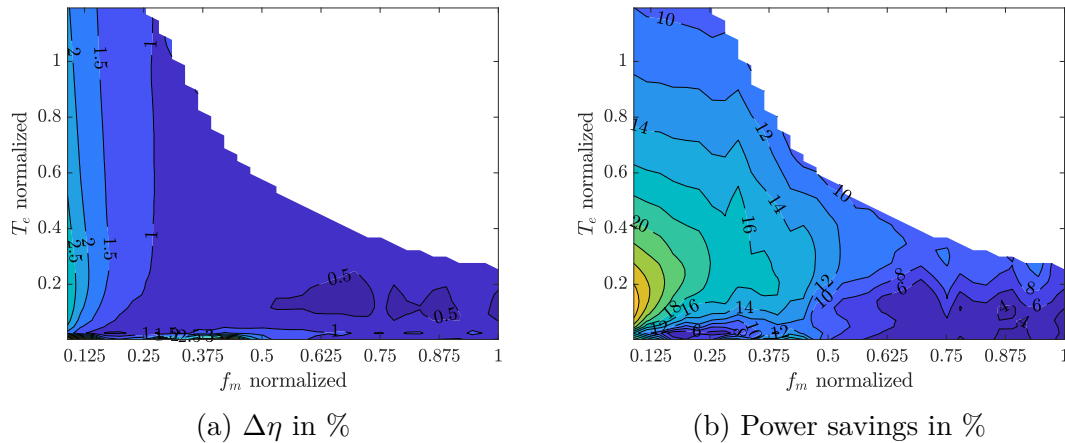
(b) Power savings in %

Figure 6.35: Efficiency gains and power savings between the optimal program and 10 kHz SVM with $\theta_I = 0°$ and $R_C = 0.5$ mΩ for the asymmetric machine

Figure 6.36(b) describing the polar machine shows a much more interesting variation in the optimal PWM method program compared to the asymmetric machine. As expected, D6ϕ SVM-B2 is suboptimal for lightly coupled machines, which allows all of the DPWM methods to share the operating space. Again, SVM is almost nowhere optimal. Figure 6.36(c) shows a much broader region of lower switching frequency, but as the polar machine has no additional 5th and 7th winding harmonics, the inverter model is less appropriate. It is therefore expected that even with IGBT's that the optimal switching frequency for large torques and low to mid speeds will increase in experiments.

(a) Optimal f_{sw} program

(b) Optimal PWM method program
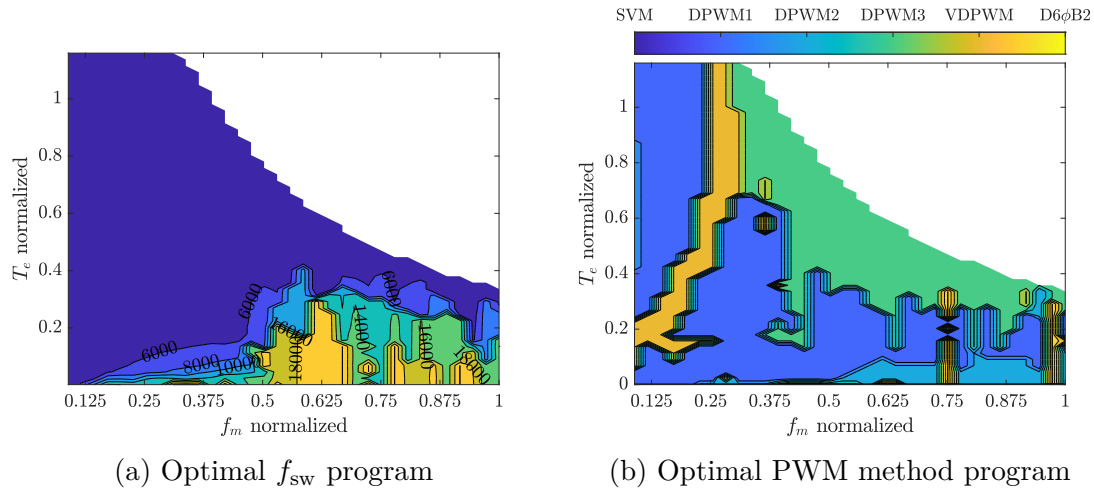
Figure 6.36: Optimal programs for the polar machine

Figure 6.37 show a similar increase in efficiency of 1% and power savings of about 15% as with the asymmetric machine. Given that the DPWM methods commute about 2/3 of the base switching frequency, the dominant loss mechanism is attributed to the switching loss. A current controller capable of controlling the machine with 2.5 kHz in that region is therefore necessary to implement the optimal programs for both the asymmetric and polar machines. Aside NVH concerns, optimizations in both machines show much promise.

(a) $\Delta\eta$ in %
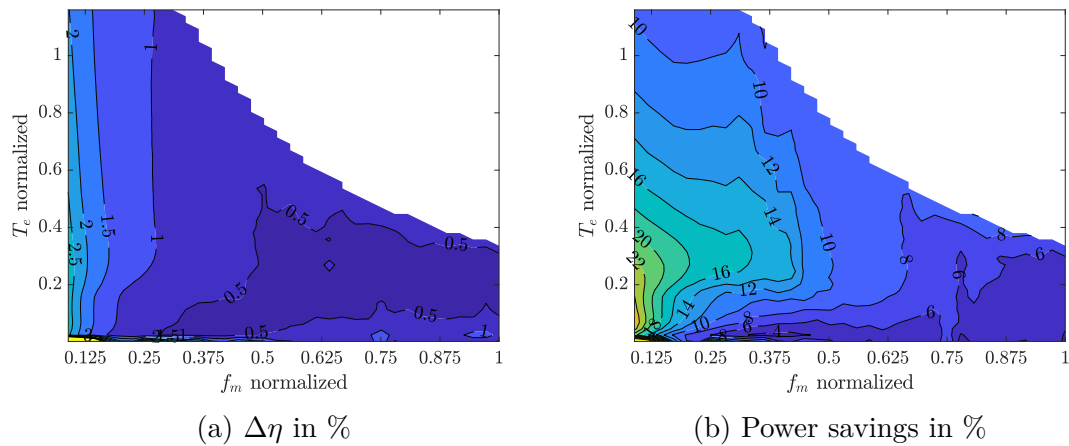
(b) Power savings in %

Figure 6.37: Efficiency gains and power savings between the optimal program and 10 kHz SVM with $\theta_I = 0°$ and $R_C = 0.5$ mΩ for the polar machine

Chapter 7

Experimental Results for an Asymmetrical Dual Three-Phase Machine and a Three-Phase Machine

The experimental results investigating two interleaving angles, various switching frequencies, and various PWM methods show that interleaving increases mostly the power losses along the isocurve modulation index $M = 2/\pi$ and low torques and that increasing the switching frequency broadly decreases machine losses. PWM data is only sufficient to confirm current angle and effective switching frequency loss dependencies. The frequency interactions in the magnet are confirmed by observing the spectrum of the sum of $d-$axis currents, which stand in for the $d-$axis linked flux. Figure 7.1 shows the layout of the components used for the measurements. The colored machine represents the dual three-phase asymmetric IPMSM, where two inverters are paginated to emphasize the test system's duality. The grayscale machine represents the loading machine, a three-phase IPMSM. The battery simulator along with the sensor arrays between it and the dual inverter and between the inverter and the machine are also shown. The blue block coupling the test and loading machine shafts represents the torque transducer. The sensor arrays and the torque and speed transducer connect to a power analyzer and an oscilloscope. Auxiliary systems like the thermal circuit with oil pumps and heat exchangers are not shown in Figure 7.1. They play an important role in not only maintaining the temperature of the machine and inverter within operating range to avoid component damage but also to ensure reliable measurements, as many loss components depend on temperature.
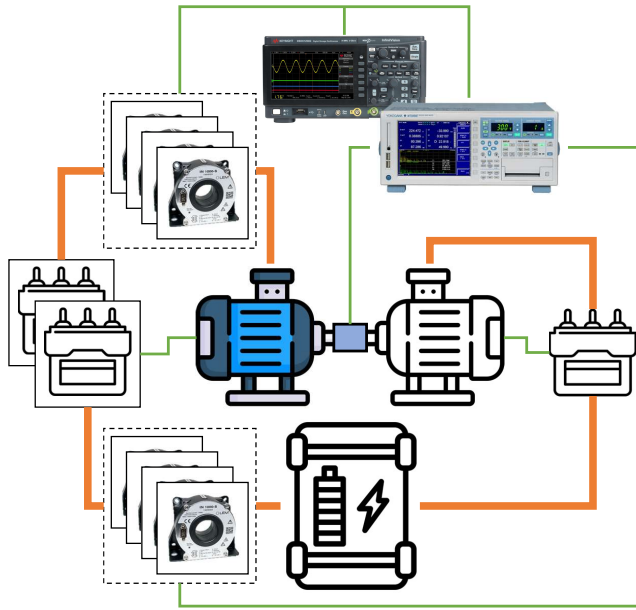
Figure 7.1: Measurement layout

7.1 Interleaving Angle Variation

One may ascertain changes in losses due to the changes in the interleaving angle, or delay, in two ways: one by driving points to steady state over the entire operating range with both angles, and the other by choosing one operating point and changing the angle to record the transient system response. In this section both test results are presented. It is found that interleaving causes an increase of c.a. 1kW, or 3% efficiency at low torques and mid-speeds, and an overall increase in losses, especially along the $M = 2/\pi \approx 0.6$ modulation index iso-curve on the torque-speed plane. Loss increases occur mainly in the stator iron and the magnets. The FEM does not capture the additional losses for low torques near the $M = 0.6$ iso-curve, but a high-frequency coupling model that completely explains the missing losses was developed and shown in Figure 5.32. The model is based on the changing magnetic permeability seen in most lamina steels with coupled Faraday and Amperès laws, which is usually not modeled using FEM. Another possible explanation for the increased losses at low torques involves the anisotropy of the non-oriented electrical steel.

7.1.1 Equilibrium Loss Difference

Figure 7.2 shows the copper losses for interleaving on and off and Figure 7.3 show the copper loss difference between interleaving on and off. Figure 7.3(a) shows negligible copper loss difference except for 325V near $M \approx 0.6$ at large torques. There, the copper losses reach 150 W. Paradoxically, one cannot say the same about loss differences in copper for 400V in the same region, suggesting another mechanism causes the additional losses in copper other than interleaving. Figure 7.2 shows the raw copper losses, which, because of the current commissioning used (MTPA), follows the current magnitude contours.

(a) $\theta_I = 90°$, $V_{\text{DC}} = 325$ V

(b) $\theta_I = 0°$, $V_{\text{DC}} = 325$ V

(c) $\theta_I = 90°$, $V_{\text{DC}} = 400$ V

(d) $\theta_I = 0°$, $V_{\text{DC}} = 400$ V
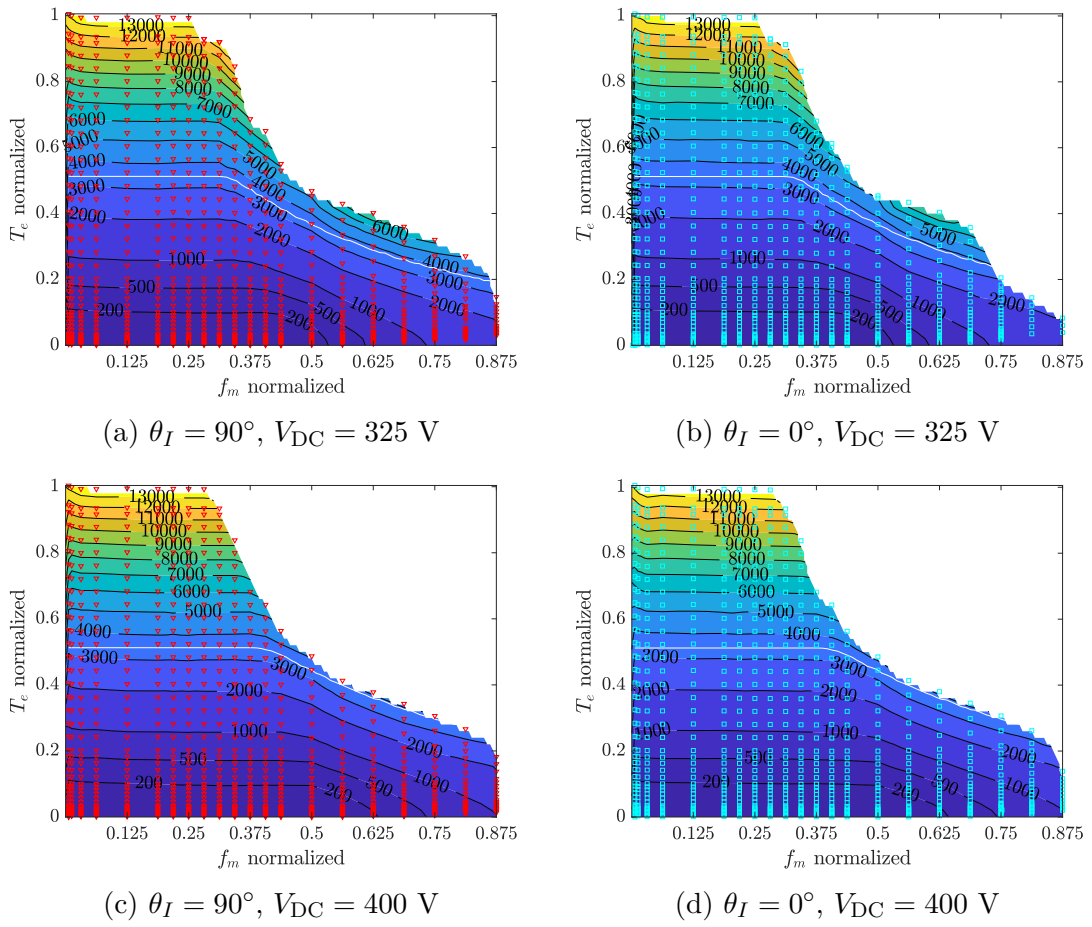
Figure 7.2: Copper loss in W

(a) $V_{\text{DC}} = 325$ V

(b) $V_{\text{DC}} = 400$ V
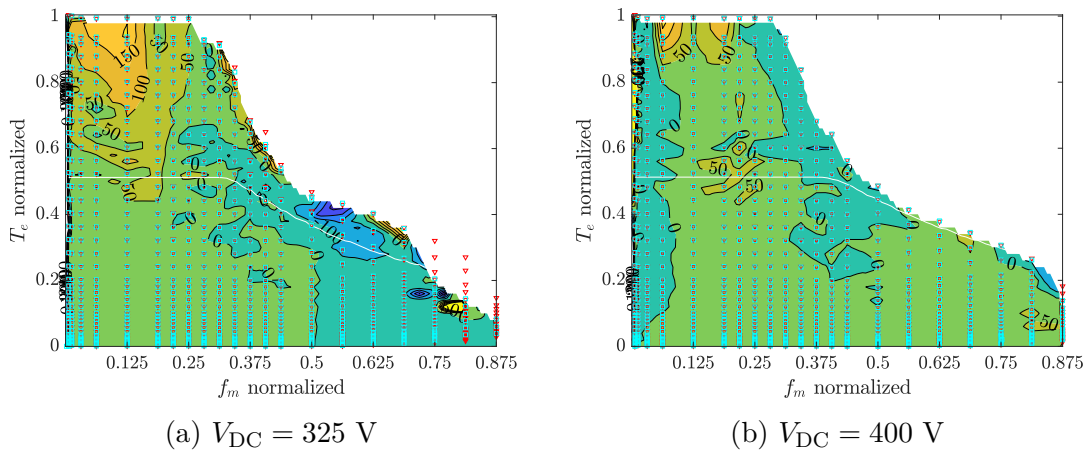
Figure 7.3: Copper loss difference, $P_{\text{Cu}}(90°) - P_{\text{Cu}}(0°)$ in W

(a) $\theta_I = 90°$, $V_{\mathrm{DC}} = 325$ V

(b) $\theta_I = 0°$, $V_{\mathrm{DC}} = 325$ V

(c) $\theta_I = 90°$, $V_{\mathrm{DC}} = 400$ V

(d) $\theta_I = 0°$, $V_{\mathrm{DC}} = 400$ V
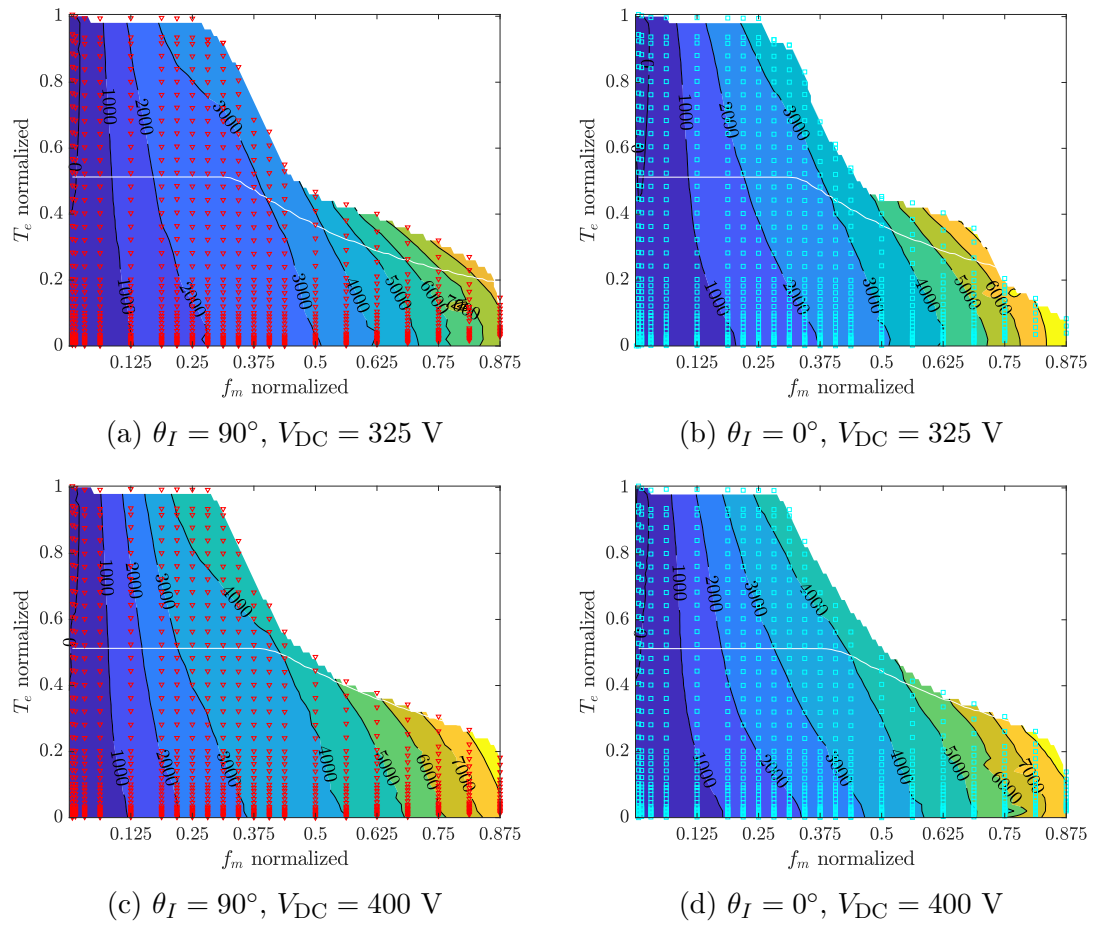
Figure 7.4: Remnant loss in W

(a) $V_{\mathrm{DC}} = 325$ V

(b) $V_{\mathrm{DC}} = 400$ V
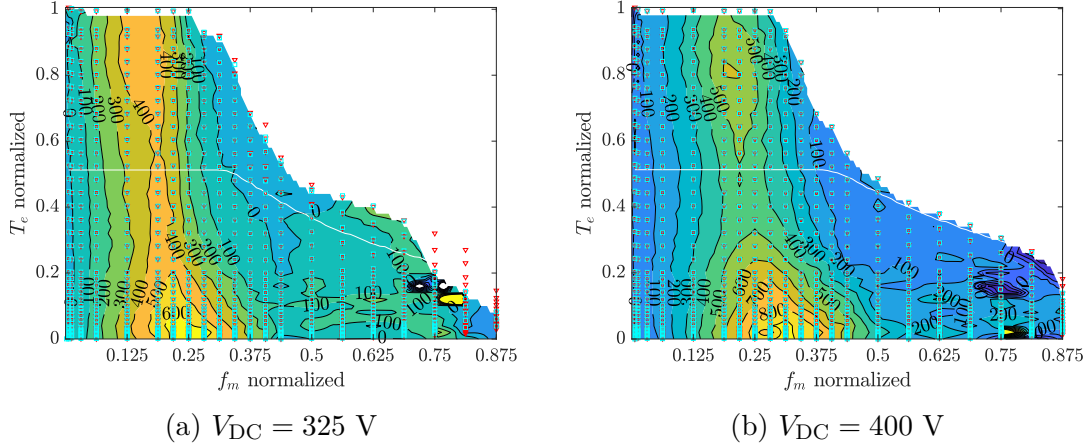
Figure 7.5: Remnant loss difference, $P_{\mathrm{Re}}(90°) - P_{\mathrm{Re}}(0°)$ in W

Figures 7.4-7.5 show the remnant loss and remnant loss difference between off-setting pulses and not offsetting pulses respectively, where remnant loss is simply the total loss minus the copper losses displayed in Figures 7.2 and 7.3. As a result, Figure 7.4 contains losses in the iron, losses in the magnets, and miscellaneous mechanical losses such as bearing friction and fluid cooling viscous and dynamic losses. Since the same bearings, coolant, coolant temperature and pressure were used for each of the tests, the loss difference shown in Figures 7.5 should represent the loss difference in the iron and magnets as a result of interleaving between dual machines. As expected, the losses increase almost everywhere. For $V_{\mathrm{DC}} = 325$ V as shown in Figure 7.5(a), the power loss difference in the region near the operational boundary between the corner speed and 0.5625 normalized speed is slightly negative, and for $V_{\mathrm{DC}} = 400$ V as shown in Figure 7.5(b) only one spot at 0.12 normalized moment and 0.75 normalized speed displays a negative loss difference.

Like Figures 7.2(b) and (d), Figure 7.4(b) has significantly reduced operating area compared to Figure 7.4(d), as the maximum power curve is rather abruptly reduced at around 0.75 normalized speed, and therefore the difference maps neglect that area. Figures 7.4(a) also has a reduced operating area compared to Figure 7.4(c), but the reduction is significantly less. In addition, the correspondence between the achieved electromagnetic torques is reduced. Since the holes, so to speak, near 0.75 normalized speed appear at ∼0.12 normalized moment for both voltages, despite the reduced operating area for 325 V, it is likely that it is independent of DC bus voltage. Namely, the stability and settling properties lead to oscillating currents and therefore different power readings. Since the hole is negative, interleaving reduces the loss peak there and likely reduces circulating currents.

Compared to the iron loss difference simulation in Figure 5.24, most losses are missing for torques less than 0.2 normalized moment. Accounting for the missing losses in this region is paramount because it lies in the continuous operation region of the machine and reduces the efficiency by 1% there. Even if interleaving is not used, coupling is large for conventional three phase IPMSMs in that region. The the losses also increase with voltage in that region, meaning that they are likely due to converter effects on the machine. Furthermore, after inspecting Figure 5.37, the loss difference between 10 kHz and 20 kHz does not account for the loss difference seen in Figures 7.5(a) and (b). As mentioned before, interleaving with $\theta_I = 90°$

creates an additional 20 kHz harmonic. The magnet losses cannot account for the loss increase either, since the additional 20 kHz harmonic in each of the i_{d1} and i_{d2} cancel upon addition, the flux as seen by the magnet does not have the additional 20 kHz harmonic. Note however, that the $2f_{sw}$ harmonic does not cancel in the stator. Also, although even non-oriented electrical steels exhibit magnetic anisotropy due to rolling [137], the inherently circular geometry of the lamina causes the magnetic field to see all magnetic property orientations within a mechanical period: from a mechanical period-averaged power loss perspective, the electrical steel is isotropic. Even isotropic steels have a permeability droop near zero magnetic fields. It then increases to its maximum to decay once more as the iron saturates. The permanent magnet however, offsets the field after the permeability maximum to allow for field-weakening operation, neutralizing any effects the zero field permeability droop may have on average. The test-setup had many long cables, but at a few meters, their inductance and mutual inductance is in the tens of nH, which is much too small to cause additional losses in the range we seek; the cables furthermore run through air, not iron, so any additional loss will occur in the copper wires. The model in Figure 5.31 approaches the desired trend, but the modeled equivalent bulk magnetic field has a heuristic factor of 9/8 and the increase in losses at large torques from mid-torques are not captured. That suggests that permeability changes with frequency. The issue then becomes that of determining the adequate high frequency permeability that the FEM model could not take into account. Since the FEM model only uses real permeability, one may posit the use of complex permeability. Complex permeability arises due to a delay between the magnetic field, H, and the magnetic field density B in time, which presupposes some equivalent resistance, i.e. loss. That loss ensues due to mostly eddy currents at high frequency with Ampère's law included in addition to Faraday's law; if Faraday's law were exclusively used, field dispersion as a result of the reaction field, and therefore complex permeability, are not modeled. Complex permeability, or field delay, is therefore a way to model the sum of the exciting and reaction fields in bulk. As a permeability, complex permeability not only varies with frequency but also with amplitude, which requires further extensive characterization of the ferromagnetic material. Since equation (5.1.3) models wide plates relevant to machine lamina with the reaction field subject to spatially uniform and time-varying H at the boundaries, only a bulk and real permeability becomes necessary, albeit with a small bulk factor as mentioned before and high-frequency characterization outside of a complex permeability framework. One may therefore conclude that the FEM's internal eddy current calculator neglects the reaction field.

One may also incorporate the permeability variation into a high-frequency coupling inductance model similar to the boundary condition-based model summarized in Table II in Chapter 7, but augmented it with inductance information, as in 5.31. Figure 5.31(a) shows the current ripple difference from said model and Figure 5.31(b) replicates the information shown in Figure 7.5 except instead of having a current level curve and the operating points it has the $M = 0.6$ and maximum power difference level curves. The modulation index $M = 0.6$ level curve is also shown in white and the maximum ripple for every level torque is shown as a dash-dot line. As one may observe, there is good agreement between the two.

(a) $V_{\text{DC}} = 325$ V   (b) $V_{\text{DC}} = 400$ V
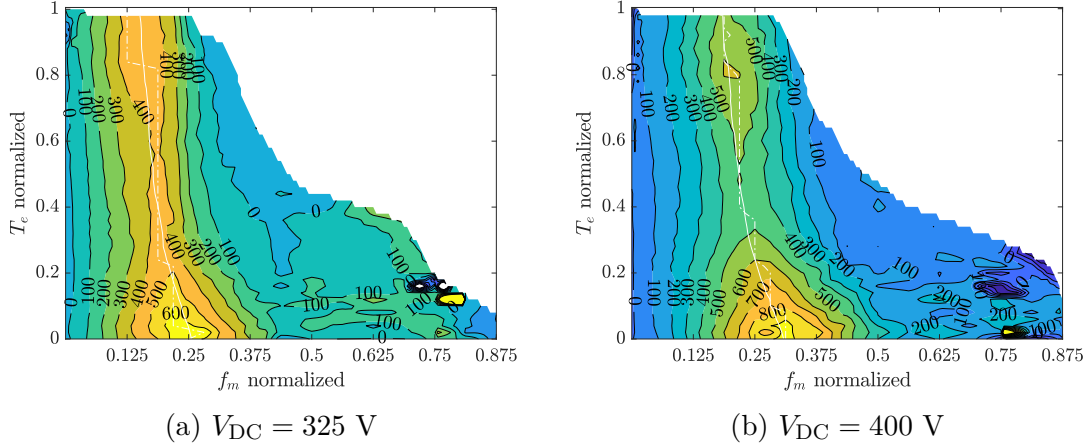
Figure 7.6: Remnant loss difference, $P_{\text{Re}}(90°) - P_{\text{Re}}(0°)$ in W

A full treatment of permeability malleability effects requires modeling the zero-field permeability droop, the material anisotropy shown in Figure 7.7, the reaction field, and permeability frequency dependence, all of which are typically not simulated in FEA due to solver convergence and simulation duration issues. Since the permeability droop encompasses such a small range of H near zero, and since the linked flux from the permanent magnet biases the field, there are few places where the $H-$field nears zero. Furthermore, flux would leak less due to the droop because the area with lower magnetic field has less permeability than if it were left constant from the permeability peak to the zero field.

(a) μ_r (b) Shiozaki diagram [137] for $\max(\mu_r)$
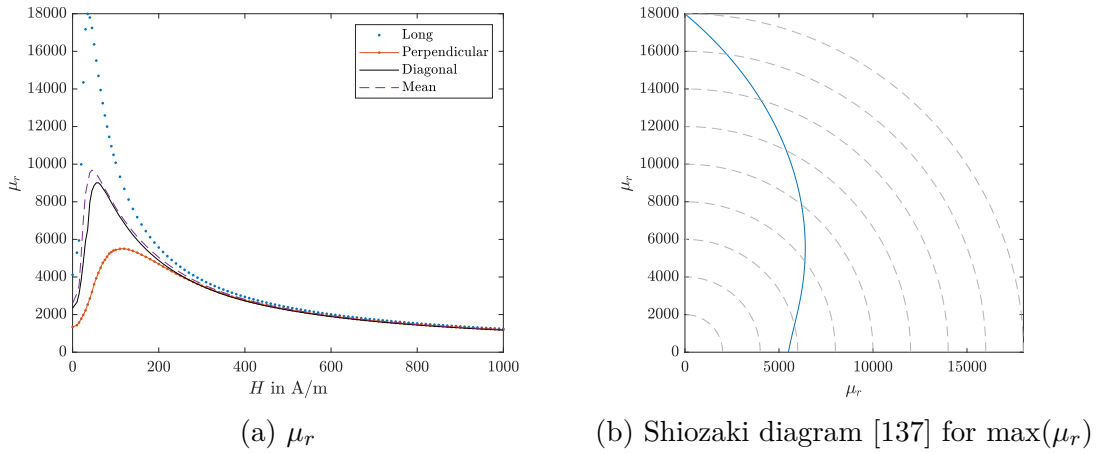
Figure 7.7: Relative magnetic permeability of non-oriented magnetic steel along different directions

7.1.2 Transient Loss Difference

To confirm that the increase in losses are caused by increasing the interleaving angle to $\theta_I = 90°$, transient measurements were recorded with a step change in the interleaving angle. Along with an increase and decrease in the mean iron temperature corresponding to a linear response to the step change, one may confirm the increased losses are caused by the change in interleaving angle. Measurements changing the

160

interleaving angle were also taken at different switching frequencies to show the independence of the increase in losses from the switching frequency, as Figure 7.8 shows. Figure 7.8 also shows the decreasing machine losses with increasing switching frequency, as observed in the equilibrium measurements. The coolant temperature was kept the same for all tests and we allowed a pause in order to have similar temperature initial conditions.

(a) $f_{sw} = 8$ kHz

(b) $f_{sw} = 10$ kHz

(c) $f_{sw} = 16$ kHz

(d) $f_{sw} = 20$ kHz
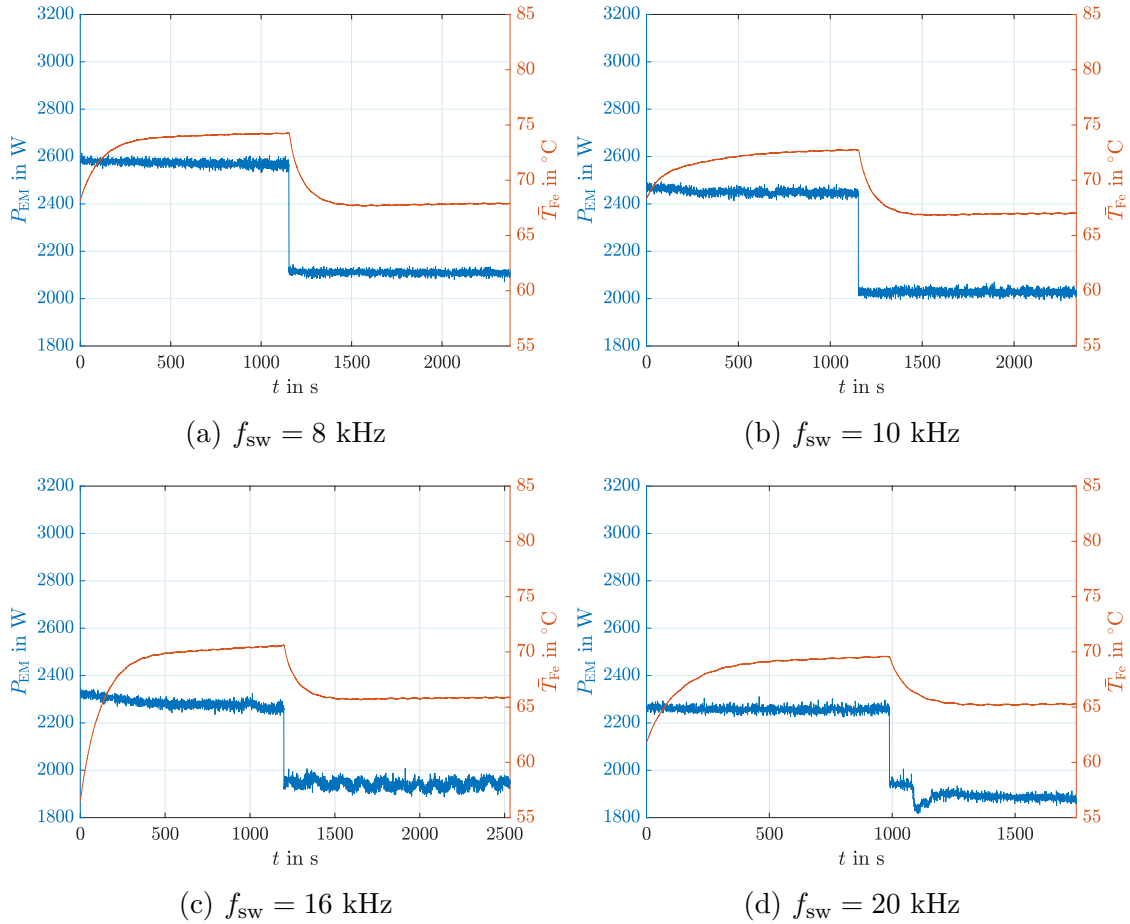
Figure 7.8: Transient loss and temperature changes at 0.1 norm. moment, 0.3125 norm. speed, and $U_{DC} = 325$ V for various switching frequencies

161

(a) $U_{\mathrm{DC}} = 325$ V   (b) $U_{\mathrm{DC}} = 400$ V
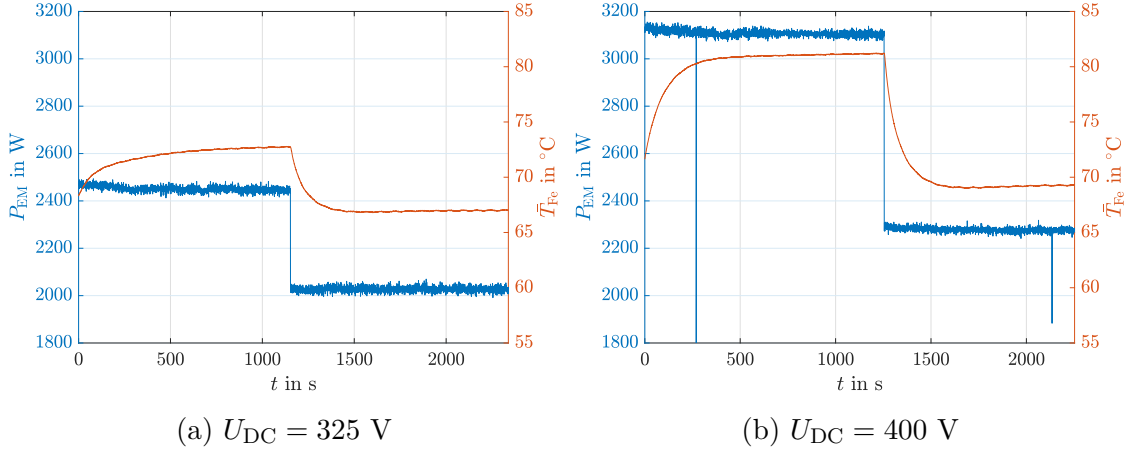
Figure 7.9: Transient loss and temperature changes at 0.1 norm. moment, 0.3125 norm. speed, and $f_{\mathrm{sw}} = 10$ kHz for various DC bus voltages
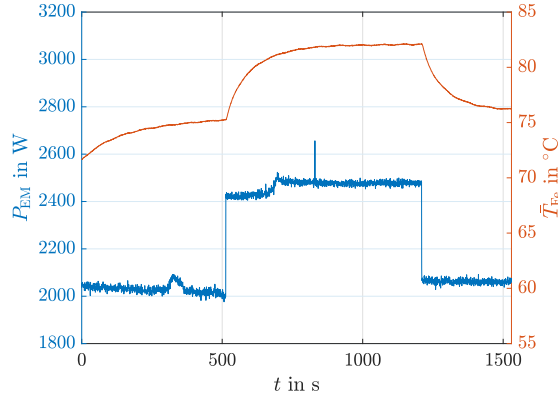
Figure 7.10: Transient loss and temperature changes at 0.1 norm. moment, 0.3125 norm. speed, $f_{\mathrm{sw}} = 10$ kHz, $U_{\mathrm{DC}} = 325$ V, and $\alpha_{\mathrm{control}} = 0°$

Figure 7.9 highlights the effect of increasing the DC bus voltage on machine losses, namely that the machine losses increase overall as well as the changes in power loss and therefore temperature. Lastly, Figure 7.10 shows an interleaving angle sequence of 0°, 90°, and 0° instead of just 90°, and 0° like Figures 7.8 and 7.9. It contains data for when the control angle between the two duals, $\alpha_{\mathrm{control}} = 0°$ instead of the usual 30°. That Figures 7.9(a) and 7.10 have similar changes in machine losses and losses overall shows that interleaving causes losses due to much larger frequencies than the fundamental, and are therefore independent of the underlying control.

7.2   Switching Frequency Variation

The reduction in machine losses and increase in inverter switching losses upon increasing switching frequency −keeping the sampling frequency the same −are presented in this chapter subsection. The results show that having the same sampling frequency with different switching frequencies introduces sampling harmonics that slightly modify the expected negative correlation between switching frequency and

machine losses.

7.2.1   Equilibrium Loss Difference in the Electrical Machine

Starting by inspecting Figure 7.11, one may notice that with any investigated switching frequency, interleaving with a 90° angle, increases machine losses almost everywhere in the torque-speed plane, especially along the $M = 0.6$ iso-curve, as explained in Chapter 7.1. The isolated troughs and peaks in all plots in Figure 7.11 are mostly due to unsettled transients, especially the one in 7.11(c) at 0.46 normalized moment and 0.0625 normalized speed. Also notice that Figure 7.11(b) and (d) reach different power levels at large speeds in the field-weakening region. That is likely because the dead-time compensation was the same irrespective of the actual dead-time, a mismatch that injects an additional and destabilizing 5th harmonic. The reduced power occurs for 0 μs dead-time, irrespective of interleaving. Destabilization occurs for lower speeds for 20 kHz switching because the dead-time compensation is a larger proportion of the switching period, and therefore commands more compensating voltage.

(a) $f_{\text{sw}} = 8$ kHz

(b) $f_{\text{sw}} = 10$ kHz

(c) $f_{\text{sw}} = 16$ kHz

(d) $f_{\text{sw}} = 20$ kHz
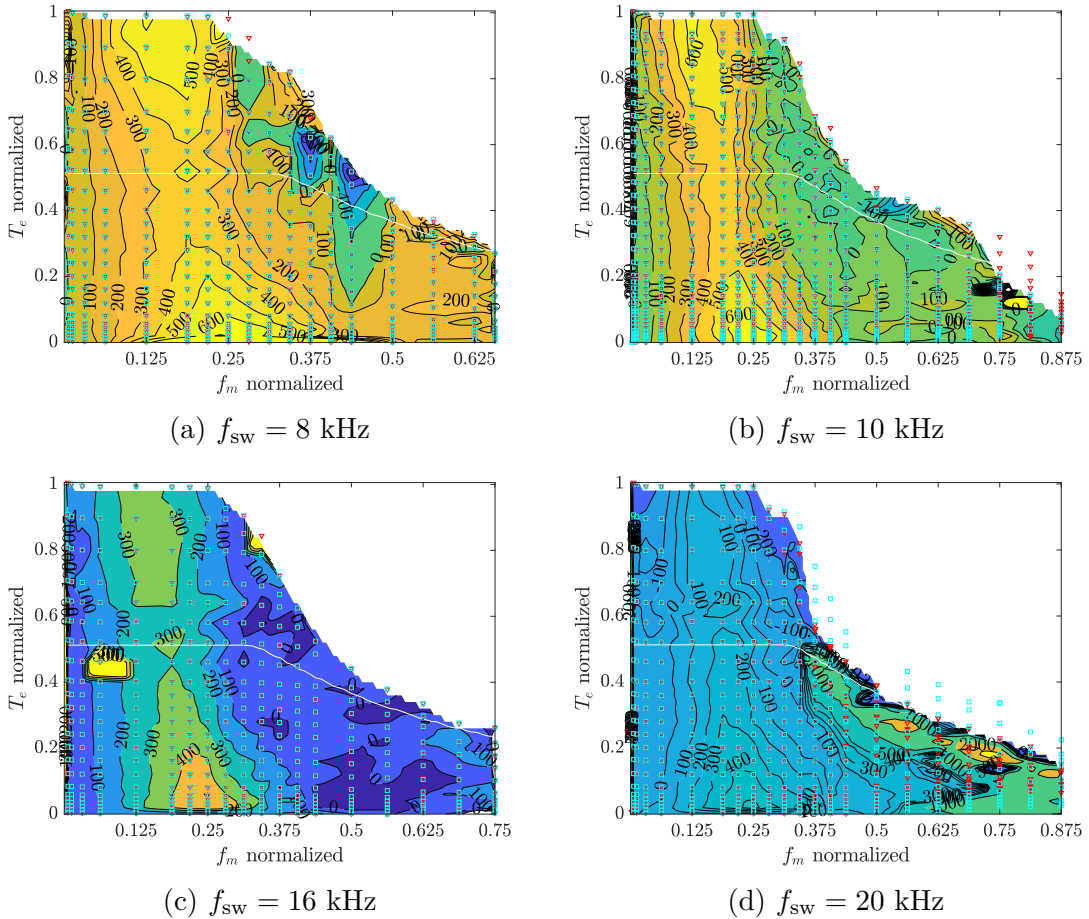
Figure 7.11: $P_{\text{EM}}(90°) - P_{\text{EM}}(0°)$

Figure 7.12 and Figure 7.13 show the different combinations of machine loss differences upon exciting the machine with switching frequencies of 8, 10, 16, and 20 kHz. Figure 7.12 shows the machine loss differences with interleaving on and Figure 7.13 shows the machine loss differences with interleaving off. The figures

show that machine losses increase with decreasing switching frequency for most operating points. Switching at 20 kHz and sampling at 10 kHz increases machine losses for large torques in the field-weakening region more than any other switching frequency. Similarly, machine losses are greater for 16 kHz than 10 kHz near the power limits and at low speeds. The reason for those trend exceptions is currently unknown but is likely due to unsettled transients.

(a) $P_{\mathrm{EM}}(10\ \mathrm{kHz}) - P_{\mathrm{EM}}(8\ \mathrm{kHz})$

(b) $P_{\mathrm{EM}}(10\ \mathrm{kHz}) - P_{\mathrm{EM}}(16\ \mathrm{kHz})$

(c) $P_{\mathrm{EM}}(10\ \mathrm{kHz}) - P_{\mathrm{EM}}(20\ \mathrm{kHz})$

(d) $P_{\mathrm{EM}}(20\ \mathrm{kHz}) - P_{\mathrm{EM}}(8\ \mathrm{kHz})$

(e) $P_{\mathrm{EM}}(20\ \mathrm{kHz}) - P_{\mathrm{EM}}(16\ \mathrm{kHz})$

(f) $P_{\mathrm{EM}}(16\ \mathrm{kHz}) - P_{\mathrm{EM}}(8\ \mathrm{kHz})$

Figure 7.12: ΔP_{EM} for different f_{sw} for $\theta_I = 90°$

(a) $P_{\mathrm{EM}}(10\text{ kHz}) - P_{\mathrm{EM}}(8\text{ kHz})$

(b) $P_{\mathrm{EM}}(10\text{ kHz}) - P_{\mathrm{EM}}(16\text{ kHz})$

(c) $P_{\mathrm{EM}}(10\text{ kHz}) - P_{\mathrm{EM}}(20\text{ kHz})$

(d) $P_{\mathrm{EM}}(20\text{ kHz}) - P_{\mathrm{EM}}(8\text{ kHz})$

(e) $P_{\mathrm{EM}}(20\text{ kHz}) - P_{\mathrm{EM}}(16\text{ kHz})$

(f) $P_{\mathrm{EM}}(16\text{ kHz}) - P_{\mathrm{EM}}(8\text{ kHz})$
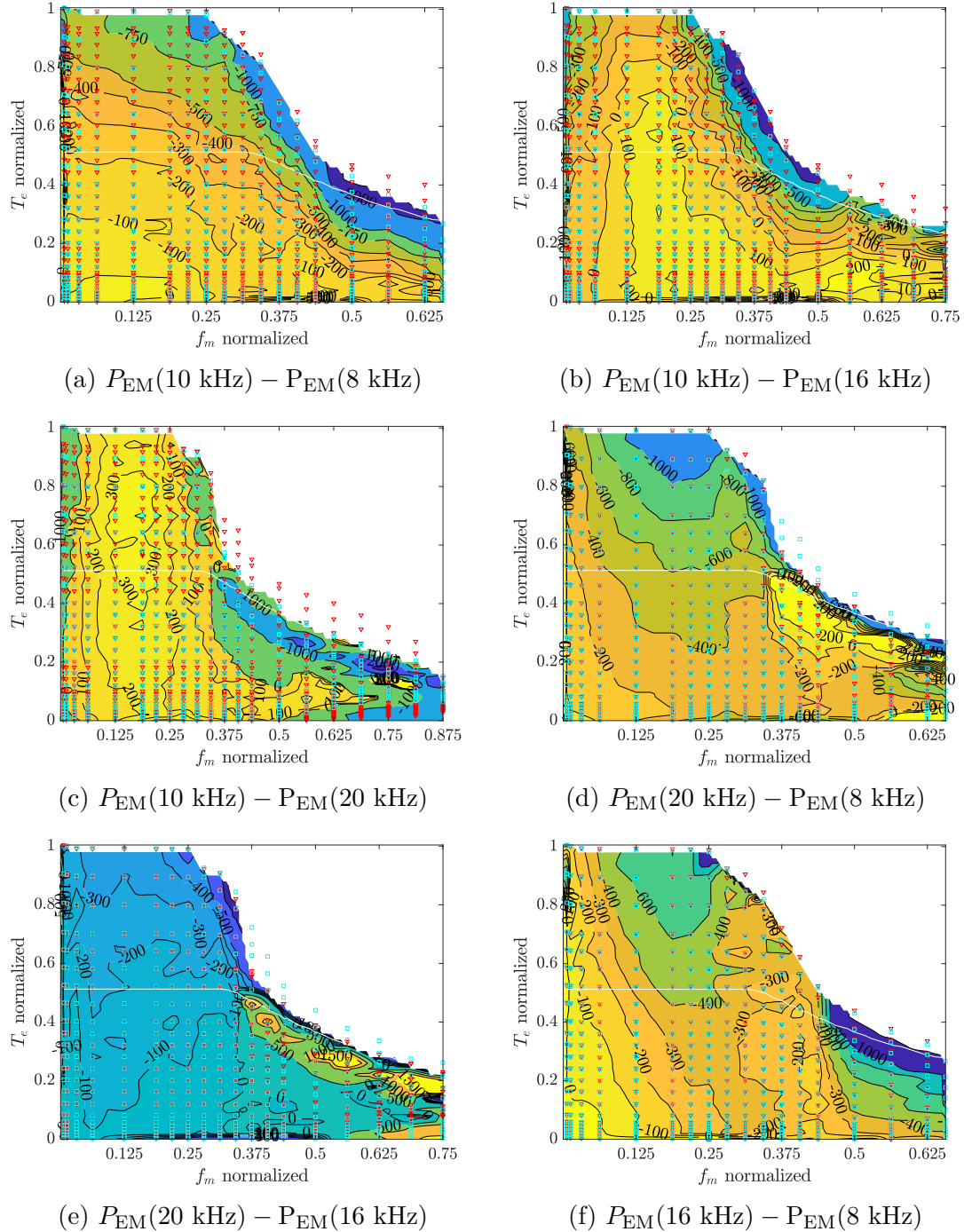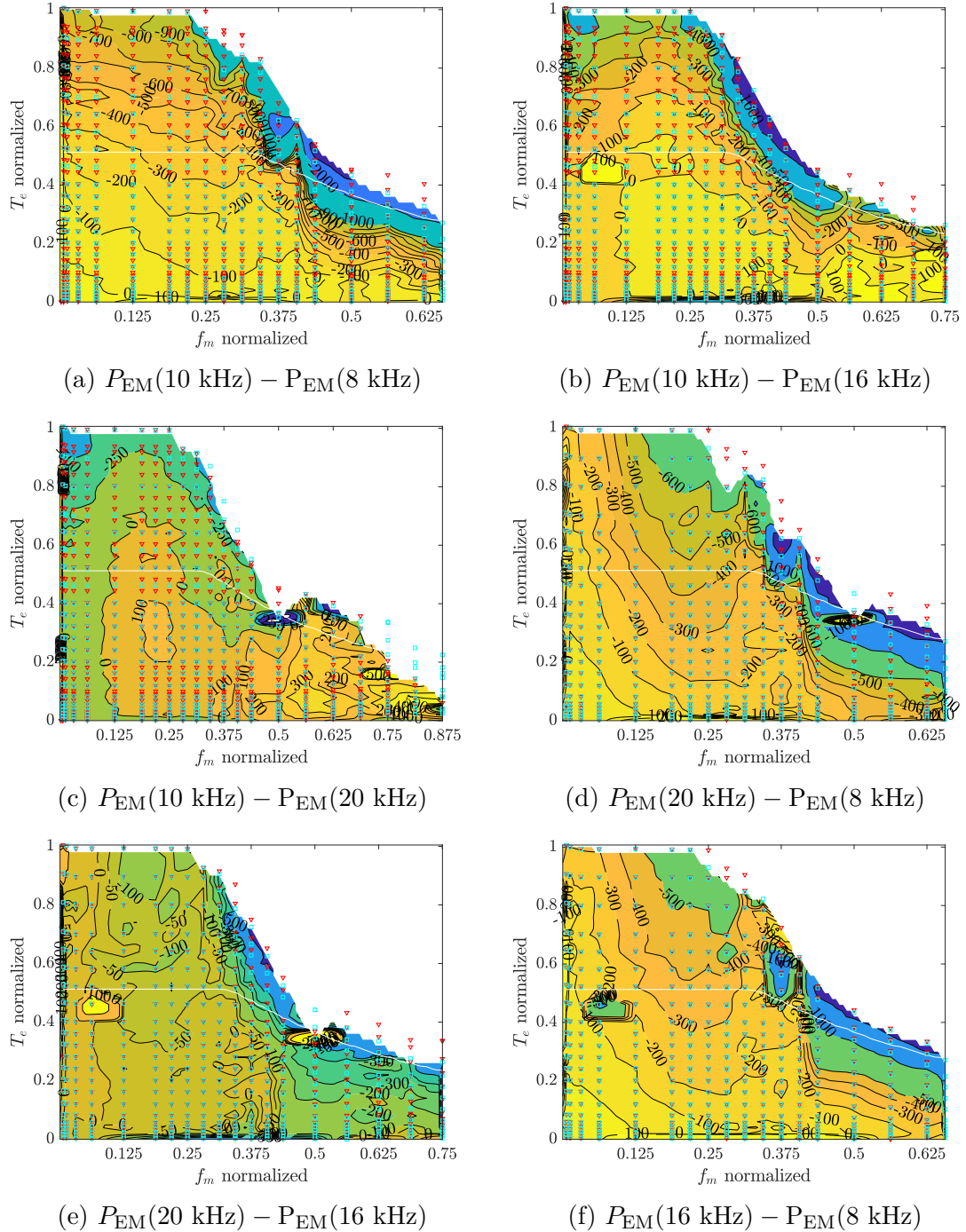
Figure 7.13: ΔP_{EM} for different f_{sw} for $\theta_I = 0°$

7.2.2 Equilibrium Loss Difference in the Inverter

(a) $f_{\mathrm{sw}} = 8$ kHz

(b) $f_{\mathrm{sw}} = 10$ kHz

(c) $f_{\mathrm{sw}} = 16$ kHz

(d) $f_{\mathrm{sw}} = 20$ kHz
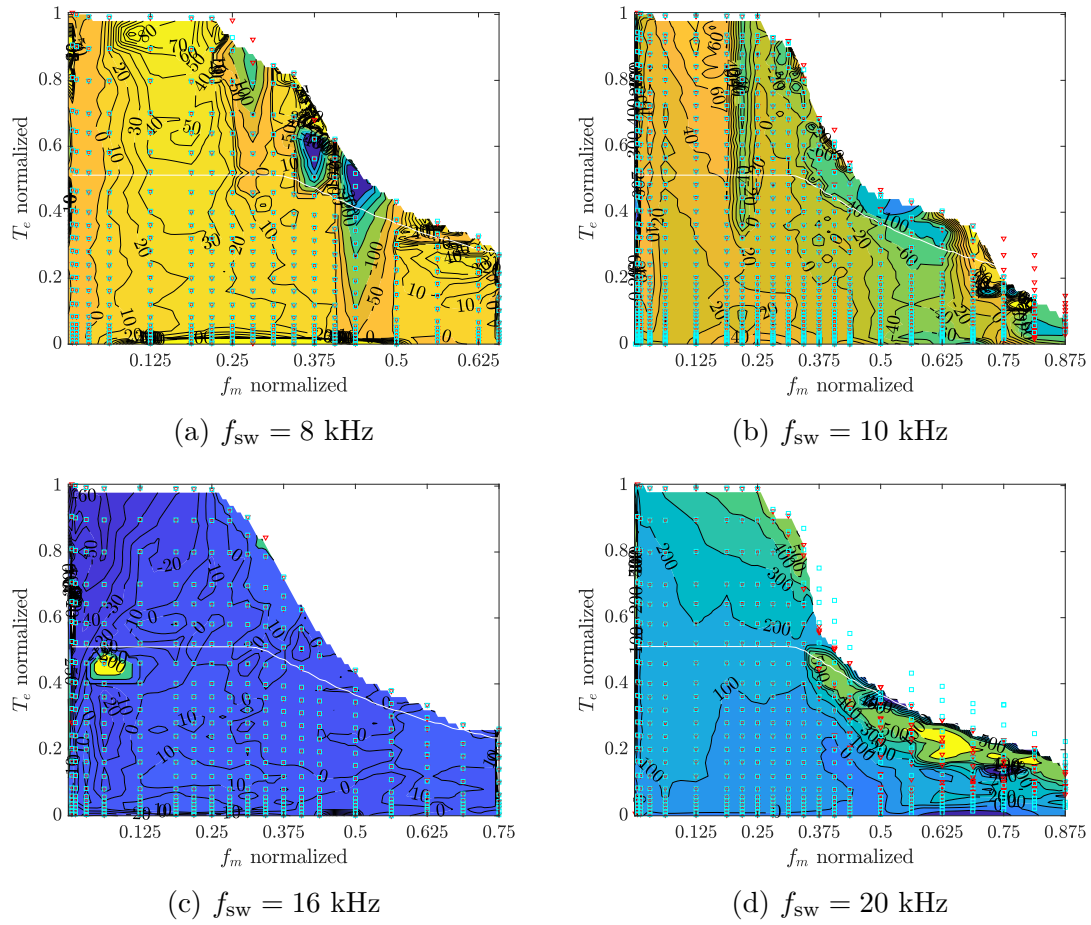
Figure 7.14: $P_{\mathrm{LE}}(90°) - P_{\mathrm{LE}}(0°)$

As Figure 7.14 shows, inverter losses due to interleaving are negligible, except for 20 kHz, where losses increase with increasing electrical power.

Figures 7.15 and 7.16 show that inverter losses increase with increasing switching frequency independent of the interleaving angle. That holds except for a few operating point islands, where transients did not have time to settle. Furthermore, inverter switching loss differences increase with increasing current magnitude, as expected.
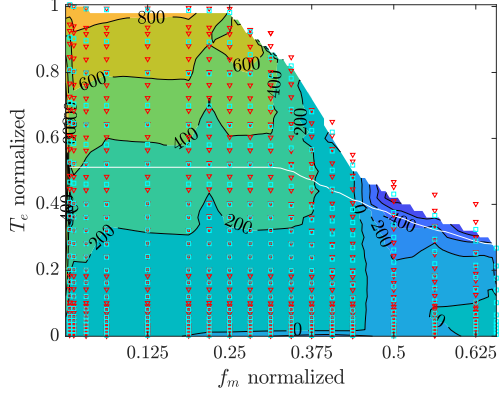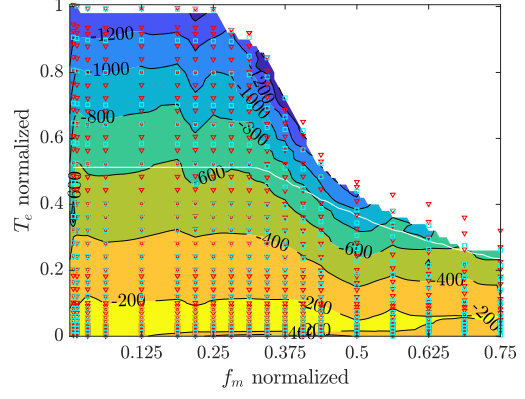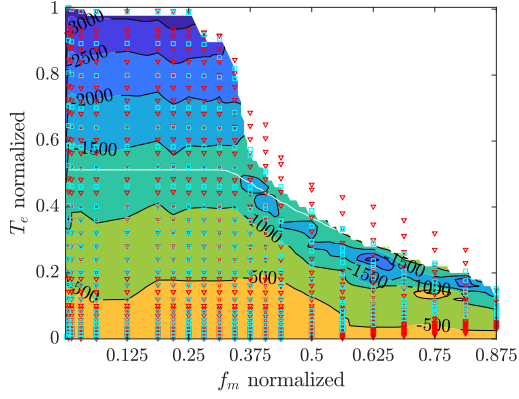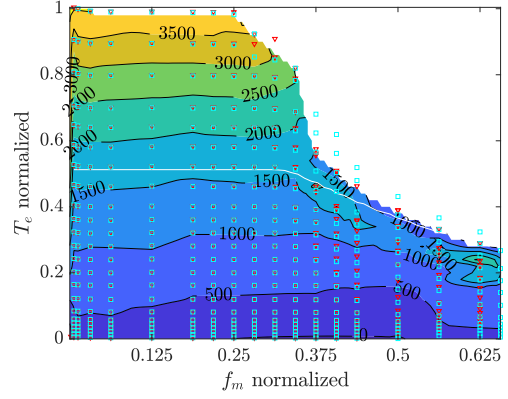
167

(a) $P_{\mathrm{LE}}(10\text{ kHz}) - P_{\mathrm{LE}}(8\text{ kHz})$

(b) $P_{\mathrm{LE}}(10\text{ kHz}) - P_{\mathrm{LE}}(16\text{ kHz})$

(c) $P_{\mathrm{LE}}(10\text{ kHz}) - P_{\mathrm{LE}}(20\text{ kHz})$

(d) $P_{\mathrm{LE}}(20\text{ kHz}) - P_{\mathrm{LE}}(8\text{ kHz})$

(e) $P_{\mathrm{LE}}(20\text{ kHz}) - P_{\mathrm{LE}}(16\text{ kHz})$

(f) $P_{\mathrm{LE}}(16\text{ kHz}) - P_{\mathrm{LE}}(8\text{ kHz})$

Figure 7.15: ΔP_{LE} for different f_{sw} for $\theta_I = 90°$

(a) $P_{LE}(10 \text{ kHz}) - P_{LE}(8 \text{ kHz})$

(b) $P_{LE}(10 \text{ kHz}) - P_{LE}(16 \text{ kHz})$
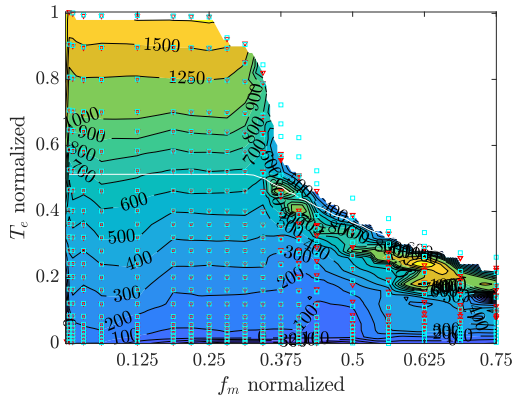
(c) $P_{LE}(10 \text{ kHz}) - P_{LE}(20 \text{ kHz})$

(d) $P_{LE}(20 \text{ kHz}) - P_{LE}(8 \text{ kHz})$

(e) $P_{LE}(20 \text{ kHz}) - P_{LE}(16 \text{ kHz})$
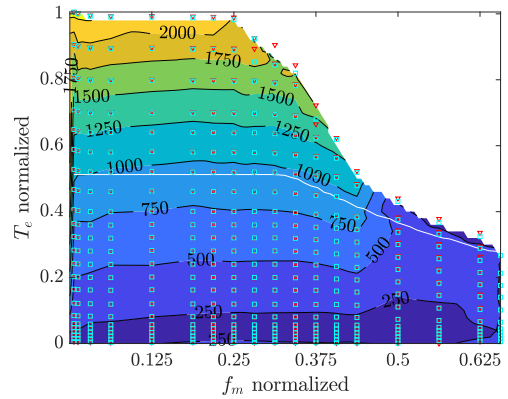
(f) $P_{LE}(16 \text{ kHz}) - P_{LE}(8 \text{ kHz})$
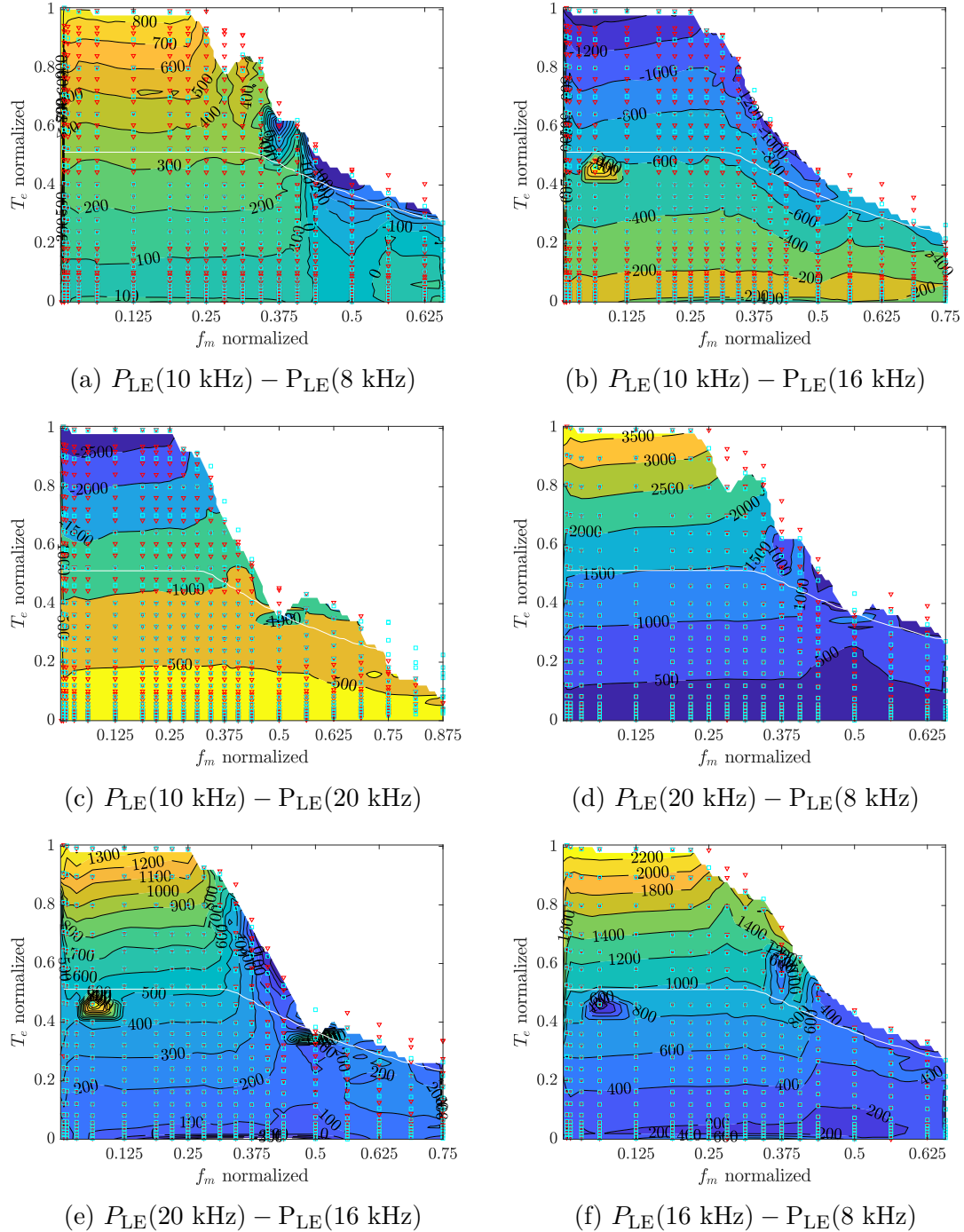
Figure 7.16: ΔP_{LE} for different f_{sw} for $\theta_I = 0°$

7.3 PWM Method Variation

This section shows comparative torque-speed maps that show the difference in machine losses −Figures 7.17 and 7.19 − and and inverter losses −Figures 7.18 and 7.20 − for select operating points in the base and field-weakening regions. Regions where the measured torque for both methods do not match do not have contours. Since that mostly happens in field-weakening regions, the figures in this section can only be interpreted in the base-speed region for PWM methods other than space-vector PWM (SVPWM). The PWM methods investigated were DPWM1, DPWM2, DPWM3, and SVPWM for the switching frequencies 9, 10, and 11 kHz. Not all combinations of PWM methods and switching frequencies could be investigated due to stability issues and inaccessibility of the basic software.

For those investigated combinations, known trends are mostly confirmed. Figure 7.17 shows that machine losses increase with decreasing switching frequency independent of the PWM method. Likewise, Figure 7.18 shows that inverter losses increase with increasing switching frequency, except for 9 kHz for DPWM1 −Figure 7.18(a) −and DPWM3 −Figure 7.18(c) −for about half of the points at lower speeds and mid-speed islands. That can be explained by the difference between the switching frequency and the sampling frequency, as the current ripple −and therefore high-frequency losses −is minimized for synchronous switching and sampling frequency. All data were recorded with 10 kHz sampling frequency, irrespective of the switching frequency.

Figure 7.19 confirms that for the investigated switching frequencies, all discontinuous methods induce more losses in the machine than space-vector modulation. Conversely, Figure 7.20 shows that all discontinuous methods induce less losses in the inverter than space-vector modulation. Both are due to that the discontinuous methods investigated, the inverter switches 2/3 less than space-vector modulation for a given switching frequency. Only for modulation indexes above 0.9 with DPWM switching at a factor of 3/2 of the frequency of SVPWM should the machine losses with SVPWM exceed those with any DPWM.

For low torques and high speeds, one can discern the additional losses due to harmonic constructive interference in Figures 7.17(d), (e), and (f). In Figure 7.17(e) especially, one can see how there is a bulge of negative machine loss difference at 0.625 normalized speed, suggesting that machine losses for 10 kHz increase at 0.625 normalized speed, as predicted by the FEM simulations in Chapter 5. However, when comparing all studied frequencies simultaneously, as opposed to just two at a time, the asynchronous sampling dominates the machine high-frequency losses, as shown in Figures 7.21-**??**. As a result of having a constant sampling frequency of 10 kHz over various switching frequencies, the harmonic constructive interference as predicted by the FEM simulations in Chapter 5 could not be observed by varying the switching frequency. Instead, the machine speed must be varied and transient measurements recorded, as displayed in Figure 7.22.

Figure 7.21(b) shows a clear loss trough for 10 kHz switching frequency, which is engulfed by other loss mechanisms at higher speeds as with Figures 7.21(d) and (f). Figures 7.21(a), (c), and (e) show the variability of the $d-$current, which although it increases with lower switching frequencies, does not translate to variability in the machine power loss calculation from the measured mechanical and electrical power.
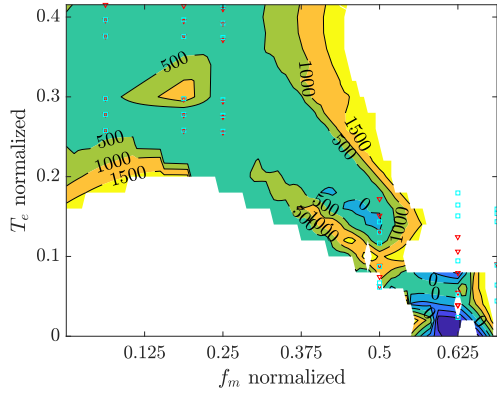
(a) $P_{\mathrm{EM}}(9\text{ kHz}) - \mathrm{P}_{\mathrm{EM}}(10\text{ kHz})$, D1
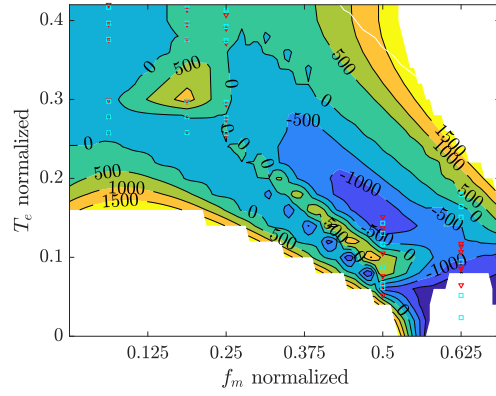
(b) $P_{\mathrm{EM}}(11\text{ kHz}) - \mathrm{P}_{\mathrm{EM}}(10\text{ kHz})$, D1
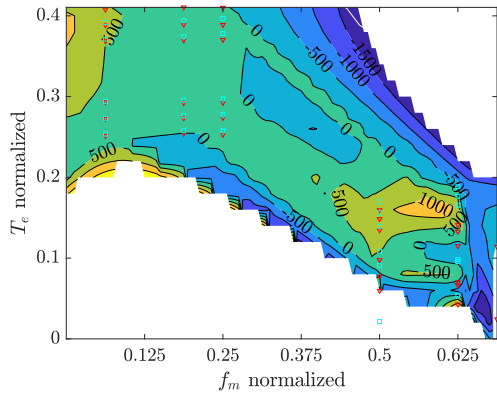
(c) $P_{\mathrm{EM}}(9\text{ kHz}) - \mathrm{P}_{\mathrm{EM}}(10\text{ kHz})$, D3
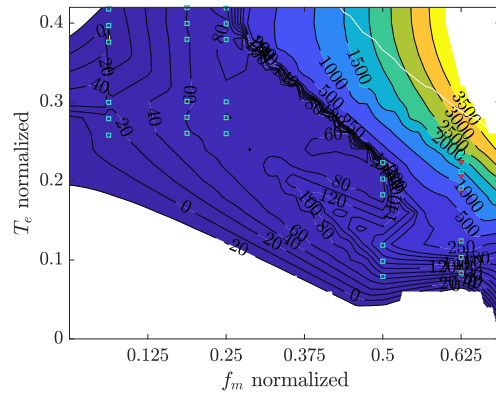
(d) $P_{\mathrm{EM}}(9\text{ kHz}) - \mathrm{P}_{\mathrm{EM}}(10\text{ kHz})$, SV
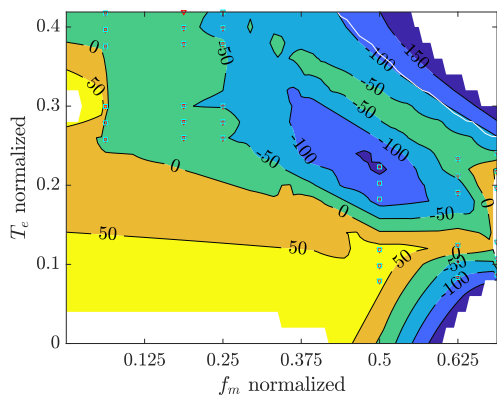
(e) $P_{\mathrm{EM}}(11\text{ kHz}) - \mathrm{P}_{\mathrm{EM}}(10\text{ kHz})$, SV
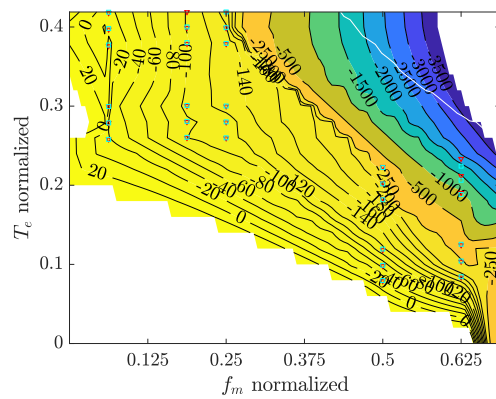
(f) $P_{\mathrm{EM}}(11\text{ kHz}) - \mathrm{P}_{\mathrm{EM}}(9\text{ kHz})$, SV

Figure 7.17: ΔP_{EM} for different f_{sw} and PWM methods for $\theta_I = 90°$

171
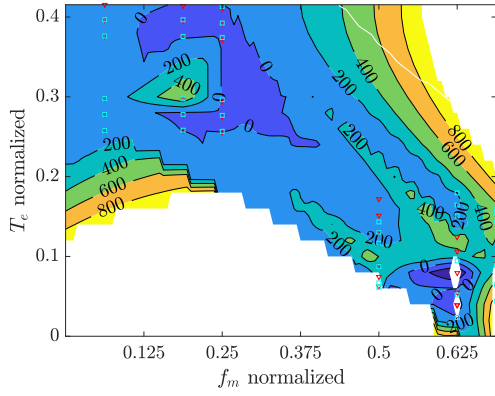
(a) $P_{\mathrm{LE}}(9\ \mathrm{kHz}) - P_{\mathrm{LE}}(10\ \mathrm{kHz})$, D1
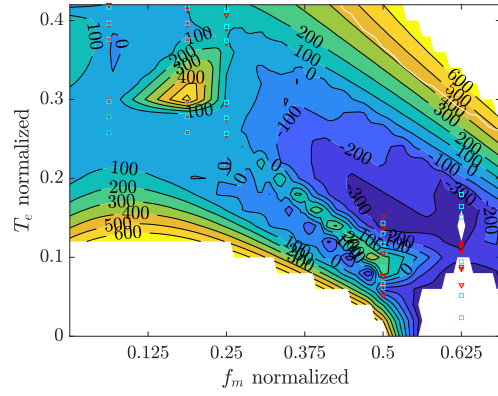
(b) $P_{\mathrm{LE}}(11\ \mathrm{kHz}) - P_{\mathrm{LE}}(10\ \mathrm{kHz})$, D1
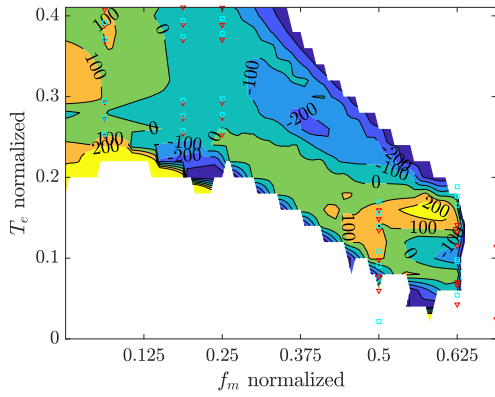
(c) $P_{\mathrm{LE}}(9\ \mathrm{kHz}) - P_{\mathrm{LE}}(10\ \mathrm{kHz})$, D3
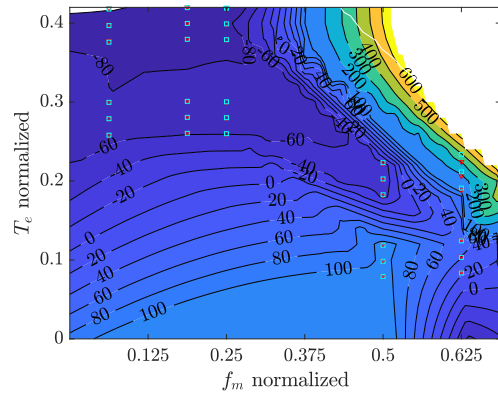
(d) $P_{\mathrm{LE}}(9\ \mathrm{kHz}) - P_{\mathrm{LE}}(10\ \mathrm{kHz})$, SV
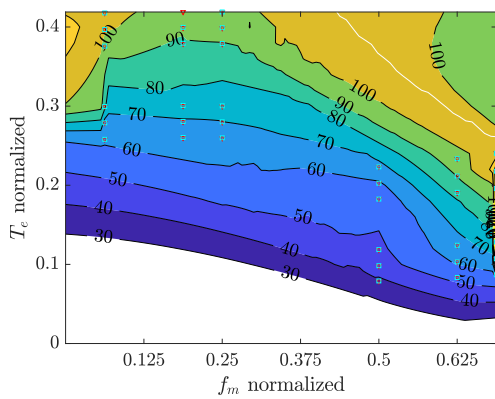
(e) $P_{\mathrm{LE}}(11\ \mathrm{kHz}) - P_{\mathrm{LE}}(10\ \mathrm{kHz})$, SV
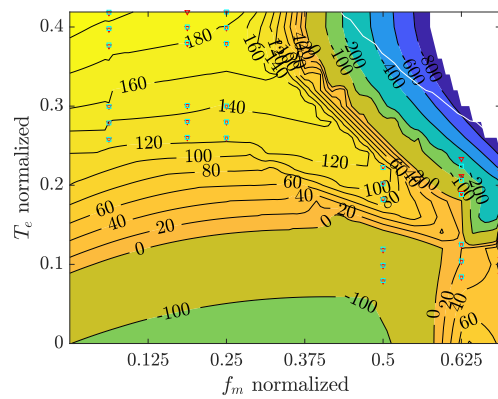
(f) $P_{\mathrm{LE}}(11\ \mathrm{kHz}) - P_{\mathrm{LE}}(9\ \mathrm{kHz})$, SV

Figure 7.18: ΔP_{LE} for different f_{sw} and PWM methods for $\theta_I = 90°$
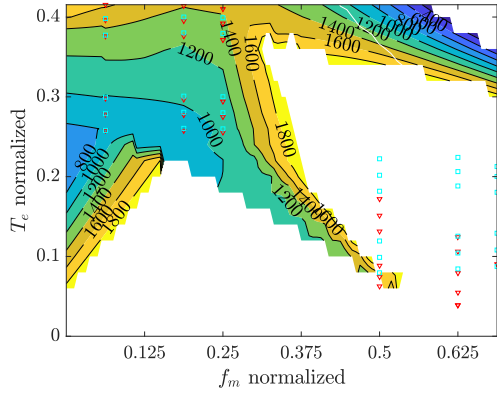
(a) $P_{\text{EM}}(\text{D1}) - P_{\text{EM}}(\text{SV})$, 9 kHz
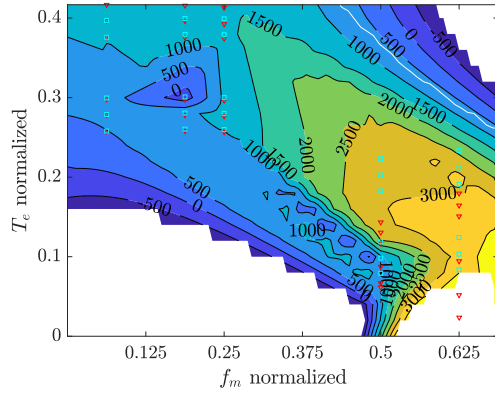
(b) $P_{\text{EM}}(\text{D1}) - P_{\text{EM}}(\text{SV})$, 10 kHz
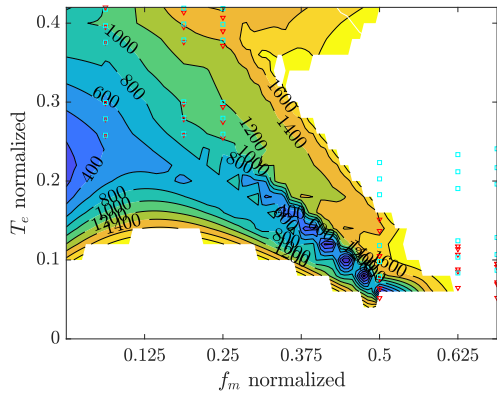
(c) $P_{\text{EM}}(\text{D1}) - P_{\text{EM}}(\text{SV})$, 11 kHz
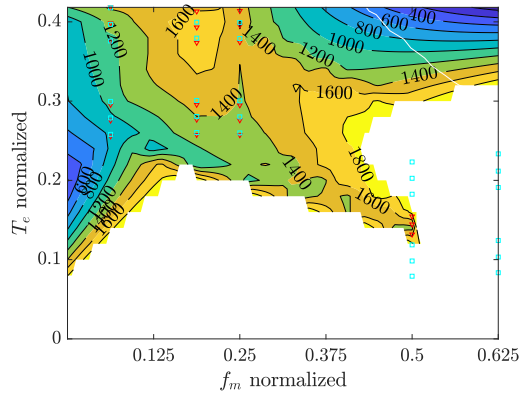
(d) $P_{\text{EM}}(\text{D2}) - P_{\text{EM}}(\text{SV})$, 10 kHz
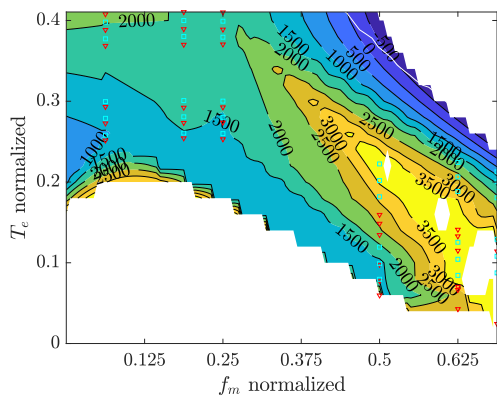
(e) $P_{\text{EM}}(\text{D3}) - P_{\text{EM}}(\text{SV})$, 9 kHz
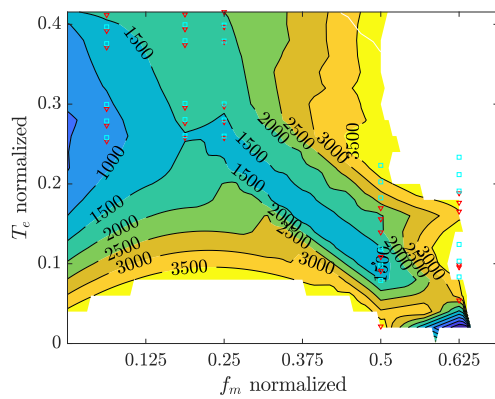
(f) $P_{\text{EM}}(\text{D3}) - P_{\text{EM}}(\text{SV})$, 10 kHz

Figure 7.19: ΔP_{EM} for different PWM methods keeping f_{sw} constant for $\theta_I = 90°$
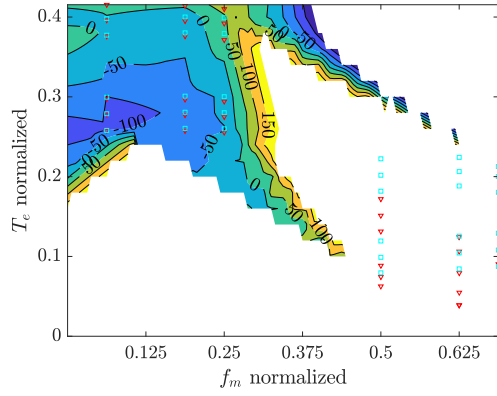
(a) $P_{\mathrm{LE}}(\mathrm{D1}) - P_{\mathrm{LE}}(\mathrm{SV})$, 9 kHz
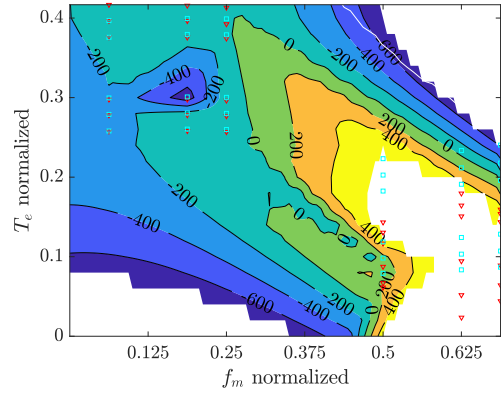
(b) $P_{\mathrm{LE}}(\mathrm{D1}) - P_{\mathrm{LE}}(\mathrm{SV})$, 10 kHz
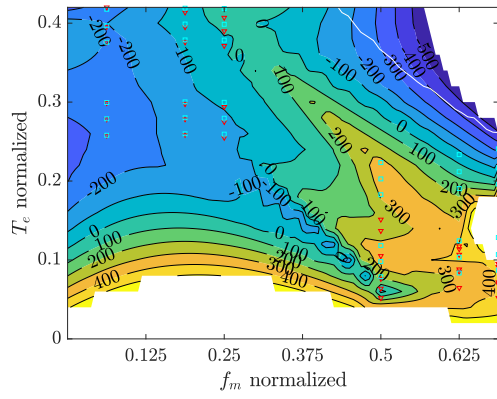
(c) $P_{\mathrm{LE}}(\mathrm{D1}) - P_{\mathrm{LE}}(\mathrm{SV})$, 11 kHz
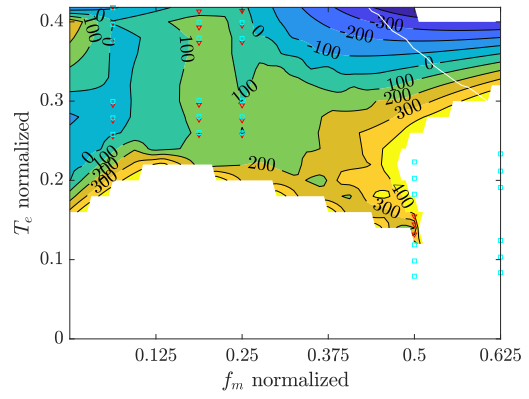
(d) $P_{\mathrm{LE}}(\mathrm{D2}) - P_{\mathrm{LE}}(\mathrm{SV})$, 10 kHz
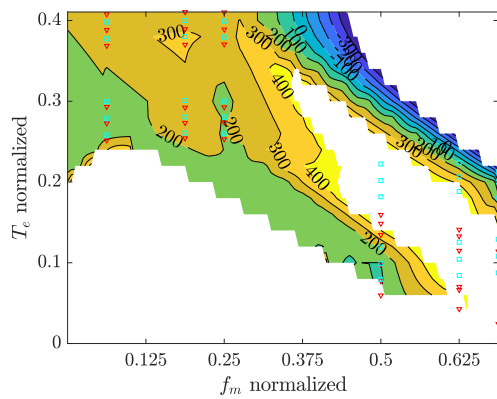
(e) $P_{\mathrm{LE}}(\mathrm{D3}) - P_{\mathrm{LE}}(\mathrm{SV})$, 9 kHz
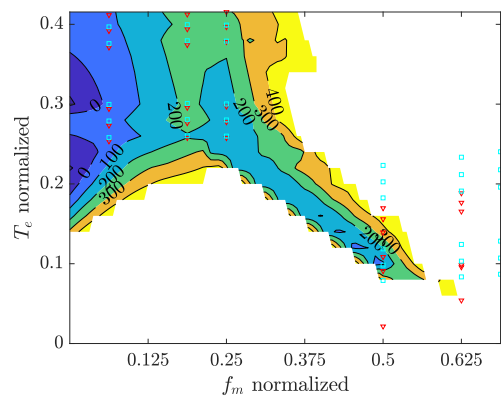
(f) $P_{\mathrm{LE}}(\mathrm{D3}) - P_{\mathrm{LE}}(\mathrm{SV})$, 10 kHz

Figure 7.20: ΔP_{LE} for different PWM methods keeping f_{sw} constant $\theta_I = 90°$
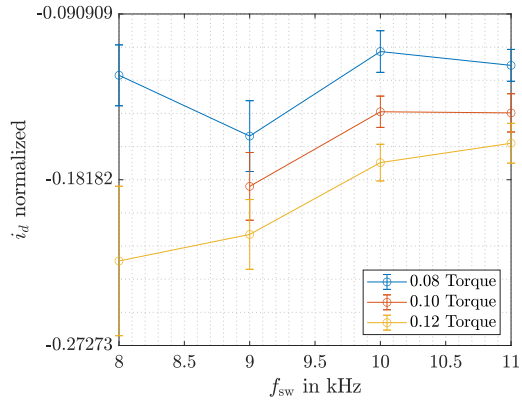
(a) $(i_{d1} + i_{d2})/2$, 0.5625 normalized speed
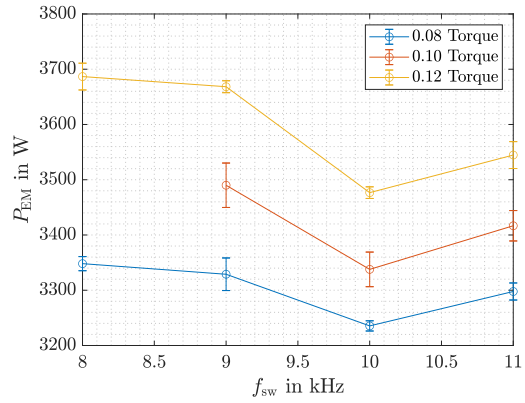
(b) P_{EM}, 0.5625 normalized speed
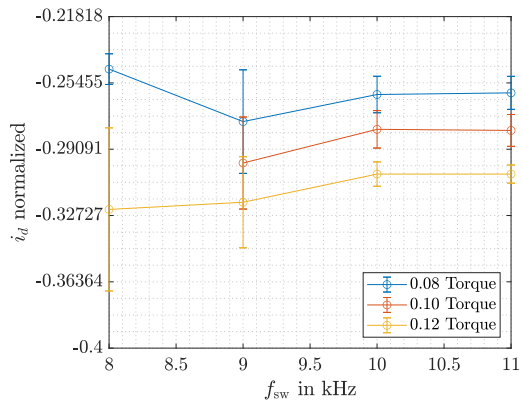
(c) $(i_{d1} + i_{d2})/2$, 0.625 normalized speed
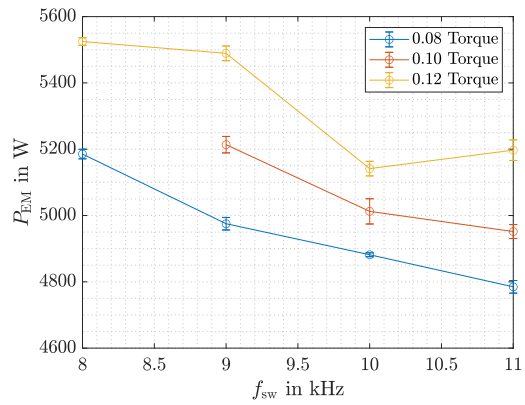
(d) P_{EM}, 0.625 normalized speed
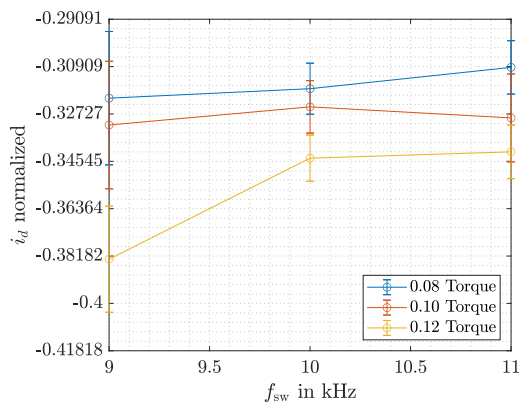
(e) $(i_{d1} + i_{d2})/2$, 0.6875 normalized speed
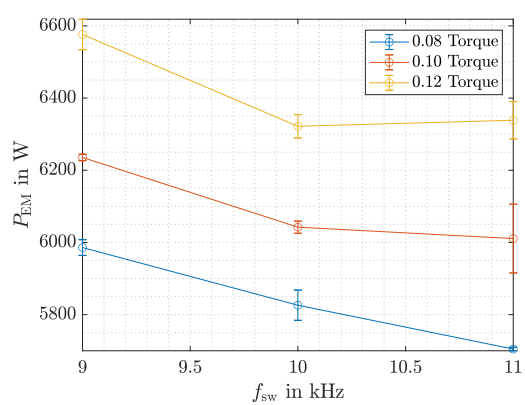
(f) P_{EM}, 0.6875 normalized speed

Figure 7.21: Experimental average $d-$current and machine loss for 10 kHz sampling frequency and $\theta_I = 0°$

The machine losses in Figure 7.21(b) increase for 11 kHz from 10 kHz switching for 0.5625 normalized speed despite almost no change in the set-point. To understand these counter-intuitive losses, the current ripple was simulated for the asymmetrical dual-three phase machine for different sampling and switching frequencies. Alluding intermittently to simulation results in Figure 5.8(a), the current ripple trough especially correlates to the machine loss troughs in Figure 7.21(b), confirming that the loss trough is due to synchronous sampling and switching frequencies. Figure 5.8(b) shows that the mutual inductance, meaning the magnetic coupling between the two duals, exaggerates the loss increases when deviating from the synchronous sampling loss trough.

7.4 Frequency Interaction in the Permanent Magnets
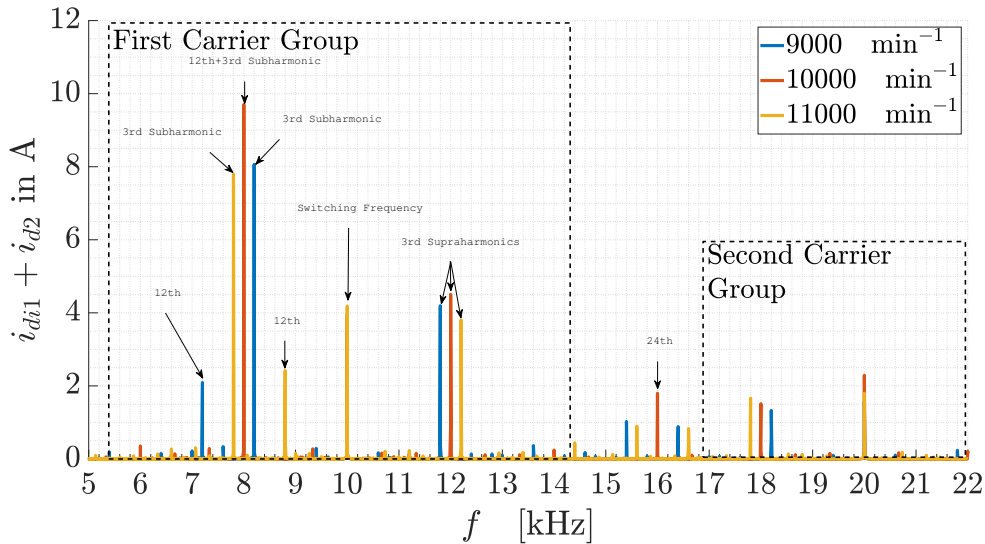
Figure 7.22: Sum of $d-$axis currents for various speeds for 0.1 norm. moment with SVPWM as calculated from phase currents with a continuous transformation.

As already analyzed in Chapter 5, there is harmonic interaction between the tooth reluctance variations as seen from the rotor and the 3rd subharmonic of the first carrier group, which exists in the rotor frame of reference as the coalescence of the 2nd and 4th subharmonics of the first carrier group in the stator frame of reference. Figure 7.22 is evidence of that, since an eight pole, 48-tooth machine at 0.625 normalized speed with an inverter switching at 10 kHz has a 12th harmonic and the 3rd subharmonic of the first carrier group at 8 kHz. The difference between Figure 7.22 and Figure 5.45 is the PWM method and the fact that the speed was varied instead of the switching frequency. The speed was varied in Figure 7.22 instead of the switching frequency to show the harmonic interactions because in the experimental data, the sampling frequency remains at 10 kHz but the switching frequency was able to be varied. Such asynchronicity is not typical of electric drives. Furthermore, the DPWM methods were not stable in that region during experiments.

Chapter 8

Experimental Optimization

In this chapter, the experimental data from the previous chapter is used to find an optimal interleaving angle and switching frequency schedule depending on the operating point. The optimum is sought to minimize the total power consumption in the machine and in the inverter. Statistical significance due to measurement error and fit to a Gaussian process with a stationary squared exponential kernel are considered. It is found that the trivial interleaving angle $\theta_I = 0°$ is optimal for all operating points, especially for low torques in the base-speed region. The optimal switching frequency is small for low speeds, increasing with speed and increasing with decreasing torque up to the field-weakening region, where it increases moderately for the dual three-phase asymmetrical machine and increases to the maximum measured switching frequency for the three-phase machine. The moderate increase in the optimal switching frequency in the field-weakening region for the asymmetrical machine compared to the three-phase machine is attributed to the anisotropy of the electrical steel in the asymmetrical machine.

8.1   Optimizing the Interleaving Angle

As shown in the simulation section, the advantages of the interleaving angle should be constrained to the capacitor current ripple and do not depend on the electrical load. Furthermore, interleaving reduces the losses in the capacitor to a much lesser degree than it increases them in the asymmetric machine but increases capacitor longevity or reduces its size. As such, one may approach the optimization of the interleaving angle as a multi-objective optimization of capacitor longevity or size reduction and machine losses. The specific cost function is shown in Equation 8.1.1, where a_c is the cost-longevity or cost per cubic meter of the capacitor, J_c is the inverse longevity or the volume of the capacitor, a_{kW} is the cost per kilo-Watt loss in the electric machine, and J_{EM} is the electric machine power loss.

$$J = a_c J_c + a_{\text{kW}} J_{\text{EM}} \tag{8.1.1}$$

Capacitor longevity and size are proxies for capacitor RMS current, so that one may also define a_c as a cost per ampere over the entire lifetime of the capacitor; it follows that J_c must be the capacitor RMS current. Setting $a_{\text{kW}} = a_{\text{kWh}} t_\ell$, where t_ℓ is the capacitor lifetime, and if J_{EM} still represents the power losses, then because a_c and a_{kWh} are in the order of one another (tens of cents under one dollar) and the

capacitor lifetime is in the order of hundreds of thousands of hours [138], $a_c \ll a_{\mathrm{kW}}$. We can therefore neglect a_c and build the binary interleaving strategy to minimize the machine losses.

For the asymmetric machine, the optimal interleaving angle minimizing machine losses for all operating points is the trivial $\theta_I = 0°$. Figure 8.3(a) might suggest a non-trivial interleaving strategy be it not for Figure 8.3(b), which shows that the regions where $\theta_I \neq 0°$, the results are not significant. The power and efficiency gains, as predicted by the FEM simulations in Chapter 5, are the most significant in the base-speed region for lower torques. There is a mismatch of about 0.5% in the efficiency gain calculation compared to the FEM simulation in Figure 5.27(a) due to the inclusion of friction losses in the experimental measurements. The trend, however, remains nearly identical because the friction losses depend on speed, rendering their contribution to efficiency loss constant or hyperbolically diminishing along the speed axis direction in the torque-speed plane. Furthermore, the FEM losses did not predict the additional losses due to ferromagnetic anisotropy at low torques, so that the experimental efficiency gains are larger for torques very near zero than predicted in the FEM.

(a) Fit

(b) Fit error as 2σ
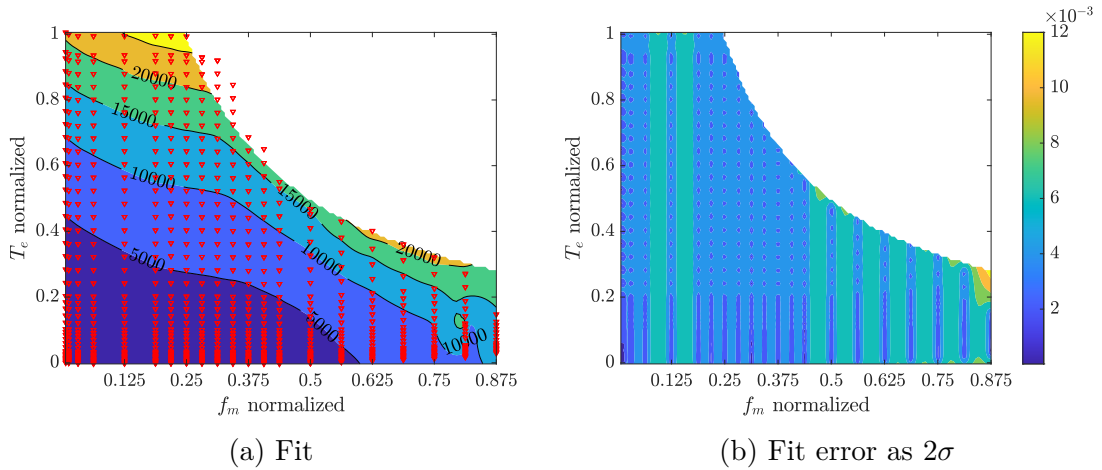
Figure 8.1: Fitted power loss at $f_{\mathrm{sw}} = 10$ kHz, $\theta_I = 90°$, 325 VDC

(a) Fit

(b) Total error as 2σ in W
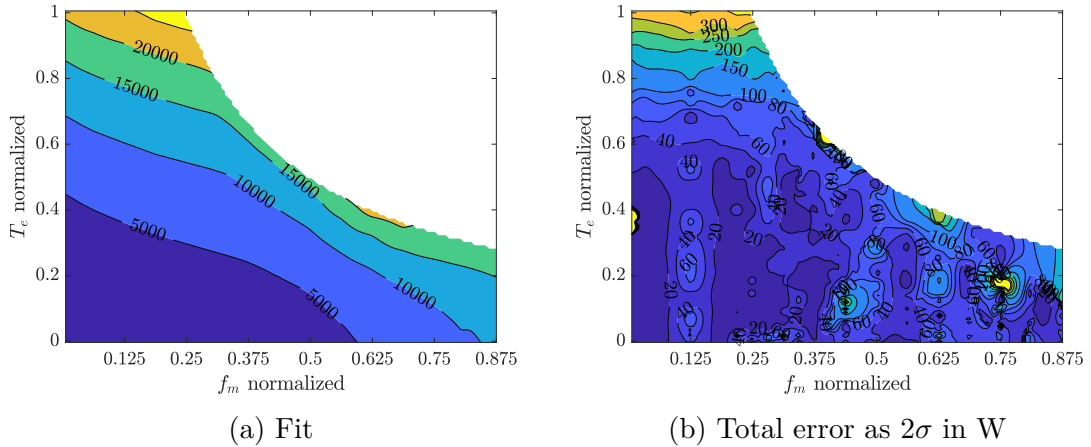
Figure 8.2: Optimal power loss, $f_{\mathrm{sw}} = 10$ kHz, 325 VDC

(a) Optimal θ_I is either 0° or 90°

(b) Significant power gain region
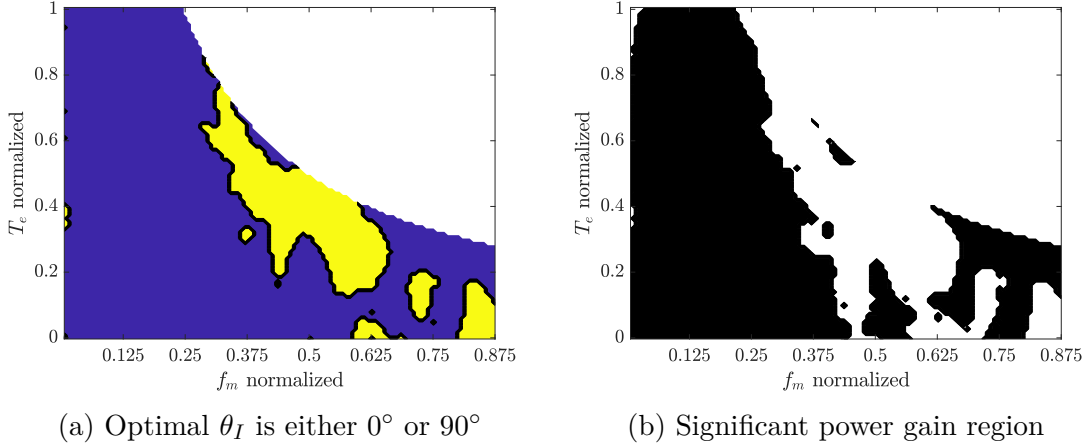
Figure 8.3: Optimal interleaving angle, $f_{\mathrm{sw}} = 10$ kHz, 325 VDC

(a) Percent power gains in %

(b) Efficiency gains in %
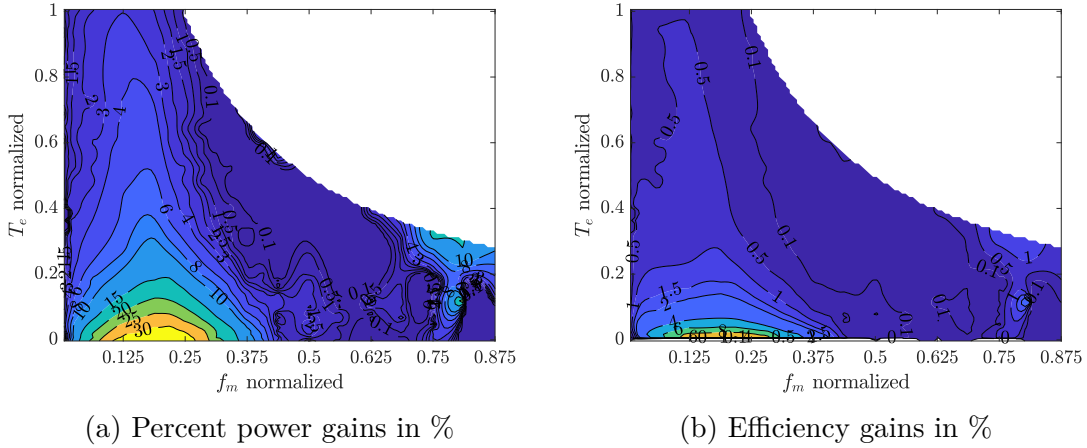
Figure 8.4: Comparison of power and efficiency gains between optimal interleaving and $\theta_I = 90°$ for 325 VDC

Figures 8.5-8.8 for 400 VDC instead of 325 VDC confirm the triviality of the optimization, namely that $\theta_{I,\mathrm{opt}} = 0°$. Again, regions where $\theta_I \neq 0°$ are not statistically significant, as shown by Figure 8.7. Since there were no FEM simulations performed for 400 VDC, it is not possible to compare the experimental results. However, the difference trends are similar to those for 325 VDC. Specifically: most of the power and efficiency gains occur in the base-speed region at low torques. The benefits, however, are slightly magnified for 400 VDC and broadly spread to larger speeds, as is expected from a parameterization that reduces current ripple, which itself is directly proportional to the DC bus voltage, and a parameterization whose benefits are mostly seen in the base-speed region.

(a) Fit

(b) Fit error as 2σ
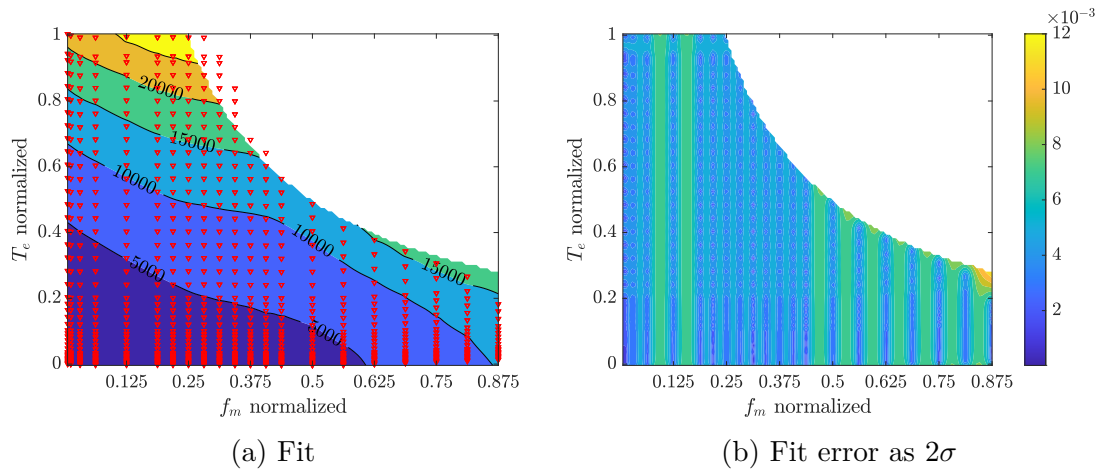
Figure 8.5: Fitted power loss at $f_{\mathrm{sw}} = 10$ kHz, $\theta_I = 90°$, 400 VDC

(a) Fit

(b) Total error as 2σ in W
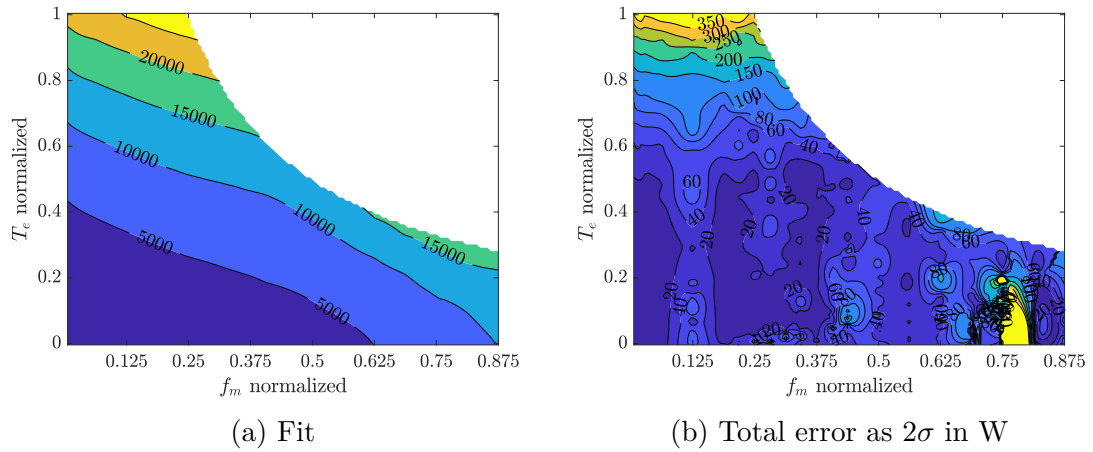
Figure 8.6: Optimal power loss, $f_{\mathrm{sw}} = 10$ kHz, 400 VDC

(a) Optimal θ_I is either 0°or 90°

(b) Significant power gain region
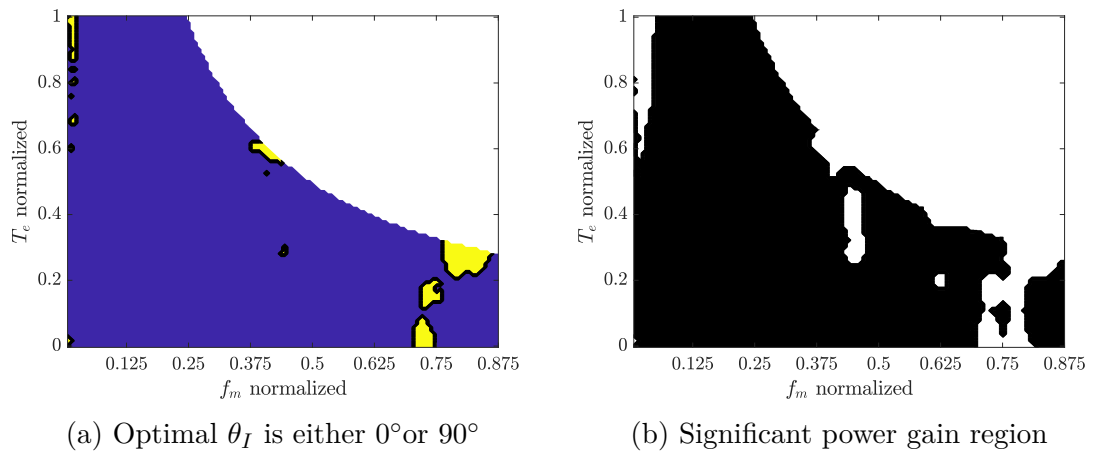
Figure 8.7: Optimal interleaving angle, $f_{\mathrm{sw}} = 10$ kHz, 400 VDC

(a) Percent power gains in %

(b) Efficiency gains in %
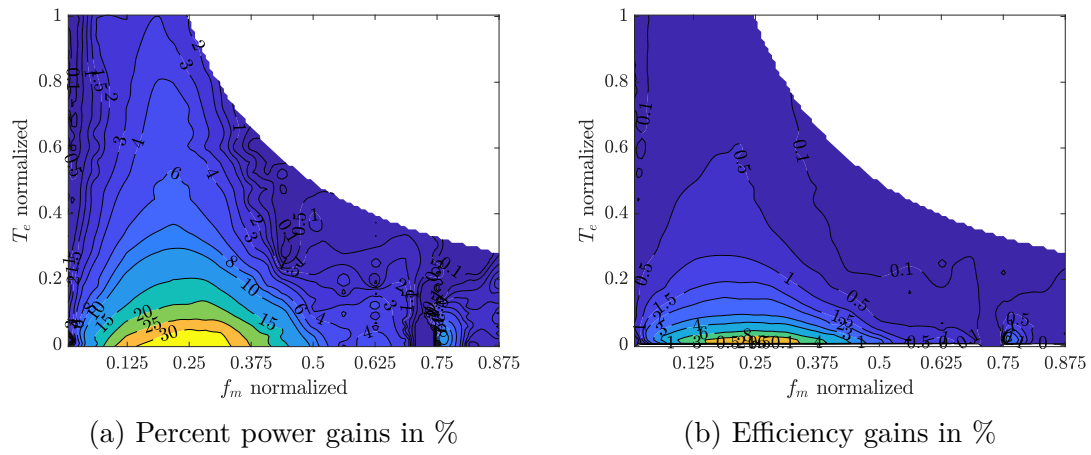
Figure 8.8: Comparison of power and efficiency gains between optimal interleaving and $\theta_I = 90°$ for 400 VDC

8.2 Optimizing the Switching Frequency

Switching frequency optimization is often dismissed as providing minimal gains to an electrical drive's efficiency. This section shows the opposite.

8.2.1 Asymmetrical Dual-Three Phase Machine

(a) Fit

(b) Fit error as 2σ
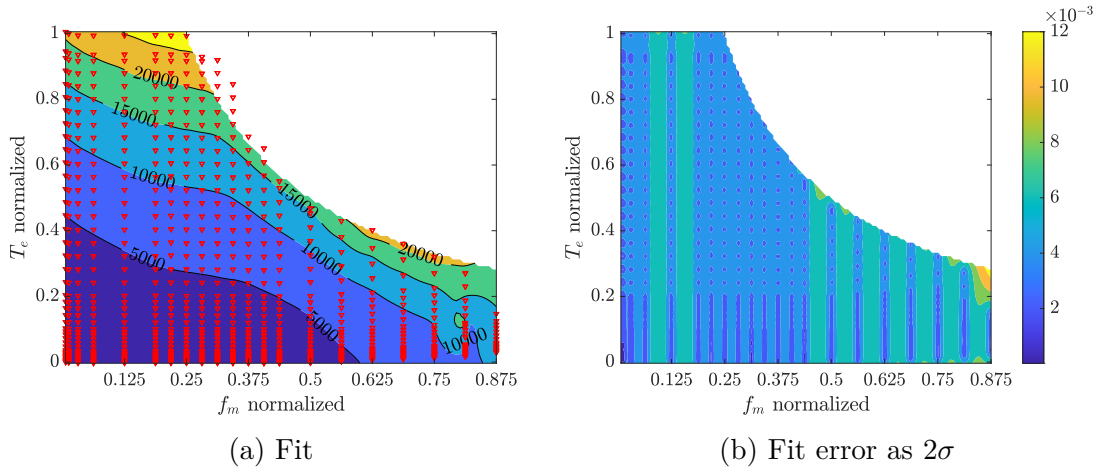
Figure 8.9: Fitted power loss at $f_{\mathrm{sw}} = 10$ kHz, $\theta_I = 90°$

(a) Fit

(b) Total error as 2σ in W
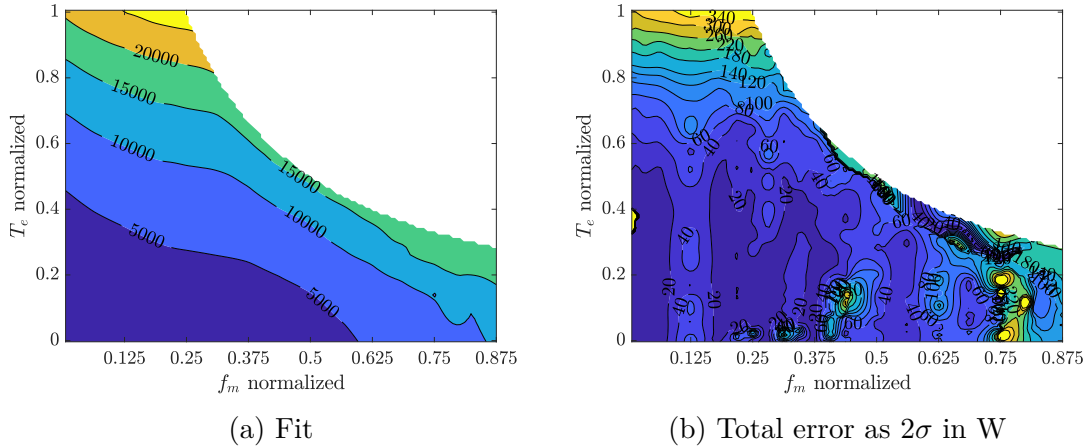
Figure 8.10: Optimal power loss, $\theta_I = 90°$

(a) Optimal f_{sw} in kHz

(b) Significant power gain region
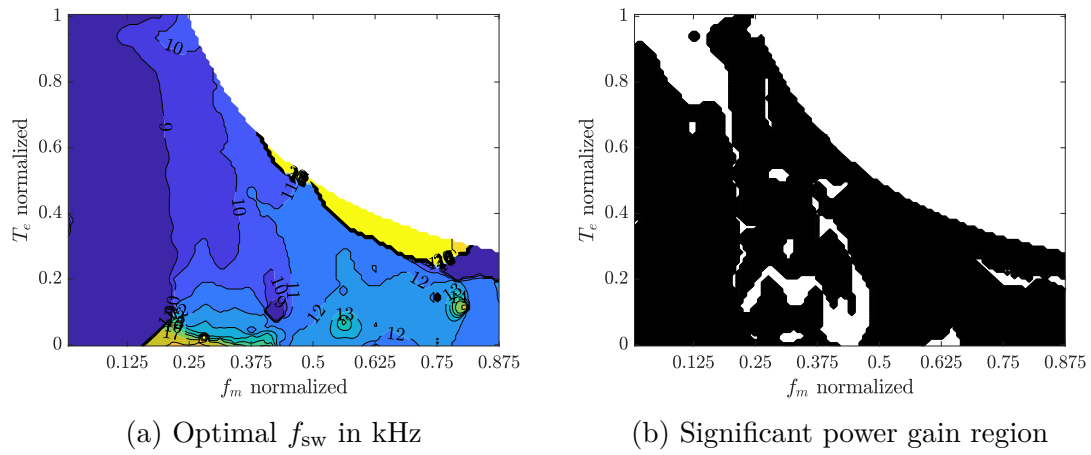
Figure 8.11: Optimal switching frequency, $\theta_I = 90°$

(a) Percent power gains in %

(b) Efficiency gains in %
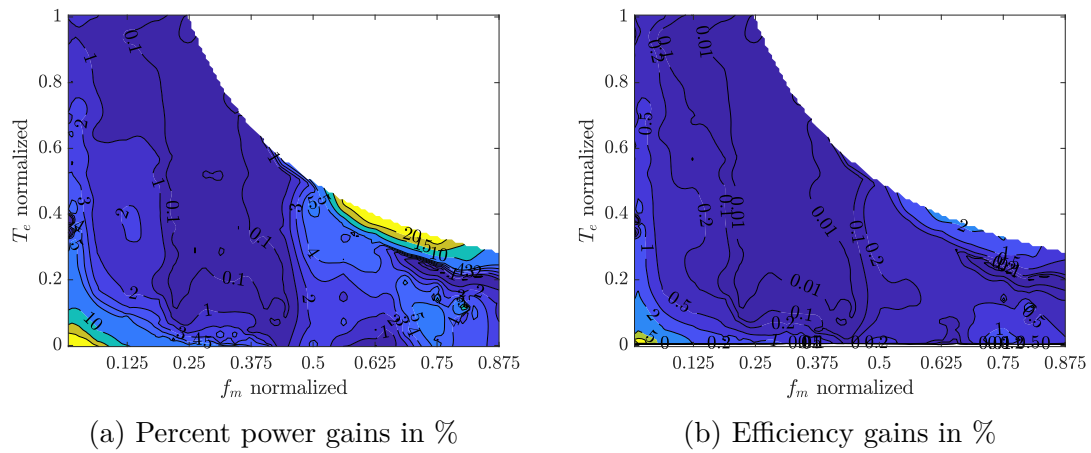
Figure 8.12: Comparison of power and efficiency gains between optimal switching and $f_{\text{sw}} = 10$ kHz, $\theta_I = 90°$

(a) Fit

(b) Fit error as 2σ
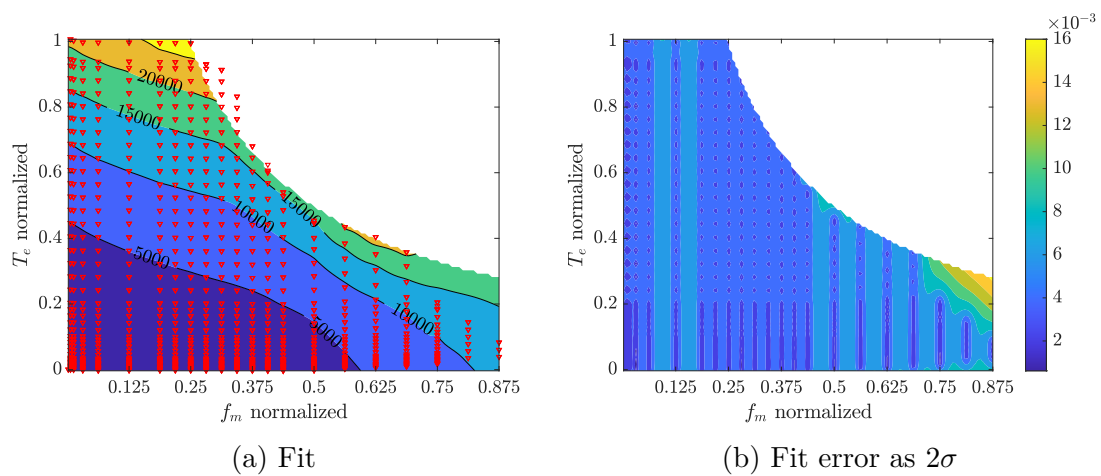
Figure 8.13: Fitted power loss at $f_{\text{sw}} = 10$ kHz, $\theta_I = 0°$

183

(a) Fit

(b) Total error as 2σ in W
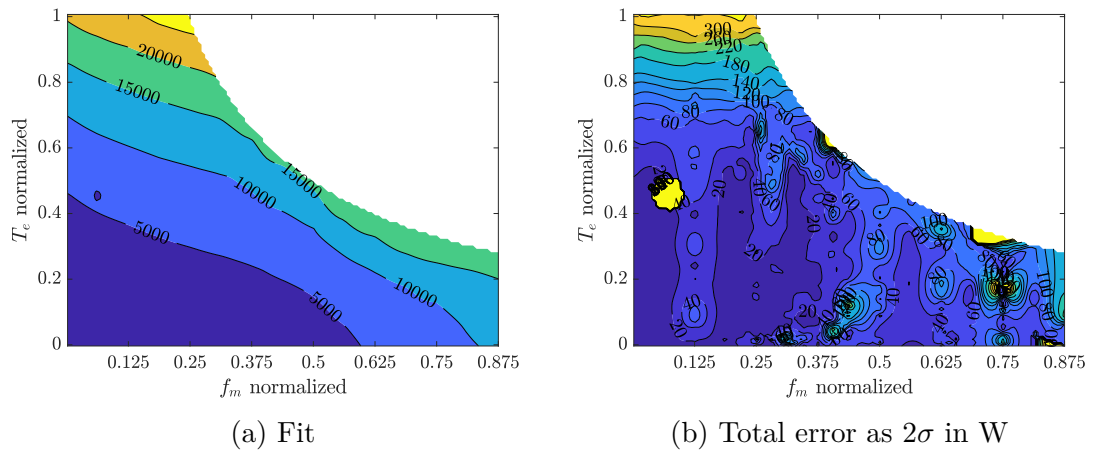
Figure 8.14: Optimal power loss, $\theta_I = 0°$

(a) Optimal f_{sw} in kHz

(b) Significant power gain region
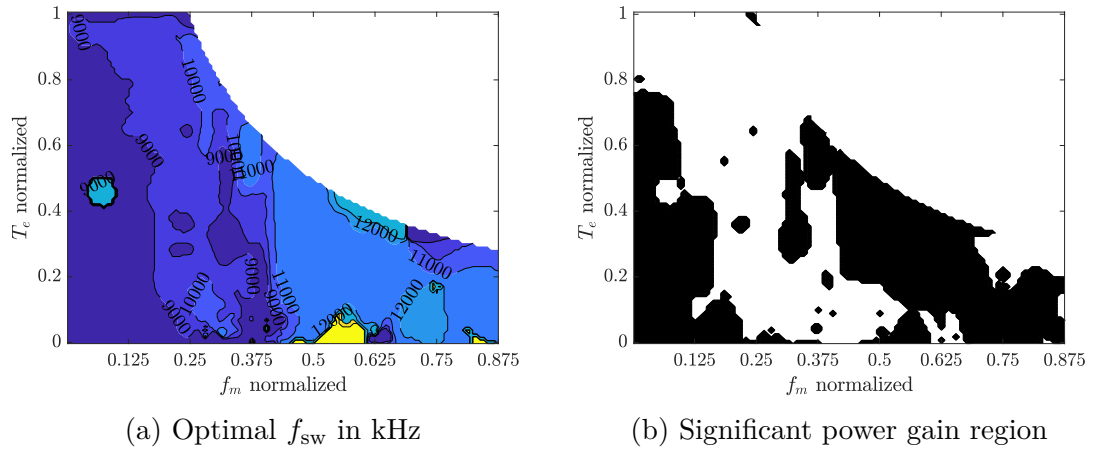
Figure 8.15: Optimal switching frequency, $\theta_I = 0°$

(a) Percent power gains in %

(b) Efficiency gains in %
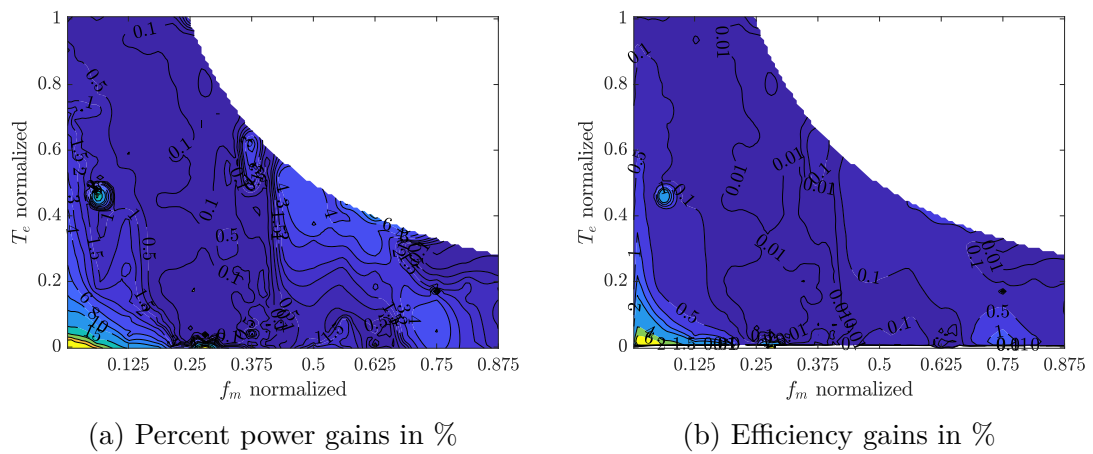
Figure 8.16: Comparison of power and efficiency gains between optimal switching and $f_{\mathrm{sw}} = 10$ kHz, $\theta_I = 0°$

8.2.2 Three Phase Machine

This three-phase machine was fed with a SiC three-phase inverter and with synchronous sampling and switching. The data was fit using Gaussian process regression with a squared exponential kernel, for maximal smoothness. As a technique to simplify the fitting, inputs and outputs are normalized. That allows for the use of a single distance parameter over the prior, rendering the data isotropic. Normalizing may in turn ambiguate the interpretation of the confidence intervals of the fit, which is why Figure 8.17(a) shows the fitted inverter and machine losses over the electrical frequency instead of the mechanical frequency: since it is already in the order of the torque, i.e. isotropic in the inputs, normalization is not necessary. Figure 8.17(b) shows the consequently unambiguated error of the fitted inverter and machine losses, albeit with re-labeled normalized mechanical speed. Since the fit error, although negligible, is not the only error source, the power measurement error must be added in quadrature to arrive at the total error. Figure 8.18 shows the optimal inverter plus machine losses and the total error estimate. A search optimization results in the switching frequency that minimizes the inverter plus machine losses over all operating points, as shown in Figure 8.19(a). Figure 8.19(b) shows the regions where the difference between the losses at the nominal $f_{sw} = 10$ kHz and the optimum are outside of the 2σ band; regions where the optimization returned an optimal switching frequency of 10 kHz are considered significant.

(a) Fit

(b) Fit error as 2σ
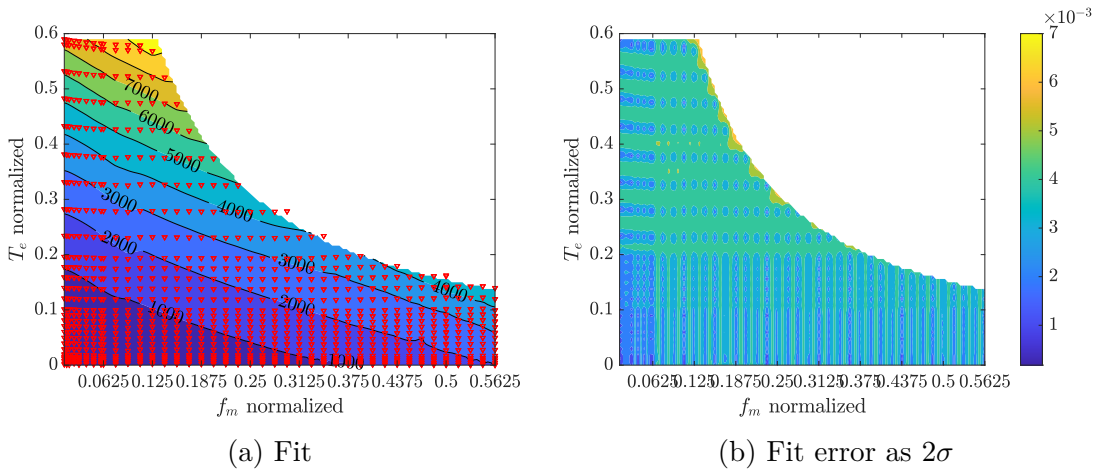
Figure 8.17: Fitted power loss at $f_{sw} = 10$ kHz

(a) Fit

(b) Total error as 2σ in W
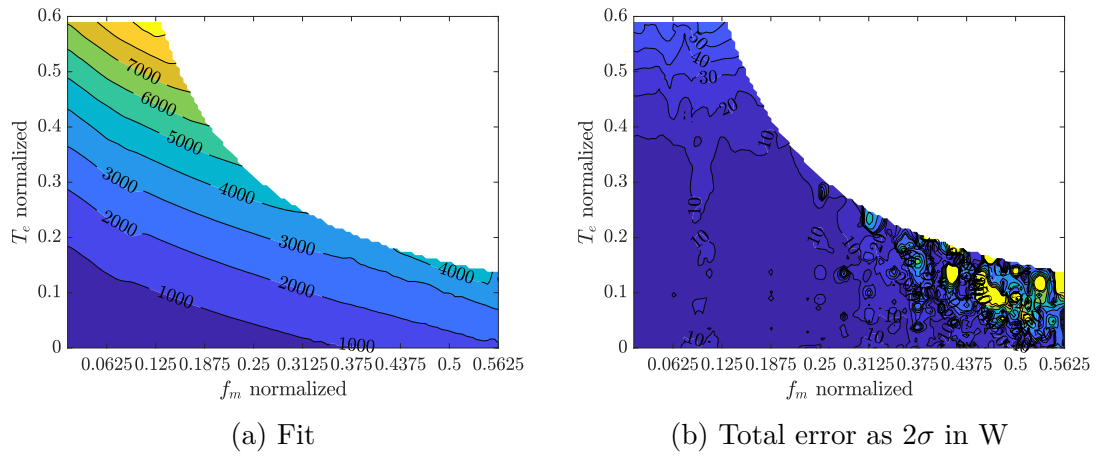
Figure 8.18: Optimal power loss

(a) Optimal f_{sw} in kHz

(b) Significant power gain region
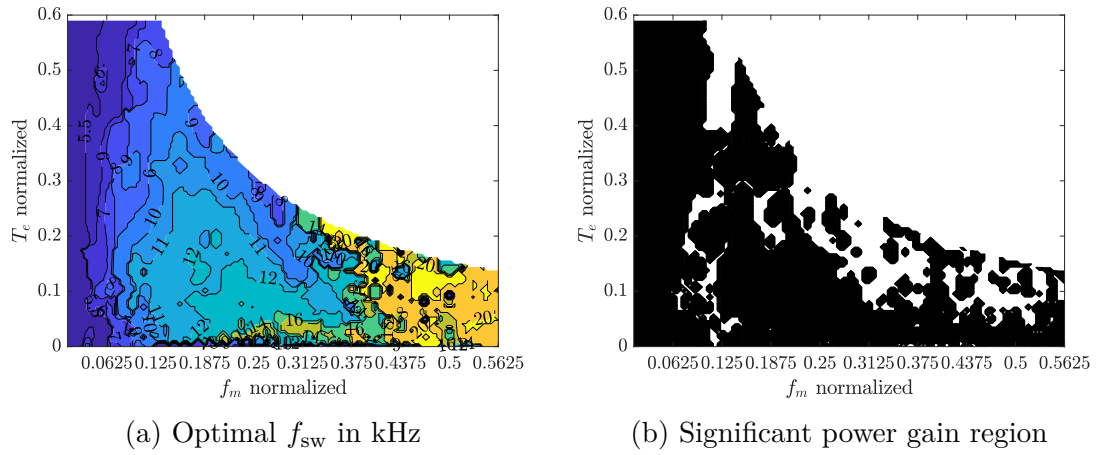
Figure 8.19: Optimal switching frequency

(a) Percent power gains in %

(b) Efficiency gains in %
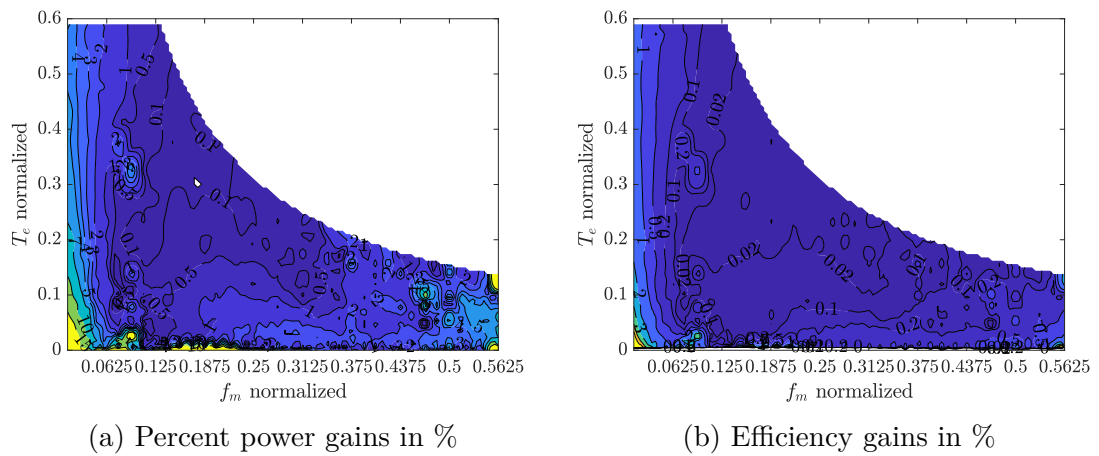
Figure 8.20: Comparison of power and efficiency gains between optimal switching and $f_{\mathrm{sw}} = 10$ kHz

As an additional comment, only three data points per torque-speed pair were recorded in order to estimate the variance. Three points does not suffice for a reliable estimate of the variance. Also, only stable operating points were investigated, resulting in the neglect of large regions. Nevertheless, the switching frequency optimization shows that reducing the switching frequency at low speeds and most torques can gain $\Delta\eta = 1\%$. Efficiency gains are reduced to $\Delta\eta = 0.02\%$ near the maximum efficiency bulge in the middle of the torque-speed plane, as Figure 8.20(b) shows. Efficiency gains begin to increase again as the speed increases further.

Chapter 9

Conclusion and Future Work

9.1 Conclusion

This work spanned an overview of synchronous machine first principles and its typical control methods. This work also encompassed electric drive high frequency loss modeling and optimization. Coupling not only in dual three-phase machines, but in conventional three-phase machines by means of the coupling coefficient ς was shown to play a crucial role in the current ripple profile over the torque-speed plane. Additional losses in the machine due to interleaving occur mostly at low torques, where the current ripple −and therefore the magnetic field density ripple −is relatively small but the permeability is relatively large: high-frequency losses are proportional to the square-root of the permeability. The FEM analysis could not capture the low-torque losses because eddy current losses were calculated in a post-processing step using just Faraday's law, as opposed to Faraday's law combined with Ampère's law, and therefore the eddy current loss difference mostly followed the current ripple difference and was independent of the permeability. Furthermore, interleaving resonates with the system's magnetic coupling, causing the most loss difference near the modulation index iso-curve with a value of $\sim 2/\pi$. The largest loss difference when interleaving or not occurs in the stator teeth where coupling between duals is spatially highest. The developed coupling model enables the calculation of the eddy currents without the need for FEM. Regarding magnet losses, machine tooth harmonics overlap with frequency components in the first carrier group at high speeds, either decreasing or increasing losses depending on the PWM method and torque level. Said component overlap was confirmed experimentally. As a result of its smoothness and its ease of use for low-dimensional modeling, the squared exponential kernel with Gaussian process regression was used to fit measured data. Measured and simulated data was routinely interpolated by using best-practices, especially input-output normalization. GPR and interpolation were used to minimize the inverter and machine losses by varying the switching frequency, PWM method, and interleaving. Adequate inverter and machine loss models were developed for that purpose. For the investigated machine and inverter, it was found that due to the losses induced in the machine compared to in the inverter including the DC link capacitor, the interleaving angle should remain at zero for strongly coupled machines like the asymmetric machine. For the polar machine the optimization offers little improvement. Reducing the switching frequency improves efficiency by about 1% especially at low speeds where switching losses dominate; increasing the switching

frequency improves efficiency at high speeds due to the reduction of high-frequency iron losses. Simulations show that for highly coupled dual three phase machines like the asymmetric machine, the D6ϕ SVM-B2 12-sector method optimizes the electric drive for all operating points except for the field-weakening region and low torques. For lightly coupled dual three phase machines, all investigated DPWM methods share the optimal operating space. SVM is almost nowhere drive-loss optimal irrespective of the coupling coefficient. Simultaneous switching frequency and PWM method optimization in simulations results in about a 1% efficiency increase for an iso-curve spanning from the corner point to the origin. The simulations regarding optimization agree well for the asymmetric machine but not too well for the polar machine, it does not have large winding harmonics and therefore the fitted inverter model overestimates inverter losses for that machine.

9.2 Future Work

Future work on first principles include the characterization of high frequency permeability outside of the framework of complex permeability which may be measured by conventional Epstein frame methods but with a DC field and small high frequency components. After constructing the minor loops for different bias fields and frequencies, one may calculate an equivalent permeability to better approximate eddy current losses in non-oriented electrical steels with the developed model. Anisotropic permeability and zero-field droops can be incorporated into FEM models by modeling half of a machine and modified permeability curves. One must simulate at least half of the machine to ensure field symmetry due to anisotropy and permeability must depend on the magnetic field angle relative to some anisotropic reference. Regarding future work on control, the low optimal switching frequencies at low speeds require special multi-input multi-output control methods since the large switching frequency assumption no longer holds. Developing such a control method and incorporating it into a variable switching-frequency strategy, preferably with zero switching at the torque-speed origin, would be interesting future work. Investigating the advantages of 12 and 24-sector PWM methods experimentally for dual three-phase IPMSMs is also necessary, as is further investigation into optimizing DPWM methods in terms of the clamping angle.

Appendix A

Electromagnetics

A.1 Analysis and Control of Permanent Magnet Machines

A.1.1 Proof of Torque Equation from Faraday's Law

After establishing that

$$\mathbf{f} = \mathbf{J} \times \mathbf{B}$$

$$\mathbf{f} = \nabla \times \left(\mathbf{H}_m + \frac{\mathbf{B}_s}{\mu} \right) \times \mathbf{B}_s \qquad \text{(A.1.1)}$$

$$\mathbf{f} = \left(\nabla \times \mathbf{H}_m + \frac{1}{\mu} \nabla \times \mathbf{B}_s - \frac{1}{\mu^2} \nabla \mu \times \mathbf{B}_s \right) \times \mathbf{B}_s$$

from Faraday, Lorentz, and Ampere's relations, the tangential component of the force is

$$f_\theta = \frac{1}{r} \left(\frac{1}{\mu^2} \frac{\partial \mu}{\partial \theta} B_s - \frac{\partial H_m}{\partial \theta} - \frac{1}{\mu} \frac{\partial B_s}{\partial \theta} \right) B_s \qquad \text{(A.1.2)}$$

Setting the magnetic flux density from the stator, the permanent magnet field strength, and the permeability quantities as

$$B_s = \hat{B}_s \cos(\theta - \phi) \qquad \text{(A.1.3)}$$

$$H_m = \hat{H}_m \cos\theta \qquad \text{(A.1.4)}$$

$$\mu = \hat{\mu} \left(\gamma + \cos^2\theta \right) \qquad \text{(A.1.5)}$$

equation (A.1.2) becomes

$$f_\theta = \frac{\hat{B}_s}{r} \left(\hat{H}_m \sin\theta \cos(\theta - \phi) + \frac{\hat{B}_s}{\hat{\mu}} \frac{\cos(\theta - \phi)}{\gamma + \cos^2\theta} \left(\sin(\theta - \phi) - \frac{2\cos\theta \sin\theta \cos(\theta - \phi)}{\gamma + \cos^2\theta} \right) \right) \qquad \text{(A.1.6)}$$

We now wish to integrate the tangential, volume-specific force (A.1.6) over the active volume of the rotor. Since the volume differential for a cylinder reads as $dV = r\, dr\, d\theta\, dl$, the tangential force is proportional to the length of the cylindrical rotor and its radius. To acquire an expression for the tangential force it is now only

necessary to integrate the expression over the angle θ over the circumference of the rotor. Said integral will be apportioned to two parts which read as

$$F_{\theta 1} = lR\hat{B}_s\hat{H}_m \int_0^{2\pi} \sin\theta \cos(\theta - \phi)\, d\theta$$

$$F_{\theta 2} = lR\frac{\hat{B}_s^2}{\hat{\mu}} \int_0^{2\pi} \frac{\cos(\theta - \phi)\sin(\theta - \phi)}{\gamma + \cos^2\theta} - \frac{2\cos\theta\sin\theta\cos^2(\theta - \phi)}{(\gamma + \cos^2\theta)^2}\, d\theta \qquad \text{(A.1.7)}$$

such that $F_\theta = F_{\theta 1} + F_{\theta 2}$. Let equation set (A.1.7) make use of $\sin(\theta + \phi) = \sin\theta\cos\phi + \cos\theta\sin\phi$ and $\cos(\theta + \phi) = \cos\theta\cos\phi - \sin\theta\sin\phi$, or the angle sum identities. For $F_{\theta 1}$,

$$
\begin{aligned}
F_{\theta 1} &= lR\hat{B}_s\hat{H}_m \int_0^{2\pi} \sin\theta\cos\theta\cos\phi + \sin^2\theta\sin\phi\, d\theta \\
&= lR\hat{B}_s\hat{H}_m \int_0^{2\pi} \frac{1}{2}\sin 2\theta\cos\phi + \frac{1}{2}(1 - \cos 2\theta)\sin\phi\, d\theta \\
&= lR\hat{B}_s\hat{H}_m\pi\sin\phi
\end{aligned}
\qquad \text{(A.1.8)}
$$

$F_{\theta 2}$ appears more complex, which is why we apportion it to two integrals. The first portion is

$$
\begin{aligned}
F_{\theta 2a} &= lR\frac{\hat{B}_s^2}{\hat{\mu}} \int_0^{2\pi} \frac{\cos(\theta - \phi)\sin(\theta - \phi)}{\gamma + \cos^2\theta}\, d\theta \\
&= lR\frac{\hat{B}_s^2}{2\hat{\mu}} \int_0^{2\pi} \frac{\sin(2\theta - 2\phi)}{\gamma + \cos^2\theta}\, d\theta \\
&= lR\frac{\hat{B}_s^2}{2\hat{\mu}} \int_0^{2\pi} \frac{\sin 2\theta\cos 2\phi - \cos 2\theta\cos 2\phi}{\gamma + \cos^2\theta}\, d\theta \\
&= lR\frac{\hat{B}_s^2}{\hat{\mu}} \left(\cos 2\phi \int_0^{2\pi} \frac{\sin\theta\cos\theta}{\gamma + \cos^2\theta}\, d\theta - \frac{\sin 2\phi}{2} \int_0^{2\pi} \frac{\cos 2\theta}{\gamma + \cos^2\theta}\, d\theta \right) \\
&= lR\frac{\hat{B}_s^2}{\hat{\mu}} \left(-\frac{\cos 2\phi}{2}\log\left|\gamma + \cos^2\theta\right|\Big|_0^{2\pi} - \frac{\sin 2\phi}{2} \int_0^{2\pi} \frac{\cos 2\theta}{\gamma + \cos^2\theta}\, d\theta \right) \\
&= -lR\frac{\hat{B}_s^2}{\hat{\mu}}\frac{\sin 2\phi}{2} \int_0^{2\pi} \frac{-1 + 2\cos^2\theta}{\gamma + \cos^2\theta}\, d\theta \\
&= -lR\frac{\hat{B}_s^2}{\hat{\mu}}\frac{\sin 2\phi}{2} \left(-\frac{1}{\sqrt{\gamma(\gamma + 1)}}\arctan\left(\sqrt{\frac{\gamma}{\gamma + 1}}\tan\theta\right)\Big|_0^{2\pi} + 2\int_0^{2\pi} \frac{\cos^2\theta}{\gamma + \cos^2\theta}\, d\theta \right) \\
&= -lR\frac{\hat{B}_s^2}{\hat{\mu}}\frac{\sin 2\phi}{2} \left(-\frac{2\pi}{\sqrt{\gamma(\gamma + 1)}} + 2\left(\theta - \sqrt{\frac{\gamma}{\gamma + 1}}\arctan\left(\sqrt{\frac{\gamma}{\gamma + 1}}\tan\theta\right)\Big|_0^{2\pi}\right) \right) \\
&= -lR\frac{\hat{B}_s^2}{\hat{\mu}}\pi\sin 2\phi\left(2\left(1 - \sqrt{\frac{\gamma}{\gamma + 1}}\right) - \frac{1}{\sqrt{\gamma(\gamma + 1)}} \right)
\end{aligned}
$$

$$\text{(A.1.9)}$$

The integral depends on γ because the antiderivative is discontinuous, which implies that the integrand had Dirac delta functions at the discontinuities of $\tan\theta$. Because it does not, we must subtract those discontinuities. Upon subtraction of those integrated Dirac impulses −which are step functions −the integral thus reveals a dependence on γ. This phenomenon is furthermore not captured by Cauchy

integration. It may be considered a wrapping of the arctan function over its period of π. The second portion is similarly

$$
\begin{aligned}
F_{\theta 2b} = & -2lR\frac{\hat{B}_s^2}{\hat{\mu}} \int_0^{2\pi} \frac{\cos\theta\sin\theta\cos^2(\theta-\phi)}{(\gamma+\cos^2\theta)^2}\,d\theta \\
= & -lR\frac{\hat{B}_s^2}{\hat{\mu}} \int_0^{2\pi} \frac{\cos\theta\sin\theta(1+\cos(2\theta-2\phi))}{(\gamma+\cos^2\theta)^2}\,d\theta \\
= & -lR\frac{\hat{B}_s^2}{\hat{\mu}} \left(\int_0^{2\pi} \frac{\cos\theta\sin\theta}{(\gamma+\cos^2\theta)^2}\,d\theta + \int_0^{2\pi} \frac{\cos 2\theta\cos 2\phi+\sin 2\theta\sin 2\phi}{(\gamma+\cos^2\theta)^2}\,d\theta \right) \\
= & -lR\frac{\hat{B}_s^2}{\hat{\mu}} \left(\frac{1}{2}\left(\frac{1}{\gamma+\cos^2\theta}\Big|_0^{2\pi}\right) + \int_0^{2\pi} \frac{\cos 2\theta\cos 2\phi+\sin 2\theta\sin 2\phi}{(\gamma+\cos^2\theta)^2}\,d\theta \right) \\
= & -lR\frac{\hat{B}_s^2}{\hat{\mu}} \left(-\cos 2\phi\left(\frac{\gamma+1/2}{\gamma+\cos^2\theta}+\log\left(2\left(\gamma+\cos^2\theta\right)\right)\right)\Big|_0^{2\pi} + \int_0^{2\pi} \frac{\sin 2\theta\sin 2\phi}{(\gamma+\cos^2\theta)^2}\,d\theta \right) \\
= & -lR\frac{\hat{B}_s^2}{\hat{\mu}}\sin 2\phi \int_0^{2\pi} \frac{\sin 2\theta}{(\gamma+\cos^2\theta)^2}\,d\theta \\
= & -lR\frac{\hat{B}_s^2}{\hat{\mu}}\sin 2\phi \left(\frac{2\gamma+1}{\sqrt{\gamma(\gamma+1)}}\arctan\left(\sqrt{\frac{\gamma}{\gamma+1}}\tan\theta\right) - \frac{(2\gamma+1+\cos 2\theta)\theta-\sin 2\theta/2}{\gamma+\cos^2\theta} \right)\Bigg|_0^{2\pi} \\
= & -lR\frac{\hat{B}_s^2}{\hat{\mu}}2\pi\sin 2\phi \left(\frac{2\gamma+1}{\sqrt{\gamma(\gamma+1)}} - 2 \right)
\end{aligned}
$$
(A.1.10)

Adding equations (A.1.9) and (A.1.10) we arrive at

$$
F_{\theta 2} = -lR\frac{\hat{B}_s^2}{\hat{\mu}}\pi\sin 2\phi\left(\frac{2\gamma+1}{\sqrt{\gamma(\gamma+1)}}-2\right) \tag{A.1.11}
$$

which results in the equation for the tangential force on the rotor, shown in equation (A.1.12).

$$
F_\theta = \pi lR\left(\hat{B}_s\hat{H}_m\sin\phi - \frac{\hat{B}_s^2}{\hat{\mu}}\sin 2\phi\left(\frac{2\gamma+1}{\sqrt{\gamma(\gamma+1)}}-2\right)\right) \tag{A.1.12}
$$

Since the lever arm is perpendicular to the tangential force and the length of the lever arm is the radius of the rotor, the electromagnetic torque is

$$
T_e = \pi lR^2\left(\hat{B}_s\hat{H}_m\sin\phi - \frac{\hat{B}_s^2}{\hat{\mu}}\sin 2\phi\left(\frac{2\gamma+1}{\sqrt{\gamma(\gamma+1)}}-2\right)\right). \tag{A.1.13}
$$

Appendix B

Control

B.1 Local Linearization of the Transformed Nonlinear Machine

B.1.1 Proof of System Order Reduction

The system equations in the rotor-synchronous frame are

$$\boldsymbol{u}_{dq} = \begin{bmatrix} R_s & -\omega_e L_q \\ \omega_e L_d & R_s \end{bmatrix} \boldsymbol{i}_{dq} + \begin{bmatrix} L_d & 0 \\ 0 & L_q \end{bmatrix} \frac{d\boldsymbol{i}_{dq}}{dt} + \begin{bmatrix} 0 \\ 1 \end{bmatrix} \omega_e \psi_{pm}, \tag{B.1.1}$$

which after defining

$$\mathbf{G} := \begin{bmatrix} R_s & -\omega_e L_q \\ \omega_e L_d & R_s \end{bmatrix}$$

$$\mathbf{L} := \begin{bmatrix} L_d & 0 \\ 0 & L_q \end{bmatrix} \tag{B.1.2}$$

$$\boldsymbol{u}'_{dq} := \boldsymbol{u}_{dq} - \begin{bmatrix} 0 \\ 1 \end{bmatrix} \omega_e \psi_{pm}$$

and taking the Laplace transform with zero initial conditions results in

$$\boldsymbol{u}'_{dq} = (\mathbf{G} + s\mathbf{L}) \, \boldsymbol{i}_{dq}. \tag{B.1.3}$$

Let the controller be

$$\boldsymbol{u}^*_{dq} = \left(\frac{1}{s}\mathbf{P} + \mathbf{Q} \right) \left(\boldsymbol{i}^*_{dq} - \boldsymbol{i}_{dq} \right) + \begin{bmatrix} 0 \\ 1 \end{bmatrix} \omega_e \psi_{pm} \tag{B.1.4}$$

where $\boldsymbol{u}^*_{dq}$ is the system input, or controller, and $\boldsymbol{i}^*_{dq}$ is the desired current command. To acquire the desired first-order closed loop system behavior with the desired bandwidth a, we first declare the desired system transfer function as

$$\boldsymbol{i}_{dq} = \frac{a}{s + a} \boldsymbol{i}^*_{dq}. \tag{B.1.5}$$

Setting $\boldsymbol{u}_{dq} = \boldsymbol{u}^*_{dq}$ results in

$$\left(\frac{1}{s}\mathbf{P} + \mathbf{Q} \right) \left(\boldsymbol{i}^*_{dq} - \boldsymbol{i}_{dq} \right) = (\mathbf{G} + s\mathbf{L}) \, \boldsymbol{i}_{dq}$$

$$(\mathbf{P} + s\mathbf{Q}) \, \boldsymbol{i}^*_{dq} = (\mathbf{P} + s\mathbf{Q} + s \, (\mathbf{G} + s\mathbf{L})) \, \boldsymbol{i}_{dq} \tag{B.1.6}$$

$$(\mathbf{P} + s\mathbf{Q} + s \, (\mathbf{G} + s\mathbf{L}))^{-1} \, (\mathbf{P} + s\mathbf{Q}) \, \boldsymbol{i}^*_{dq} = \boldsymbol{i}_{dq}.$$

It follows that after setting the matrices in equation (B.1.6) to the transfer function in equation (B.1.5),

$$\left(\mathbf{P} + s\mathbf{Q} + s\left(\mathbf{G} + s\mathbf{L}\right)\right)^{-1}\left(\mathbf{P} + s\mathbf{Q}\right) = \frac{a}{s + a}$$

$$\frac{s + a}{a}\left(\mathbf{P} + s\mathbf{Q}\right) = \left(\mathbf{P} + s\mathbf{Q} + s\left(\mathbf{G} + s\mathbf{L}\right)\right)$$

$$\left(\frac{s}{a} + 1\right)\left(\mathbf{P} + s\mathbf{Q}\right) = \left(\mathbf{P} + s\mathbf{Q} + s\left(\mathbf{G} + s\mathbf{L}\right)\right) \qquad \text{(B.1.7)}$$

$$\frac{1}{a}\left(\mathbf{P} + s\mathbf{Q}\right) = \mathbf{G} + s\mathbf{L}$$

$$\mathbf{P} + s\mathbf{Q} = a\mathbf{G} + sa\mathbf{L}$$

holds. Thereafter one may simply match states to arrive at

$$\begin{aligned} \mathbf{P} &= a\mathbf{G} \\ \mathbf{Q} &= a\mathbf{L} \end{aligned} \qquad \text{(B.1.8)}$$

as claimed.

Bibliography

[1] R. Shaw, Y. Luo, T. Cheong, S. A. Halim, S. Chaturvedi, M. Hashizume, G. Insarov, Y. Ishikawa, M. Jafari, A. Kitoh, J. Pulhin, C. Singh, K. Vasant, and Z. Zhang, *Climate Change 2022: Impacts, Adaptation, and Vulnerability, Contribution of Working Group II to the Sixth Assessment Report of the Intergovernmental Panel on Climate Change*, ch. 10: Transportation. Cambridge University Press, 2022.

[2] F. F. Chen, *An Indispensable Truth: How Fusion Power Can Save the Planet.* 233 Spring Street, New York, NY, 10013: Springer Science+Business Media LLC, 2011.

[3] D. I. Armstrong McKay, A. Stall, J. F. Abrams, R. Winkelmann, B. Sakschewski, S. Loriani, I. Fetzer, S. E. Cornell, J. Rockström, and T. M. Lenton, "Exceeding 1.5°C global warming could trigger multiple climate tipping points," *Science*, vol. 377, September 2022.

[4] IEA, *Global EV Outlook 2023: Catching up with climate ambitions.* Paris: International Energy Agency, April 2023. CC BY 4.0.

[5] J. W. Kolar, H. Ertl, and F. C. Zach, "Analytically Closed Optimization of the Modulation Method of a PWM Rectifier System with High Pulse Rate," in *PCIM'90 Conference*, (Munich), PCIM, June 1990.

[6] J. W. Kolar, H. Ertl, and R. C. Zach, "Influence of the Modulation Method on the Conduction and Switching Losses of a PWM Converter System," *IEEE Transactions on Industry Applications*, vol. 27, pp. 1063–1075, Nov./Dec. 1991.

[7] D. Jiang and F. Wang, "Study of analytical current ripple of three-phase pwm converter," in *27$^{\text{th}}$ Applied Power Electronics Conference and Exposition*, (Orlando), IEEE, February 2012.

[8] D. Jiang and F. F. Wang, "Variable Switching Frequency PWM for Three-Phase Converters Based on Current Ripple Prediction," *IEEE Transactions on Power Electronics*, vol. 28, pp. 4951–4961, November 2013.

[9] A. Andersson, D. Lennström, and A. Nykänen, "Influence of Inverter Modulation Strategy on Electric Drive Efficiency and Perceived Sound Quality," *IEEE Transactions on Transportation Electrification*, vol. 2, pp. 24–35, March 2016.

[10] H. Stemmler and T. Eilinger, "Spectral Analysis of the Sinusoidal PWM with Variable Switching Frequency for Noise Reduction in Inverter-Fed Induction Motors," in *Proceedings of the Power Electronics Specialist Conference*, (Taipei), IEEE, June 1994.

[11] O. Oñederra, I. Kortabarria, I. M. de Alegría, J. Andreu, and J. I. Gárate, "Three-Phase VSI Optimial Switching Loss Reduction Using Variable Switching Frequency," *IEEE Transactions on Power Electronics*, vol. 32, pp. 6570–6576, August 2017.

[12] G. Holmes and T. A. Lipo, *Pulse Width Modulation for Power Converters*. 445 Hoes Lane, Piscataway, NJ 08854: IEEE Press, 2003.

[13] V. Blasko, "Analysis of a Hybrid PWM Based on Modified Space-Vector and Triangle-Comparison Methods," *IEEE Transactions on Industry Applications*, vol. 33, pp. 756–764, May/June 1997.

[14] A. M. Hava, R. J. Kerkman, and T. A. Lipo, "A High-Performance Generalized Discontinuous PWM Algorithm," *IEEE Transactions on Industry Applications*, vol. 34, pp. 1059–1071, September/October 1998.

[15] O. Ojo, "The Generalized Discontinuous PWM Scheme for Three-Phase Voltage Source Inverters," *IEEE Transactions on Industrial Electronics*, vol. 51, pp. 1280–1289, December 2004.

[16] J. Kolar and S. Round, "Analytical calculation of the RMS current stress on the DC-link capacitor of voltage-PWM converter systems," *IEE Proc.-Electr. Power Appl.*, vol. 153, pp. 535–543, July 2006.

[17] A. Boglietti, R. Bojoi, A. Cavagnino, and A. Tenconi, "Efficiency Analysis of PWM Inverter Fed Three-Phase and Dual Three-Phase High Frequency Induction Machines for Low/Medium Power Applications," *IEEE Transactions on Industrial Electronics*, vol. 55, pp. 2015–2023, May 2008.

[18] J.-R. Fu and T. A. Lipo, "Disturbance-Free Operation of a Multiphase Current-Regulated Motor Drive with an Opened Phase," *IEEE Transactions on Industry Applications*, vol. 30, pp. 1267–1274, September/October 1994.

[19] E. Levi, "Multiphase Electric Machines for Variable-Speed Applications," *IEEE Transactions on Industrial Electronics*, vol. 55, pp. 1893–1909, May 2008.

[20] E. Levi, "Advances in Converter Control and Innovative Exploitation of Additional Degrees of Freedom for Multiphase Machines," *IEEE Transactions on Industrial Electronics*, vol. 63, pp. 433–448, January 2016.

[21] L. Alberti and N. Bianchi, "Experimental Tests of Dual Three-Phase Induction Motor Under Faulty Operating Condition," *IEEE Transactions on Industrial Electronics*, vol. 59, pp. 2041–2048, May 2012.

[22] M. Barcaro, N. Bianchi, and F. Magnussen, "Analysis and Tests of a Dual Three-Phase 12-Slot 10-Pole Permanent-Magnet Motor," *IEEE Transactions on Industry Applications*, vol. 46, pp. 2355–2362, November/December 2010.

[23] K. Gopakumar, V. Ranganathan, and S. Bhat, "An Efficient PWM Technique for Split Phase Induction Motor Operation Using Dual Voltage Source Inverters," in 28th *IEEE Industry Applications Conference*, (Toronto), IEEE, October 1993.

[24] Y. Zhao and T. A. Lipo, "Space Vector PWM Control of Dual Three-Phase Induction Machine Using Vector Space Decomposition," *IEEE Transactions on Industry Applications*, vol. 31, pp. 1100–1109, September/October 1995.

[25] J. Prieto, E. Levi, F. Barrero, and S. Toral, "Output Current Ripple Analysis for Asymmetrical Six-Phase Drives Using Double Zero-Sequence Injection PWM," in 37th *Conference of the IEEE Industrial Electronics Society*, (Melbourne), IEEE, January 2011.

[26] P. A. Dahono, "Analysis and Minimization of Output Current Ripple of Multiphase PWM Inverters," in 37th *IEEE Power Electronics Specialists Conference*, (Jeju), IEEE, June 2006.

[27] C. Lascu, L. Asiminoaei, I. Boldea, and F. Blaabjerg, "High Performance Current Controller for Selective Harmonic Compensation in Active Power Filters," *IEEE Transactions on Power Electronics*, vol. 22, pp. 1826–1835, September 2007.

[28] X. Yuan, W. Merk, H. Stemmler, and J. Allmeling, "Stationary-Frame Generalized Integrators for Current Control of Active Power Filters with Zero Steady-State Error for Current Harmonics of Concern under Unbalanced and Distorted Operating Conditions," *IEEE Transactions on Industry Applications*, vol. 38, pp. 523–532, March/April 2002.

[29] C. D. Schauder and S. A. Moran, "Multiple reference frame controller for active filters and power line conditioners," *U.S. Patent 5309353A*, pp. 523–532, May 1994.

[30] J. Karttunen, S. Kallio, J. Honkanen, P. Peltoniemi, and P. Silventoinen, "Partial Current Harmonic Compensation in Dual Three-Phase PMSMs Considering the Limited Available Voltage," *IEEE Transactions on Industrial Electronics*, vol. 64, pp. 1038–1048, February 2017.

[31] L. R. Limongi, R. Bojoi, and G. G. nad Alberto Tenconi, "Digital Current-Control Schemes," *IEEE Industrial Electronics Magazine*, pp. 20–31, March 2009.

[32] Y. Lei, H. Bing-xin, W. Ke-yin, and L. Ying, "A novel current vector decomposition controller design for six-phase permanent magnet synchronous motor," *Journal of Central South University*, vol. 23, pp. 841–849, April 2016.

[33] H. S. Che, E. Levi, M. Jones, W.-P. Hew, and N. A. Rahim, "Current Control Methods for an Asymmetrical Six-Phase Induction Motor Drive," *IEEE Transactions on Power Electronics*, vol. 29, pp. 407–417, January 2014.

[34] L. Xu and L. Ye, "Analysis of a Novel Stator Winding Structure Minimizing Harmonic Current and Torque for Dual Six-Step Converter-Fed High Power AC Machines," *IEEE Transactions on Industry Applications*, vol. 31, pp. 84–90, January/February 1995.

[35] D. Hadiouche, L. Baghli, and A. Rezzoug, "Space-Vectro PWM Techniques for Dual Three-Phase AC Machine: Analysis, Performance Evaluation, and DSP Implementation," *IEEE Transactions on Industry Applications*, vol. 42, pp. 1112–1122, July/August 2006.

[36] K. Marouani, L. Baghli, D. Hadiouche, A. Kheloui, and A. Rezzoug, "A New PWM Strategy Based on a 24-Sector Vector Space Decomposition for a Six-Phase VSI-Fed Dual Stator Induction Motor," *IEEE Transactions on Industrial Electronics*, vol. 55, pp. 1910–1920, May 2008.

[37] B. Cougo, G. Gateau, T. Meynard, M. Bobrowska-Rafal, and M. Cousineau, "PD Modulation Scheme for Three-Phase Parallel Multilevel Inverters," *IEEE Transactions on Industrial Electronics*, vol. 59, pp. 690–700, February 2012.

[38] D. Hadiouche, H. Razik, and A. Rezzoug, "Study and Simulation of Space Vector PWM Control of Double-Star Induction Motors," in *7th International Power Electronics Congress CIEP*, (Acapulco), IEEE, October 2000.

[39] A. Muqorobin, P. A. Dahono, and A. Purwadi, "Analysis and Minimization of Output Current Ripple of Inverter-Fed Six-Phase AC Motors," in *12th International Conference on Power Electronics and Drive Systems*, (Honolulu), IEEE, December 2017.

[40] R. Nelson and P. Krause, "Induction Machine Analysis for Arbitrary Displacement between Multiple Winding Sets," in *Annual Meeting of the IEEE Industry Applications Society*, (Milwaukee), IEEE, October 1973.

[41] E. Klingshirn, "High Phase Order Induction Motors- Part I-Description and Theoretical Considerations," *IEEE Transactions on Power Apparatus and Systems*, vol. PAS-102, pp. 47–53, January 1983.

[42] E. Klingshirn, "High Phase Order Induction Motors- Part II-Description and Theoretical Considerations," *IEEE Transactions on Power Apparatus and Systems*, vol. PAS-102, pp. 54–59, January 1983.

[43] Y. Demir and M. Aydin, "A Novel Asymmetric and Unconventional Stator Winding Configuration and Placement for a Dual Three-Phase Surface PM Motor," *IEEE Transactions on Magnetics*, vol. 53, November 2017.

[44] T. Meynard, A.-M. Lienhardt, V. Devanneaux, P. Brodeau, Ruelland, and J.-P. Carayon, "Device with a Polyphase Electrical Machine, and Related Electrical Machine," *U.S. Patent 8564238B2*, October 2013.

[45] D. Jarrot, Y. Lefevre, C. Henaux, and T. Meynard, "Synchronous Motor Winding Segmentation for Parallel Interleaved Inverters," in *22th International Conference on Electrical Machines*, (Lausanne), IEEE, September 2016.

[46] D. Zhang, F. Wang, R. Burgos, R. Lai, and D. Boroyevich, "DC-Link Ripple Current Reduction for Paralleled Three-Phase Voltage-Source Converters with Interleaving," *IEEE Transactions on Power Electronics*, vol. 26, pp. 1741–1753, June 2011.

[47] R. Bojoi, M. Caponet, G. Grieco, M. Lazzari, A. Tenconi, and F. Profumo, "Computation and Measurements of the DC Link Current in six-phase Voltage Source PWM Inverters for AC Motor Drives," in *Proc. Power Conversion Conference*, (Osaka), IEEE, April 2002.

[48] G.-J. Su and L. Tang, "A Segmented Traction Drive System with a Small DC Bus Capacitor," in *IEEE Energy Conversion Congress and Exposition*, (Raleigh), IEEE, September 2012.

[49] S. Bhattacharya, D. Mascarella, and G. Joos, "Interleaved SVPWM and DPWM for dual three-phase inverter-PMSM: An automotive application," in *Transportation Electrification Conference and Expo*, (Dearborn), IEEE, June 2014.

[50] P. A. Dahono, "Analysis and Minimization of Output Current Ripple of Multiphase PWM Inverters," in 37th *IEEE Power Electronics Specialists Conference*, (Jeju), IEEE, June 2006.

[51] L. Asiminoaei, E. Aeloiza, P. N. Enjeti, and F. Blaabjerg, "Shunt Active-Power-Filter Topology Based on Parallel Interleaved Inverters," *IEEE Transactions on Industrial Electronics*, vol. 55, pp. 1175–1189, March 2008.

[52] D. Zhang, F. Wang, R. Burgos, R. Lai, and D. Boroyevich, "Impact of Interleaving on AC Passive Components of Paralleled Three-Phase Voltage-Source Converters," *IEEE Transactions on Industry Applications*, vol. 46, pp. 1042–1054, May/June 2010.

[53] S. K. Miller, T. Beechner, and J. Sun, "A Comprehensive Study of Harmonic Cancellation Effects in Interleaved Three-Phase VSCs," in *IEEE Power Electronics Specialists Conference*, (Orlando), IEEE, June 2007.

[54] P.-L. Wong, P. Xu, B. Yang, and F. C. Lee, "Performance Improvements of Interleaving VRMs with Coupling Inductors," *IEEE Transactions on Power Electronics*, vol. 16, pp. 499–507, July 2001.

[55] F. Ueda, K. Matsui, M. Asao, and K. Tsuboi, "Parallel-Connections of Pulsewidth Modulated Inverters Using Current Sharing Reactors," *IEEE Transactions on Power Electronics*, vol. 10, pp. 673–679, November 1995.

[56] G. Gohil, L. Bede, R. Teodorescu, T. Kerekes, and F. Blaabjerg, "An Integrated Inductor for Parallel Interleaved Three-Phase Voltage Source Converters," *IEEE Transactions on Power Electronics*, vol. 31, pp. 3400–3414, May 2016.

[57] G. Gohil, R. Maheshwari, L. Bede, T. Kerekes, R. Teodorescu, M. Liserre, and F. Blaabjerg, "Modified Discontinuous PWM for Size Reduction of the Circulating Current Filter in Parallel Interleaved Converters," *IEEE Transactions on Power Electronics*, vol. 30, pp. 3457–3470, July 2015.

[58] Z. Quan and Y. W. Li, "Impact of PWM Schemes on the Common-Mode Voltage of Interleaved Three-Phase Two-Level Voltage Source Converters," *IEEE Transactions on Industrial Electronics*, vol. 66, pp. 852–864, February 2019.

[59] K. Xing, F. C. Lee, D. Borojevic, Z. Ye, and S. Mazumder, "Interleaved PWM with Discontinuous Space-Vector Modulation," *IEEE Transactions on Power Electronics*, vol. 14, pp. 906–917, September 1999.

[60] L. Xing and J. Sun, "Motor drive system EMI reduction by asymmetric interleaving," in *12*[th] *Workshop on Control and Modeling for Power Electronics*, (Boulder), IEEE, June 2010.

[61] Y. Huang, Y. Xu, W. Zhang, and J. Zou, "PWM Frequency Noise Cancellation in Two-Segment Three-Phase Motor Using Parallel Interleaved Inverters," *IEEE Transactions on Power Electronics*, vol. 34, pp. 2515–2525, March 2019.

[62] H. Huang, W. Zhang, Y. Xu, and J. Zou, "PWM Frequency Noise Reduction in Dual-Segment Three-Phase PMSM with Magnetically Coupled Inductors and Parallel Interleaved Inverters," in *22*[th] *International Conference on Electrical Machines and Systems*, (Harbin), IEEE, August 2019.

[63] H.-H. Hsu and Y.-Y. Tzou, "FPGA Control and Implementation of a Multiphase-Interleaved PWM Inverter for a Segmented PMSM," in *11*[th] *International Conference on Power Electronics and Drive Systems*, (Sydney), IEEE, June 2015.

[64] A. Soualmi, F. Dubas, D. Depernet, A. Randria, and C. Espanet, "Study of copper losses in the stator windings and pm eddy-current losses for pm synchronous machines taking into account influence of pwm harmonics," in *15*[th] *International Conference on Electrical Machines and Systems*, (Sapporo), IEEE, October 2012.

[65] M. van der Geest, H. Polinder, and J. Ferreira, "Influence of PWM switching frequency on the losses in PM machines," in *International Conference on Electrical Machines*, (Berlin), IEEE, September 2014.

[66] G. Müller, K. Vogt, and B. Ponick, *Berechnung elektrischer Maschinen*. Weinheim: WILEY-VCH Verlag GmbH & Co KGaA, 2008.

[67] R. B. Inderka, C. E. Carstensen, and R. W. D. Donker, "Eddy currents in medium power switched reluctance machines," in *33*[rd] *Power Electronics Specialists Conference*, (Cairns), IEEE, June 2002.

[68] S. Iwasaki, R. P. Deodhar, Y. Liu, A. Pride, Z. Zhu, and J. J. Bremner, "Influence of PWM on the Proximity Loss in Permanent-Magnet Brushless AC Machines," *IEEE Transactions on Industry Applications*, vol. 45, pp. 1359–1367, July/August 2009.

[69] P. H. Mellor, R. Wrobel, and N. McNeill, "Investigation of proximity losses in a high speed brushless permanent magnet motor," in *41*[st] *Industry Applications Conference*, (Tampa), IEEE, October 2006.

[70] M. S. Raven, "Impedance and skin effect measurements for a large regular planar copper wire meander," *Acta Technica*, vol. 61, pp. 91–105, January 2016.

[71] S. K. Mukerji, M. George, M. B. Ramamurthy, and K. Asaduzzaman, "EDDY CURRENTS IN SOLID RECTANGULAR CORES," *Progress In Electromagnetics Research B*, vol. 7, pp. 117–131, 2008.

[72] A. Andersson and T. Thiringer, "Inverter Losses Minimization Using Variable Switching Frequency Based On Multi-objective Optimization," in *International Conference on Electrical Machines*, (Berlin), IEEE, September 2014.

[73] D. Jiang, Q. Li, X. Han, and R. Qu, "Variable Switching Frequency PWM for Torque Ripple Control of AC Motors," in *19*[th] *International Conference on Electrical Machines and Systems*, (Chiba), IEEE, November 2016.

[74] L. Chang and T. M. Jahns, "Prediction and Evaluation of PWM-Induced Current Ripple in IPM Machines Incorporating Slotting, Saturation, and Cross-Coupling Effects," in *20*[th] *International Conference on Electrical Machines and Systems*, (Sydney), IEEE, August 2017.

[75] F. Ramirez and M. Pacas, "Finite Control Set Model Based Predictive Control of a PMSM with Variable Switching Frequency and Torque Ripple Optimization," in *International Exhibition and Conference for Power Electronics, Intelligent Motion, Renewable Energy and Energy Management*, (Nuremberg), IEEE, May 2016.

[76] F. D. Ramirez-Figueroa and M. Pacas, "FPGA Implementation of a Predictive Control for a PMSM with Variable Switching Frequency," in *International Aegean Conference on Electrical Machines & Power Electronics*, (Side), IEEE, September 2015.

[77] F. Yang, A. R. Taylor, H. Bai, B. Cheng, and A. A. Khan, "Using d-q Transformation to Vary the Switching Frequency for Interior Permanent Magnet Synchronous Motor Drive Systems," *IEEE Transactions on Transportation Electrification*, vol. 1, pp. 277–2015, October 2015.

[78] J. Lemmens, P. Vanassche, and J. Driesen, "Optimal Control of Traction Motor Drives Under Electrothermal Constraints," *IEEE Journal of Emerging and Selected Topics in Power Electronics*, vol. 2, pp. 249–263, June 2014.

[79] J. Ottosson, M. Alakula, and D. Hagstedt, "Electro-Thermal Simulations of a Power Electronic Inverter for a Hybrid Car," in *International Electric Machines and Drives Conference*, (Niagara Falls), IEEE, May 2011.

[80] N. Takahashi, M. Morishita, D. Miyagi, and M. Nakano, "Examination of Magnetic Properties of Magnetic Materials at High Temperature Using a Ring Specimen," *IEEE Transactions on Magnetics*, vol. 46, pp. 548–551, February 2010.

[81] S. Xue, J. Feng, S. Guo, J. Peng, W. Chu, and Z. Zhu, "A New Iron Loss Model for Temperature Dependencies of Hysteresis and Eddy Current Losses in Electrical Machines," *IEEE Transactions on Magnetics*, vol. 54, January 2018.

[82] A. Boglietti, P. Ferraris, M. Lazzari, and M. Pastorelli, "Change of the Iron Losses with the Switching Supply Frequency in Soft Magnetic Materials by PWM Inverter," *IEEE Transactions on Magnetics*, vol. 31, pp. 4250–4252, November 1995.

[83] W. Martinez, S. Odawara, and K. Fujisaki, "Iron Loss Characteristics Evaluation Using a High-Frequency GaN Inverter Excitation," *IEEE Transactions on Magnetics*, vol. 53, November 2017.

[84] A. Boglietti, P. Ferraris, M. Lazzari, and F. Profumo, "Effects of Different Modulation Index on the Iron Losses in Soft Magnetic Materials Supplied by PWM Inverter," *IEEE Transactions on Magnetics*, vol. 29, pp. 3234–3236, November 1993.

[85] P. Karlovsky, O. Lipcak, and J. Bauer, "Iron Loss Minimization Strategy for Predictive Torque Control of Induction Motor," *MDPI electronics*, vol. 9, March 2020.

[86] A. Boglietti, A. Cavagnino, D. M. Ionel, M. Popescu, D. A. Staton, and S. Vaschetto, "A General Model to Predict the Iron Losses in PWM Inverter-Fed Induction Motors," *IEEE Transactions on Industry Applications*, vol. 46, pp. 1882–1890, September/October 2010.

[87] A. Boglietti, M. Chiampi, M. Repetto, O. Bottauscio, and D. Chiarabaglio, "Loss Separation Analysis in Ferromagnetic Sheets under PWM Inverter Supply," *IEEE Transactions on Magnetics*, vol. 34, pp. 1240–1242, July 1998.

[88] Y. Miyama, M. Hazeyama, S. Hanioka, N. Watanabe, A. Daikoku, and M. Inoue, "PWM Carrier Harmonic Iron Loss Reduction Technique of Permanent-Magnet Motors for Electric Vehicles," *IEEE Transactions on Industry Applications*, vol. 52, pp. 2865–2871, July/August 2016.

[89] F. Deng and T. W. Nehl, "Analytical Modeling of Eddy-Current Losses Caused by Pulse-Width-Modulation Switching in Permanent-Magnet Brushless Direct-Current Motors," *IEEE Transactions on Magnetics*, vol. 34, pp. 3728–3736, September 1998.

[90] E. Barbisio, F. Fiorillo, and C. Ragusa, "Predicting Loss in Magnetic Steels Under Arbitrary Induction Waveform and With Minor Hysteresis Loops," *IEEE Transactions on Magnetics*, vol. 40, pp. 1810–1819, July 2004.

[91] H. Fukunaga, T. Eguchi, Y. Ohta, and H. Kakehashi, "Core Loss in Amorphous Cut Cores with Air Gaps," *IEEE Transactions on Magnetics*, vol. 25, pp. 2694–2698, May 1989.

[92] A. Krings and J. Soulard, "Overview and Comparison of Iron Loss Models for Electrical Machines," *Journal of Electrical Engineering-elektrotechnicky Casopis*, vol. 10, pp. 162–169, 2010.

[93] J. Reinert, A. Brockmeyer, and R. W. D. Doncker, "Calculation of Losses in Ferro- and Ferrimagnetic Materials Based on the Modified Steinmetz Equation," *IEEE Transactions on Industry Applications*, vol. 37, pp. 1055–1061, July/August 2001.

[94] K. Venkatachalam, C. R. Sullivan, T. Abdallah, and H. Tacca, "Accurate Prediction of Ferrite Core Loss with Nonsinusoidal Waveforms Using Only Steinmetz Parameters," in *Workshop on Computers in Power Electronics*, (Mayaguez), IEEE, June 2002.

[95] G. Bertotti, *Hysteresis in Magnetism for Physicists, Materials Scientists, and Engineers.* 525 B Street, Suite 1900, San Diego, CA 92101: Academic Press, Inc., 1998.

[96] L. Dupré, M. D. Wulf, D. Makaveev, V. Permiakov, A. Pulnikov, and J. Melkebeek, "Modelling of electromagnetic losses in asynchronous machines," *International Journal for Computation and Mathematics in Electrical and Electronic Engineering*, vol. 22, no. 4, pp. 1061–1065, 2003.

[97] K. Yamazaki and Y. Kato, "Iron Loss Analysis of Interior Permanent Magnet Synchronous Motors by Considering Mechanical Stress and Deformation of Stators and Rotors," *IEEE Transactions on Magnetics*, vol. 50, February 2014.

[98] N. Yogal, C. Lehrmann, M. Henke, and H. Zheng, "Measurement, Simulation and Calculation Using Fourier Transformation of Iron Losses for Electrical Steel Sheets with Higher Frequency and Temperature Effects," in *12th International Conference on Electrical Machines*, (Lausanne), IEEE, September 2016.

[99] A. Bergqvist, A. Lundgren, and G. Engdahl, "Experimental testing of an anisotropic vector hysteresis model," *IEEE Transactions on Magnetics*, vol. 33, pp. 4152–4154, September 1997.

[100] L. Dupré, R. V. Keer, and J. Melkebeek, "A Study of the Influence of Laser Cutting and Punching on the Electromagnetic Behavious of Electrical Steel Sheets Using a Combined Finite Element-Dynamic Preisach Model," in *4th International Workshop on Electric and Magnetic Fields*, (Montefiore), pp. 195–200, Assoc. Ingé, 1998.

[101] H. Zhao, C. Ragusa, O. de la Barrière, M. Khan, C. Appino, and F. Fiorillo, "Magnetic Loss Versus Frequency in Non-Oriented Steel Sheets and Its Prediction: Minor Loops, PWM, and the Limits of the Analytical Approach," *IEEE Transactions on Magnetics*, vol. 53, November 2017.

[102] G. von Pfingsten, S. Steentjes, M. Hombitzer, D. Franck, and K. Hameyer, "Influence of Winding Scheme on the Iron-Loss Distribution in Permanent Magnet Synchronous Machines," *IEEE Transactions on Magnetics*, vol. 50, April 2014.

[103] S. Naidu, "Simulation of the hysteresis phenomenon using Preisach's theory," *IEE Proceedings*, vol. 137A, pp. 73–79, March 1990.

[104] D. D. Reljić, D. Z. Matić, D. G. Jerkan, D. V. Oros, and V. V. Vasić, "The Estimation of Iron Losses in a Non-Oriented Electrical Steel Sheet Based on the Artificial Neural Network and the Genetic Algorithm Approaches," in *IEEE International Energy Conference*, (Cavtat), IEEE, May 2014.

[105] N. Urasaki, T. Senjyu, and K. Uezato, "A Novel Calculation Method for Iron Loss Resistance Suitable in Modeling Permanent-Magnet Synchronous Motors," *IEEE Transactions on Energy Conversion*, vol. 18, pp. 41–47, March 2003.

[106] J. Richter, A. Dollinger, and M. Doppelbauer, "Iron Loss and Permanent Measurement of Permanent Magnet Synchronous Machines," in *International Conference on Electrical Machines*, (Berlin), IEEE, September 2014.

[107] K. Yamazaki and Y. Seto, "Iron Loss Analysis of Interior Permanent-Magnet Synchronous Motors−Variation of Main Loss Factors Due to Driving Condition," *IEEE Transactions on Industry Applications*, vol. 42, pp. 1045–1052, July/August 2006.

[108] D. Kowal, P. Sergeant, L. Dupré, and H. Karmaker, "Comparison of Frequency and Time-Domain Iron and Magnet Loss Modeling Including PWM Harmonics in a PMSG for a Wind Energy Application," *IEEE Transactions on Energy Conversion*, vol. 30, pp. 476–486, June 2015.

[109] D. Kowal, P. Sergeant, L. Dupré, and L. Vandenbossche, "Comparison of Iron Loss Models for Electrical Machines With Different Frequency Domain and Time Domain Methods for Excess Loss Prediction," *IEEE Transactions on Magnetics*, vol. 51, January 2015.

[110] K. Yamazaki, Y. Kanou, Y. Fukushima, S. Ohki, A. Nezu, T. Ikemi, and R. Mizokami, "Reduction of Magnet Eddy-Current Loss in Interior Permanent-Magnet Motors With Concentrated Windings," *IEEE Transactions on Industry Applications*, vol. 46, pp. 2434–2441, November/December 2010.

[111] Y. Kawase, T. Ota, and H. Fukunaga, "3-D Current Analysis in Permanent Magnet of Interior Permanent Magnet Motors," *IEEE Transactions on Magnetics*, vol. 36, pp. 1863–1866, July 2000.

[112] K. Yamazaki and A. Abe, "Loss Investigation of Interior Permanent-Magnet Motors Considering Carrier Harmonics and Magnet Eddy Currents," *IEEE Transactions on Industry Applications*, vol. 45, pp. 659–665, March/April 2009.

[113] R. Nuscheler, "Two-Dimensional Analytical Model for Eddy-Current Rotor Loss Calculation of PMS Machines with Concentrated Stator Windings and a Conductive Shield for the Magnets," in *International Conference on Electrical Machines*, (Rome), IEEE, September 2010.

[114] M. Mirzaei, A. Binder, B. Funieru, and M. Susic, "Analytical Calculations of Induced Eddy Currents Losses in the Magnets of Surface Mounted PM

Machines With Consideration of Circumferential and Axial Segmentation Effects," *IEEE Transactions on Magnetics*, vol. 48, pp. 4831–4841, December 2012.

[115] M. Paradkar and J. Böcker, "3D Analytical Model for Estimation of Eddy Current Losses in the Magnets of IPM Machine Considering the Reaction Field of the Induced Eddy Currents," in *IEEE Energy Conversion Congress and Exposition*, (Montreal), IEEE, September 2015.

[116] S. K. Mukerji, M. George, M. B. Ramamurthy, and K. Asaduzzaman, "EDDY CURRENTS IN LAMINATED RECTANGULAR CORES," *Progress In Electromagnetics Research*, vol. 83, pp. 435–445, 2008.

[117] P. Sergeant, H. Vansompel, A. Hemeida, A. V. den Bossche, and L. Dupré, "A Computationally Efficient Method to Determine Iron and Magnet Losses in VSI-PWM Fed Axial Flux Permanent Magnet Synchronous Machines," *IEEE Transactions on Magnetics*, vol. 50, August 2014.

[118] W.-Y. Huang, A. Bettayeb, R. Kaczmarek, and J.-C. Vannier, "Optimization of Magnet Segmentation for Reduction of Eddy-Current Losses in Permanent Magnet Synchronous Machine," *IEEE Transactions on Energy Conversion*, vol. 25, pp. 381–387, June 2010.

[119] K. Yamazaki, Y. Fukushima, and M. Sato, "Loss Analysis of Permanent-Magnet Motors With Concentrated Windings−Variation of Magnet Eddy-Current Loss Due to Stator and Rotor Shapes," *IEEE Transactions on Industry Applications*, vol. 45, pp. 659–665, July/August 2009.

[120] M. Merdzan, J. Paulides, and E. Lomonova, "Comparative analysis of rotor losses in high-speed permanent magnet machines with different winding configurations considering the influence of the inverter pwm," in 10th *International Conference on Ecological Vehicles and Renewable Energies*, (Monte Carlo), IEEE, March–April 2015.

[121] J. Lange, S. Wachter, T. Engelhardt, S. Oechslen, and A. Heitmann, "Highly integrated electric axle," in *E-MOTIVE Expert Forum on Electric Vehicle Drives*, (Schweinfurt), FVA, September 2019.

[122] P.-O. Gronwald and T. A. Kern, "Traction motor cooling systems, a literature review and comparative study," *IEEE Transactions on Transportation Electrification*, vol. 7, pp. 2892–2813, December 2021.

[123] B. Deusinger and A. Binder, "Quantitative Analysis and Finite Element Modeling for Indirect Efficiency Determination of Permanent Magnet Machines," in 10th *International Conference on Energy Efficiency in Motor Driven Systems*, (Rome), European Commission, September 2017.

[124] T. M. Jahns, "Flux-Weakening Regime Operation of an Interior Permanent-Magnet Synchronous Motor Drive," *IEEE Transactions on Industry Applications*, vol. IA-23, pp. 681–689, July/August 1987.

[125] S. Morimoto, Y. Takeda, T. Hirasa, and K. Taniguchi, "Expansion of Operating Limits for Permanent Magnet Motor by Current Vector Control Considering Inverter Capacity," *IEEE Transactions on Industry Applications*, vol. 26, pp. 866–871, September/October 1990.

[126] S. Morimoto, Y. Tong, Y. Takeda, and T. Hirasa, "Loss Minimization Control of Permanent Magnet Synchronous Motor Drives," *IEEE Transactions on Industrial Electronics*, vol. 41, pp. 511–517, October 1994.

[127] L. Schwager, A. Tüysüz, C. Zwyssig, and J. W. Kolar, "Modeling and Comparison of Machine and Converter Losses for PWM and PAM in High-Speed Drives," *IEEE Transactions on Industry Applications*, vol. 50, pp. 995–1006, March/April 2014.

[128] A. G. Sarigiannidis and A. G. Kladas, "Switching Frequency Impact on Permanent Magnet Motors Drive System for Electric Actuation Applications," *IEEE Transactions on Magnetics*, vol. 51, March 2015.

[129] M. Stempfle, Y. Han, J. Wölfle, N. Tröster, and J. Roth-Stielow, "Influence of Different Switching Frequencies and Modulation Techniques on IPMSM and Inverter Losses Optimizing the Overall Drive Train Efficiency," in *International Exhibition and Conference for Power Electronics, Intelligent Motion, Renewable Energy and Energy Management*, (Nuremberg), VDE, May 2017.

[130] W. P. Houser, "Deriving the Lorentz force equation from Maxwell's equations," in *Proceedings IEEE SoutheastCon 2002*, (Columbia, SC, USA), IEEE, April 2002.

[131] M. Meyer and J. Böcker, "Optimum Control for Interior Permanent Magnet Synchronous Motors (IPMSM) in Constant Torque and Flux Weakening Range," in *EPE-PEMC Conference*, (Portorož), 2006.

[132] N. Marmolejo and M. Doppelbauer, "Influence of interleaved converters on iron losses in dual three-phase permanent magnet machines," in *Proceedings of the 10th International Conference on Power Electronics (PEMD 2020)*, (Online Conference), IET, September 2021.

[133] N. Marmolejo, X. Tang, and M. Doppelbauer, "Influence of different pulse-width modulation methods on magnet losses in permanent magnet synchronous machines," in *Proceedings of the 22nd European Conference on Power Electronics and Applications (EPE'20 ECCE Europe)*, (Lyon, France), IEEE, October 2020.

[134] X. Tang, "Untersuchung des Einflusses der Segmentierung und Umrichter-Parameter auf Magnetverluste einer sechsphasigen permanentmagnetisch erregten Synchronmaschine," Master's thesis, Universit at Stuttgart, 2019.

[135] A. E. Hayek, P. Venet, R. Mitova, M.-X. Wang, G. Clerc, and A. Sari, "Aging laws of electrolytic capacitors," in *Evolution of Functional Performance and Expected Lifetime of Electrical Equipment (ELTEE)*, (Grenoble, France), pp. 16–17, HAL, October 2018.

[136] R. Gallay, "Metallized Film Capacitor Lifetime Evaluation and Failure Mode Analysis," May 2014.

[137] M. Shiozaki and Y. Kurosaki, "Anisotropy of Magnetic Properties in Non-Oriented Electrical Steel Sheets," *Textures and Microstructures*, vol. 11, pp. 159–170, 1989.

[138] M. Salcone and J. Bond, "Selecting film bus link capacitors for high performance inverter applications," in *International Electric Machines and Drives Conference*, (Miami, FL, USA), IEEE, May 2009.

List of Figures